THE UNIVERSITY OF CHICAGO

LEVERAGING CONTROL OF THE SECONDARY SPHERE WITH FE AND NI COMPLEXES OF A REDOX-ACTIVE DIHYDRAZONOPYRROLE LIGAND FEATURING PENDANT PROTONS

A DISSERTATION SUBMITTED TO
THE FACULTY OF THE DIVISION OF THE PHYSICAL SCIENCES
IN CANDIDACY FOR THE DEGREE OF
DOCTOR OF PHILOSOPHY

DEPARTMENT OF CHEMISTRY

BY
KATE ASHLEY JESSE

CHICAGO, ILLINOIS
AUGUST 2021

Table of Contents

List of Figures

Chapter 1

Chapter 2

Chapter 3

Chapter 4

Appendix 1

Appendix 2

Appendix 3

Appendix 4

List of Schemes

Introduction

Chapter 1

Chapter 2

Chapter 3

Chapter 4

Appendix 3

List of Tables

Chapter 2

Chapter 4

Appendix 1

Appendix 2

Appendix 3

Appendix 4

List of Abbreviations

acac	Acetylacetonate
Avg	Average
br	Broad
Bu	Butyl
calcd	Calculated
cm	Centimeter
cm^{-1}	Wavenumber
CSD	Cambridge Structural Database
CV	Cyclic voltammogram
Cy	Cyclohexyl
d	Doublet or deuterium
dba	Dibenzylideneacetone
DCM	Dichloromethane
dd	Doublet of doublets
d_x	Compound with x deuterium atoms
DFT	Density Functional Theory
DHP	Dihydrazonopyrrole
DIPy	Diiminopyrrole
DME	1,2-dimethoxyethane
DMSO	Dimethylsulfoxide
e	Electron
EPR	Electron paramagnetic Resonance

eq	Equivalents
equiv	Equivalents
EXAFS	X-ray Absorption Fine Structure
eV	Electron Volt
Fc	Ferrocene
G	Gauss
g	Gram
g	Electron g-factor
GC	Gas Chromatography
GHz	Gigahertz
Hz	Herzt
iPr	Isopropyl
IR	Infrared
J	NMR Coupling Constant
k	Rate constant
kcal	Kilocalorie
m	Multiplet
M	Concentration in molarity
mg	milligram
MHz	Megahertz
mM	Millimolar
mm	millimeter
MS	Mass Spectrometry

mV	Millivolt
mmol	Millimole
mol	Mole
nm	Nanometer
NMR	Nuclear Magnetic Resonance
PDI	Pyridine diimine
Ph	Phenyl
q	Quartet
R	Generic organic group or R-factor
RT	Room temperature
S	Spin quantum number
s	Singlet or second
t	Triplet or time
*t*Bu	*Tert*-butyl
TEP	Tolman Electronic Parameter
Tf	SO_2CF_3
THF	Tetrahydrofuran
TMS	Trimethylsilyl
UV	Ultraviolet
V	Volt
Vis	Visible
wR	Weighted R-factor
XAS	X-ray absorption spectroscopy

XRD	X-ray Diffraction
δ	Chemical Shift
°	Degree
°C	Degrees Celsius
ε	Extinction Coefficient
η^x	Hapticity of order x
λ	Wavelength
µA	Microamps
μ_B	Bohr magneton
μ_{eff}	Effective magnetic moment
Å	Angstrom
^1H	Hydrogen-1
^{11}B	Boron-11
^{19}F	Fluorine-19
^{13}C	Carbon-13
^{31}P	Phosphorous-31
$\{^1H\}$	Proton decoupled
Def2-TZVP, etc	Basis sets for DFT
B3P, etc	DFT functionals

Acknowledgements

First and foremost, I would like to thank my advisor, Prof. John Anderson for his guidance throughout my graduate career. I have particularly appreciated his willingness and availabiliity to discuss my project ideas, regardless of how realistic or not realistic they were. I also really appreciate the mentorship opportunities he made available to me so that I could further develop those skills. Next, I would like to thank my committee members, Prof. Michael Hopkins and Prof. Mark Levin, for helpful discussions. I would like to also thank the Anderson group in general for helpful discussions.

I would like to thank the other members of the bifunctional subgroup in general for sharing a glovebox with me and for helpful discussions. I would have been utterly lost without the mentorship of Prof. Mu-Chieh Chang during my first and second year. I also appreciate the opportunities I had to work on various projects with Dr. Andrew McNeece both before and after his graduation. I also would like to thank him for an inumerable amount of helpful discussions pertaining to my project, crystallography, and for generally letting me bounce ideas off of him. Next, I would like to thank Sophie Anferov for helpful discussions and a seemingly never ending number of puns that she would share as we worked in the glovebox. I would also like to thank Vennela Mannava for being a wonderful mentee. It was an honor to watch her grow as a researcher and I look forward to seeing what she works on in graduate school.

I would like to thank Dr. Alexander Filatov, Prof. Mu-Chieh Chang, and Dr. Andrew McNeece for mentoring me as a crystallographer. Dr. Filatov’s insight and advice was particularly invaluable, and I appreciate the opportunities he provided for me to improve my collection and solving techniques for SXRD. I would like to thank Dr. Valerie Keller and Dr. Britni Ratliff for their mentorship in problem set design, flipped classroom techniques, and teaching in general. Participating in the collaborative learning program was one of my favorite experiences during graduate school.

Finally, I would like to thank the people who supported me outside of my academic pursuits. First, I would like to thank my mom and dad, who have always been my biggest cheerleaders. My dad use to tell me how proud he was every time we spoke and I wish he could come to my defense to see what I have been working on for the past five years. Next, I would like to thank my friends, from Portland, college, and all of the wonderful people I have met here at the University of Chicago. I would like to thank S. J. for his unfailing love, support, and helpful discussions. Last, I would like to thank the Tuesday crew, i.e. Dr. Amanda McQuade and Jared Goldberg. They are in no small part responsible for keeping me sane during the past year and a half. I could not ask for a better support system.

Abstract

Hydrogen transfer chemistry is an important due to its wide variety of applications in industrial processes and pharmaceutical development. For this reason, there has been extensive research into catalyst design for reactions involving hydrogen transfer reactivity. Homogenous catalysts are attractive for studies due to the relative ease of their characterization. Metal-ligand cooperativity can allow first row transition metals to catalyze multi-electron and multi-proton processes, and, as such, has become an important tool in in transition metal catalyzed chemical synthesis and industrial transformations such as hydrogenation. For example, the use of redox-active ligands can allow first row transition metals that often facilitate 1 electron chemistry to facilitate 2 electron chemistry. Additionally, pendant protons on the ligand have been found to facilitate proton shuttling and engage in hydrogen bonding interactions that stabilize reactive intermediates. Recent work combining these two strategies into a single ligand scaffold has been found to be extremely effective at facilitating challenging multi-electron and multi-proton reactivity. In these studies, a 2,5-dihydrazonopyrrole (DHP) ligand scaffold was utilized in complexes with Ni and Fe. This ligand scaffold can store a full H_2 equivalent in the ligand scaffold itself in addition to the redox capabilities of the metal center.

In Chapter 1, I discuss a DHP complex with Ni, where an H_2 equivalent can be stored on the ligand periphery without metal-based redox changes and can be leveraged for catalytic hydrogenations. Kinetic and computational analysis suggests ligand hydrogenation proceeds by H_2 association followed by H-H scission. This complex is an unusual example where a synthetic system can mimic biology's ability to mediate H_2 transfer via secondary coordination sphere-based processes.

DHP ligands have been isolated in a variety of redox and protonation states when complexed to Ni, but the redox-state of this ligand scaffold is less obvious when complexed to metal centers with more accessible redox couples. In Chapter 2, I discuss the synthesis of a new series of Fe-DHP complexes with phenyl groups on the hydrazone arms in two distinct oxidation states. Detailed characterization supports that the redox-chemistry in this set is still primarily ligand based. These complexes exist as 5-coordinate species with an open coordination site offering the possibility of enhanced reactivity. Additionally, the solvatochromism of these complexes is discussed.

In Nature, enzymes carefully control the movement of protons and electrons via amino acids in the secondary sphere of the enzyme active site. This allows for precise reactivity using kinetically inert oxidants, such as O_2. Harnessing metal-ligand cooperativity to control the secondary sphere of molecular catalysts mimics the strategies used in nature. Chapter 3 discusses the DHP ligand with *tert*-butyl groups on the hydrazone pincer arms complexed to Fe. This complex has a hydrogenated ligand which can donate two electrons and two protons to a substrate. In the presence of O_2, this complex reduces O_2 via a high spin Fe(III)-hydroperoxo intermediate which features a $DHP^{\bullet}$ ligand radical. This intermediate is characterized by a variety of spectroscopic and computational techniques. This reactivity mimics that of Fe enzymes.

In Chapter 4, we discuss a family of bisneocuproine complexes of Fe^{2+} and Co^{2+} have been investigated for neocuproine redox noninnocence. A series of redox isomers of $M(neocuproine)_2^{n+}$ (where n = 2, 1, and 0 for Co and 2 and 0 for Fe) were synthesized and thoroughly characterized. The electronic structure of these complexes was rigorously investigated using a variety of techniques, including X-ray absorption spectroscopy, Mössbauer spectroscopy, X-ray diffraction, electron paramagnetic resonance spectroscopy, and magnetic measurements. All of these techniques are consistent with ligand-based reduction events to generate radical neocuproine complexes. Thus, neocuproine adds to a growing family of chelating N-donor type ligands that participate in redox noninnocence and may be useful for future catalyst and reaction design.

This thesis also contains multiple appendices which contain supporting data for the previous chapters.

Preface

All chapters have an independent compound numbering system. Characterization spectra are provided in the corresponding appendix for each chapter.

Introduction

Hydrogen transfer and the controlled transfer of H_2 is broadly applicable to a variety of reactions in the field of chemistry. For example, in the Haber-Bosch process, and industrial process for nitrogen fixation, N_2 is reacted with three equivalents of H_2 to form two equivalents of NH_3. This reaction was used to convert 144,000 tons of N_2 to NH_3 globally in 2020 with an expected increase in production of 4% in the next four years.[1] Nitrogen fixation is of vital importance for producing fertilizer and is largely responsible for the green revolution after the discovery of the Haber-Bosch process in the early 1990s.[1,2] Similarly, Fischer-Tropsch chemistry, which is used to hydrogenate CO by reacting it with H_2 to form hydrocarbons and water, is done on an industrial scale for the production of gasoline and other liquid fuels.[3] Hydrogenation of the C–O ether bond in biopolymers such as cellulose to produce the corresponding sugar monomer is a useful tool in biomass degradation.[4] Additionally, hydrogenation is crucial to a variety of organic transformations used in pharmaceutical development.[5]

Scheme i. Applications of hydrogenation reactions.

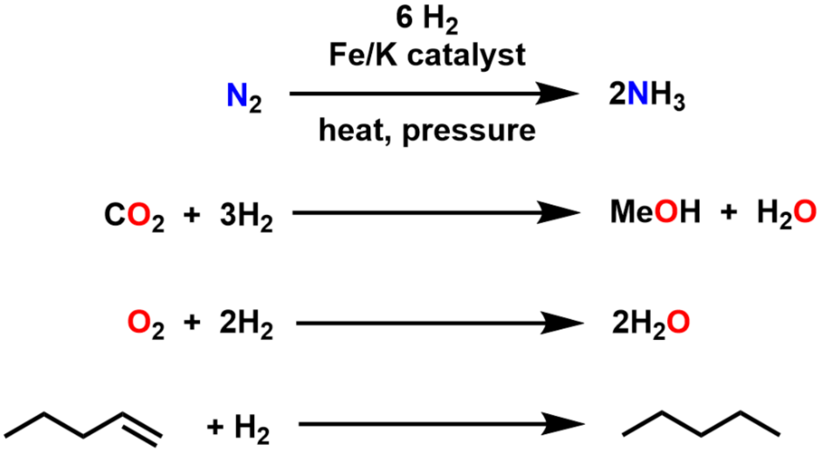

Given the variety of important applications, there is considerable interest in catalyst development for hydrogen transfer chemistry. Homogeneous, molecular systems are particularly attractive due to the relative ease of their characterization as compared to heterogeneous catalysts. Additionally, the mechanism of homogeneous systems can be investigated to increase our understanding of how to precisely control the movement of protons and electrons in the reaction and how to control reaction selectivity. Much of the work in the development of hydrogen transfer catalysts have used second and third row transition metals, which tend to facilitate $2e^-$ type chemistry.[6] These catalysts have been developed to hydrogenate with extraordinary stereo- and regioselectivity. This has been achieved through control of both the primary and secondary sphere of these catalyst. The primary sphere refers to the environment directly bound to the metal center and is largely controlled by ligand donor strength and sterics. The secondary sphere refers to the environment surrounding the active metal site. In the case of second and third row transition metal catalyst, the use of chiral ligands has been extremely useful in creating a secondary sphere that promotes stereoselective hydrogenation of organic molecules.[7]

Scheme ii. Primary vs. secondary sphere on a molecular metal catalyst.

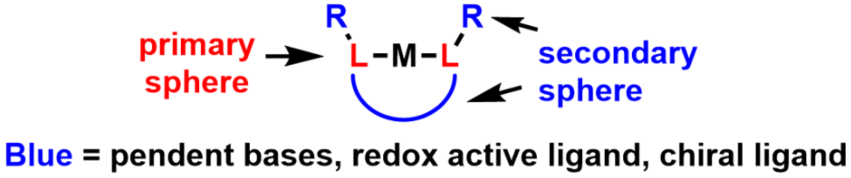

In recent years, there has been a push towards the development of catalysts featuring first row transition metals such as Ni, Co, and Fe as these metals are more abundant, less expensive, and less toxic than the more commonly used second and third row transition metals. Unlike second and third row transition metals, first row transition metals can facilitate $1e^-$ or $2e^-$ type chemistry, providing them with a wider range of possible reaction paths and mechanisms. The use of strongly donating ligands such as NHC’s to mediate the primary sphere have been somewhat useful in promoting productive hydrogenation chemistry with first row transition metal catalysts.[8] However, metal-ligand cooperativity has been particularly useful in controlling the movement of protons and electrons when using first row transition metal catalysts.[9] Two strategies that have seen considerable attention are the use of redox-active ligands and ligands with pendant protons to facilitate shuttling electrons, shuttling protons, or stabilizing reactive intermediates.[10] These strategies are inspired by nature, where enzymes are able to facilitate a wide variety of reactions by controlling both the primary and secondary sphere of the enzyme active site.

Redox-active ligands. Redox-active ligands have gained increasing recognition for their role in mediating the potential of redox events in molecular catalysts. These noninnocent ligands typically feature extended π-conjugated systems that can support ligand radicals upon oxidation or reduction of the ligand, and as such, the utility of bidentate redox-active ligands such as bipyridine, phenanthroline, quinoline, and other NN bidentate ligands has been broadly explored.[11] For example, the redox-activity of bipyridine in Re and Mn bipyridine electrocatalysts allows these complexes to mediate the reduction of CO_2 to CO at a lower redox potential than otherwise observed. This is due to the accessibility of an initial ligand-based reduction pathway, which in turn allows CO_2 to bind at the start of the catalytic cycle.[12] Additionally, the mechanism of this reduction can be tuned by switching out bipyridine for a different redox-active ligand, such as 2-phenylazopyridine.[13]

Redox-active ligand are also used to promote $2e^-$ chemistry with first-row transition metal catalysts. To do this, the redox-active ligand will function as an electron sink to temporarily store electrons, which can later be donated to substrate. When combined with the redox-activity of the metal center, this can allow for 2 or more electrons to be donated to a given substrate. Pyridine diamine (PDI) ligands feature prominently in this capacity, and can be used to promote cyclization, polymerization, C–C bond formation, and borylation among other reactions.[14] For example, Scheme iii shows the Fe(PDI) complex is able to promote a [2+2] cycloaddition of 1,7-octadiene by donating 1 e^- from the PDI ligand and 3 e^- from the Fe center, for an overall 4 e^- reaction.[15] Other conjugated pincer ligands also feature prominently in this area.[16]

Scheme iii. [2+2] cyclization reaction using a redox-active PDI ligand.

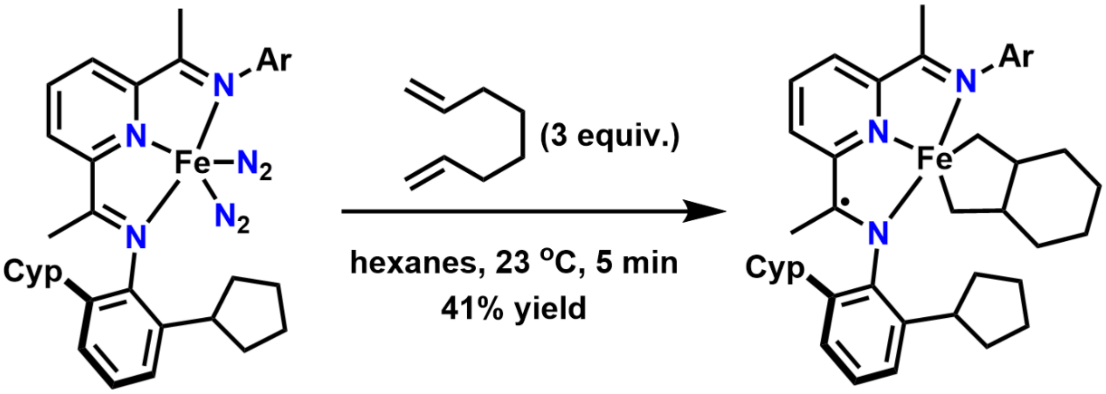

Hydrogen donor ligands. Another common strategy within the umbrella of metal-ligand cooperativity is the use of hydrogen donor ligands. These ligands have acidic/basic sites that can promote proton shuttling, or provide hydrogen-bonding interactions that stabilize reactive intermediates.[17] One powerful example of this is in a Ni electrocatalyst, where the phosphine ligand features pendant amine bases that shuttle protons to the metal center to promote electrocatalytic H_2 evolution.[18] Similarly, it has been shown with PNP pincer ligands with a pyridine backbone that a proton can be pulled off of the ligand backbone and subsequently donated to substrate. This results in a dearomatization of the pyridine moiety in the ligand backbone, which can be rearomatized upon protonation. In a recent example, a Zn(PNP) complex was used to catalyze the hydrogenation of imines and ketones.[19] A more traditional example of this phenomena is that of the Noyori type catalyst, where the H_2 is split across the metal and the ligand in the hydrogenation reaction mechanism.[20]

Scheme iv. Metal-complexes featuring ligand that can reversibly donate protons to substrate. Protons colored red are those involved in hydrogenation reactions.

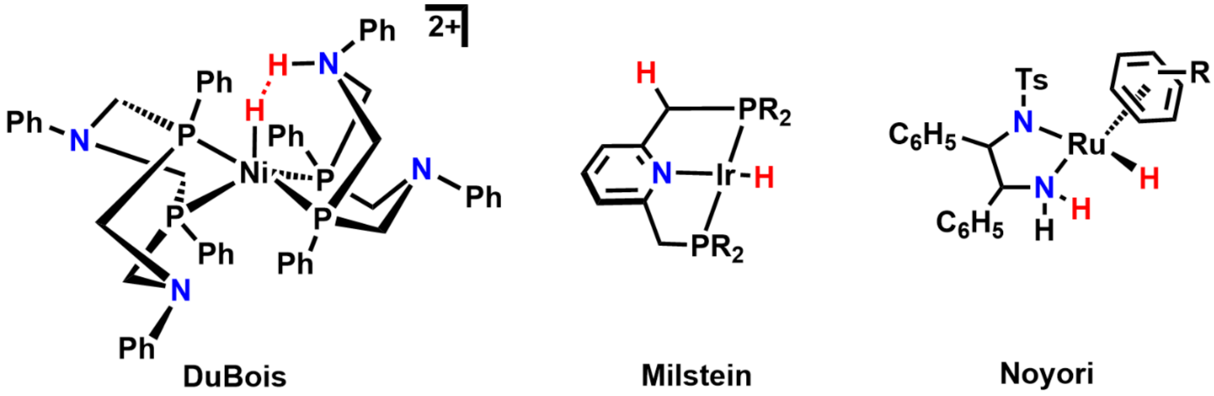

Alternatively, pendant hydrogen atoms can be used in hydrogen-bonding interaction to stabilize reactive intermediates. This has been particularly explored in the context of stabilizing reactive metal-oxygen complexes. For example, a high spin Fe(IV)-oxo has been stabilized using a using a combination of strongly donating urea groups from the ligand in the primary sphere and hydrogen-bonding interactions between amines and the O-atom of the oxo ligand in the secondary sphere.[21] A similar strategy of using hydrogen bonding interactions has been used to stabilize an Fe(III)-O intermediate in the catalytic reduction of nitrate and perchlorate. The hydrogen bonding interactions between the amines of the ligand scaffold and the oxo were observed crystallographically.[22] Another interesting application of this strategy is for the stabilization of a fluoride ligand via hydrogen bonding interactions with phenol alcohol moieties off the ligand backbone.[23] All of these examples demonstrate how powerful hydrogen bonding can be in stabilizing reactive complexes and, more generally, the utility of incorporating acidic or basic groups into the secondary sphere of a catalyst.

Redox-active ligands featuring proton responsive groups. While the transfer of protons or electrons via ligand noninnocence are powerful strategies individually, a growing field of study aims to combine these strategies for the transfer of H-atoms or of full H_2 equivalents.[24] This should allow for greater reactivity with less reactive metal centers in catalyst or allow for the transfer of multiple equivalents of H_2, such as the hydrogenation of O_2 to two equivalents of H_2O rather than one equivalent of H_2O_2 or the hydrogenation of CO to methanol rather than formate. This idea has been studied in the context of external H-atom acceptors such as TEMPO$^\bullet$ or benzoquinone and shows great promise for increasing catalytic activity.[25] A recent example used 2,5-di-*tert*-butyl-p-benzoquinone as a cocatalyst with a Pd complex to enable catalytic sp^2-sp^2 C-C bond formation with molecular oxygen as the oxidant.[26] Nitrogen reduction has been achieved using SmI and alcohols or water as a hydrogen atom source, which allows for the reaction to occur with a turnover frequency of 117 per minute in the presence of a Mo catalyst.[27]

Incorporation of benzoquinone as an H-atom acceptor into the ligand backbone has been investigated as well. When coordinated to a metal center, the quinone backbone can donate two protons and two electrons to a substrate. The metal center can donate additional electrons. When complexed to Pd, this has been used to reduce O_2 and form H_2O, as well as reduce nitric oxide, nitrous oxide, 1-azido adamantane, trimethylamine n-oxide, and 1,4-benzoquinone.[28] While this example demonstrates the utility of incorporating H-atom donors into the ligand backbone for mediating challenging reactivity, this ligand was difficult to modify and still required the use of a second row transition metal. Ligands that are redox-active and proton responsive have also been used in conjunction with first row transition metals.[29] Additionally, the bifunctionality of these ligands can promote 2 e^- hydrogenation reactions when metal centers that are not redox active are used, such as Zn or Al.[30]

Scheme v. Ligand-based donation of H_2 for the hydrogenation of O_2 to form water.

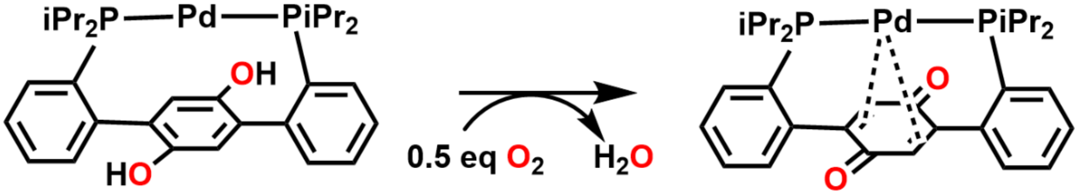

Dihydrazonopyrroles as redox-active, proton responsive ligands. Recent work in the Anderson group has focused on using a dihydrazonopyrrole (DHP) ligand scaffold. This scaffold has three possible protonation states and three possible redox states, which in turn allows it to act as an H-atom donor or acceptor. In total, the ligand backbone should be able to hold one full equivalent of H_2 that can be donated to substrate without accessing the electrons from the metal center. Additionally, this scaffold is synthesized via a condensation reaction of an appropriate hydrazine with the acyl precursor, making it easily modifiable at the R position.

Scheme vi. Dihydrozonopyrrole (DHP) ligand scaffold complexed to a metal center.

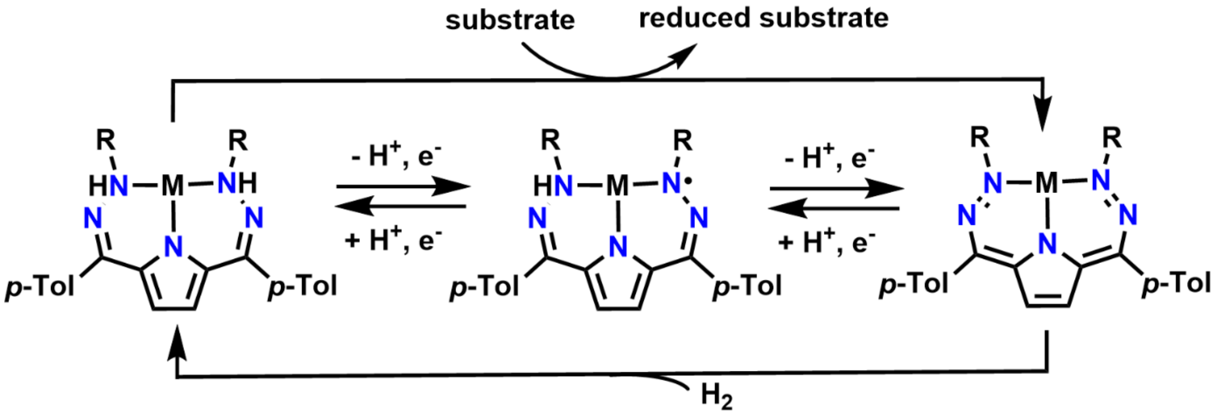

Thus far, investigations have focused on Ni(DHP) complexes, and have demonstrated that this bifunctional approach is useful for activating small molecules such as H_2O and O_2. With the phenyl derivative of this ligand (^{Tol,Ph}DHP), Ni complexes could be isolate in all three redox states of the ligand as well as in two different protonation states.[31] Additionally, it was found that T-shaped Ni complexes could be isolated. When in the ligand radical state, the Ni(^{Tol,Ph}DHP$^{\bullet}$) complex was found to homolytically activate H_2O to form a Ni dimer with a bridging hydroxide, where one ligand was oxidized and the other was reduced and protonated. This dimer could react further to oxidize phosphines and C–H bonds.[32] With the *tert*-butyl derivative of this ligand (${}^{\mathrm{Tol},t\mathrm{Bu}}$DHP), the analogous T-shaped Ni complex with a ligand radical could be reacted with O_2 or air to form a Ni-superoxo. This Ni-superoxo could then be used to oxidize toluene or benzylalchol to benzaldehyde with heating, where the reaction was stoichiometric in O-atoms.[33] These reactions demonstrated the utility of the DHP scaffold for activating small molecules, they did not demonstrate the desired donation/acceptance of H_2 across the ligand scaffold for productive reductive chemistry. In this thesis, I show how the ${}^{t\mathrm{Bu},\mathrm{Tol}}$DHP ligand (${}^{t\mathrm{Bu},\mathrm{Tol}}$DHP = 2,5-bis((2-t-butylhydrazono)(p-tolyl)methyl)-pyrrole) can facilitate simple hydrogenation chemistry when complexes with Ni. Additionally, I will discuss the redox chemistry of DHP when complexed to Fe. I will then discuss my investigations into the hydrogen transfer reactivity of Fe complexes of the ${}^{t\mathrm{Bu},\mathrm{Tol}}$DHP ligand and how this can be harnessed for oxidative chemistry.

References

---

[1] U.S. Geological Survey, 2020, Nitrogen (Fixed)-Ammonia, accessed May 10th, 2021, at URL https://pubs.usgs.gov/periodicals/mcs2021/mcs2021-nitrogen.pdf.

[2] (a) Ghavam, S.; Vahdati, M.; Wilson, I. A. G.; Styring, P. *Front. Energy Res.* **2021**, *9*, 1–19.; (b) Geddes B.A., Oresnik I.J. (2016) The Mechanism of Symbiotic Nitrogen Fixation. In: Hurst C. (eds) The Mechanistic Benefits of Microbial Symbionts. Advances in Environmental Microbiology, vol 2. Springer, Cham.

[3] Cheng, K.; Kang, J.; King, D. L.; Subramanian, V.; Zhou, C.; Zhang, Q.; Wang, Y. *Advances in Catalysis for Syngas Conversion to Hydrocarbons*, 1st ed.; Elsevier Inc., 2017; Vol. 60.

[4] (a) Stummann, M. Z.; Høj, M.; Gabrielsen, J.; Clausen, L. R.; Jensen, P. A.; Jensen, A. D. s*Renew. Sustain. Energy Rev.* **2021**, *143*, 1–15.; (b) De Schouwer, F.; Claes, L.; Vandekerkhove, A.; Verduyckt, J.; De Vos, D. E. *ChemSusChem* **2019**, *12*, 1272–1303.

[5] (a) Hayler, J. D.; Leahy, D. K.; Simmons, E. M. *Organometallics* **2019**, *38*, 36–46.; (b) Basu D., Achanta S., Kumar N.U., Rehani R.B., Bandichhor R. (2019) Application of Organometallic Catalysts in API Synthesis. In: Colacot T., Sivakumar V. (eds) Organometallics in Process Chemistry. Topics in Organometallic Chemistry, vol 65. Springer, Cham. https://doi.org/10.1007/3418_2019_31.

[6] (a) Mwansa, J. M.; Page, M. I. *Catal. Sci. Technol.* **2020**, *10*, 590–612.; (b).Fritz, M.; Schneider, S. In *The Periodic Table II: Catalytic, Materials, Biological and Medical Applications*; Mingos, D. M. P., Ed.; Springer International Publishing: Cham, 2019; pp 1–36. (c) R. H. Crabtree, *Organometallic Chemistry of the Transition Metals, 6th Edition*, 2014.

[7] (a) Wang, X.; Han, Z.; Wang, Z.; Ding, K. *Acc. Chem. Res.* **2021**, *54*, 668–684.; (b) Zhang, W.; Chi, Y.; Zhang, X. *Acc. Chem. Res.* **2007**, *40*, 1278–1290.

[8] (a) Fortman, G. C.; Nolan, S. P. *Chem. Soc. Rev.* **2011,** *40*, 5151-5169.; (b) Hopkinson, M. N.; Richter, C.; Schedler, M.; Glorius, F. *Nature* **2014,** *510* (7506), 485-496.

[9] (a) Alig, L.; Fritz, M.; Schneider, S. *Chem. Rev.* **2019**, *119*, 2681–2751.; (d) M. L. Pegis, C. F. Wise, D. J. Martin and J. M. Mayer, *Chem. Rev.*, **2018**, *118*, 2340-2391.; (b) Chirik, P. J. *Acc. Chem. Res.* **2015**, *48*, 1687–1695.; (g) T. Zell and D. Milstein, *Acc. Chem. Res.*, **2015**, *48*, 1979-1994.; (c) Chirik, P. J.; Wieghardt, K. *Science* **2010**, *327*, 794–795.

[10] (a) Liao, Q.; Liu, T.; Johnson, S. I.; Klug, C. M.; Wiedner, E. S.; Morris Bullock, R.; Dubois, D. L. *Dalt. Trans.* **2019**, *48*, 4867–4878; (b) K. C. Macleod, R. A. Lewis, D. E. Derosha, B. Q. Mercado and P. L. Holland, *Angew. Chem. Int. Ed.*, **2017**, *56*, 1069–1072.; (d) Chirik, P. J. *Acc. Chem. Res.* **2015**, *48* 1687–1695.; (e) Liu, T.; Liao, Q.; O'Hagan, M.; Hulley, E. B.; DuBois, D. L.; Bullock, R. M. *Organometallics* **2015**, *34*, 2747–2764.; (g) Lyaskovskyy, V.; De Bruin, B. *ACS Catal.* **2012**, *2*, 270–279.; (h) Kaim, W. *Inorg. Chem.* **2011**, *50*, 9752–9765.

---

[11] (a) Gilroy, J. B.; Otten, E. *Chem. Soc. Rev.* **2020**, *49*, 85.; (b) Joannou, M. V; Darmon, J. M.; Bezdek, M. J.; Chirik, P. J. *Polyhedron* **2019**, *159*, 308–317. (c) Sinha, S.; Das, S.; Sikari, R.; Parua, S.; Brandaõ, P.; Demeshko, S.; Meyer, F.; Paul, N. D. *Inorg. Chem.* **2017**, *56*, 14084–14100.; (d) England, J.; Bill, E.; Weyhermu, T.; Neese, F.; Atanasov, M.; Wieghardt, K. *Inorg. Chem.* **2015**, *54*, 12002–12018.; (e) Wang, M.; Bill, E.; Weyhermüller, T.; Wieghardt, K. *Can. J. Chem.* **2014**, *92*, 913–917.; (f) Connick, W. B.; Bilio, A. J. Di; Hill, M. G.; Winner, J. R.; Gray, H. B. *Inorganica Chim. Acta* **1995**, *240*, 169–173.

[12] (a) McKinnon, M.; Ngo, K. T.; Sobottka, S.; Sarkar, B.; Ertem, M. Z.; Grills, D. C.; Rochford, J. *Organometallics* **2019**, *38*, 1317–1329.; (b) Riplinger, C.; Sampson, M. D.; Ritzmann, A. M.; Kubiak, C. P.; Carter, E. A. *J. Am. Chem. Soc.* **2014**, *136*, 16285–16298.

[13] Matson, B. D.; Mcloughlin, E. A.; Armstrong, K. C.; Waymouth, R. M.; Sarangi, R. *Inorg. Chem.* **2019**, *58* , 7453–7465.

[14] (a) Bezdek, J.; Al-bahily, K.; Korobkov, I.; Chirik, P. J. *Organometallics* **2017**, *36*, 4215–4223.; (b) Bezdek, M. J.; Guo, S.; Chirik, P. J. *Science* **2016**, *354*, 730–733.; (c) Lau, K. C.; Jordan, R. F. *Organometallics* **2016**, *35*, 3658–3666.; (d) Schaefer, B. A.; Margulieux, G. W.; Tiedemann, M. A.; Small, B. L.; Chirik, P. J. *Organometallics* **2015**, *34*, 5615–5623.; (e) Cladis, D. P.; Kiernicki, J. J.; Fanwick, P. E.; Bart, S. C. *Chem. Commun.* **2013**, *49*, 4169–4171.

[15] Joannou, M. V.; Hoyt, J. M.; Chirik, P. J. *J. Am. Chem. Soc.* **2020**, *142*, 5314–5330.

[16] (a) Ott, J. C.; Wadepohl, H.; Gade, L. H. *Inorg. Chem.* **2021**, *60*, 3927.; (b) Alig, L.; Fritz, M.; Schneider, S. *Chem. Rev.* **2019**, *119*, 2681;. (c) Bagh, B.; Broere, D. L. J.; Sinha, V.; Kuijpers, P. F.; Van Leest, N. P.; De Bruin, B.; Demeshko, S.; Siegler, M. A.; Van Der Vlugt, J. I. *J. Am. Chem. Soc.* **2017**, *139*, 5117–5124.; (d) Broere, D. L. J.; Van Leest, N. P.; De Bruin, B.; Siegler, M. A.; Van Der Vlugt, J. I. *Inorg. Chem.* **2016**, *55*, 8603–8611.(e) Wong, J. L.; Sanchez, R. H.; Logan, J. G.; Zarkesh, R. A.; Zillera, J. W.; Heyduk, *Chem. Sci.* **2013**, *4*, 1906–1910.

[17] a) Duan, P.-C.; Schulz, R. A.; Römer, A.; Van Kuiken, B. E.; Dechert, S.; Demeshko, S.; Cutsail III, G. E.; DeBeer, S.; Mata, R. A.; Meyer, F. *Angew. Chem. Int. Ed.* **2021**, *60*, 1891; c) Kounalis, E.; Lutz, M.; Broere, D. L. J. *Organometallics* **2020**, *39*, 585.; (e) Loewen, N. D.; Thompson, E. J.; Kagan, M.; Banales, C. L.; Myers, T. W.; Fettinger, J. C.; Berben, L. A. *Chem. Sci.* **2016**, *7*, 2728–2735.; h) M. Rakowski Dubois and D. L. Dubois, *Acc. Chem. Res.*, **2009**, *42*, 1974-1982.

[18] Helm, M. L.; Stewart, M. P.; Bullock, M. R.; DuBois, M. R.; DuBois, D. L. *Science* **2011**, *333*, 863–867.

[19] Rauch, M.; Kar, S.; Kumar, A.; Avram, L.; Shimon, L. J. W.; Milstein, D. *J. Am. Chem. Soc.* **2020**, *142*, 14513–14521.

[20] (a) Ikariya, T.; Murata, K.; Noyori, R., *Org. Biomol. Chem.* **2006,** *4*, 393-406. (b) Noyori, R.; Hashiguchi, S., *Acc. Chem. Res.* **1997,** *30*, 97-102.

---

[21] Hill, E. A.; Weitz, A. C.; Onderko, E.; Romero-Rivera, A.; Guo, Y.; Swart, M.; Bominaar, E. L.; Green, M. T.; Hendrich, M. P.; Lacy, D. C.; Borovik, A. S. *J. Am. Chem. Soc.* **2016**, *138*, 13143–13146.

[22] Ford, C. L.; Park, Y. J.; Matson, E. M.; Gordon, Z.; Fout, A. R. *Science* **2016**, *354* (6313), 741–743.

[23] Moore, C. M.; Szymczak, N. K. *Chem. Commun.* **2015**, *51* (25), 5490–5492.

[24] Lindley, B. M.; Bruch, Q. J.; White, P. S.; Hasanayn, F.; Miller, A. J. M. *J. Am. Chem. Soc.* **2017,** *139*, 5305-5308.

[25] (a) Anson, C. W.; Stahl, S. S. *J. Am. Chem. Soc.* **2017**, *139*, 18472–18475.; (b) Gerken, J. B.; Stahl, S. S. *ACS Cent. Sci.* **2015**, *1*, 234–243.

[26] Salazar, C. A.; Flesch, K. N.; Haines, B. E.; Zhou, P. S.; Musaev, D. G.; Stahl, S. S. *Science* **2021**, *370*, 1454–1460.

[27] Ashida, Y.; Arashiba, K.; Nakajima, K.; Nishibayashi, Y., *Nature* **2019,** *568* (7753), 536-540.

[28] Horak, K. T.; Agapie, T. *J. Am. Chem. Soc.* **2016**, *138*, 3443–3452.

[29] a) Charette, B. J.; Ziller, J. W.; Heyduk, A. F. *Inorg. Chem.* **2021**, *60*, 1579–1589.; c) M. J. Drummond, C. L. Ford, D. L. Gray, C. V. Popescu and A. R. Fout, *J. Am. Chem. Soc.*, **2019**, *141*, 6639-6650.; d) Rosenkoetter, K. E.; Wojnar, M. K.; Charette, B. J.; Ziller, J. W.; Heyduk, A. F. *Inorg. Chem.* **2018**, *57*, 9728–9737.; g) R. Jain, A. A. Mamun, R. M. Buchanan, P. M. Kozlowski and C. A. Grapperhaus, *Inorg. Chem.*, **2018**, *57*, 13486-13493.; h) F. Schneck, M. Finger, M. Tromp and S. Schneider, *Chem. Eur. J.*, **2017**, *23*, 33-37.; j) A. Dauth, U. Gellrich, Y. Diskin-Posner, Y. Ben-David and D. Milstein, *J. Am. Chem. Soc.*, **2017**, *139*, 2799-2807.; l) Delgado, M.; Gilbertson, J. D. *Chem. Commun.* **2017**, *53* (81), 11249–11252. m) P. O. Lagaditis, B. Schluschaß, S. Demeshko, C. Würtele and S. Schneider, *Inorg. Chem.*, **2016**, *55*, 4529-4536.; q) B. W. Purse, L. H. Tran, J. Piera, B. Åkermark and J. E. Bäckvall, *Chem. Eur. J.*, **2008**, *14*, 7500–7503.

[30] b) T. J. Sherbow, E. J. Thompson, A. Arnold, R. I. Sayler, R. D. Britt, L. A. Berben, *Chem. - Eur. J.*, **2019**, *25*, 454-458.; e) M. B. Ward, A. Scheitler, M. Yu, L. Senft, A. S. Zillmann, J. D. Gorden, D. D. Schwartz, I. Ivanović-Burmazović and C. R. Goldsmith, *Nature Chem.*, **2018**, *10*, 1207-1212.; f) R. Pramanick, R. Bhattacharjee, D. Sengupta, A. Datta and S. Goswami, *Inorg. Chem.*, **2018**, *57*, 6816-6824.; p) T. W. Myers, L. A. Berben, *Chem. Sci.*, **2014,** *5*, 2771-2777.;

[31] Chang, M.-C.; McNeece, A. J.; Hill, E. A.; Filatov, A. S.; Anderson, J. S. *Chem. Eur. J.* **2018**, *24*, 8001–8008.

[32] Chang, M. C.; Jesse, K. A.; Filatov, A. S.; Anderson, J. S. *Chem. Sci.* **2019**, *10*, 1360–1367.

[33] Mcneece, A. J.; Jesse, K. A.; Xie, J.; Filatov, A. S.; Anderson, J. S. *J. Am. Chem. Soc.* **2020**, *142*, 10824–10832.

Chapter One: Catalytic Hydrogenation Enabled by Ligand-Based Storage of Hydrogen

This chapter has been adapted from the following: McNeece, A. J.*; Jesse, K. A.*; Filatov, A. S.; Schneider, J. E.; Anderson, J. S. *Chem. Commun.* **2021**, *57*, 3869–3872.

*These authors contributed equally

Introduction

The controlled transfer of multiple equivalents of protons and electrons is fundamental to many important chemical reactions. While H_2 is a potent reducing agent, transition metal catalysts are often required to overcome kinetic barriers to activating H_2. Transition metals often mediate reductive transformations via hydride intermediates arising from oxidative addition of H_2 which then perform insertion reactivity.[1] While this primary sphere H_2 transfer is well-established, especially with second- or third-row metals, such two electron processes can be much more challenging with first-row metals.

One strategy to improve the reactivity of first row complexes in these transformations is to engage the secondary coordination sphere. Nature uses this approach, frequently relying on proton/electron transfer from the protein scaffold or cofactors to supply reducing equivalents to transition metal active sites.[2] The elegance of these systems has inspired synthetic chemists to discover new molecular systems which can mimic this reactivity. Incredible advances have been made in designing ancillary ligand scaffolds that can mediate electron transfer,[3] hydrogen bonding,[4] or proton shuttling.[5] Nevertheless, supporting ligand systems which can store both protons and electrons are still uncommon.[6] Recently several well-defined systems that can reversibly store H-atom equivalents have been reported.[7] Systems that can store full H_2 equivalents in a supporting ligand backbone are still rare.[8]

To explore this relatively scarce area I have been investigating reversible ligand-based H_2 transfer using dihydrazonopyrrole (DHP) complexes of Ni.[9] The 2,5-pyrrole pincer scaffold is attractive for this reactivity because $2e^-$ reduction/oxidation of the conjugated system coupled with protonation/deprotonation of the pincer arms can reversibly transfer H_2 without any redox changes at the metal center (Scheme 1). We have previously demonstrated that this scaffold can support the storage of both protons and electrons, but this reactivity had been limited to storage of an electron or H-atom equivalent, not storage of a full H_2 equivalent.[9a,b] I now report that Ni complexes of the previously reported ${}^{t\mathrm{Bu,Tol}}$DHP ligand (${}^{t\mathrm{Bu,Tol}}$DHP = 2,5-bis((2-t-butylhydrazono)(p-tolyl)methyl)-pyrrole) can support secondary sphere storage of H_2 across the ligand backbone. Furthermore, this reactivity is reversible and enables hydrogenation catalysis. Kinetic and computational analysis indicates that ligand hydrogenation proceeds in a process that is first-order in [Ni] and involves H_2 association followed by H–H scission.

Scheme 1 - 1. Ligand based storage of H_2 on dihydrazonopyrrole scaffolds.

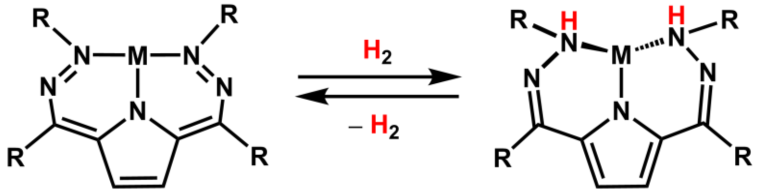

Results and Discussion

Scheme 1 - 2. Synthesis of **1** and **2** and interconversion of **2** and **3** with H_2 and benzoquinone.

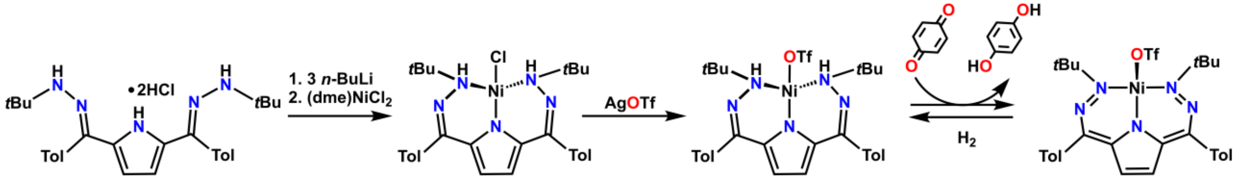

1 2 3

Synthesis and characterization of (^{tBu,Tol}DHPH$_2$)Ni$^+$ salts .

Deprotonation of the previously reported ^{tBu,Tol}DHP • 2HCl with 3 eq. of n-BuLi followed by dropwise addition to (dme)NiCl$_2$ (dme = 1,2-dimethoxyethane) in THF provides (^{tBu,Tol}DHPH$_2$)NiCl (**1**) as a red crystalline solid in 56% yield (Scheme 1 - 2). The ^{1}H NMR spectrum of **1** shows diamagnetic signals indicating a symmetric DHP environment, with a new broad singlet resonance at 5.98 ppm which is assigned to the two N–H protons on the ligand scaffold (Appendix 1). Analysis by single crystal X-ray diffraction (SXRD) shows a twisted square planar complex with the Ni square plane rotated from the plane of the central pyrrole ring by ~30° (Figure 1 - 1, left). The Ni–Nhydrazone bonds are 1.938(2) and 1.946(2) Å, which are ~0.1 Å longer than those seen in the previously reported T-shaped complex (^{tBu,Tol}DHP$^{\bullet}$)Ni, likely due to both weaker donation and greater steric strain from the protonated nitrogens. Within the ligand scaffold, the N–N bonds are 1.454(3) and 1.460(2) Å which are significantly longer than other ^{tBu,Tol}DHP or ^{Ph,Tol}DHP complexes (~1.37 Å), supporting ligand-based redox changes. The N–H protons can be located in the difference map and are oriented towards the Cl ligand. The Cl···H distances are ~2.55 Å and the N–H–Cl angles are 104°. Both values are consistent with hydrogen bonding interactions, as have been observed in other M–Cl complexes.[10] Distinct stretches are also observed by IR spectroscopy at 3241 and 3166 cm^{-1}, further confirming the presence of N–H groups (Appendix 1).

Figure 1 - 1. Solid state structure of **1** (top), and **2** (bottom) with ellipsoids set to 50% probability, and all C–H hydrogens omitted for clarity. Hydrogen bonding interactions shown with dashed lines. Ni shown in green, C in grey, N in blue, O in red, F in bright green, Cl also in bright green (labelled), and S in yellow. Selected bond lengths (Å): **1**: Ni–Cl: 2.1817(7) Å, Ni–N1: 1.938(2), Ni–N3: 1.824(2), Ni–N5: 1.946(2), N1–N2: 1.454(3), N4–N5: 1.460(2). **2**: Ni–O: 1.952(1) Å, Ni–N1: 1.955(1), Ni–N3: 1.812(1), Ni–N5: 1.964(1), N1–N2: 1.455(2), N4–N5: 1.460(2).

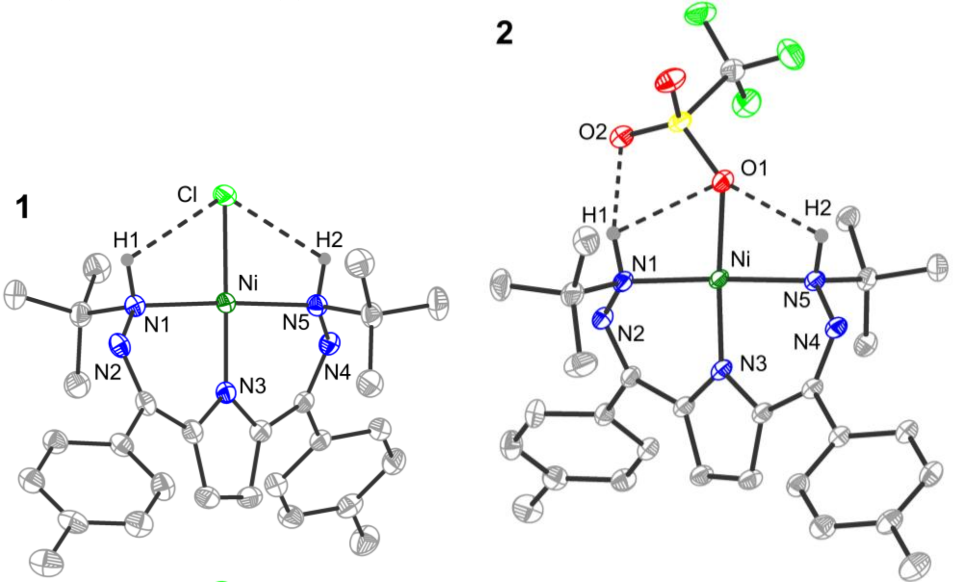

We then investigated the reactivity of **1** to determine whether the ligand-stored H_2 equivalent could be transferred to substrates. However, **1** shows little to no reactivity with substrates including air, olefins, and carbonyls. We hypothesized that a comparatively strongly coordinating Cl^- ligand might inhibit reactivity by occupying a potential site of substrate coordination and therefore abstracted this ligand. Complex **1** reacts cleanly with AgOTf to give the corresponding triflate complex (^{tBu,Tol}DHPH$_2$)NiOTf (**2**) (Scheme 1 - 1). SXRD analysis shows a structure very similar to that of **1** with the triflate bound in the fourth coordination site (Figure 1 - 1, right). Hydrogen bonding interactions to the triflate ligand are also clear, with one interaction to O_2 of moderate strength and two weaker interactions to O1 based on O···H distances of ~1.9 and 2.4 Å respectively.

Reactivity with H_2 and benzoquinone.

We then turned to see if this ligand substitution enabled H_2 transfer reactivity. Hydrogen transfer was tested by stirring **2** with benzoquinone at room temperature which resulted in slow formation of hydroquinone and the previously reported dehydrogenated complex (^{tBu,Tol}DHP)NiOTf (**3**) as indicated by ^{1}H NMR spectroscopy (Scheme 1 - 1, Appendix 1).[9c] This reactivity demonstrates an unusual example where an H_2 equivalent stored on a ligand backbone can be transferred to a substrate. Examples of H_2 transfer between a supporting ligand and a substrate are rare.[8]

In order to determine whether catalytic H_2 transfer was possible, we then investigated whether **2** could be regenerated from **3** with H_2 gas. Encouragingly, ^{1}H NMR analysis of this reaction indicates that complex **2** is formed as the major product when **3** is reacted with one atmosphere of H_2 with mild heating. Given this result, we then placed **3** and excess benzoquinone under an atmosphere of H_2 to determine whether catalytic hydrogenation was feasible. Monitoring by ^{1}H NMR spectroscopy at room temperature shows conversion of **3** to **2** with concomitant conversion of two equivalents of benzoquinone to hydroquinone indicating this process is catalytic. This reactivity provides important proof of concept for ligand-based H_2 transfer and shows the viability of the DHP scaffold for reversible H_2 donation.

Mechanistic studies of the H_2 splitting across the ligand backbone.

We were interested in understanding more about the mechanistic details of addition of H_2 to the ligand backbone and therefore we performed kinetic analyses on the interconversion of **3** and **2**. Monitoring the reaction of **3** with H_2 by UV-visible spectroscopy shows conversion of **3** to **2** with kinetics consistent with a first-order reaction in [Ni] under pseudo first-order conditions

(Figure 1 - 2). Comparison of the product peak intensities at 355 nm with intensities from isolated 2 indicates a high yield for this conversion (>80%), consistent with ^{1}H NMR analysis (Appendix 1), but some small amount of an intermediate or byproduct with an absorbance around 550 nm is also formed. We have thus far been unable to obtain further information on this species. The first order dependence on [Ni] for the consumption of **3** is consistent with the hypothesis of a single metal complex reacting to store H_2 across the ligand framework as opposed to a bimolecular reaction, as has been observed in the homolytic activation of O–H bonds with a related ^{Ph,Tol}DHP complex.[9b]

An Eyring analysis shows a $\Delta H^{\ddagger}$ of 13.9(4) kcal/mol and $\Delta S^{\ddagger}$ of −18(5) cal/(molK), which gives an overall $\Delta G^{\ddagger}$ at 298 K of ~21 kcal/mol (Figure 1 - 2). The comparatively large and negative $\Delta S^{\ddagger}$ suggests that association of H_2 is at least rate-contributing. We also performed the same analysis with D_2 to determine the deuterium kinetic isotope effect (KIE) for this hydrogenation reaction. Comparison of the rates under H_2 versus D_2 shows an inverse deuterium KIE of 0.8(1). If scission of the H–H bond was the sole rate contributing step a normal primary KIE would be expected. In contrast, the observed inverse KIE for this hydrogenation reaction could potentially arise from an equilibrium isotope effect (EIE) in an H_2 binding pre-equilibrium.[11] For this reason, as well as the convolution of the energetics of the H_2 cleavage steps by an H_2 association step, we have examined this reaction in more detail through additional calculations.

Figure 1 - 2. Kinetic analysis of the hydrogenation of **3** to **2**. (A) UV-vis traces of **3** under 1 atmosphere of H_2 at 40 °C taken every 10 minutes. The asterisk indicates a small but intensely colored impurity. (B) Decay of the absorbance at 650 nm with an exponential fit as described in the ESI shown in red. Inset: Eyring analysis with linear fit ($R^2 = 0.99$) in red to determine the activation parameters for the hydrogenation as described in the text and Appendix 1A.

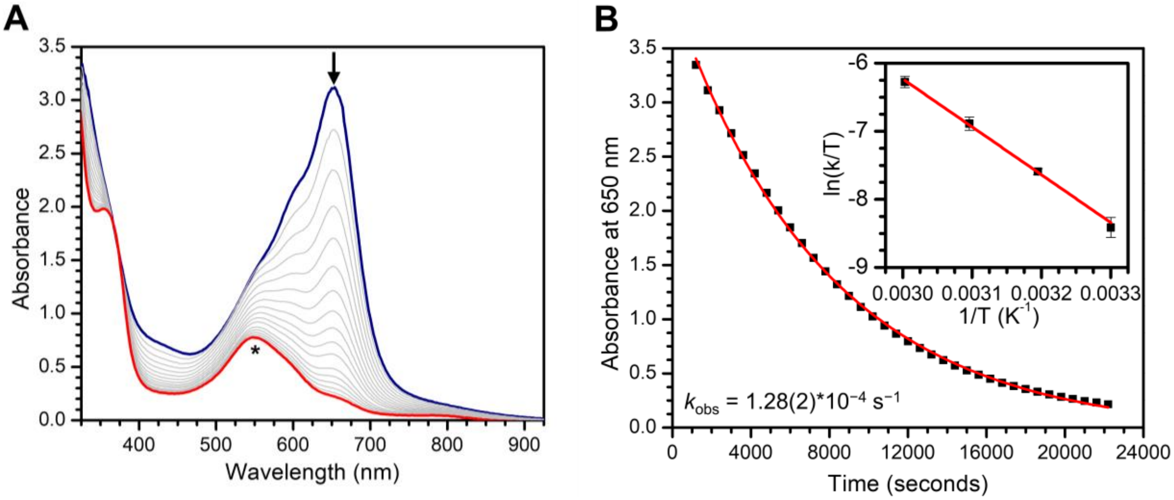

We have examined the thermodynamics of H_2 addition to the ligand framework by performing density functional theory (DFT) calculations. We initially attempted calculations on OTf^--bound species but observed dissociation of the anion along the reaction coordinate. Experimental evidence for OTf^- dissociation is equivocal (Appendix 1), but the increased reactivity on moving from **1** to **2** supports that anion dissociation may be required for reactivity. To simplify our computational analysis, we have instead examined the energetics and geometries of H_2 cleavage along a singlet manifold starting from a putative cationic intermediate $[(^{tBu,Tol}DHP)Ni]^+$ (Figure 1 - 3).

Figure 1 - 3. DFT computed geometries and energies of H_2 splitting. Calculations were carried out with the B3P functional and a def2-TZVP basis set, with a def2-TZVPP basis set on Ni. Ni is shown in green, C in gray, N in blue, and H in white. Note that only H-atoms stemming from the H_2 ligand are shown.

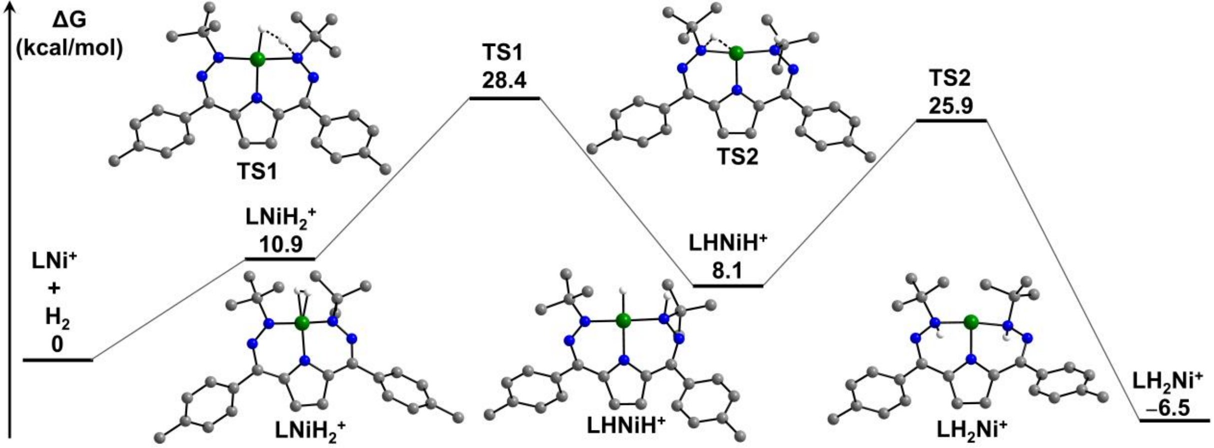

The first optimized transition state is an H_2 splitting step across the Ni–N bond to form the intermediate hydride species [($^{t\text{Bu,Tol}}$DHPH)NiH]$^+$. This transition state is 28.4 kcal/mol higher in energy than [($^{t\text{Bu,Tol}}$DHP)Ni]$^+$ + H_2. The second transition state has a similar barrier of 25.9 kcal/mol versus [(tBu,TolDHP)Ni]$^+$ + H_2 and results in the favorable (−6.5 kcal/mol from the reactants) formation of the hydrogenated product. Examining the Mulliken charge densities of the H-atoms along the reaction coordinate suggests that TS1 is best described as a proton transfer. While the charges in TS2 are much more covalent, the balanced reaction and Mulliken charges suggests this is step is best considered as a hydride transfer. Overall, this analysis suggests that H_2 binding and scission should be accessible with reasonably good agreement between theoretical and experimental energetics.

These calculations also enable us to test the origin of the inverse experimental KIE. Examination of the isotope dependence of the first transition state (TS1) suggests that a primary KIE would be expected in contrast with experimental observations. Conversely, if the isotope dependence of free H_2/D_2 and ($^{t\text{Bu,Tol}}$DHP)NiH$_2^+$/($^{t\text{Bu,Tol}}$DHP)NiD$_2^+$ are considered, an inverse isotope dependence is predicted for reversible H_2 binding, consistent with experiment. These observations suggest that the origin of the observed isotope dependence likely arises from an H_2 association EIE.[11] Similar inverse isotope effects have recently been observed in paramagnetic transition metal systems as well as across bimetallic frustrated Lewis pairs.[12]

Efforts to observe the putative Ni-hydride intermediate experimentally were undertaken. Monitoring the H_2 splitting reaction by ^1H NMR in d_8-THF at 50 °C shows a feature at −10.38 ppm which grows in and then decays over the course of the reaction from **3** to **2** (Figure 1 – 4). The location of this feature as well as its transient presence during the H_2 splitting reaction is consistent with the formation of a Ni-hydride that then undergoes a hydride transfer from Ni to the ligand. While not direct evidence for a Ni-hydride intermediate, these data are consistent with the mechanistic picture predicted by DFT.

Figure 1 - 4. ^1H NMR of the reaction of **3** with H_2 to form **2** in d_8-THF at 50 °C.

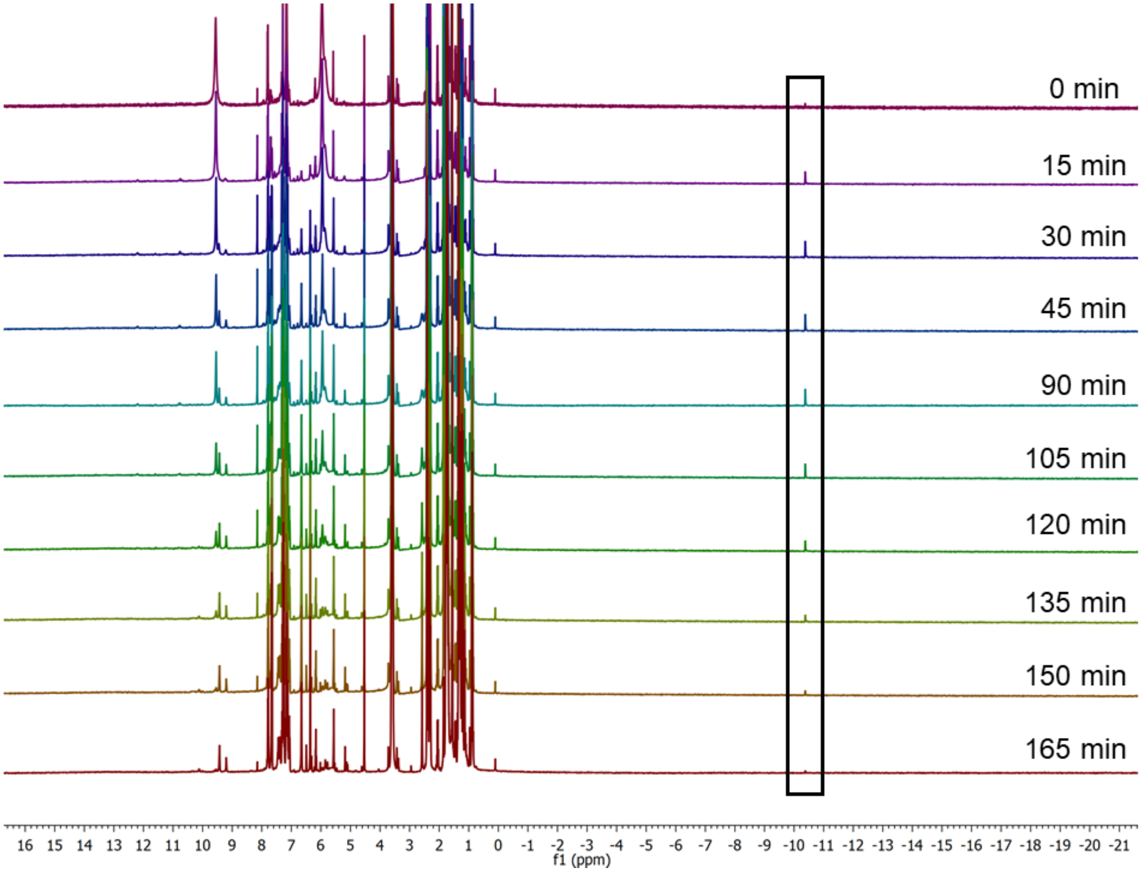

Conclusions

The studies presented here show an unusual example of metal-ligand cooperativity enabled hydrogenation reactivity where the ligand can store a full H_2 equivalent. The catalytic hydrogenation of benzoquinone provides an important proof of concept for this area. Kinetic data show that the bifunctional splitting of H_2 proceeds in a process that is first-order in [Ni], but that proceeds with an inverse deuterium isotope dependence. Calculations suggest that H_2 scission is energetically accessible and that the source of the observed inverse deuterium isotope dependence is an EIE arising from H_2 association. While catalytic hydrogenations of other substrates have been less successful thus far, the enhanced reactivity in moving from **1** to **2** (Cl^- to OTf^-) suggests that the primary metal coordination sphere still plays an important role in this primarily ligand-centered reactivity and offers a potential avenue to expand hydrogenation reactivity to other substrates.

Experimental

General Considerations. All reagents were purchased from commercial suppliers and used without further purification unless otherwise specified. Compound **3** was synthesized as previously reported.[9c] All manipulations were carried out under an atmosphere of N_2 using standard Schlenk and glovebox techniques. Glassware was dried at 180 °C for a minimum of two hours and cooled under vacuum prior to use. Solvents were dried on a solvent purification system from Pure Process Technology and stored over 4 Å molecular sieves under N_2. Tetrahydrofuran was stirred over NaK alloy and run through an additional activated alumina column prior to use to ensure dryness. Solvents were tested for H_2O and O_2 using a standard solution of sodium-benzophenone ketyl radical anion. C_6D_6 was dried by passage over a column of activated alumina and stored over 4 Å molecular sieves in the glovebox. ^1H, $^{13}C\{^1H\}$, and $^{19}F\{^1H\}$ spectra were recorded on Bruker DRX

400 or 500 spectrometers. Chemical shifts are reported in ppm units referenced to residual solvent resonances for ^{1}H and ^{13}C{^{1}H} spectra, UV-vis spectra were recorded on a Thermo Evolution 300 spectrometer and addition of gases was performed by injecting via syringe into a cuvette sealed with a septum. UV-visible spectra at elevated temperature were done using a Unisoku Cryostat. IR was recorded on a Bruker Tensor II. GC/MS was collected on an Agilent SQ GCMS with 5977A single quad MS and 7890B GC. Elemental analysis was performed by Midwest Microlabs. Electrochemical measurements were performed using a BAS Epsilon potentiostat and analyzed using BAS Epsilon software version 1.40.67NT. Cyclic voltammetry measurements were made using a glassy carbon working electrode, platinum wire counter electrode, and silver wire pseudo-reference electrode, and referenced to internal Fc/Fc$^+$.

X-Ray Structure Determination. Crystal Structure Determination. The diffraction data were measured at 100 K on a Bruker D8 VENTURE with PHOTON 100 CMOS detector system equipped with a Mo-target micro-focus X-ray tube (λ = 0.71073 Å) or at the Advanced Photon Source of Argonne National Laboratory (beamline 15-ID-B,C,D) using X-ray radiation with a wavelength of λ = 0.41328 Å. Data reduction and integration were performed with the Bruker APEX3 software package (Bruker AXS, version 2015.5-2, 2015). Data were scaled and corrected for absorption effects using the multi-scan procedure as implemented in SADABS (Bruker AXS, version 2014/5, 2015, part of Bruker APEX3 software package). The structure was solved by the dual method implemented in SHELXT[13] and refined by a full-matrix least-squares procedure using OLEX23[14] software package (XL refinement program version 2014/7[15]). Suitable crystals were mounted on a cryo-loop and transferred into the cold nitrogen stream of the Bruker D8 Venture diffractometer. Most of the hydrogen atoms, with the exception of N–H protons which were located in the difference map, were generated by geometrical considerations and constrained to idealized geometries and allowed to ride on their carrier atoms with an isotropic displacement parameter related to the equivalent displacement parameter of their carrier atoms.

Density Functional Theory: Geometry Optimizations. Structures were optimized in ORCA using the B3P functional and def2-TZVPP basis set on Ni, def2-TZVP basis set on all other atoms.[16,17,18] Frequency calculations were performed to confirm the structures are the lowest point on the potential energy surface. For calculation of the thermodynamics of H_2 splitting, the cationic species were calculated in the absence of triflate counterions.

Density Functional Theory: Kinetic Isotope Effects. To assess the consistency of the proposed mechanism with the experimentally observed inverse KIE we estimated the semiclassical transition state using our DFT optimized structures and vibrational calculations. Enthalpies and entropies at 323 K were calculated using the formula of an ideal gas, assuming all rotations as rigid rotors and all vibrations as harmonic oscillators.[19] Performing these calculations for both isotopomers gave ΔH, $T\Delta S$, and ΔG values for the losses of enthalpy, entropy, and free energy upon deuteration for each species. The ΔH values are all positive whereas the $T\Delta S$ values are all negative, reflecting how deuterated isotopomers contain less zero point energy and a larger number of thermally available configurations. These tendencies reinforce to give positive ΔG for all species. The difference between the ΔG of two species gives a $\Delta\Delta G$ value, which represents the change in relative free energy between the two species upon deuteration. When these two species are the reactant and a transition state (or product), the semiclassical isotope effect is exp(–ΔΔG/kT). A positive value of ΔΔG indicates an inverse isotope effect and a negative value indicates a normal isotope effect. The elementary step of H_2 splitting (i.e. progression of $LNiH_2$ to TS1) is estimated to have a normal KIE; however, an inverse isotope effect is estimated for the binding of H_2. This analysis suggests that the entire reaction has a calculated isotope effect near unity, as determined experimentally (although a small normal effect is estimated rather whereas a small inverse effect is observed). Furthermore, these calculations suggest that the origin of the inverse isotope dependence is from H_2 association, as might be expected for an EIE.

Synthesis of ($^{tBu,Tol}DHPH_2$)NiCl (1). To a stirring THF solution of ^{tBu,Tol}DHP•2HCl (0.105 g, 0.200 mmol, 15 mL) was added *n*-BuLi (2.0 M in hexanes, 0.23 mL, 0.59 mmol, 2.9 eq) which resulted in a color change to clear red. This solution was then added dropwise to a stirring THF solution of (dme)$NiCl_2$ (0.045 g, 0.20 mmol, 1 eq, 3 mL) resulting in a reddish/tan solution. This was stirred for 2 hours, then filtered and all volatiles were removed in-vacuo. The resulting red oil was washed with petroleum ether (10 mL), resulting in ($^{tBu,Tol}DHPH_2$)NiCl as a tan powder. Single crystals could be obtained by crystallization of the petroleum ether wash at −35 °C Yield: 0.060 g, 56%. ^{1}H NMR (C_6D_6, 400 MHz, 25° C) δ = 7.87 (d, *J* = 8 Hz, 4H, Tol C–H), 7.06 (d, *J* = 8 Hz, 4H, Tol C–H), 6.55 (s, 2H, Pyrrole C–H), 5.99 (s, 2H, N–H), 2.12 (s, 6H, Tol-CH_3), 1.19 (s, 18H, *t*Bu-CH_3). $^{13}C\{^1H\}$ NMR (C_6D_6, 125 MHz, 25° C) δ = 166.84, 141.15, 134.94, 130.56, 129.97, 129.49, 119.93, 64.78, 29.09, 21.67. UV-vis, nm in THF (ε, $M^{-1}cm^{-1}$): 362 (8806). IR (cm^{-1}, THF solution, CaF_2 windows): 3241 (w, N–H), 3166 (m, N–H), 618 (w), 1585 (m, C=N), 1553 (m), 1470 (s), 1364 (s), 1314 (m), 1250 (m), 1179 (s), 1131 (w). HRMS (ESI) Calc'd for $[M+H]^+$: 536.2091 Found: 536.2058. Anal Calc'd (**1** + pentane) C 65.1 H 7.95 N 11.5 Found C 65.5, H 6.7 N 12.4.*

Synthesis of (^{tBu,Tol}DHPH$_2$)NiOTf (2) To a stirring THF solution of (^{tBu,Tol}DHPH$_2$)NiCl (0.025 g, 0.040 mmol, 5 mL) was added a THF solution of AgOTf (0.012 g, 0.047 mmol, 1.2 eq, 2 mL), resulting in immediate precipitation of a white powder. The reaction was stirred for 20 minutes, then filtered and all volatiles were removed *in vacuo*, giving [(^{tBu,Tol}DHPH$_2$)Ni]OTf as an oily yellow residue. Yield: 0.026 g, 90%. Single crystals could be obtained by slow evaporation of diethyl ether at room temperature overnight. ^{1}H NMR (C_6D_6, 400 MHz, 25° C) δ = 7.78 (d, *J* = 8 Hz, 4H, Tol C–H), 7.05 (d, *J* = 8 Hz, 4H, Tol C–H), 6.45 (s, 2H, Pyrrole C–H), 6.25 (s, 2H, N–H), 2.11 (s, 6H, Tol-CH$_3$), 1.15 (s, 18H, *t*Bu-CH$_3$). ^{13}C{^{1}H} NMR (C_6D_6, 125 MHz, 25° C) 166.2, 140.9, 133.5, 129.8, 128.8, 120.3, 64.9, 27.3, 20.9. ^{19}F{^{1}H} NMR (C_6D_6, 125 MHz, 25° C) −77. UV-vis, nm in THF (ε, $M^{-1}cm^{-1}$): 356 (8508). IR (cm^{-1}, THF solution, CaF$_2$ windows): 3250 (w, N–H), 3197 (m, N–H), 1615 (w), 1588 (s, C=N), 1483 (w), 1381 (m), 1337 (s), 1209 (w). HRMS (ESI) Calc’d for $[M+H]^+$: 650.1923 Found: 650.1891. Anal Calc’d (**2** + THF) C 54.9 H 6.1 N 9.7 Found C 54.2 H 6.6 N 9.5.*

*Complexes **1** and **2** are both extremely greasy or co-crystallize with solvent making them difficult to rigorously dry. Combustion analysis routinely gives values different than theory and potentially more consistent with solvates. Nevertheless, the combination of data acquired supports the assignment and purity of these species.

Synthesis of 2 via H$_2$ splitting from 3. A C_6D_6 solution of **3** was removed from the glovebox in a J-young NMR tube, degassed via three freeze-pump-thaw cycles, and placed under an atmosphere of H_2. After two hours at room temperature **2** appeared in the ^1H NMR, and after heating the reaction to 50 °C overnight full conversion to **2** was observed.

Synthesis of 3 via hydrogenation of Benzoquinone. A solution of **2** (0.0007 g, 0.001 mmol) in d_8-toluene was combined with benzoquinone (0.0015 g, 0.013 mmol, 13 eq) in a J-young NMR tube. This was monitored by ^1H NMR over the next week for conversion to **3**.

Catalytic Reaction of 3 with Benzoquinone.

By ^1H NMR: A C_6D_6 solution of **3** (0.005 g, 0.0077 mmol) and benzoquinone (0.0025 g, 0.02 mmol, 3 eq) was removed from the glovebox in a J-young NMR tube, degassed via three freeze-pump-thaw cycles, and placed under an atmosphere of H_2. Monitoring by ^1H NMR showed the slow appearance of **2** and ~2 eq of hydroquinone over the course of two days at room temperature based on integration.

By GC-MS: A d_8-toluene solution of **3** (0.003 g, 0.0046 mmol) and benzoquinone (0.010 g, 0.09 mmol, 20 eq) was removed from the glovebox in a J-young NMR tube, degassed via three freeze-pump-thaw cycles, and placed under an atmosphere of H_2. Monitoring by ^1H NMR showed the slow appearance of **2** and hydroquinone over the course of 7 days at room temperature. The solution was dried, dissolved in DCM, and filtered for GCMS. The relative integrations of peaks in the chromatogram corresponding to benzoquinone and hydroquinone to determine that of the 20 eq. of benzoquione added to the reaction mixture, ~2 equivalents had been hydrogenated to hydroquinone.

GC-MS Controls:

1. A *d₈*-toluene solution benzoquinone (0.010 g, 0.09 mmol) was removed from the glovebox in a J-young NMR tube, degassed via three freeze-pump-thaw cycles, and placed under an atmosphere of H_2. Monitoring by ^{1}H NMR showed no appearance of hydroquinone over the course of 7 days at room temperature. The solution was dried, dissolved in DCM, and filtered for GCMS. A peak corresponding to benzoquinone was observed, but no peak corresponding to hydroquinone was observed.
2. GC-MS was collected on a solution of benzoquinone in DCM.
3. GC-MS was collected on a solution of hydroquinone in DCM.

Kinetics of H_2 splitting. In a 20 mL vial in the glovebox, a 2 mM stock solution of **3** was prepared by dissolving 5.6 mg of crystalline complex in 4 mL of THF. This was used to prepare either 0.4 mM or 0.2 mM samples used for UV-vis by dilution and was stored at −35 °C between experiments. Each sample was transferred to a standard 1 cm cuvette under nitrogen. This was then placed in a Unisoku CoolSpek cryostat set at 30, 40, 50, or 60 °C. The solution was allowed to equilibrate for 5 minutes prior to collection of an initial spectrum of the sample. Immediately after this 0.5 mL of H_2 (0.02 mmol, 25 equiv. (0.4 mM samples) or 50 equiv. (0.2 mM samples)) was syringed into the cuvette and bubbled through the UV-vis solution. Spectra were collected for a minimum of 2 half-lives. Experiments were done in triplicate for each temperature.

Data Analysis: Eyring Analysis

The intensity of the absorbance at 650 nm was plotted against time in seconds then fit using an exponential function in Origin 8.5 to obtain the rate for each experiment. The rates at each temperature were averaged and the standard deviation was determined. This was used for an Eyring analysis where the standard deviation of the rate at each temperature is shown as vertical error bars.

To report an Eyring analysis, the rate constant k must be calculated.

For a reaction where:

$$\text{Rate} = k[H_2][Ni]$$

under pseudo-first order conditions (i.e. $[H_2] >>> [Ni]$), one can simplify the rate to:

$$\text{Rate} = k_{obs}[Ni]$$

This means that $[H_2]$ is included in k_{obs}, and thus

$$k = k_{obs}/ [H_2]$$

In the experimental setup, 0.5 mL of H_2 gas was added to a UV-vis cuvette with 2 mL of reaction mixture in THF and 2 mL of headspace. This should result in a partial pressure of 0.2 atm H_2 at equilibrium. The reaction was stirred for the duration of the experiment, such that it is reasonable to assume that equilibrium was achieved within minutes of H_2 addition. $[H_2]$ in THF was estimated using mole fraction data at varying pressure and temperatures (E. Brunner, *J. Chem. Eng. Data*, 1985, **30**, 269–273.). The mole fraction at 298.15 K at varying H_2 pressures was plotted and a linear fit was determined (Figure S12). This was repeated for the published data at 323.15 K (Figure S12). The slopes of these lines were then plotted versus temperature and a linear fit was determined, where the slope is in units of mole fraction $H_2{*}MPa^{-1}{*}K^{-1}$ (Figure S12). This trendline was used to calculate the mole fraction H_2 per atm H_2 at the temperatures used in the Eyring analysis. Given that the temperature range used is relatively small, the linear fit used in this calculation should be a reasonable approximation. From there, the partial pressure of H_2 was used to calculate the mole fraction at a given temperature. This was then used to determine the concentration of H_2 in solution, and subsequently the rate constant (see Table 1A - 1 and Table 1A - 2 for calculated values).

The rates calculated were then used for the Eyring analysis to give a line of best fit with an R^2 value of 0.99:

$$y = -7024.59934x + 14.84064$$

Error in the y-intercept used to determine $\Delta S^{\ddagger}$ was determined by assuming plus or minus one order of magnitude in the mole fraction of H_2. This resulted in $\Delta S^{\ddagger} = -18 \pm 5$ cal/mol.

Error in the slope used to determine $\Delta H^{\ddagger}$ was determined by propagation of error in the line of best fit (i.e. error in the slope calculated for the line of best fit). This resulted in $\Delta H^{\ddagger} = 13.9 \pm 0.4$ kcal/mol

This analysis requires the following assumptions:

1) The $[H_2]$ in the (stirred) solution was at equilibrium within minutes of H_2 addition.
2) The mole fraction of H_2 per atm in THF will correlate in a linear fashion to temperature within a limited temperature range.
3) [Ni] is dilute enough that it will not influence the $[H_2]$.

References

---

[1] R. H. Crabtree, *Organometallic Chemistry of the Transition Metals, 6th Edition*, 2014.

[2] (a) D. F. Baumgardner, W. E. Parks and J. D. Gilbertson, *Dalton Trans.*, **2020**, *49*, 960-965.; (b) S. A. Cook, E. A. Hill and A. S. Borovik, *Biochemistry*, **2015**, *54*, 4167-4180..

[3] (a) R. Arevalo and P. J. Chirik, *J. Am. Chem. Soc.*, **2019**, *141*, 9106-9123.; (b) O. R. Luca and R. H. Crabtree, *Chem. Soc. Rev.*, **2013**, *42*, 1440-1459.

[4] S. A. Cook and A. S. Borovik, *Acc. Chem. Res.*, **2015**, *48*, 2407-2414.

[5] (a) M. L. Pegis, C. F. Wise, D. J. Martin and J. M. Mayer, *Chem. Rev.*, **2018**, *118*, 2340-2391.; (b) T. Zell and D. Milstein, *Acc. Chem. Res.*, **2015**, *48*, 1979-1994.; (c) M. Rakowski Dubois and D. L. Dubois, *Acc. Chem. Res.*, **2009**, *42*, 1974-1982.

[6] L. Alig, M. Fritz and S. Schneider, *Chem. Rev.*, **2019**, *119*, 2681-2751.

[7] (a) M. J. Drummond, C. L. Ford, D. L. Gray, C. V. Popescu and A. R. Fout, *J. Am. Chem. Soc.*, **2019**, *141*, 6639-6650.; (b) K. E. Rosenkoetter, M. K. Wojnar, B. J. Charette, J. W. Ziller and A. F. Heyduk, *Inorg. Chem.*, **2018**, *57*, 9728-9737. (c) M. B. Ward, A. Scheitler, M. Yu, L. Senft, A. S. Zillmann, J. D. Gorden, D. D. Schwartz, I. Ivanović-Burmazović and C. R. Goldsmith, *Nature Chem.*, **2018**, *10*, 1207-1212.; (d) A. Dauth, U. Gellrich, Y. Diskin-Posner, Y. Ben-David and D. Milstein, *J. Am. Chem. Soc.*, **2017**, *139*, 2799-2807. (e) G. W. Margulieux, M. J. Bezdek, Z. R. Turner and P. J. Chirik, *J. Am. Chem. Soc.*, **2017**, *139*, 6110-6113.; (f) E. J. Thompson and L. A. Berben, *Angew. Chem. Int. Ed.*, **2015**, *54*, 11642-11646.

[8] (i) T. J. Sherbow, E. J. Thompson, A. Arnold, R. I. Sayler, R. D. Britt, L. A. Berben, *Chem. - Eur. J.*, **2019**, *25*, 454-458.; (h) R. Jain, A. A. Mamun, R. M. Buchanan, P. M. Kozlowski and C. A. Grapperhaus, *Inorg. Chem.*, **2018**, *57*, 13486-13493.; (g) R. Pramanick, R. Bhattacharjee, D. Sengupta, A. Datta and S. Goswami, *Inorg. Chem.*, **2018**, *57*, 6816-6824.; (e) F. Schneck, M. Finger, M. Tromp and S. Schneider, *Chem. Eur. J.*, **2017**, *23*, 33-37.; (f) B. M. Lindley, Q. J. Bruch, P. S. White, F. Hasanayn and A. J. M. Miller, *J. Am. Chem. Soc.*, **2017**, *139*, 5305–5308.; (d) P. O. Lagaditis, B. Schluschaß, S. Demeshko, C. Würtele and S. Schneider, *Inorg. Chem.*, **2016**, *55*, 4529-4536.; (c) J. T. Henthorn, S. Lin and T. Agapie, *J. Am. Chem. Soc.*, **2015**, *137*, 1458-1464.; (b) T. W. Myers, L. A. Berben, *Chem. Sci,*. **2014**, *5*, 2771-2777.; (a) B. W. Purse, L. H. Tran, J. Piera, B. Åkermark and J. E. Bäckvall, *Chem. Eur. J.*, **2008**, *14*, 7500–7503.

[9] (a) A. J. McNeece, K. A. Jesse, J. Xie, A. S. Filatov, J. S. Anderson, *J. Am. Chem. Soc.* **2020**, *142*, 10824-10832.; (b) M-C. Chang, K. A. Jesse, A. S. Filatov, J. S. Anderson, *Chem Sci.*, **2019**, *10*, 1360-1367.; (c) M-C. Chang, A. J. McNeece, E. A. Hill, A. S. Filatov, J. S. Anderson. *Chem. Eur. J.*, **2018**, *24*, 8001-8008.

[10] (a) T. Steiner, *Angew. Chem. Int. Ed.*, **2002**, *41*, 48-76.; (b) G. Aullón, D. Bellamy, A. Guy Orpen, L. Brammer and Eric A. Bruton, *Chem. Commun.*, **1998**, 653-654.

---

[11] (a) M. Gómez-Gallego and M. A. Sierra, *Chem. Rev.*, **2011**, *111*, 4857-4963.; (b) W. D. Jones, *Acc. Chem. Res.*, **2003**, *36*, 140-146. (c) D. G. Churchill, K. E. Janak, J. S. Wittenberg and G. Parkin, *J. Am. Chem. Soc.*, **2003**, *125*, 1403-1420.

[12] (a) Y. Zhang, M. K. Karunananda, H.-C. Yu, K. J. Clark, W. Williams, N. P. Mankad and D. H. Ess, *ACS Catalysis*, **2019**, *9*, 2657-2663. (b) D. E. Prokopchuk, G. M. Chambers, E. D. Walter, M. T. Mock and R. M. Bullock, *J. Am. Chem. Soc.*, **2019**, *141*, 1871-1876.

[13] G. M. Sheldrick. *Acta Cryst***. 2015**, *A71*, 3- 9

[14] O. V. Dolomanov, L. J. Bourhis, R. J. Gildea, A. K. Howard, H. Puschmann, *J. Appl. Cryst*. **2009**. *42*, 339

[15] (a) G. M. Sheldrick. *Acta Cryst*. **2008**, *A64*, 112-122; (b) G. M. Sheldrick, *Acta Cryst*. **2015,** *C71*, 3-8.

[16] F. Neese, Wiley interdisciplinary Reviews - Computational Molecular Science, **2012**, *2* (1), 73–78.

[17] F. Weigend and R. Ahlrichs, *Phys. Chem. Chem. Phys.*, **2005**, *7*, 3297–3305.

[18] F. Weigend, *Phys. Chem. Chem. Phys.*, 2006, **8**, 1057–1065.

[19] T. L. Hill, *An Introduction to Statistical Thermodynamics.*, Dover Publications, Newburyport, 2012.

Chapter Two: Iron(II) Complexes Featuring a Redox-Active Dihydrazonopyrrole Ligand

This chapter has been adapted from the following: Jesse, K. A.; Chang, M-C.; Filatov, A. S.; Anderson, J. S. *ZAAC*. Accepted.

Introduction

Ni complexes with DHP ligands have been essential in establishing the noninnocence of this ligand framework. In particular, we have found that Ni complexes of this family demonstrate reversible ligand-based storage of both protons and electrons as well as engaging in oxidative small molecule reactivity.[1] The redox-activity of this system is predominantly ligand based as Ni centers, particularly in square planar geometries, have a strong bias for a divalent oxidation state. As such, we were interested in exploring complexes where the localization of redox reactions was more ambiguous due to a more redox-active metal center, namely Fe, which readily populates both Fe(II) and Fe(III) oxidation states. Here we report the development of Fe complexes of the ligand ^{Ph,Tol}DHP (2,5-bis((2-phenylhydrazono)(*p*-tolyl)methyl)-pyrrole) in two distinct oxidation states. These complexes adopt 5- or 6-coordinate geometries which also opens up additional possible sites for substrate binding and reactivity. Unlike the related Ni-system, we have been unable to isolate ligand-hydrogenated complexes of this system with Fe. However, the initial metalation reaction requires the presence of an external H-atom abstractor, suggesting that ligand-based H-atoms are present as reactive intermediates. Most importantly, we have performed detailed characterization of the electronic structure of these complexes revealing that despite the enhanced redox-flexibility of the Fe center, oxidation is still predominantly localized on the supporting pincer ligand. This suggests that Fe complexes could exhibit enhanced reactivity due to the possibility of combined ligand- and metal-based redox reactivity.

Results and Discussion

Synthesis and characterization of Fe(^{Ph,Tol}DHP$^•$)(PMe$_3$)$_2$ (1).

Scheme 2 - 1. Synthesis of **1** and **2**.

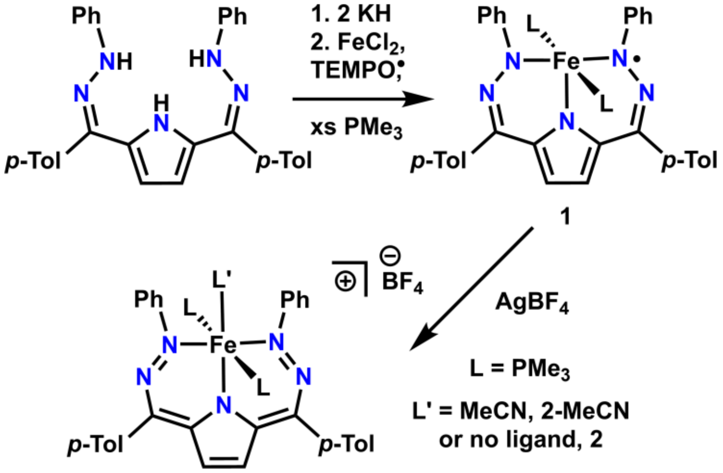

The previously reported ^{Ph,Tol}DHP ligand[1c] was deprotonated with two equivalents of KH in THF, then filtered and condensed to form a red powder putatively assigned as the doubly deprotonated ligand salt. This powder was added dropwise as a suspension to a 1:1 mixture of FeCl$_2$ and TEMPO$^•$ in diethylether in the presence of excess PMe$_3$ to deter the binding of two ^{Ph,Tol}DHP ligands to a single Fe center. After work-up, (^{Ph,Tol}DHP$^•$)Fe(PMe$_3$)$_2$ (**1**) is obtained as a dark green solid in 31% crystalline yield (**Error! Reference source not found.**). IR spectroscopy s hows no evidence for the presence of N–H features suggesting that the additional H-atom present on ^{Ph,Tol}DHP have been abstracted as H-atoms by the added TEMPO$^•$. While we do not have evidence for specific Fe-containing species with N–H functionalities, we note that syntheses carried out in the absence of TEMPO$^•$ result in a red-brown solid that appears to be a complex mixture of products by NMR spectroscopy and has an N–H stretch at 3333 cm^{-1} by IR spectroscopy (Appendix 2). The need for an H-atom abstractor to form **1** in conjunction with the N-H stretch seen in the absense of TEMPO$^•$ by IR spectroscopy suggests that such hydrogenated ligand complexes are likely intermediates, as has been observed in the related Ni systems discussed in Chapter One.[1c]

Figure 2 - 1. Solid state structure of **1**. Ellipsoids are set to 50% probability. Hydrogen atoms have been ommitted for clarity. Fe is shown in orange, C in grey, N in blue, and P in purple.

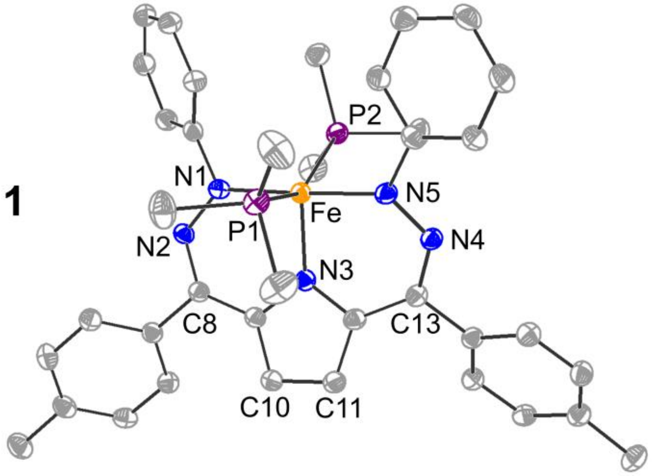

Single crystals of **1** suitable for single-crystal X-ray diffraction (SXRD) were grown from a vapor diffusion of petroleum ether into toluene at room temperature overnight (Figure 2 - 1). The SXRD structure of **1** reveals an intermediate geometry between square pyramidal and trigonal bipyramidal ($\tau_5 = 0.45$). The ^{Ph,Tol}DHP ligand is bound symmetrically through the beta-N of the hydrazone arms while the two PMe_3 ligands are trans to each other. The Fe-$N_{hydrazone}$ bond distance averages 1.923(2) Å while the Fe-$N_{pyrrole}$ bond distance is 1.937(2) Å (Table 2 - 1). These long Fe-ligand distances are suggestive of a high spin Fe center.[2] Consistent with this hypothesis, the ^{1}H NMR shows four broadened and shifted signals as would be expected for a paramagnetic complex (Appendix 2). Evan's method gives a μ_{eff} of 4.6 B.M. consistent with an overall spin of $S = {}^{3}/_{2}$. Similarly, EPR of **1** shows an $S = {}^{3}/_{2}$ rhombic signal featuring g_{eff} values at $g = 5.13$, 2.83, and 1.81 (Appendix 2). This overall spin suggests that the complex is best assigned as either a high spin Fe(II) complex anti-ferromagnetically coupled to a dianinoic ^{Ph,Tol}DHP ligand-based radical (^{Ph,Tol}DHP$^{\bullet}$) or as a high spin Fe(I) center featuring an oxidized mono-anionic ligand.

Table 2 - 1. Selected bond lengths of **1**, **2**, **2-MeCN**, and related Ni complexes (Å).

	1	**2 -MeCN**	**2**	**Ni(^{Ph,Tol}DHP$^{\bullet}$)**[a]	**[Ni(^{Ph,Tol}DHP)]$^{+}$** [a,b]
M[c]-N1	1.930(2)	1.923(2)	1.875(2)	1.866(2)	1.864(2)
M-N3	1.937(2)	1.916(2)	1.861(2)	1.863(2)	1.860(2)
M-N5	1.916(2)	-[d]	1.861(2)	1.872(2)	1.869(2)
M-P1	2.3980(6)	2.3343(5)	2.3657(9)	2.2319(7)	2.2630(7)
M-P2	2.4219(6)	-	2.3289(9)	-	-
N1-N2	1.351(2)	1.318(2)	1.329(3)	1.342(2)	1.302(2)
N2-C8	1.306(3)	1.345(2)	1.350(3)	1.319(3)	1.348(2)
N4-C13	1.316(3)	-	1.347(4)	1.322(2)	1.342(3)
N4-N5	1.356(3)	-	1.330(3)	1.337(3)	1.314(2)
C10-C11	1.393(3)	1.354(4)	1.351(4)	1.371(3)	1.346(3)

[a] These complexes also feature a PMe_3 ligand. [1c]

[b] BF_4 counterion

[c] M = Fe for **1**, **2-MeCN**, and **2**. M = Ni for Ni(^{Ph,Tol}DHP$^{\bullet}$) and [Ni(^{Ph,Tol}DHP)]$^{+}$

[d] no bond length listed due to crystallographic symmetry or a difference in coordination number/geometry

Comparison to Ni complexes featuring the same ^{Ph,Tol}DHP ligand in oxidized and radical states (Table 2 - 1) indicates **1** is best considered an Fe(II) center antiferromagnetically coupled to a ligand radical. The C–C pyrrole backbone, N–N, and N–C bond distances most closely align with a ligand radical. This assignment is supported by density functional theory (DFT) calculations. Optimization of **1** was first attempted as a quartet but resulted in a complex with two unpaired electrons on Fe ferromagnetically coupled to a ligand based radical. This electronic configuration seemed unlikely, so **1** was then optimized with a broken symmetry treatment. This shows spin density on the ligand of opposite character from the spin density on the high-spin Fe(II) center.

Mulliken spin density indicates that 0.72 electrons are localized on ^{Tol,Ph}DHP, supporting the assignment of a primarily ligand based radical (Appendix 2).

Cyclic voltammetry (CV) of **1** in THF shows a reversible feature at −0.73 V and a quasi-reversible feature at −1.31 V vs. Fc/Fc^{+} with an open circuit potential of −0.89 V (Appendix 2).These features are similar to those observed in related Ni systems suggesting that these redox events are ligand based despite the possibility of Fe-based redox chemistry.[1] Another possible assignment for **1** is that of an intermediate spin Fe(III) center coordinated to a trianionic, reduced ^{Ph,Tol}DHP ligand. However, these CV data, where the ligand can be both reduced and oxidized once, along with other spectroscopic characterization shown below suggests that the best assignment for **1** is still that of a high spin Fe(II) center antiferromagnetically coupled to a ^{Ph,Tol}DHP ligand radical. Interestingly, there are not any additional redox couples that might be assigned to an Fe-based oxidation within the THF solvent window. Unfortunately, attempts to reduce **1** with a variety of reagents, such as KC_8, cobaltocene, decamethylcobaltocene, sodium naphthalenide, or NaHg, invariably led to a complex mixture of products.

Synthesis and characterization of Fe(^{Ph,Tol}DHP)(PMe_3)$_2$ (2).

As might be predicted by the reversibility of the feature at −0.73 V vs. Fc/Fc^{+}, oxidation of **1** with $AgBF_4$ in acetonitrile is more tractable, and addition of oxidant results in an immediate color change from deep green to dark blue. Further color changes are observed upon workup and drying, and the oxidized complex [(^{Ph,Tol}DHP)Fe(PMe_3)$_2$][BF_4] (**2**) is isolated as a maroon powder in 91% yield. Notably, this maroon solid regains a blue color if redissolved in acetonitrile. ^{1}H NMR of **2** in CD_3CN shows a symmetric diamagnetic species with two bound PMe_3 ligands (Appendix 2). This indicates that upon oxidation, the Fe(II) center transitions from a high spin manifold to a low spin manifold. While Fe(II) complexes feature prominently in spin-crossover applications,[3] examples where spin-crossover can be triggered by redox events are still uncommon.[4]

Figure 2 - 2. Solid state structures of **2-MeCN**, and **2**. Ellipsoids are set to 50% probability. Hydrogen atoms and counterions have been ommitted for clarity. Fe is shown in orange, C in grey, N in blue, and P in purple.

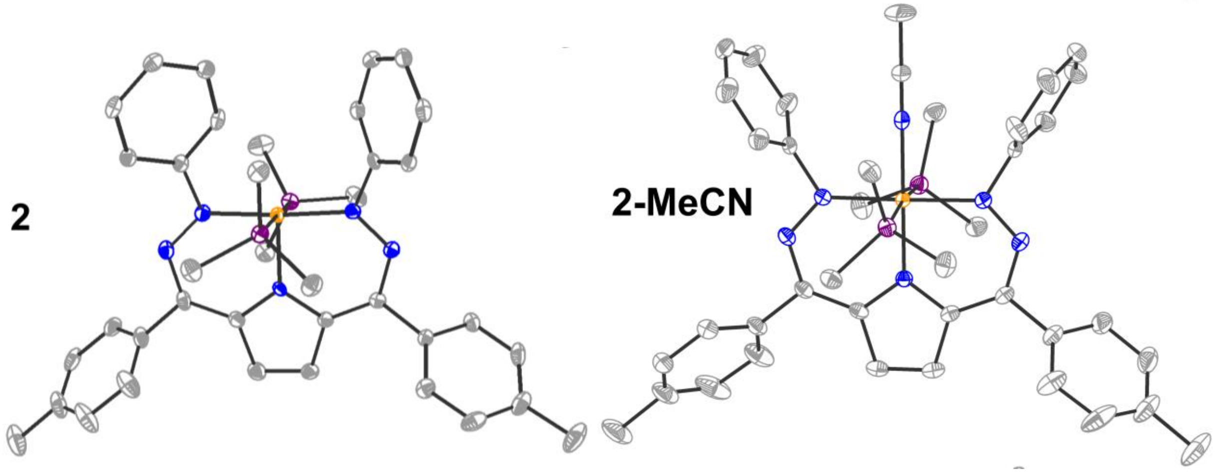

Single crystals suitable for X-ray diffraction were grown by vapor diffusion of diethylether into concentrated acetonitrile solutions. The SXRD structure obtained from crystals grown in this way shows a pseudo-octahedral geometry, with an acetonitrile adduct in the previously open coordination site trans to the pyrrole N to give the solvento adduct **2-MeCN** (Scheme 2 - 1). As would be expected for a low spin Fe(II) center, the Fe-N$_{\text{hydrazone}}$ and Fe-N$_{\text{pyrrole}}$ distances show a slight contraction from those of **1** to 1.923(1) and 1.916(2) Å respectively. Additionally, the pyrrole C-C backbone bond is contracted to 1.354(4) Å, indicative of ligand oxidation (Table 2 - 1).

Given that an acetonitrile adduct was observed from the dark blue crystals analyzed by X-ray diffraction, we hypothesized that the color changes observed upon drying/dissolution may arise from acetonitrile binding. To investigate this, **2** was dried, then dissolved in a variety of solvents. It was found that in coordinating solvents such as acetonitrile or DMF, the solution turned blue, while in less coordinating solvents, such as THF, the solution turned green. In benzene, **2** was sparingly soluble and produced a red solution (Appendix 2). While dilute due to poor solubility, the ^{1}H NMR spectrum of **2** in C_6D_6 shows diamagnetic signals, consistent with a low-spin species. Together, these observations suggested that the color changes for **2** were arising from variable solvent coordination. To investigate the possibility of a solvent-free 5-coordinate complex, **2** was crystallized from a vapor diffusion of petroleum ether into THF. The SXRD structure obtained from these pale green crystals show a 5-coordinate pseudo-square pyramidal complex ($\tau_5 = 0.04$). The ligand bond distances are a close match for those found in complex **2-MeCN**, consistent with an oxidized ^{Ph,Tol}DHP ligand (Table 2 - 1). The Fe–P distances are similar to **2-MeCN**. However, there is a noticeable contraction of the Fe-N bonds upon the removal of the axial MeCN adduct. We hypothesize that the lessened steric bulk around Fe should allow the ^{Ph,Tol}DHP ligand to bind more closely, resulting in the contracted Fe-N bond lengths seen crystallographically (Table 2 - 1). The Fe-P and Fe-N bond length contractions in **2-MeCN** and **2** from **1** suggest that both of these oxidized complexes feature a low-spin Fe center. These combined observations suggest that **2** can bind solvents in its open coordination site, but that it maintains a low-spin Fe(II) electronic structure throughout. Therefore, the change from a high spin Fe(II) center in **1** to a low spin Fe(II) center in **2** is a product of ligand oxidation rather than solvent coordination.

Oxidation state of 1 and 2 by XAS.

All of the data acquired on **1** and **2** support ligand-based oxidation events. However, concretely assigning ligand versus metal-based redox localization is challenging and typically requires multiple orthogonal analyses. To further verify that the oxidation of **1** to **2** was ligand-based, Fe K-edge X-ray absorption spectroscopy (XAS) was conducted on solid powders of the two complexes. Overlaying the X-ray absorption near edge structure (XANES) spectra of these complexes show that **1** and **2** have effectively identical K-edge's at 7121.3 eV (Figure 2 - 3). This data concretely supports that the oxidation state of Fe in **1** and **2** is the same, and that the oxidation is ligand-based.

Figure 2 - 3. Fe K-edge X-ray absorption spectra of **1** and **2** as powders. Both samples feature a K-edge inflection point at 7121.3 eV. Inset: Derivative spectra of K-edge XAS. **2** is offset for ease of visualization.

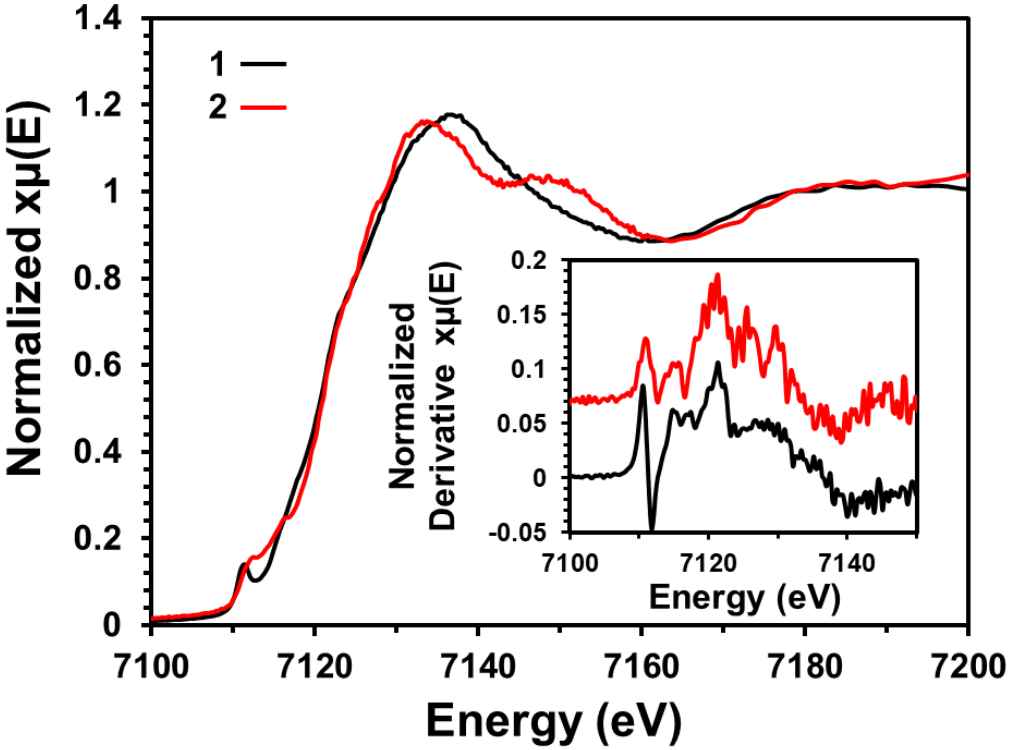

By UV-visible spectroscopy, **2** dissolved in acetonitrile features two additional absorbances at 644 and 940 nm as compared to the UV-visible spectrum of **2** in benzene (Appendix 2). Interestingly, these absorbances align reasonably well with absorbances seen in **1** at 616 and 912 nm respectively. In particular, broad absorbances in the 800 to 1000 nm range have been seen in related Ni complexes that feature a DHP ligand radical.[1] The presence of these features may imply that in solution with coordinating solvents such as acetonitrile **2** might adopt an electronic structure with a low-spin Fe(III) metal center antiferromagnetically coupled to a ligand based radical. Notably, in the solid state **2-MeCN** shows no evidence for variable temperature redox-changes as the structures collected at both 100 K and at room temperature show nearly identical parameters (Appendix 2). To investigate the possibility of a redox tautomerization in solution, XAS was collected of **2-MeCN** in a polyethylene glycol matrix with added acetonitrile (Appendix 2). However, the XANES spectrum for **2-MeCN** prepared in this way shows a similar edge position to that observed for **1** and **2**. These data suggest that the difference in UV-visible spectra between **2-MeCN** and **2** arises from the changing coordination environment at the Fe center as opposed to a different redox distribution induced by ligand binding.

Conclusions

The data presented here describe a series of Fe(II) complexes in various redox states. Notably, while Fe should possess an accessible Fe(III) oxidation state, all structural and spectroscopic characterization of the products indicate that these redox events are primarily ligand based. While the Fe oxidation state does not appear to change upon oxidation, the Fe(II) center does undergo a redox-induced spin-crossover from high-spin to low-spin. Finally, the oxidized complex **2** displays solvatochromism arising from solvent binding in the open coordination site in this complex. While hydrogenated versions of **1** and **2** have not been isolated, the need for an H-atom abstractor (TEMPO$^{\bullet}$) in the synthesis of **1** suggests that hydrogenated complexes are present as reactive intermediates.

Experimental

General Methods. All chemicals were purchased from commercial suppliers and used without further purification. All manipulations were carried out under an atmosphere of N_2 using standard Schlenk and glovebox techniques. Glassware was dried at 180 °C for a minimum of two hours and cooled under vacuum prior to use. Solvents were dried on a solvent purification system from Pure Process Technologies and stored over 4 Å molecular sieves under N_2. Tetrahydrofuran (THF) and diethyl ether (Et_2O) was stirred over NaK alloy and run through an additional alumina column prior to use to ensure dryness. Solvents were tested for H_2O and O_2 using a standard solution of sodium-benzophenone ketyl radical anion. CD_3CN, C_6D_6, and d_8-toluene were dried over 4 Å molecular sieves under N_2. ^{1}H, $^{13}C\{^{1}H\}$, $^{31}P\{^{1}H\}$, $^{19}F\{^{1}H\}$, and $^{11}B\{^{1}H\}$ NMR spectra were recorded on Bruker DRX 400 or 500 spectrometers. Chemical shifts are reported in ppm units referenced to residual solvent resonances for ^{1}H and $^{13}C\{^{1}H\}$ spectra. UV-visible spectra were recorded on a Bruker Evolution 300 spectrometer and analyzed using VisionPro softwar. IR spectra were obtained on a Bruker Tensor II spectrometer with the OPUS software suite. All IR samples were prepared nujol mulls and collected between KBr plates. EPR spectra were recorded on an Elexsys E500 Spectrometer with an Oxford ESR 900 X-band cryostat and a Bruker Cold-Edge Stinger. EPR data was fit using a least-squares fit in SpinCount. Electrochemical measurements were performed using a BAS Epsilon potentiostat and analyzed using BAS Epsilon software version 1.40.67NT. Cyclic voltammetry measurements were made using a glassy carbon working electrode, platinum wire counter electrode, and silver wire pseudo-reference electrode, and referenced to external Fc/Fc^{+}. Single crystal X-ray diffraction data were collected in-house using Bruker D8 Venture diffractometer equipped with Mo microfocus X-ray tube ($\lambda = 0.71073$ Å) or at the Advanced Photon Source of Argonne National Laboratory (beamline 15-ID-B,C,D) using X-ray radiation with a wavelength of $\lambda = 0.41328$ Å. X-ray near-edge absorption spectra (XANES) were employed to probe the local environment of Fe. Powder samples were prepared by material grinding finely. A Teflon window was sealed on one side with Kapton tape and powder was then transfer transferred to the inside of this ring before compacting with a Teflon rod and sealing the remaining face with Kapton tape. In the case of RT solution samples, powder was dissolved with minimal solvent, then added to melted polyethylene glycol and mixed well. This was allowed to cool then transfered to a teflon window sealed on one side with Kapton tape. After transfer of the material, the window was sealed with Kapton tape. All sample preparation was performed under an inert atmosphere. Data were acquired at the Advanced Photon Source at Argonne National Labs with a bending magnet source with ring energy at 7.00 GeV. Fe K-edge data were acquired at the MRCAT 9-BM-B,C and 10-BM beam lines. The incident, transmitted and reference X-ray intensities were monitored using gas ionization chambers. A metallic iron foil standard was used as a reference for energy calibration and was measured simultaneously with experimental samples. X-ray absorption spectra were collected at room temperature. Data collected was processed using the Demeter software suite[11] by extracting the EXAFS oscillations $\chi(k)$ as a function of photoelectron wavenumber k. The theoretical paths were generated using FEFF6 and the models were determined using the fitting program Artemis.

X-Ray Structure Determination. Crystal Structure Determination. The diffraction data were measured at 100 K on a Bruker D8 VENTURE with PHOTON 100 CMOS detector system equipped with a Mo-target micro-focus X-ray tube (λ = 0.71073 Å) or at the Advanced Photon Source of Argonne National Laboratory (beamline 15-ID-B,C,D) using X-ray radiation with a wavelength of λ = 0.41328 Å. Data reduction and integration were performed with the Bruker APEX3 software package (Bruker AXS, version 2015.5-2, 2015). Data were scaled and corrected for absorption effects using the multi-scan procedure as implemented in SADABS (Bruker AXS, version 2014/5, 2015, part of Bruker APEX3 software package). The structure was solved by the dual method implemented in SHELXT[5] and refined by a full-matrix least-squares procedure using

OLEX23[6] software package (XL refinement program version 2014/7[7]). Suitable crystals were mounted on a cryo-loop and transferred into the cold nitrogen stream of the Bruker D8 Venture diffractometer. C-H hydrogen atoms were generated by geometrical considerations, constrained to idealized geometries, and allowed to ride on their carrier atoms with an isotropic displacement parameter related to the equivalent displacement parameter of their carrier atoms.

Density Functional Theory: Geometry Optimizations: Geometry optimization calculations were performed with ORCA[8] software suite using density functional theory (DFT). Geometries were fully optimized starting from coordinates generated from finalized cifs of the compound crystal structures. The B3P functional was used with a basis set of def2-SVP on H, def2-TZVPP on Fe, N, and P, and def2-TZVP on C atoms. The resulting structures were confirmed to be minima on the potential energy surface by frequency calculations using ORCA[5]. Frequency calculations were also conducted using the B3P functional and previously listed basis sets for each atom type. For **1**, the structure was optimized with a broken symmetry calculation using flipspin.

$Fe(PhDHP^{\bullet})(PMe_3)_2$ (1). In a 20 mL vial, PhDHP-H_2 (500 mg, 1 eq.) was dissolved in THF (10 mL) with stirring. KH (83 mg, 2 equiv.) were added as a solid and allowed react until all bubbling had stopped (~10 minutes) and the solution was bright red. The solution was then filtered and condensed under vacuum to form a red oil. This was taken up in petroleum ether and then dried under vacuum to form a red powder (PhDHP-K_2). In a 20 mL vial, $FeCl_2$ (11.3 mg, 0.09 mmol, 1 eq.) was dissolved in diethyl ether (12 mL) in the presence of excess PMe_3 (0.1 mL, 0.9 mmol, 10 eq.) and TEMPO• (15.3 mg, 0.1 mmol, 1.1 eq.) to form a deep red solution. Separately, PhDHP-K_2 (50 mg, 0.09 mmol, 1 equiv.) was stirred in diethyl ether (5 mL) to form a suspension. This suspension was added dropwise to form a deep green solution. Once the PhDHP-K_2 had been added, the reaction was allowed to stir for 20 minutes, filtered, then condensed under vacuum.

This was washed with petroleum ether (10 mL), taken up in toluene again (4 mL), filtered, and dried under vacuum. This was taken up in toluene (4 mL), filtered, then condensed to a concentrated solution. The pure product was obtained by a two-layer crystallization of petroleum ether and the concentrated reaction solution in toluene at −35 °C. Yield: 31%. Single crystals suitable for XRD were obtained by a vapor diffusion of petroleum ether into a concentrated solution of product in toluene at room temperature overnight. ^{1}H NMR (400 MHz, d_8-toluene , RT): $\delta = 25.49$ (bs), 15.00 (bs), 13.13 (bs), −5.80 (bs). Magnetic Susceptibility: Evans' Method (C_6D_6, RT, μ_B): $\mu_{eff} = 4.6$. EPR experimental (g_{eff}): 5.13, 2.83, 1.81. EPR simulated (g_z, g_x, g_y): 2.17, 2.28, 1.98. IR (nujol mull, cm^{-1}): 2794 (C-H, w), 1583 (s), 1509 (m), 1243 (s), 1216 (m), 1096 (s). UV-vis, nm in THF, (ε, M^{-1}cm^{-1}): 480 (3796), 616 (6612), 690 (5024), 768 (3918), 912 (1018). Anal. Calc **1** + pentane. C, 67.89; H, 7.42; N, 9.21; Found: C, 68.34; H, 6.54; N, 9.98. Note: These combustion results represent the most consistent data we have obtained. Complex **1** is unstable and decomposes slowly in the solution or solid state, making obtaining accurate combustion analysis difficult.

[Fe(^{Tol,Ph}DHP)(PMe_3)$_2$(MeCN)][BF_4] (2-MeCN). In a 20 mL vial, **1** (25 mg, 0.04 mmol, 1 eq.) was dissolved in acetonitrile (10 mL). Separately, $AgBF_4$ (7 mg, 0.04 mmol, 1 eq.) was dissolved in acetonitrile (2 mL), then added to the reaction vial dropwise with stirring to form a deep blue solution. This was allowed to stir for 20 minutes. It was then filtered and condensed under vacuum. The maroon solid was washed with toluene (5 mL), then taken up in acetonitrile, filtered, then condensed for form a concentrated solution in acetonitrile. One drop of PMe_3 was then added, then a vapor diffusion of diethylether into this concentrated solution of product in acetonitrile with excess PMe_3 was set up for final purification. Crystals could be obtained overnight at room temperature. Yield: 91% . Single crystals suitable for XRD were obtained by vapor diffusion of diethylether into acetonitrile or by vapor diffusion of petroleum ether into a solution of **2** in THF. ^{1}H NMR (400 MHz, CD_3CN, RT): δ = 8.12 (s, 2), 7.67 (d, 4), 2.45 (s, 6), 0.39 (bs, 16). ^{13}C{^{1}H} NMR (400 MHz, CD_3CN, RT): δ = 138.72, 138.22, 137.07, 135.09, 131.59, 129.61, 128.97, 127.42, 125.83, 124.78, 124.54, 20.88, 12.66. ^{31}P{^{1}H} NMR (400 MHz, CD_3CN, RT): δ = 6.5. ^{19}F{^{1}H} NMR (500 MHz, CD_3CN, RT): δ -151.9. ^{11}B{^{1}H} NMR (400 MHz, CD_3CN, RT): δ −1.2. IR (nujol mull, cm^{-1}): 2721 (C-H, m), 2669 (C-H, m), 2599 (C-H, w), 1957 (w), 1663 (w), 1586 (m), 1306 (s), 1283 (s), 1170 (s), 1055 (s), 933 (s). UV-vis, nm in acetonitrile, (ε, M^{-1}cm^{-1}): 534 (2661), 644 (4244), 728 (5113), 940 (1135). UV-vis, nm in acetonitrile, (ε, M^{-1}cm^{-1}): 536 (2127), 746 (2037), 676 (755). Anal. Calc. **2** + MeCN, C, 58.84; H, 5.80; N, 10.29; Found: C, 58.49; H, 5.83; N, 10.23.

References

---

[1] (a) McNeece, A. J.; Jesse, K. A.; Xie, J.; Filatov, A. S.; Anderson, J. S. *J. Am. Chem. Soc.* **2020**, *142*, 10824–10832.; (b) Chang, M. C.; Jesse, K. A.; Filatov, A. S.; Anderson, J. S. *Chem. Sci.* **2019**, *10*, 1360–1367.; (c) Chang, M.-C.; McNeece, A. J.; Hill, E. A.; Filatov, A. S.; Anderson, J. S. *Chem. Eur. J.* **2018**, *24*, 8001–8008

[2] a) Zheng, H.; Langner, K. M.; Shields, G. P.; Hou, J.; Kowiel, M.; Allen, F. H.; Murshudov, G.; Minor, W. *Acta Crystallogr. Sect. D Struct. Biol.* **2017**, *73*, 316–325.; b) Nishida, Y.; Kida, S.; Ray, X.-. *Dalt. Trans.* **1987**, 1157–1161.

[3] a) Batten, S. R.; Bjernemose, J.; Jensen, P.; Leita, B. A.; Murray, K. S.; Moubaraki, B.; Smith, J. P.; Toftlund, H. *J. Am. Chem. Soc.* **2020**, *142*, 17670−17680. b) García-Lopez, V.; Waerenborgh, J. C.; Vieira, B. J. C.;´ Clemente-Leon, M.; Coronado, E., *Dalton Trans.* **2018**, *47*, 9156−9163.; c) Shatruk, M.; Phan, H.; Chrisostomo, B. A.; Suleimenova, A. *Coord. Chem. Rev.* **2015**, *289−290*, 62−73.; d) Halcrow, M. A. In *Spin-Crossover Materials: Properties and Applications;* Wiley-Blackwell: Oxford, 2013.; e) Tissot, A.; Shepherd, H. J.; Toupet, L.; Collet, E.; Sainton, J.; Molnar, G.; Guionneau, P.; Boillot, M.-L. *Eur. J. Inorg. Chem.* **2013**, *2013*, 1001−1008.; f) Murray, K. S., *Eur. J. Inorg. Chem.* **2008**, *2008*, 3101−3121.

[4] a) Govor, E. V.; Al-Ameed, K.; Chakraborty, I.; Coste, C. S.; Govor, O.; Sanakis, Y.; McGrady, J. E.; Raptis, R. G. *Angew. Chem. Int. Ed.* **2017**, *56*, 582–586.; b) Min, K. S.; DiPasquale, A. G.; Rheingold, A. L.; White, H. S.; Miller, J. S. *J. Am. Chem. Soc.* **2009**, *131*, 6229–6236.

[5] G. M. Sheldrick. *Acta Cryst***. 2015**, *A71*, 3- 9.

[6] O. V. Dolomanov, L. J. Bourhis, R. J. Gildea, A. K. Howard, H. Puschmann, *J. Appl. Cryst*. **2009**. *42*, 339.

[7] (a) G. M. Sheldrick. *Acta Cryst*. **2008**, *A64*, 112-122; (b) G. M. Sheldrick, *Acta Cryst*. **2015,** *C71*, 3-8.

[8] (a) Neese, F. "The Orca Program System" *Wiley Interdisciplinary Reviews: Computational Molecular Science* **2012**, *2*, 73-78. (b) H - Kr: A. Schaefer, H. Horn and R. Ahlrichs, *J. Chem. Phys.* **1992**, *97*, 2571. (c) A. Schaefer, C. Huber and R. Ahlrichs, *J. Chem. Phys.* **1994** *100*, 5829. (d) F. Weigend, R. Ahlrichs, *Phys. Chem. Chem. Phys.* **2005**, 7, 3297.

Chapter Three: Metal-ligand Cooperativity Enabled Reduction of O_2 via an Fe(III)-Hydroperoxo Intermediate

Introduction

The use of ligands that can facilitate the movement of both protons and electrons[1] in synthetic applications has drawn inspiration from biology. For example, the terminal oxidant in cytochrome P450 enzymes, Compound I, consists of an Fe(IV)-oxo moiety with an additional oxidizing equivalent partially delocalized across a redox-active thiolate and pyrrole-based heme ligands.[2] Other enzymes, such as cytochrome C oxidase, selectively reduce molecular O_2 to water with the aid of an elaborate secondary coordination sphere including a copper center poised above the heme binding site.[3] This varied reactivity is controlled by the enzyme environment as well as the carefully choreographed delivery of proton and electron, or H-atom equivalents. Still, there are common intermediates which feature in most enzymatic systems, one of which is an Fe(III)-hydroperoxo which results from formal H-atom delivery to an Fe(III)-superoxo intermediate from the secondary coordination sphere provided by the enzyme superstructure.[2,4]

One strategy for better understanding the structure and reactivity of these Fe-hydroperoxo intermediates is the use of model complexes.[5] Many of these complexes are generated by reacting a starting Fe(II) complex with H_2O_2.[6] Another common route is to first generate an Fe(III)-superoxo, which can be reacted with acid to then form the Fe(III)-hydroperoxo complex.[7] Far fewer examples of Fe(III)-hydroperoxo complexes generated directly from O_2 exist. A notable example of an Fe(III)-hydroperoxo complex generated from O_2 comes from the Goldberg group, where an amine group on the ligand scaffold functions as the H source.[8] This may suggest that ligand noninnocence is important for generating Fe(III)-hydroperoxo complexes directly from O_2.

Here, we utilize the previously reported pyrrole-based ligand scaffold $^{t\mathrm{Bu,Tol}}$DHP ligand ($^{t\mathrm{Bu,Tol}}$DHP = 2,5-bis((2-*t*-butylhydrazono)(*p*-tolyl)methyl)-pyrrole) that can donate two electrons and two protons to a substrate.[9] When metalated with Ni(II), this complex can catalytically hydrogenate benzoquinone as discussed in Chapter One, but reactivity with more challenging substrates was not observed. Chapter Two discusses how a phenyl derivative of the DHP ligand, when metalated to Fe(II), can be isolated in multiple ligand redox states despite the more accessible redox couples of Fe relative to Ni. However, this phenyl substituted scaffold did not support isolable complexes with a hydrogenated ligand.[10] In this chapter I will discuss how the $^{t\mathrm{Bu,Tol}}$DHP ligand can be metalated with an Fe(II) center such that the redox and protonation capabilities of the ligand can be used in conjunction with the redox couples of the Fe center toward the reduction of a substrate. With this starting material, we are able to use O_2 as an oxidant to form an unusual Fe(III)-hydroperoxo intermediate. This reactivity relies on the ligand acting as both as an electron and proton donor analogous to the protein superstructure of biological systems. These complexes have been characterized by a variety of spectroscopic techniques in addition to kinetic and computational studies. Reactivity studies show that this system performs O-atom transfer to PPh_3 and H-atom abstraction from both C–H and N–H bonds. This study demonstrates the utility of redox-active ligands that are also proton responsive for facilitating challenging small molecule activation and oxidative reactivity with green oxidants.

Synthesis and Characterization of Fe(^{Tol,tBu}DHP-H$_2$)(DMAP)Cl (1)

Scheme 3 - 1. Metalation of ^{tBu,Tol}DHP-H$_2$•2HCl with FeCl$_2$.

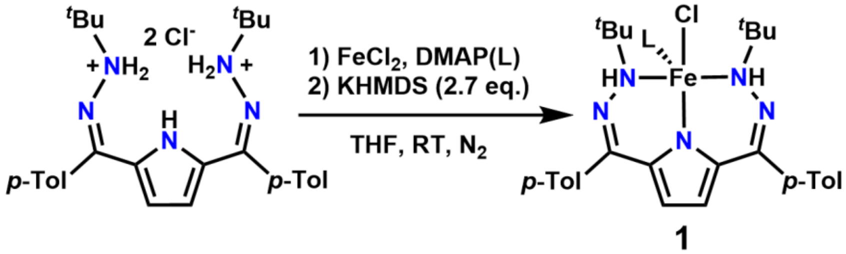

The dihydrazonopyrrole ligand, ^{Tol,tBu}DHP was synthesized as the HCl salt as described previously and metalated via addition to a solution of FeCl$_2$ and dimethylaminopyridine (DMAP) in THF, followed by the addition of 2.7 equivalents of potassium hexamethyldisilazide (KHMDS).[11] After workup, an orange powder was isolated in 71% mass yield. Vapor diffusion of petroleum ether into a toluene solution of **1** at room temperature overnight in the glovebox resulted in square, orange crystals suitable for single crystal X-ray diffraction (SXRD). From these data, the product was assigned as Fe(^{Tol,tBu}DHP-H$_2$)(DMAP)Cl (**1**), where the beta N of each hydrazone arm features an N–H bond (Figure 3 -1). The H on the beta-N of the hydrazone moieties were found in the difference map and further confirmed by stretches at 3182 and 3170 cm^{-1} via infrared (IR) spectroscopy (Appendix 3). By SXRD, the complex is pseudo-square pyramidal, with a τ_5 value of 0.017. Furthermore, the *t*-butyl groups of the hydrazone arms of the pincer ligand are strained out of the ligand plane. This creates an overall asymmetric complex in the solid state, where one side of the pincer ligand has closer through space interactions with the DMAP ligand and the other side of the pincer ligand is pushed out into the open coordination site of the Fe(II)-complex. This asymmetry results in one of the beta-N H-atoms being positioned close to where a substrate is most likely bind to the Fe-center, thus creating a promising environment for substrate hydrogenation via H-atom abstraction from the ligand. This poised N–H group represents a biomimetic approach to controlling the delivery of reducing equivalents to substrates.

Figure 3 - 1. Solid state structure of **1** looking down the Cl-Fe-N3 bond (left) and looking down the Fe-N6 bond (right). Fe (orange), N (blue), C (gray), Cl (lime green), H (white). N-H protons were found in the difference map and refined. Selected bond lengths (Å). Fe1-Cl1: 2.2651(7), Fe1-N1: 2.399(2), Fe1-N3: 2.035(3), Fe1-N5: 2.362(2), Fe1-N6: 2.098(2), N1-N2: 1.416(3), N2-C8: 1.293(3), N4-N5: 1.410(3), N4-C13: 1.288(3), C10-C11: 1.390(4). Selected bond angles (°). N1-Fe1-N5: 152.93(8), N3-Fe1-Cl1: 153.00(1).

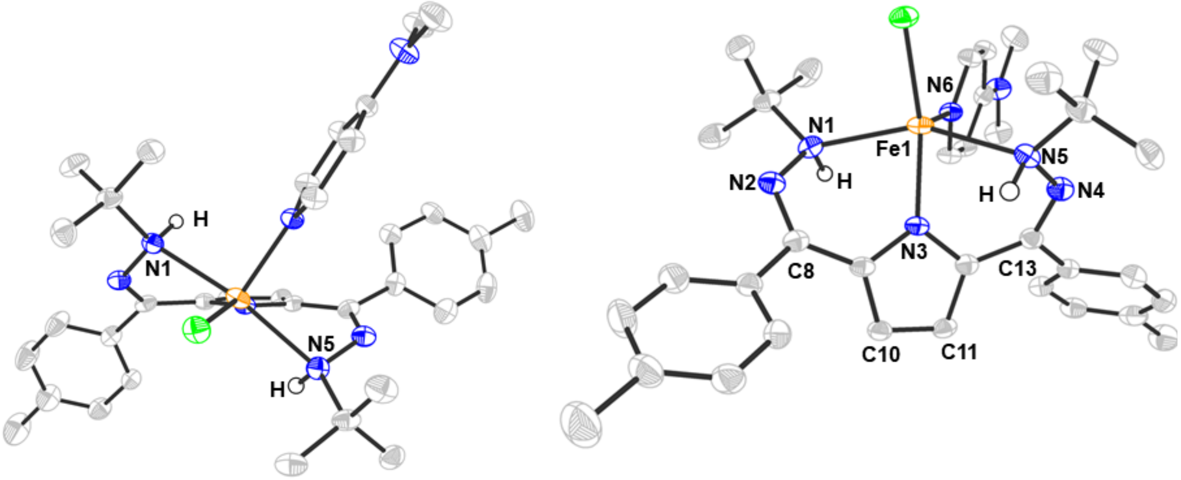

By SXRD, the Fe–N bond lengths were found to be 2.399(2) and 2.362(2) Å respectively to the hydrazone arms and 2.035(2) Å to the pyrrole N, consistent with a high spin Fe(II) center.[12] This spin and oxidation state for the Fe center was further supported by solution state magnetic measurements, with a μ_{eff} = 5.0 μ_B by Evans method. Both experiments are consistent with the expected $S = 2$ spin for a high spin Fe(II) complex. EPR spectroscopy in parallel mode on a 15 mM solution in toluene at 15 K shows a broad feature at $g = 8.4$, which is also consistent with an $S = 2$ complex. The paramagnetic nature of this complex was further supported via ^{1}H NMR in C_6D_6, which features 7 broad features ranging from 29.20 ppm to 3.44 ppm. Assuming equivalence for the $^{t\text{Bu,Tol}}$DHP-H_2 ligand in solution, one would expect 9 features in the ^{1}H NMR. This suggests that some features, likely those with higher proximity to the high spin Fe(II) center, have been broadened or shifted to such an extent that they are no longer visible. It further suggests that the hydrazone arms equilibrate in solution, resulting in an overall symmetric complex in solution at room temperature, unlike in the solid state crystal structure.

Reactivity in the presence of molecular oxygen

The reaction of molecular O_2 with **1** in toluene was monitored at low temperature by UV-vis spectroscopy (Figure 3 - 2). Complex **1** is largely featureless at wavelengths longer than 400 nm. Upon addition of excess O_2 to a 0.35 mM solution in toluene at –60 °C, broad features grew in throughout the spectrum assigned as complex **2** (Figure 3 - 2, top left). After 20 minutes, a new species, **3**, began to grow in (Figure 3 - 2, top right). The conversion between **2** and **3** is convoluted suggesting that the lifetime of **2** is short even at temperatures as low as –80 °C. However, intermediate **3** is stable once it is formed and persists without noticeable decomposition at temperatures up to –40 °C.

Kinetic studies were conducted to better understand the transformation observed by UV-vis spectroscopy. Kinetic analysis of the transformation from **1** to **2** was conducted under pseudo first-order conditions by monitoring the growth and disappearance of the peak in the UV-vis spectrum at 996 nm to avoid overlap between the features in **2** and **3**. The transformation from **1** to **2** did not fit standard zero-, first-, or second-order kinetics well. This suggests a complicated pre-equilibrium or a mixture of products, that is likely further convoluted by the transient nature of **2** and its conversion to **3** concomitantly with its formation. In contrast the transformation from **2** to **3** was found to follow first-order kinetics in Fe using an exponential fit of the data (Appendix 3). Eyring analysis of the transformation from **2** to **3** gives an $\Delta H^{\neq} = 7.6(1.0)$ kcal/mol and $\Delta S^{\neq} = -34(4.9)$ cal/mol K^{-1}. These activation parameters are similar to those observed for the reaction of an Fe(III)-superoxo complex with acid to a Fe(III)-hydroperoxo complex, where both feature a macrocyclic N-methylated cyclam ligand.[13] Furthermore, one might expect a negative entropy of activation for an intramolecular H-atom transfer from the ^{Tol,tBu}DHP-H$_2$ ligand to a superoxo lignad due to reorganization energy cost. Therefore, these activation parameters may suggest that an Fe(III)-superoxo complex is present in the mixture that is **2**, which then reacts further to form an Fe(III)-hydroperoxo complex, **3**.

Figure 3 - 2. UV-vis of a 0.35 mM solution of **1** in toluene at –60 °C upon addition of 0.5 mL of O$_2$ where **1** is black, **2** is green, **3** is red, and **4** is blue. Top, left: Formation of **2** with scans every 1 minute starting 2 minutes after O$_2$ addition. Top, right: Formation of **3** from **2** with scans every 5 minutes. Bottom, left: Growth of **4** from **3** at –10 °C from a 0.35 mM solution of **1** in toluene. scans every 10 minutes. Bottom, right: dependence of rate on temperature from which the activation parameters have been obtained for the reaction from **2** to **3**.

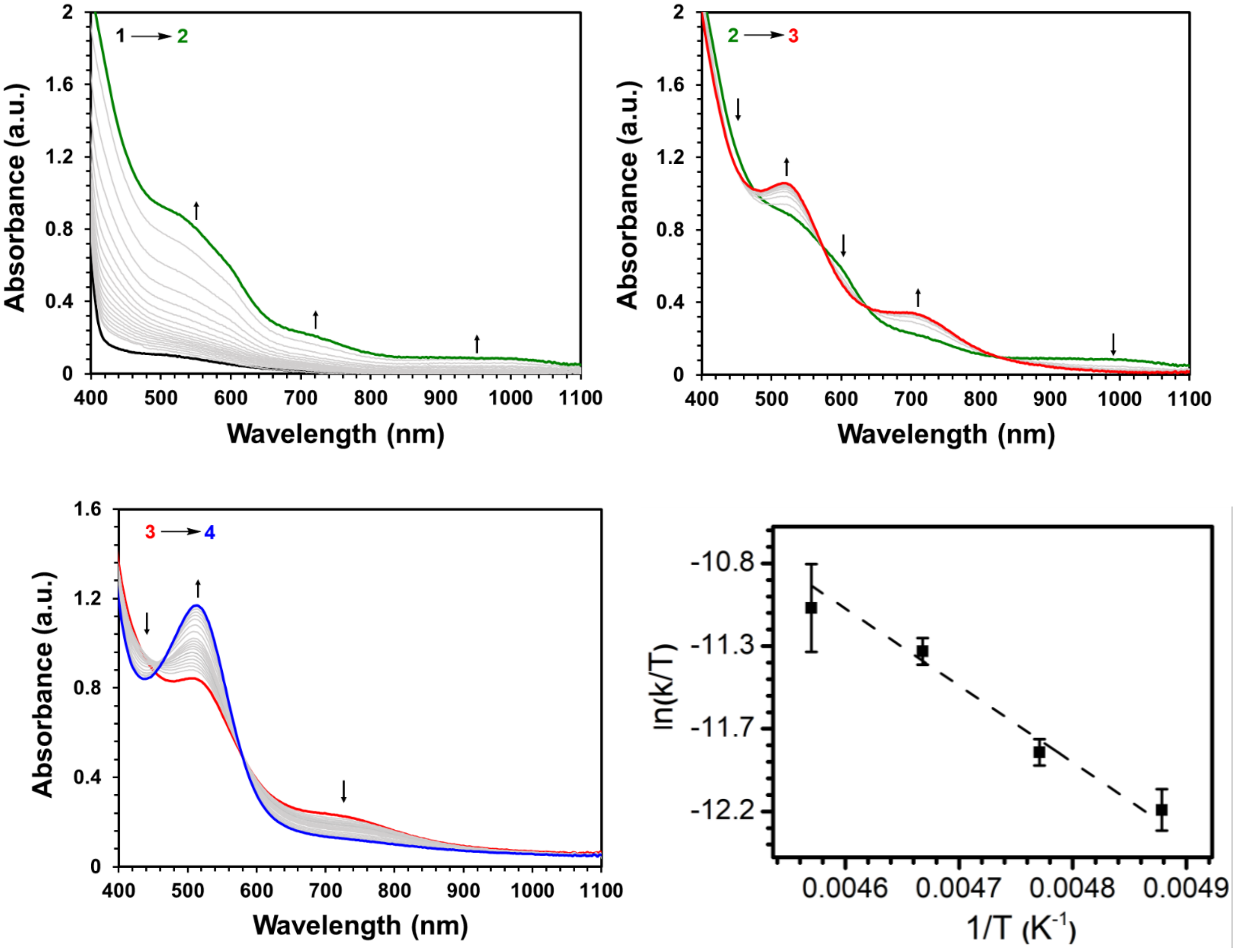

The first-order kinetics in the conversion of **2** to **3** in the UV-vis suggest that the nuclearity of the Fe complexes is maintained in this transformation. This observation suggests that if **2** were mononuclear, then bimolecular pathways could be ruled out. To test this hypothesis, reactions at

−40 °C with 0.5 equivalents and 1 equivalent of O_2 were monitored by UV-vis spectroscopy, then compared to the spectrum of **3** formed in the presence of excess O_2 (Appendix 3). These data showed that at least 1 equivalent of O_2 must be added to the reaction to generate the same intensity of signals as observed with excess O_2. When only 0.5 equivalents of O_2 were used, the absorbances for **3** only reached 50% of the intensity seen in the presence of excess O_2. These observations argue against the formation of dimeric complexes such as bridging peroxo species, and furthermore suggest that **3** is a mononuclear Fe complex.

Figure 3 - 3. Mössbauer spectra of **3** with $\delta = 0.460(2)$ mm/s and $\Delta Eq = 0.765(3)$ mm/s.

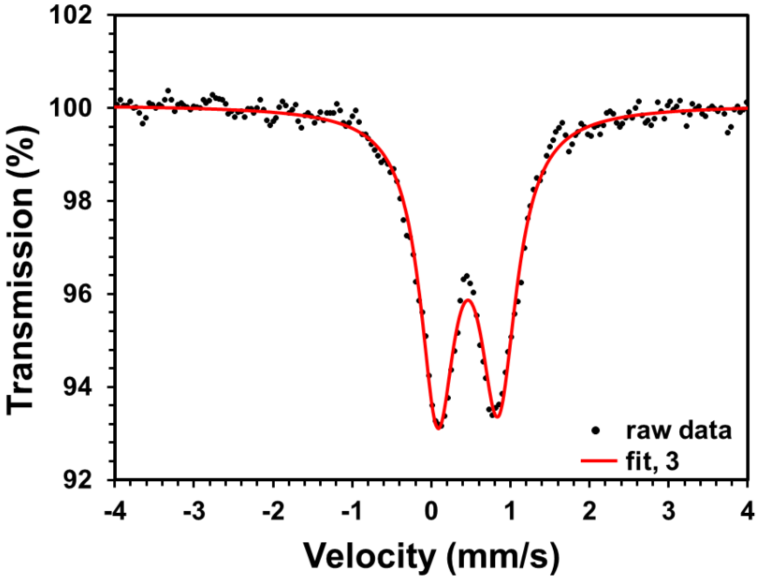

Given the stability of **3** below –40 °C, we were able to characterize the complex as a frozen solution by a variety of techniques. By Mössbauer spectroscopy (Figure 3 - 3), **3** has an isomer shift of 0.460(2) mm/s, consistent with a high spin Fe(III) center. The relatively small quadrupole splitting of 0.765(3) mm/s is similarly consistent with a high spin Fe(III) center. X-ray absorption spectroscopy collected on **1** and **3** shows an increase in the K-edge energy consistent with an increase in the oxidation state from an Fe(II) complex to an Fe(III) complex (Appendix 3). Numerous attempts were made to grow crystals suitable for X-ray diffraction at –78 °C. However, none were successful.

Upon the reaction of **1** with O_2, two likely high spin Fe(III) complexes that could form are an Fe(III)-superoxo complex featuring a $^{t\mathrm{Bu,Tol}}$DHP-H_2 ligand, or an Fe(III)-hydroperoxo complex, where an H-atom has been abstracted by a putative superoxo precursor to form the $^{t\mathrm{Bu,Tol}}$DHP-H$^\bullet$ ligand radical and a hydroperoxo ligand. Both complexes would be expected to have an overall spin of $S = 2$ assuming the $S = {}^5/_2$ Fe(III) center coupled anti-ferromagnetically to the ligand based radical of the superoxo ligand or the $^{t\mathrm{Bu,Tol}}$DHP-H$^\bullet$ ligand respectively. EPR spectroscopy in parallel mode of **3** as a 15 mM frozen solution at 15 K in toluene was collected to test for this hypothesized spin-state. The EPR spectrum of **3** shows a feature at $g = 10.6$ consistent with an $S = 2$ species, as would be expected for either of these assignments (Appendix 3).

Figure 3 - 4. Isotopic labeling studies using IR spectra of the reaction of **1** with O_2 at RT to form **3** in a mixture of products. $^{16}O_2$ vs. $^{18}O_2$ reacted with **1** collected as a thin film on a KBr plate to look for an O–O stretch. Inset: difference spectrum.

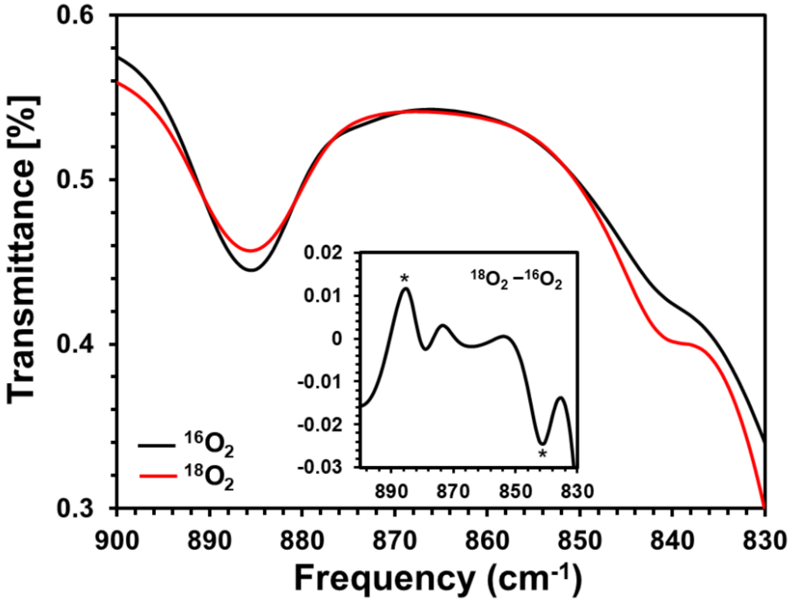

IR spectroscopy of the reaction mixture of **3** and **4** as a solution in chlorobenzene or as a thin film on KBr plates was used to probe the vibrational frequencies for the putative O–O, O–H, and N–H stretches for an Fe(III)-superoxo complex and an Fe(III)-hydroperoxo complex using isotopic labeling studies. When $^{18}O_2$ was used, a disappearance of the feature at 885 cm^{-1} and the growth of a new feature at 842 cm^{-1} is observed via IR spectroscopy (Figure 3 – 4, Appendix 3). The wavenumbers of these vibrations more closely align with an O–O stretch for an Fe(III)-hydroperoxo assignment rather than with an Fe(III)-superoxo. A superoxo complex would be expected to have an O–O stretch between 1000-1300 cm^{-1}.[14] Additionally, two features are seen at 3420 cm^{-1} and 3230 cm^{-1}, which could be assigned either as two N–H stretches or as an N–H and O–H stretch for an Fe(III)-superoxo and Fe(III)-hydroperoxo respectively (Figure 3 – 5). Given the much higher intensity of the feature at 3420 cm^{-1} relative to the feature at 3230 cm^{-1}, it seemed likely that these stretches are not both N–H moieties, but rather an N–H and an O–H, consistent with an Fe(III)-hydroperoxo complex. IR spectroscopy of this mixture was collected using a deuterated version of **1**, where the metalation was completed using 81% enriched $^{t\mathrm{Bu,Tol}}$DHP-D_2•2DCl ligand salt (Appendix 3). When reacted with O_2, IR spectroscopy of this reaction with the deuterated version of **1** showed a growth of a feature at 2546 cm^{-1}, which correspond to an O–H to O–D shift (Figure 3 - 5). Similarly, the feature at 3230 cm^{-1} largely disappears when **1** is enriched with deuterium and grows in at 2404 cm^{-1}. Both shifts are within error of the expected shift assuming a perfect harmonic oscillator model. Isotopic labeling with $^{18}O_2$ was also conducted, but little to no shift was observed in the O–H of N–H features. While a small shift would be expected, the lack of visible shift is likely due to a combination of complicating factors, including the broadness of these features and the convoluted nature of the reaction mixture. Together, these vibrational data are most consistent with an Fe(III)-hydroperoxo complex rather than an Fe(III)-superoxo complex.

Figure 3 - 5. Isotopic labeling studies using IR spectra of the reaction of **1** with O_2 at RT to form **3** in a mixture of products. Proteo- vs. deutero-**1** (81% enriched) reacted with $^{16}O_2$ collected as concentrated solutions in chlorobenzene.

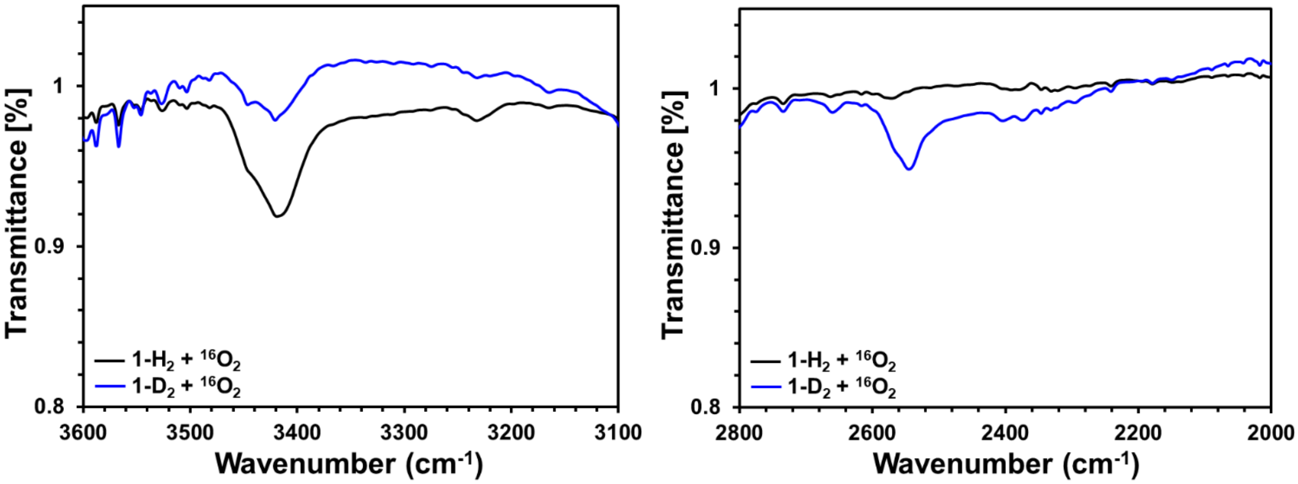

Computational Analysis of 3

Finally, the identity of **3** was investigated using density functional theory (DFT). Geometry optimizations and frequency calculations for both the putative Fe(III)-superoxo and Fe(III)-hydroperoxo complexes were done using the B3P hybrid functional. A single point calculation was then run using the optimized geometries to obtain the theoretical isomer shift and quadrupole splitting mössbauer parameters. The best results were obtained using the TPSSh functional, with a basis set of CP(PPP) on Fe, and an increased polarization on all other atoms except H.[15] These calculations suggest that an Fe(III)-hydroperoxo is the best fit for the mössbauer data. The theoretical isomer shift of 0.47 mm/s and quadrupole splitting of –0.85 mm/s are in good agreement with the experimentally determined values. Time dependent DFT (TDDFT) was also run to calculate the theoretical UV-vis spectrum of the proposed Fe(III)-superoxo and Fe(III)-hydroperoxo complexes using the PBE0 functional on the previously optimized geometries. The theoretical spectrum for a 6-coordinate Fe(III)-hydroperoxo complex with a ligand based radical was found to be a good fit for the experimental spectrum while the Fe(III)-superoxo complex was not (Appendix 3), further suggesting that the correct assignment for **3** is that of an Fe(III)-hydroperoxo with a ligand based radical on $^{t\text{Bu,Tol}}$DHP-H$^{\bullet}$. Additionally the experimental UV-vis data for **3** is consistent with literature UV-vis data where a strong feature grows in at ~500 nm upon the formation of an Fe(III)-hydroperoxo which arises from metal to ligand charge transfer (MLCT) from the Fe-center to the hydroperoxo ligand.[7ac,8,10] TDDFT of the Fe(III)-hydroperoxo with a ligand based radical is also consistent with MLCT causing the peak at 518 nm. Furthermore, TDDFT suggests that the second feature in these data at 714 nm is likely due to a MLCT between the Fe-center and the ligand based radical of the $^{t\text{Bu,Tol}}$DHP-H$^{\bullet}$ ligand (Appendix 3). This presence of a low energy absorbance was previously seen with isolated $^{t\text{Bu/Ph,Tol}}$DHP ligand radicals on Ni centers, further suggesting that the assignment of **3** with a ligand based radical on $^{t\text{Bu,Tol}}$DHP-H$^{\bullet}$ is correct (Scheme 3 – 2).[10,11]

Scheme 3 - 2. Reaction of **1** with O_2. L = dimethylaminopyridine (DMAP)

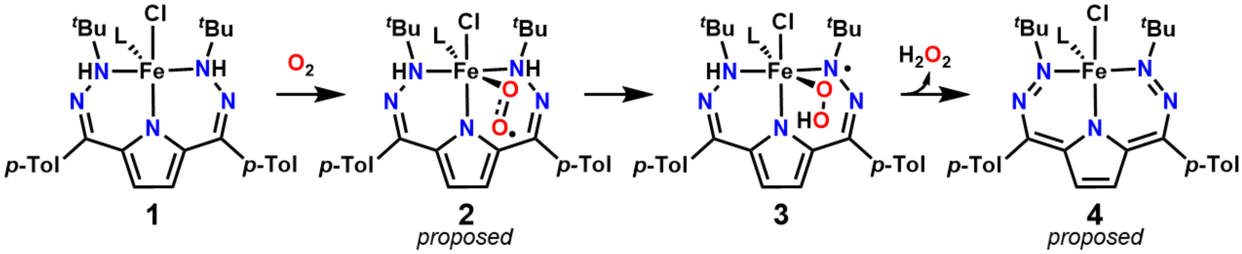

Characterization of 4

Upon warming **3** reacts further to form a new complex **4** by UV-vis spectroscopy (Figure 3 - 2). Unfortunately, **4** is not stable and will slowly bleach over time, making characterization challenging (Appendix 3). One possible assignment for **4** is that of an Fe(IV)-oxo which forms by abstracting a second H-atom from the $^{t\text{Bu,Tol}}$DHP-H$^{\bullet}$ ligand and releasing water. This would result in an oxidized $^{t\text{Bu,Tol}}$DHP ligand in addition to the highly oxidized Fe(IV) center, mimicking the reactivity of cytochrome P450. Another possibility is that when the second H-atom is abstracted from the ligand, H_2O_2 is released and an Fe(II) complex featuring an oxidized $^{t\text{Bu,Tol}}$DHP ligand is formed. Mössbauer spectra of a mixture of **3** and **4** shows an isomer shift of 0.380(3) mm/s and a quadrupole splitting of 1.315(17) mm/s for **4**, which best aligns with a low spin Fe(II) center or an Fe(III) center (Appendix 3). When TEMPO$^\bullet$ is added to a UV-vis solution of **1** to putatively remove two H-atoms, absorbances matching those seen for **4** grow in (Appendix 3). While circumstantial, these data suggest that the net reactivity of this system may be to release H_2O_2 when reacted with molecular oxygen and form Fe($^{t\text{Bu,Tol}}$DHP), where the $^{t\text{Bu,Tol}}$DHP ligand has been oxidized.

To determine if H_2O_2 was formed from the reaction of **1** with O_2, chemical tests were conducted. H_2O_2 reacts stoichiometrically with 1,3-diphenylisobenzofuran (DPBF) to form 9-hydroxyanthracen-10(9H)-one.[16] The reaction of **1** with O_2 was conducted, then reacted with 5 equivalents of DPBF. However, no 9-hydroxyanthracen-10(9H)-one was observed by gas chromatography-mass spectrometry (GC-MS), as would be expected if H_2O_2 had been produced.

To determine if water was produced in this reaction and originated from **1**, isotopic labeling studies were utilized. Deuterated ligand salt (93% enriched) was metalated following the previously described procedure. The deuterated complex **1** was then reacted as a concentrated solution in THF with an excess of O_2 at room temperature for 5 minutes. The volatiles of this reaction were vacuum transferred and ^2H NMR was collected. Three peaks were seen in the ^2H NMR, corresponding to a small natural abundance of d_8-THF and a new peak. This peak was compared to a D_2O standard peak (Appendix 3) and was found to match the shift of D_2O (Appendix 3). This suggests that water is formed during the reaction. A control experiment of the THF solvent background was also collected. These indicated that no D_2O was present prior to the reaction of deuterated **1** with O_2 and thus, the peak which forms after the reaction is likely from D_2O. This indicates that the overall reaction of **1** with O_2 not only releases water as a byproduct, but that the proton source is the ^{tBu,Tol}DHP-H_2 ligand rather than some outside source. Therefore, ligand non-innocence must be invoked in the observed reactivity.

While these isotopic labeling studies provide encouraging evidence for ligand noninnocence, the question of how to best assign **4** remains. Although the production of an Fe(IV)-oxo complex and water from the reaction of **1** with O_2 would provide a balanced reaction, mössbauer studies definitively rule out the presence of and Fe(IV) complex. One possible explanation is that an Fe(IV)-oxo complex does form briefly, but subsequently reacts rapidly with a substrate for C–H or N–H activation such that the Fe(IV)-oxo is never observed. This could result in an Fe(III)-OH complex, which could match the observed mössbauer data. Alternatively, H_2O_2 could form, and then degrade to water and O_2 in the presence of Fe too quickly for the H_2O_2 to be observed. Given that the reaction of **1** with H-atom abstractors by UV-vis spectroscopy results in a spectrum with absorbances largely identical to **4**, I have tentatively assigned **4** as Fe(^{tBu,Tol}DHP), where the ^{tBu,Tol}DHP ligand has been oxidized (Scheme 3 – 2).

Oxidative reactivity

Encouraged by the biomimetic nature of **1**, oxidative reactivity in the presence of molecular oxygen was investigated. By low temperature UV-vis spectroscopy, **3** was found to react with 10 equivalents of PPh_3 slowly at –40 °C. We speculated that **3** may perform O-atom transfer to PPh_3 and form $OPPh_3$. When this reaction is conducted in a J-young tube and monitored by ^{31}P NMR at room temperature, 1 equivalent of $OPPh_3$ formed, consistent with our hypothesis (Appendix 3). When the reaction was done in the presence of ${}^{18}O_2$, enrichment of the isotopically labeled $OPPh_3$ product was observed by GC-MS analysis (Appendix 3). This demonstrates that the active oxidant is the added O_2.

The reactivity of **3** and **4** towards H-atom abstraction was also investigated with diphenylhydrazine (DPH) and dihydroanthracene (DHA). Complex **3** was found to react with DPH at –40 °C by UV-vis, but not DHA, suggesting that **3** is sufficiently reactive to abstract an H-atom from a relatively weak N–H bond, but not from the stronger C–H bond or that the C–H abstraction is very slow at this low temperature. A series of experiments at room temperature were then conducted and analyzed by GC-MS showing C–H activated products and O-atom transfer products for both DHA and PPh_3. Overall, the observed reactivity is consistent with oxidation occurring from either **3** or a combination of **4** and the water or H_2O_2 byproduct.

Conclusions

In this study, we have synthesized a series of oxidized Fe complexes with water or H_2O_2 as a byproduct from a redox-active Fe(II) complex featuring pendant H-atom equivalents and molecular O_2. This includes an unusual Fe(III)-hydroperoxo complex with a ^{tBu,Tol}DHP-H$^{\bullet}$ ligand based radical. These intermediates were characterized by a variety of spectroscopic and computational techniques in addition to kinetic studies of the transformation between intermediates. Reactivity is consistent with the assignment of these species. This study demonstrates that the combination of redox-active ligands and pendant H donors allows for the mononuclear activation of O_2 and facilitates the controlled movement of protons and electrons. Furthermore, this reactivity is reminiscent of nature’s strategy of using redox active organic frameworks, Fe metal centers, and pendant protons shuttled from nearby amino acids in enzymes to mediate challenging reactivity with O_2.

Experimental

General Methods. All chemicals were purchased from commercial suppliers and used without further purification. All manipulations were carried out under an atmosphere of N_2 using standard Schlenk and glovebox techniques. Glassware was dried at 180 °C for a minimum of two hours and cooled under vacuum prior to use. Solvents were dried on a solvent purification system from Pure Process Technologies and stored over 4 Å molecular sieves under N_2. Tetrahydrofuran (THF) was stirred over NaK alloy and run through an additional alumina column prior to use to ensure dryness. Solvents were tested for H_2O and O_2 using a standard solution of sodium-benzophenone ketyl radical anion. CD_3CN, C_6D_6, and d_8-toluene were dried over 4 Å molecular sieves under N_2. ^1H and $^2H\{^1H\}$ NMR spectra were recorded on Bruker DRX 400 or 500 spectrometers. Chemical shifts are reported in ppm units referenced to residual solvent resonances for ^1H and $^2H\{^1H\}$ spectra. UV-Vis Spectra were recorded on a Bruker Evolution 300 spectrometer and analyzed using VisionPro softwar. IR spectra were obtained on a Bruker Tensor II spectrometer with the OPUS software suite. All IR samples were prepared nujol mulls or collected between KBr plates. EPR spectra were recorded on an Elexsys E500 Spectrometer with an Oxford ESR 900 X-band cryostat and a Bruker Cold-Edge Stinger. EPR data was analyzed using SpinCount. Single crystal X-ray diffraction data were collected in-house using Bruker D8 Venture diffractometer equipped with Mo microfocus X-ray tube (λ = 0.71073 Å). X-ray near-edge absorption spectra (XANES) were employed to probe the local environment of Fe. Powder samples were prepared by material grinding finely. A Teflon window was sealed on one side with Kapton tape and powder was then transfer transferred to the inside of this ring before compacting with a Teflon rod and sealing the remaining face with Kapton tape. After transfer of the material, the window was sealed with Kapton tape. All sample preparation was performed under an inert atmosphere. Frozen solution samples were prepared by making a concentrated solution in THF of the starting material, removing the sample from the glovebox, cooling the sample in a bath, then reacting the sample with O_2 by syringing the gas into the sample and bubbling through. After allowing to react, the sample was exposed to air and precooled pipette was used to transfer the solution to a Teflon window lined on one side with Kapton tape. The solution was frozen using liquid nitrogen, then stored in liquid nitrogen until collection. Data were acquired at the Advanced Photon Source at Argonne National Labs with a bending magnet source with ring energy at 7.00 GeV. Fe K-edge data were acquired at the MRCAT 9-BM-B,C beam line. The incident, transmitted and reference X-ray intensities were monitored using gas ionization chambers. A metallic iron foil standard was used as a reference for energy calibration and was measured simultaneously with experimental samples. X-ray absorption spectra were collected at room temperature. Data collected was processed using the Demeter software suite by extracting the EXAFS oscillations $\chi(k)$ as a function of photoelectron wavenumber k. The theoretical paths were generated using FEFF6 and the models were determined using the fitting program Artemis17. Zero-field ^{57}Fe Mössbauer spectra were obtained at 80 K using a ^{57}Co/rhodium source. Samples were prepared in an MBraun nitrogen glove box. A typical powder sample contained approximately 60 mg of compounds suspended in a plastic cap. Another cap with a slightly smaller diameter was squeezed into the previous sample cap to completely encapsulate the solid sample mixture. Frozen solution samples were prepared as concentrated solutions of ^{57}Fe enriched **1** in toluene in the glovebox, removed from the glovebox under nitrogen, placed in a cold bath of −78 °C or −40 °C, and reacted with an excess of O_2 which was bubbled through the solution. After reacting for the desired amount of time, the solution was exposed to air and pipetted with a precooled pipette into a plastic cap and frozen in liquid nitrogen. Another cap with a slightly smaller diameter was squeezed into the previous sample cap to completely encapsulate the frozen sample mixture. All spectra were analyzed using the WMOSS

Mössbauer Spectral Analysis Software. Note that the accuracy of the fit parameters may be overestimated as the error in the Fe foil calibration is 0.01 mm/s.

X-Ray Structure Determination. The diffraction data were measured at 100 K on a Bruker D8 VENTURE with PHOTON 100 CMOS detector system equipped with a Mo-target micro-focus X-ray tube (λ = 0.71073 Å. Data reduction and integration were performed with the Bruker APEX3 software package (Bruker AXS, version 2015.5-2, 2015). Data were scaled and corrected for absorption effects using the multi-scan procedure as implemented in SADABS (Bruker AXS, version 2014/5, 2015, part of Bruker APEX3 software package). The structure was solved by the dual method implemented in SHELXT[18] and refined by a full-matrix least-squares procedure using OLEX23[19] software package (XL refinement program version 2014/7[3,20]). Suitable crystals were mounted on a cryo-loop and transferred into the cold nitrogen stream of the Bruker D8 Venture diffractometer. C-H hydrogen atoms were generated by geometrical considerations, constrained to idealized geometries, and allowed to ride on their carrier atoms with an isotropic displacement parameter related to the equivalent displacement parameter of their carrier atoms.

Density Functional Theory: Geometry Optimizations. Geometry optimization calculations were performed with ORCA[21] software suite using density functional theory (DFT). Geometries were fully optimized starting from coordinates generated from finalized cifs of the compound crystal structures. The B3P functional was used with a basis set of def2-SVP on H, def2-TZVPP on Fe, N, and P, and def2-TZVP on C atoms. The resulting structures were confirmed to be minima on the potential energy surface by frequency calculations using ORCA. Frequency calculations were also conducted using the B3P functional and previously listed basis sets for each atom type. NOTE: The calculated structure for Fe(III)($^{t\text{Bu,Tol}}$DHP-H$^{\bullet}$)(DMAP)(Cl)(OOH) has one imaginary frequency of −288 cm^{-1} which corresponds to the O–H dihedral wagging frequency. The magnitude of this imaginary frequency is due to the larger mass of O relative to C.

Fe($^{\text{Tol,tBu}}$DHP-H$_2$)(DMAP)Cl (1). In a 20 mL vial in the glovebox, 3 mL of THF was added to FeCl$_2$ (24.4 mg, 1 eq, 0.19 mmol). A solution of dimethylaminopyrrole (23.6 mg, 1 eq., 0.19 mmol) in 2 mL of THF was added to the FeCl$_2$ suspension and stirred until a white suspension formed. The [$^{\text{Tol,tBu}}$DHP-H$_4$][Cl]$_2$ ligand salt22 (100 mg, 1 eq., 0.19 mmol) was dissolved in 5 mL THF and added to the Fe solution to form a bright yellow suspension in a yellow solution. After stirring for 10 minutes, KHMDS (103.9 mg, 2.7 eq., 0.52 mmol) dissolved in 1 mL THF was added dropwise with stirring. The solution turned from orange with a yellow precipitate, to colorless with a white precipitate, to colorless and no precipitate, to a deep orange-brown. Immediately after the addition of KHMDS, the reaction mixture was condensed under vacuum. The resulting brown solid was taken up in toluene, filtered, and condensed under vacuum, then washed with petroleum ether (10 mL). After drying, the pure bulk product was obtained as a pale orange solid. Yield: 90 mg, 71%. Single crystals suitable for XRD were grown via vapor diffusion of petroleum ether into a concentrated solution of product in toluene overnight at room temperature. ^{1}H NMR (400 MHz, CD$_3$CN, RT): δ = 29.20 (bs), 10.48 (bs), 8.56 (bs), 6.00 (bs), 5.69 (bs), −3.44 (bs). Magnetic Susceptibility: Evans' Method (C$_6$D$_6$, RT, μ_B): μ_{eff} = 5.0; IR (Nujol mull between KBr plates, cm^{-1}): 3180 (N–H, w), 3170 (N–H, w), 1641 (s). Mössbauer (80 K, mm/s) δ = 1.090(6); ΔE_Q =

2.367(9). UV-vis, nm in toluene, (ε, $M^{-1}cm^{-1}$): 516 (286). Anal. Calc. C, 64.07; H, 7.07; N, 14.94; Found: C, 64.65; H, 7.40; N, 14.03.

Reactivity with PPh_3, DHA, and diphenylhydrazene (DPH). A 0.35 mM solution of **1** in toluene was prepared in the glovebox in an air-tight cuvette with a septa. After cooling to −40 °C, 0.5 mL of O_2 was added via syringe and allowed to react until the absorbances for **3** had fully grown in. Then, 10 equivalents of PPh_3 was added as a solution in toluene via syringe and monitored over time. This same procedure was followed for DHA (10 equivalents to a 0.35 mM solution of **1**) and DPH (20 equivalents to a 0.42 mM solution of **1**). This was repeated at room temperature solutions of **1** with 20 equivalents of PPh_3 and DHA, and 10 equivalents of DPH respectively. The substrate was added 10 minutes after reacting with 6 mL of O_2 to ensure that 3 had fully formed. When the reaction had finished bleaching, these reactions were analyzed by GC-MS.

Reactivity with PPh_3 by NMR. An NMR solution was prepared with 5 mg of **1** in toluene (C_7H_8) with a septa NMR cap. This was then reacted with 10 equivalents of PPh_3 (added via syringe). Then, 6 mL of O_2 was bubbled through the solution using a syringe at room temperature. This was allowed to react at overnight at room temperature, then analyzed by $^{31}P\{^1H\}$ NMR:

Reactivity with diphenylisobenzofuran (DPBF). In a 20 mL glass vial, **1** (5 mg, 1 eq.) was dissolved in toluene (1 mL) and sealed with a septa in the nitrogen glovebox. This was removed from the glovebox and 3 mL of O_2 was added and allowed to react for 30 minutes at room temperature. The septa was removed and vacuum was pulled on the reaction mixture until the volume was halved. This was then reacted with DPBF (10.3 mg, 5 eq.) in the glovebox and allowed to stir for 3 hours. This was then filtered and analyzed by GCMS.

Deuteration of the [^{Tol,tBu}DHP-H_4][Cl]$_2$ ligand salt. In a 20 mL vial, [^{Tol,tBu}DHP-H_4][Cl]$_2$ ligand salt (100 mg, 1 eq., 0.19 mmol) was dissolved in THF (10 mL). This was cooled in a −35 °C freezer for 20 minutes. The solution was removed from the freezer and nBuLi (0.39 mL of a 2.5 M solution in diethylether, 5 eq., 0.96 mmol) was added dropwise with stirring at room temperature, causing the reaction to turn a deep red. This was allowed to stir for 5 minutes, slowing warming to room temperature, then DCl or *d*$_4$-acetic acid (5 eq., 0.96 mmol) was added while stirring, causing the reaction to lighten to a golden yellow-orange. The reaction was condensed under vacuum, taken up in toluene and filtered to remove LiCl, then recondensed. The resulting oil was taken up in THF (1 mL) and recrystallized via layer recrystallization with petroleum ether in the glovebox overnight. Yield: 50%. Percent enrichment by ^{1}H NMR: 93%.

^{2}H{^{1}H} NMR of products from the reaction of 1 with O_2. To a 25 mL schlenk tube, 30 mg. of **1** was dissolved in THF (0.7 mL), and 12 mL of O_2 was bubbled through the solution via syringe. This was allowed to react for 5 minutes, then the volatiles were vacuum transferred. This solution was analyzed directly using ^{2}H{^{1}H} NMR.

Eyring Analysis. To perform an Eyring analysis for the reaction of **2** to **3** under O_2, the intensity of the absorbance at 996 nm was monitored at a variety of temperatures. This feature was chosen because it was the only feature from the mixture of products in **2** that was not convoluted by features of **3** and because the feature is at its most intense when the isosbestic transformation of **2** to **3** begins. Thus, the rate of the formation of **3** was determined by the rate of disappearance of the feature at 996 nm using an exponential fit to the data. The spectrum with the greatest intensity at 996 nm was not included in the fit as this should be a transition point between the growth of **2** and the conversion of **2** to **3**.

The rates calculated for the Eyring analysis of the reaction of **2** to **3** give a line of best fit with an R^2 value of 0.95:

$$y = -380.2x + 6.5208$$

Error in the y-intercept used to determine $\Delta S^{\ddagger}$ was determined by propagation of error in the line of best fit (i.e. error in the y-intercept for the line of best fit). This resulted in $\Delta S^{\ddagger} = -34 \pm 4.9$ cal/mol.

Error in the slope used to determine $\Delta H^{\ddagger}$ was determined by propagation of error in the line of best fit (i.e. error in the slope calculated for the line of best fit). This resulted in $\Delta H^{\ddagger} = 7.6 \pm 1.0$ kcal/mol.

References

---

[1] a) Charette, B. J.; Ziller, J. W.; Heyduk, A. F. *Inorg. Chem.* **2021**, *60*, 1579–1589.; b) T. J. Sherbow, E. J. Thompson, A. Arnold, R. I. Sayler, R. D. Britt, L. A. Berben, *Chem. - Eur. J.*, **2019**, *25*, 454-458.; c) M. J. Drummond, C. L. Ford, D. L. Gray, C. V. Popescu and A. R. Fout, *J. Am. Chem. Soc.*, **2019**, *141*, 6639-6650.; d) Rosenkoetter, K. E.; Wojnar, M. K.; Charette, B. J.; Ziller, J. W.; Heyduk, A. F. *Inorg. Chem.* **2018**, *57*, 9728–9737.; e) M. B. Ward, A. Scheitler, M. Yu, L. Senft, A. S. Zillmann, J. D. Gorden, D. D. Schwartz, I. Ivanović-Burmazović and C. R. Goldsmith, *Nature Chem.*, **2018**, *10*, 1207-1212.; f) R. Pramanick, R. Bhattacharjee, D. Sengupta, A. Datta and S. Goswami, *Inorg. Chem.*, **2018**, *57*, 6816-6824.; g) R. Jain, A. A. Mamun, R. M. Buchanan, P. M. Kozlowski and C. A. Grapperhaus, *Inorg. Chem.*, **2018**, *57*, 13486-13493.; h) F. Schneck, M. Finger, M. Tromp and S. Schneider, *Chem. Eur. J.*, **2017**, *23*, 33-37.; i) G. W. Margulieux, M. J. Bezdek, Z. R. Turner and P. J. Chirik, *J. Am. Chem. Soc.*, **2017**, *139*, 6110-6113.; j) A. Dauth, U. Gellrich, Y. Diskin-Posner, Y. Ben-David and D. Milstein, *J. Am. Chem. Soc.*, **2017**, *139*, 2799-2807.; k) B. M. Lindley, Q. J. Bruch, P. S. White, F. Hasanayn and A. J. M. Miller, *J. Am. Chem. Soc.*, **2017**, *139*, 5305–5308.; l) Delgado, M.; Gilbertson, J. D. *Chem. Commun.* **2017**, *53* (81), 11249–11252. m) P. O. Lagaditis, B. Schluschaß, S. Demeshko, C. Würtele and S. Schneider, *Inorg. Chem.*, **2016**, *55*, 4529-4536.; n) J. T. Henthorn, S. Lin and T. Agapie, *J. Am. Chem. Soc.*, **2015**, *137*, 1458-1464.; o) Moore, C. M.; Szymczak, N. K. *Chem. Sci.* **2015**, *6*, 3373–3377.; p) T. W. Myers, L. A. Berben, *Chem. Sci.*, **2014,** *5*, 2771-2777.; q) B. W. Purse, L. H. Tran, J. Piera, B. Åkermark and J. E. Bäckvall, *Chem. Eur. J.*, **2008**, *14*, 7500–7503.

[2] (a) Yosca, T. H.; Ledray, A. P.; Ngo, J.; Green, M. T. *J. Biol. Inorg. Chem.* **2017**, *22*, 209–220.; (b) Ortiz De Montellano, P. R. *Chem. Rev.* **2010**, *110*, 932–948.; (c) Denisov, I. G.; Makris, T. M.; Sligar, S. G.; Schlichting, I. *Chem. Commun.* **2005**, *105*, 2253–2277.; (d) Meunier, B.; Visser, P. De; Shaik, S. *Chem. Rev.* **2004**, *104*, 3947–3980.

[3] (a) Adam, S. M.; Wijeratne, G. B.; Rogler, P. J.; Diaz, D. E.; Quist, D. A.; Liu, J. J.; Karlin, K. D. *Chem. Rev.* **2018**, *118*, 10840–11022.; (b) Solomon, E. I.; Sundaram, U. M.; Machonkin, T. E. *Chem. Rev.* **1996**, *96*, 2563–2605.

[4] (a) Mishra, A.; Aja, E.; Fletcher, H. M. *Sci. Rep.* **2020**, *10*, 1–13.; (b) Martins, M. C.; Romão, C. V.; Folgosa, F.; Borges, P. T.; Frazão, C.; Teixeira, M. *Free Radic. Biol. Med.* **2019**, *140*, 36–60.; (c) Mathé, C.; Weill, C. O.; Mattioli, T. A.; Berthomieu, C.; Houée-Levin, C.; Tremey, E.; Nivière, V. *J. Biol. Chem.* **2007**, *282* (30), 22207–22216.; (d) Katona, G.; Carpentier, P.; Nivière, V.; Amara, P.; Adam, V.; Ohana, J.; Tsanov, N.; Bourgeois, D. *Science* **2007**, *316* (April), 449–453.

[5] (a) Battistella, B.; Ray, K. *Coord. Chem. Rev.* **2020**, *408*, 213176.; (b) Jasniewski, A. J.; Que, L. *Chem. Rev.* **2018**, *118*, 2554–2592.; (c) Baglia, R. A.; Zaragoza, J. P. T.; Goldberg, D. P. *Chem. Rev.* **2017**, *117*, 13320–13352.

---

[6] (a) Wegeberg, C.; Browne, W. R.; McKenzie, C. J. *Inorg. Chem.* **2019**, *58*, 8983–8994.; (b) Kal, S.; Que, L. *Angew. Chemie* **2019**, *158*, 8484–8488.; (c) Xu, S.; Veach, J. J.; Oloo, W. N.; Peters, K. C.; Wang, J.; Perry, R. H.; Que, L. *Chem. Commun.* **2018**, *54*, 8701–8704.; (d) Serrano-Plana, J.; Acuña-Parés, F.; Dantignana, V.; Oloo, W. N.; Castillo, E.; Draksharapu, A.; Whiteoak, C. J.; Martin-Diaconescu, V.; Basallote, M. G.; Luis, J. M.; Que, L.; Costas, M.; Company, A. *Chem. Eur. J.* **2018**, *24* (20), 5331–5340.; (e) Widger, L. R.; Jiang, Y.; McQuilken, A. C.; Yang, T.; Siegler, M. A.; Matsumura, H.; Moënne-Loccoz, P.; Kumar, D.; de Visser, S. P.; David P., G. *Dalt. Trans.* **2014**, *43*, 7522–7532.; (f) Simaan, A. J.; Girerd, J.; Wieghardt, K.; Bill, E. **2001**, *40*, 6538–6540.

[7] (a) Li, F.; Meier, K. K.; Cranswick, M. A.; Chakrabarti, M.; Heuvelen, K. M. Van; Eckard, M.; Que, L. *J. Am. Chem. Soc.* **2011**, *133*, 7256.; (b) Cho, J.; Jeon, S.; Wilson, S. A.; Liu, L. V; Kang, E. A.; Braymer, J. J.; Lim, M. H.; Hedman, B.; Hodgson, K. O.; Valentine, J. S.; Solomon, E. I.; Nam, W. *Nature* **2011**, *180*, 8–11.; (c) Nam, E.; Alokolaro, P. E.; Swartz, R. D.; Gleaves, M. C.; Pikul, J.; Kovacs, J. A. *Inorg. Chem.* **2011**, No. 13, 1592–1602.; (d) Shearer, J.; Scarrow, R. C.; Kovacs, J. A. **2002**, *124*, 11709–11717.

[8] Jiang, Y.; Telser, J.; Goldberg, D. P. *Chem. Commun.* **2009**, 6828–6830.

[9] McNeece, A. J.; Jesse, K. A.; Filatov, A. S.; Schneider, J. E.; Anderson, J. S. *Chem. Commun.* **2021**, *57* , 3869–3872.

[10] Jesse, K. A.; Chang, M-C.; Filatov, A. S.; Anderson, J. S. *ZAAC*. Accepted.

[11] Mcneece, A. J.; Jesse, K. A.; Xie, J.; Filatov, A. S.; Anderson, J. S. *J. Am. Chem. Soc.* **2020**, *142*, 10824–10832.

[12] (a) Zheng, H.; Langner, K. M.; Shields, G. P.; Hou, J.; Kowiel, M.; Allen, F. H.; Murshudov, G.; Minor, W. *Acta Crystallogr. Sect. D Struct. Biol.* **2017**, *73*, 316–325.; (b) Nishida, Y.; Kida, S.; Ray, X.-. *Dalt. Trans.* **1987**, 1157–1161.

[13] Kim, Y. M.; Cho, K.-B.; Cho, J.; Wang, B.; Chunsen, L.; Shaik, S.; Nam, W. *J. Am. Chem. Soc.* **2013**, No. 135, 8838–8841.

[14] Noh, H.; Cho, J. Coord. Chem. Rev. **2019**, *382*, 126−144.

[15] Römelt, M.; Ye, S.; Neese, F. *Inorg. Chem.* **2009**, *48* (3), 784–785.

[16] Żamojć, K.; Zdrowowicz, M.; Rudnicki-Velasquez, P. B.; Krzymiński, K.; Zaborowski, B.; Niedziałkowski, P.; Jacewicz, D.; Chmurzyński, L.; *Free Radical Research*. **2017**, *51*, 38-46.

[17] (a) Ravel, B., Newville, M., ATHENA, ARTEMIS, HEPHAESTUS: data analysis for X-ray absorption spectroscopy using IFEFFIT. *J. Synchr. Radn.*, **2005**, *12*, 537-541 (b) Newville, M., IFEFFIT: interactive EXAFS analysis and FEFF fitting. *J. Synchr. Radn.* **2001**, *8*, 322-324; (c) Rehr, J. J.; Albers, R. C. *Rev. Mod. Phys.* **2000**, *72*, 621-654.

[18] G. M. Sheldrick, *Acta Cryst*. **2015,** *C71*, 3-8.

---

[19] O. V. Dolomanov, L. J. Bourhis, R. J. Gildea, A. K. Howard, H. Puschmann, *J. Appl. Cryst*. **2009**. *42*, 339.

[20] G. M. Sheldrick. *Acta Cryst*. **2008**, *A64*, 112-122.

[21] (a) Neese, F. "The Orca Program System" *Wiley Interdisciplinary Reviews: Computational Molecular Science* **2012**, *2*, 73-78. (b) H - Kr: A. Schaefer, H. Horn and R. Ahlrichs, *J. Chem. Phys.* **1992**, *97*, 2571. (c) Rb - Xe: A. Schaefer, C. Huber and R. Ahlrichs, *J. Chem. Phys.* **1994** *100*, 5829. (d) F. Weigend, R. Ahlrichs, *Phys. Chem. Chem. Phys.* **2005**, 7, 3297.

[22] A. J. McNeece, K. A. Jesse, J. Xie, A. S. Filatov, J. S. Anderson. *J. Am. Chem. Soc.* **2020**, *142*, 10824-10832.

Chapter Four: Neocuproine as a Redox-active Ligand Platform on Iron and Cobalt

This chapter has been adapted from the following: Jesse, K. A.; Filatov, A. S.; Xie, J.; Anderson, J. S. *Inorg. Chem.* **2019**, *58*, 9057–9066.

Introduction

As an archetypal redox-active unit, aromatic heterocycles have featured prominently in the area of redox-active ligands, including phenanthroline,[1] bipyridine,[2] quinoline based ligands,[3] and conjugated N-donor type ligands.[4] Within this family, 2,9-dimethyl-1,10-phenanthroline, also known by its common name neocuproine, should be a similarly useful scaffold. Neocuproine is commercially available at low cost, making it an attractive ligand platform for investigations into catalyst development. Furthermore, neocuproine has the potential to act as a redox-active ligand as its conjugation should allow it to act as an electron sink. The methyl groups ortho to the nitrogen atoms sterically prevent more than two ligands from binding to a metal center, leaving coordination sites open for potential substrate binding. Each ligand may be reduced, thus suggesting that bisneocuproine complexes could potentially facilitate two electron transfers independent of the redox properties of the metal center.

Neocuproine and phenanthroline based ligands have been used extensively for transition metal reactivity. Neocuproine has often been used for biological applications as an indicator for the presence of Cu due to its distinctive absorbance in the UV-vis region upon metalation.[5] Neocuproine Cu complexes have also been used as reductants for other metal salts.[6] However, oxidation and reduction when bound to Cu occurs at the metal center rather than being ligand-based. Milstein and coworkers used a phenanthroline substituted phosphine ligand bound to Ru to facilitate the dehydrogenation and coupling of primary alcohols to esters and the coupling of primary amines and primary alcohols to form imines and esters.[7] No change in ligand redox state was observed during these reactions, though an off-cycle path did result in activation and hydrogenation of the ligand backbone. Similarly, Chirik and coworkers used a neocuproine based mono-phosphine ligand with Co^{2+} to investigate C–H borylation and identified the redox state of the ligand to be singly reduced upon metalation.[8] However, ligand-based redox events were not invoked in the observed reactivity. Stahl and coworkers successfully utilized a Pd complex with neocuproine for oxidative Heck type reactions.[9] While the use of neocuproine over other chelating N donors did increase the product yield, all redox activity was proposed to occur on the Pd center. Macchi and coworkers also investigated how Pd-neocuproine complexes facilitate the reduction of nitroarenes to anilines using $[Pd(neocuproine)(NO_3)_2]$ as a starting material.[10] This investigation concluded that noninnocent ligand reactivity of the nitrate played a role, but no redox activity of neocuproine was noted. Furthermore, a range of first-row transition metal complexes with neocuproine[11] or related ligands[12] have been identified, but reduction of these complexes is generally assigned as metal-based. Nocera and coworkers do assign ligand noninnocence in a related bisbathocuproine-Ni complex based on structural and electronic absorption data.[13]

I have been broadly interested in investigating the storage of redox equivalents on ligands, such as with the previously published dihydrazonopyrrole (DHP) ligand scaffold discussed in the above chapters.[14] I found it likely that neocuproine could serve as a redox noninnocent ligand, but noted that this redox activity had not been systematically explored. I therefore set out to carefully evaluate the redox-activity of neocuproine bound to first-row transition metals. I have found that bisneocuproine complexes of Fe^{2+} and Co^{2+} do indeed demonstrate redox noninnocence with multiple accessible redox states per complex. In this work I report the synthesis of a redox series of these complexes and detailed characterization of their ligand-based reductions.

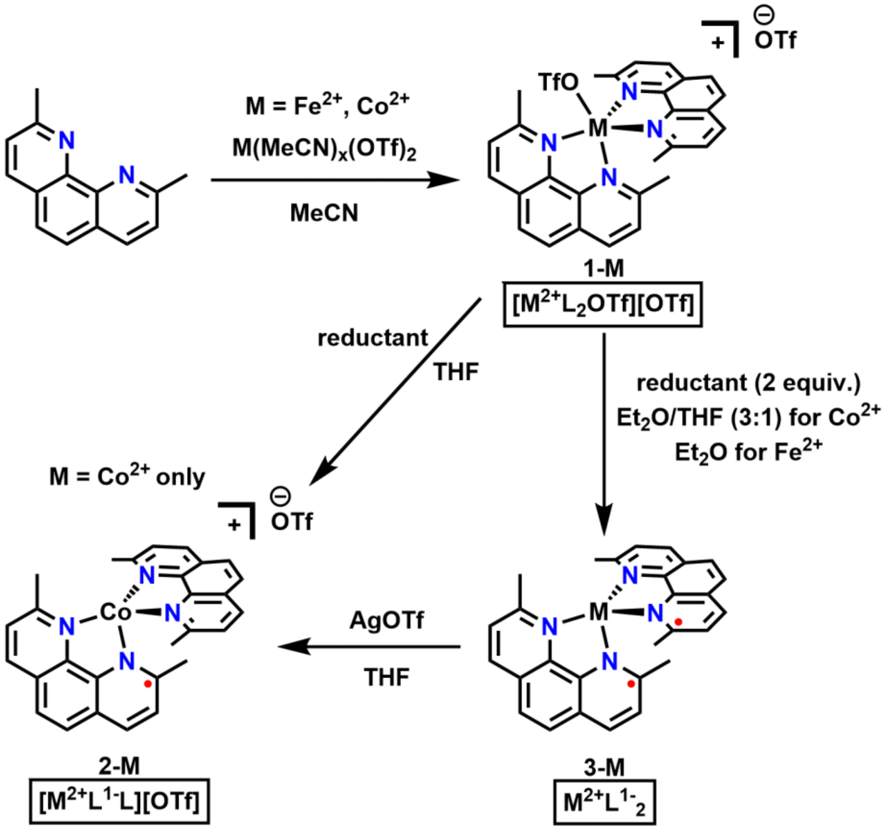

Scheme 4 - 1. Synthesis of bisneocuproine complexes of Fe^{2+} and Co^{2+}. **1-Fe** can be doubly reduced to **3-Fe** using KC_8 or $NaC_{10}H_8$. **1-Co** can be singly reduced to **2-Co** using KC_8 or Cp_2Co, and doubly reduced to **3-Co** using KC_8 or $Cp^*{}_2Co$. Radicals shown in red.

Results and Discussion

Synthesis of M(neocuproine)$_2^{2+}$ Complexes

$[Fe(neocuproine)_2OTf][OTf]$ (**1-Fe**) was synthesized by stirring two equivalents of neocuproine with $Fe(MeCN)_2OTf_2$ in acetonitrile and subsequently isolating yellow crystals in good yield (Scheme 1). The formation of **1-Fe** was confirmed by ^1H NMR spectroscopy, which shows four paramagnetically shifted peaks that integrate in a roughly 1:1:1:3 ratio (Appendix 4). The presence of only four peaks suggests that the two neocuproine ligands are equivalent in solution. The expected high spin state of Fe^{2+} is supported by paramagnetically shifted ^1H NMR peaks as well as by a μ_{eff} of 5.06 μ_B observed using Evans' method. Additionally, **1-Fe** remains high spin in the solid state as shown by a room temperature χT of 3.65 cm^3K/mol determined via variable temperature magnetic measurements (Appendix 4). The crystal structure of **1-Fe** features an average Fe-N distance of 2.149(2) Å, which is consistent with a high spin Fe^{2+} complex with a spin only value of $S = 2$ (Figure 4 - 1, Table 4 - 1).[15] In the solid state, **1-Fe** has one triflate counterion coordinated to the metal center through an oxygen while the other counterion is outer sphere, resulting in an overall pseudo-trigonal bipyramidal geometry. A single, broad peak is found at −64 ppm in the room temperature ^{19}F NMR spectrum, suggesting that the two triflate counterions are exchanging in solution (Appendix 4). Complex **1-Fe** was further characterized by IR spectroscopy, UV-vis spectroscopy, and elemental analysis (Appendix 4).

[Co(neocuproine)$_2$OTf][OTf] (**1-Co**) was synthesized in an analogous manner to **1-Fe**, with the exception that an excess of neocuproine is required to form pure **1-Co** (Scheme 4 - 1). When only two equivalents were used, a mixture of two complexes formed as evidenced by eight paramagnetically shifted peaks in the ^{1}H NMR spectrum (Appendix 4). These complexes also co-crystallize in a 1:1 ratio from a concentrated solution of acetonitrile with diethylether resulting in crystals suitable for single crystal X-ray diffraction (SXRD). SXRD shows the two complexes to be **1-Co** and Co(neocuproine)OTf$_2$MeCN (Appendix 4). The addition of excess neocuproine to this mixture or the [Co(MeCN)$_6$][OTf]$_2$ starting salt enables the isolation of pure **1-Co** in good yield after work-up as confirmed by ^{1}H NMR spectroscopy (Figure S5). **1-Co** has a μ_{eff} of 4.30 μ_B from Evans' method and a solid state χT of 2.78 cm^3K/mol at room temperature consistent with an expected high spin $S = {}^3/_2$ Co^{2+} metal center (Appendix 4). Electron paramagnetic resonance (EPR) spectroscopy of **1-Co** shows a rhombic $S = {}^3/_2$ signal with simulated *g*-values of 2.35, 2.08, and 1.87, further supporting the presence of a high spin Co^{2+} center (Appendix 4). The crystal structure of **1-Co** features an average Co-N bond distance of 2.090(2) Å which also supports the presence of a high spin Co^{2+} center (Table 4 - 1).[15,16] Analogous to **1-Fe**, **1-Co** has one triflate counterion coordinated in the solid state resulting in a pseudo-trigonal bipyramidal geometry. A single broad peak at −75 ppm in the ^{19}F NMR spectrum again suggests that these triflate counterions are exchanging in solution (Appendix 4). **1-Co** was further characterized by UV-vis spectroscopy, IR spectroscopy, and elemental analysis (Appendix 4). It should be noted that a related complex of Co^{2+} with a tetradentate tethered bisneocuproine ligand has been previously isolated and characterized by cyclic voltammetry (CV), but no characterization of redox congeners was reported.[12c]

Figure 4 - 1. Single crystal X-ray diffraction of complexes **1-Fe**, **1-Co**, **2-Co**, **3-Fe**, and **3-Co**. Hydrogen atoms and solvent molecules have been omitted for clarity. Outer sphere anions were also omitted in the case of **1-Fe** and **1-Co**. Ellipsoids are shown at 50% probability. C is shown in gray, N in blue, O in red, S in yellow, F in bright green, Fe in orange, and Co in pink.

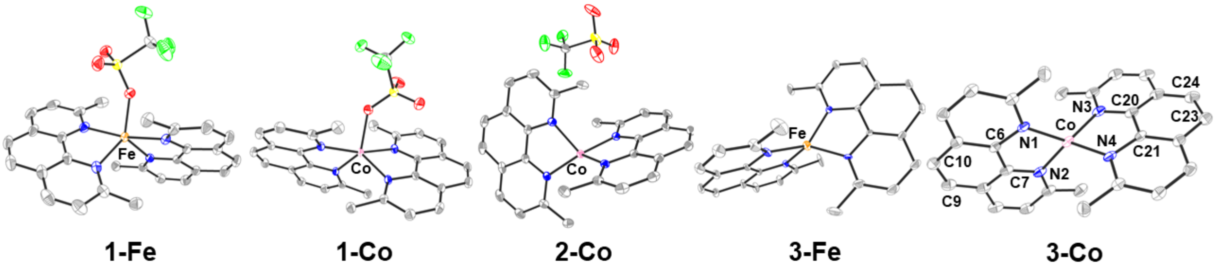

1-Fe **1-Co** **2-Co** **3-Fe** **3-Co**

Table 4 - 1. Selected Bond Lengths for **1-Fe**, **1-Co**, **2-Co**, **3-Fe**, and **3-Co** (Å)

	1-Fe[2]	**1-Co**[2]	**2-Co**	**3-Fe**[3]	**3-Co**[3]
M-N1[1]	2.166(2)	2.083(2)	1.978(1)	2.04(2)	1.96(1)
M-N2	2.145(2)	2.105(2)	2.046(1)	1.98(2)	2.010(9)
M-N3	2.154(2)	2.078(2)	1.969(1)	2.05(2)	1.97(1)
M-N4	2.130(2)	2.097(2)	2.011(1)	1.97(2)	1.98(1)
C6-C7	1.417(4)	1.434(3)	1.429(2)	1.40(2)	1.41(2)
C9-C10	1.344(5)	1.350(4)	1.353(3)	1.33(2)	1.34(2)
C20-C21	1.436(3)	1.430(4)	1.426(2)	1.38(2)	1.40(2)
C23-C24	1.348(4)	1.354(5)	1.351(3)	1.37(3)	1.39(2)

[1] Numbering for atoms as shown on the structure of **3-Co**

[2] Average bond lengths for two molecules in the unit cell

[3] Bond lengths shown for one of the molecules in the asymmetric unit. The difference in bond lengths between the two molecules in the asymmetric unit is less than the error in the measurements.

Electrochemistry

CV of **1-Fe** in acetonitrile shows three reversible couples (Appendix 4). One couple comes at −2.34 V vs. Fc/Fc^+ and is speculatively assigned as an Fe^{2+}/Fe^+ couple. The remaining two couples overlap and are centered at −1.5 V vs. Fc/Fc^+ (Figure 4 - 2). These overlapping couples have been assigned to ligand reductions for each neocuproine bound to Fe^{2+}. The overlap suggests that a singly reduced complex with one anionic neocuproine ligand radical and one neutral neocuproine ligand is not stable towards disproportionation, but a putative doubly reduced complex with two anionic ligand radicals bound to an Fe^{2+} center (**3-Fe**) should be chemically accessible.

CV of **1-Co** in acetonitrile similarly has three one electron couples, but unlike Fe, all three of these couples are well separated (Appendix 4). The couples at −1.17 V and −1.72 V have each been assigned to the reduction of one neocuproine ligand bound to Co^{2+} to form an anionic ligand radical (Figure 4 - 2). These couples are comparable to those reported for a closely related Co^{2+} complex.[66] The separation of these ligand couples supports that, unlike with Fe^{2+}, a singly reduced Co^{2+} complex with one anionic neocuproine ligand radical and one neutral neocuproine ligand (**2-Co**) should be chemically accessible. Additionally, a doubly reduced complex with two anionic radical neocuproine ligands (**3-Co**) should also be accessible. The final couple at −2.26 V is tentatively assigned as the metal centered Co^{2+}/Co^{+} couple.

Figure 4 - 2. Cyclic voltammetry of 3 mM solutions of **1-Fe** and **1-Co** in acetonitrile. Scan rate: 100 mV/s. Electrolyte: 5 mM $[Bu_4N][PF_6]$. Scans were run oxidatively.

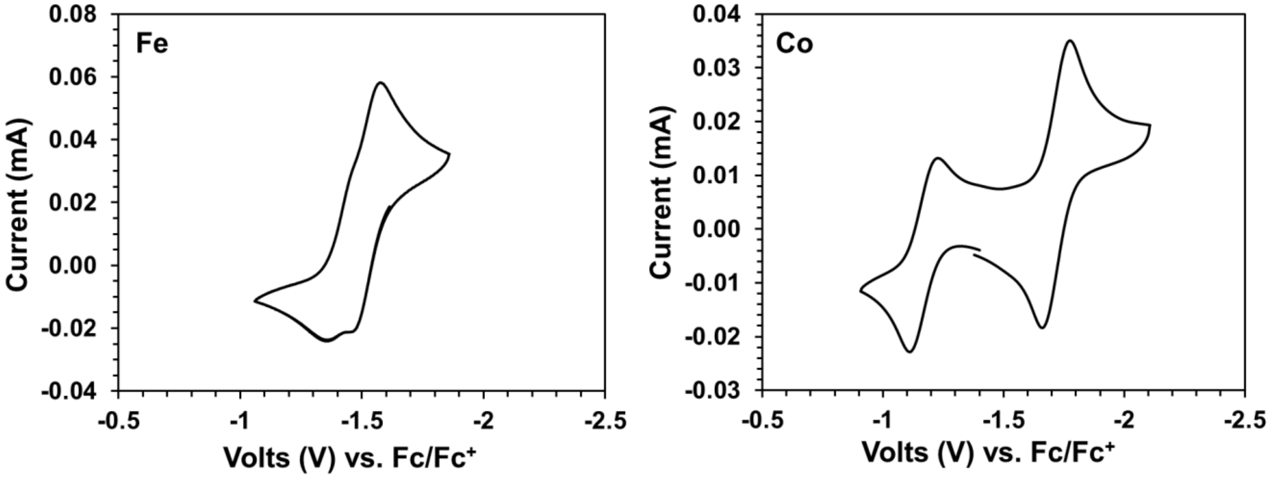

Synthesis of Reduced Complexes

3-Fe and **3-Co** were both synthesized by adding two equivalents of reductant to a suspension of **1-Fe** and **1-Co** respectively (Scheme 4 - 1). While multiple chemical reducing agents such as $NaC_{10}H_8$ and Cp_2^*Co were also found to produce the desired product, KC_8 was generally utilized as the byproducts of graphite and KOTf were easier to separate. The ^1H NMR spectrum of **3-Fe** shows three paramagnetically shifted peaks that roughly integrate in a 1:1:3 ratio (Appendix 4). They are assigned to two distinct backbone neocuproine proton environments and the methyl groups respectively. The third peak corresponding to the neocuproine backbone was not observed and may be too broad for observation. The ^{1}H NMR spectrum of **3-Co** also features three paramagnetically shifted peaks (Appendix 4). Unlike with **3-Fe**, these peaks integrate with a roughly 1:2:3 ratio, suggesting that two of the neocuproine backbone peaks overlap.

We anticipated that **3-Fe** would possess an electronic structure consisting of a high spin Fe^{2+} center with two ligand-based radicals. Thus, the anticipated overall spin state of **3-Fe** was $S = 1$ should the radicals couple antiferromagnetically to the metal center as might be expected. This electronic structure is consistent with the solution phase Evans' method μ_{eff} of 2.90 μ_B and the solid state χT of 1.05 cm^{3}K/mol (Appendix 4). Analogously, the expected $S = {}^1/_2$ overall spin state of **3-Co** was confirmed in solution with an Evans' method μ_{eff} of 2.08 μ_B and in the solid state with a χT of 0.56 cm^{3}K/mol (Appendix 4). EPR spectroscopy of **3-Co** shows a signal consistent with $S = {}^1/_2$ at $g = 2.38$. The signal shows hyperfine structure which was fit as coupling to both Co and four equivalent N atoms from the neocuproine radical ligands (Figure 4 - 3).

Figure 4 - 3. Electron paramagnetic resonance spectroscopy of 10 mM **3-Co** in acetonitrile at 10 K (black) and a simulation of the data (red). $g_z = 2.700$, $g_y = 2.360$, $g_x = 2.063$. Co hyperfine coupling parameters (MHz): $A_x = 153$, $A_y = 10$, $A_z = 10$. N hyperfine coupling parameters (4 equivalent centers, MHz): $A_x = 31.60$, $A_y = 0.78$, $A_x = 0.64$. MW Frequency = 9.631 GHz. MW Power = 2.0 mW. The nuclear spin of ^{59}Co and ^{14}N is 7/2 and 1 respectively.

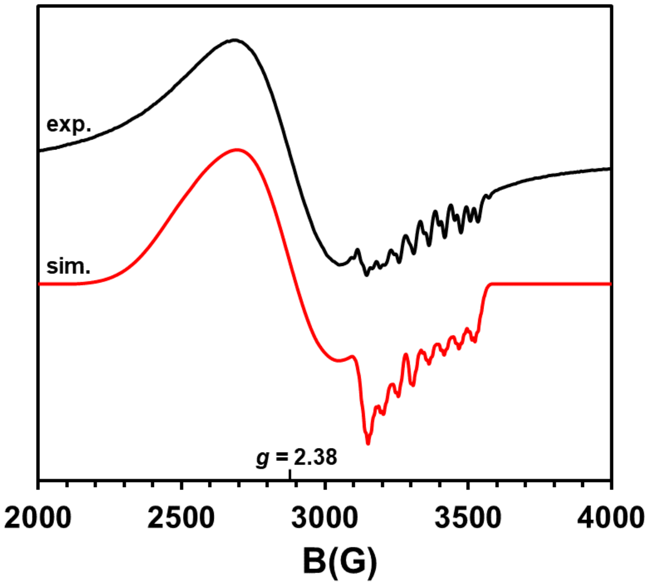

Several data collection attempts were carried out both in-house and using synchrotron radiation to obtain SXRD data on **3-Fe** and **3-Co**. While the precision of the best available X-ray analyses of both complexes is limited by the quality of the collected data, the results are sufficient for comparison with the other complexes in the series. These data show that both **3-Fe** and **3-Co** have pseudo C_{2v} symmetry around the metal center with a general decrease in bond lengths as compared to **1-Fe** and **1-Co** respectively. Furthermore, their M–N distances are still well within the normal range for the presence of a high spin M^{2+} center. In order to further verify the crystallographically determined bond lengths for **3-Fe** and **3-Co**, extended X-ray absorption fine structure data (EXAFS) from X-ray absorption spectroscopy (XAS) was fit for the first shell of these complexes. For **3-Fe**, Fe-N bond lengths of 1.95(1) Å and 2.02(1) Å were determined from this fit (Appendix 4). This decrease in Fe–N bond length in **3-Fe** as compared to **1-Fe** aligns with the observed trends in the crystal structure. Similarly, Co–N bond lengths of 1.96(2) Å and 2.00(2)

Å were determined from the EXAFS fit of **3-Co** (Appendix 4). This again aligns well with the trend of decreasing Co–N bond length upon reduction seen in the crystal structures. Both suggest an increased donor strength anticipated for anionic radical neocuproine ligands and that the high spin nature of the Fe^{2+} and Co^{2+} metal center is maintained in **3-Fe** and **3-Co**. Furthermore, **3-Fe** and **3-Co** exhibit intense features at ~800 nm in their UV-vis spectra which are absent in spectra of **1-Fe** and **1-Co**. These features are consistent with the π-π* of an organic radical (Appendix 4).[17] Thus, the structures of **3-Fe** and **3-Co** are consistent with two ligand-based reductions. Both **3-Fe** and **3-Co** complexes were further characterized by IR spectroscopy and elemental analysis (Appendix 4).

The CV of both the Fe and Co complexes showed electrochemical reversibility for the ligand couples. Therefore, chemical reversibility was investigated by taking **3-Fe** and **3-Co** each with an excess of AgOTf in acetonitrile and mixing. By ^1H NMR, the peaks corresponding to the diradical complexes disappeared and the peaks corresponding to **1-Fe** and **1-Co** formed (Appendix 4). In the case of Co, some amount of Co(neocuproine)$(OTf)_2$MeCN and free neocuproine was also present in the spectrum, while Fe only showed free neocuproine as the main byproduct of the reaction.

Reduction of **1-Co** to **2-Co** was first attempted by the addition of one equivalent of a reductant such as Cp_2Co or KC_8 to **1-Co** in THF at room temperature. This resulted in the formation of a new complex by ^1H NMR with four paramagnetically shifted features that roughly integrate in a 1:1:1:3 ratio (Figure S9). These features were assigned to three distinct proton environments on the neocuproine backbone and the methyl groups respectively. The presence of only four paramagnetic features is consistent with two equivalent neocuproine ligands bound to Co^{2+}, with radical delocalization between the two neocuproine ligands on the NMR timescale.

Crystals suitable for SXRD were obtained by vapor diffusion of diethyl ether into a concentrated solution of the reaction mixture in acetonitrile (Figure 4 - 1). While this method appeared to generate the desired product by NMR spectroscopy, all attempts to purify this product in bulk were contaminated by residual salts. Therefore, an alternative route was employed where **3-Co** was oxidized with one equivalent of AgOTf to generate **2-Co** (Scheme 4 - 1). The pure material obtained in this manner showed the same paramagnetic features in the ^{1}H NMR spectrum as seen when reduction of **1-Co** was employed. Pure **2-Co** was found to have a single, sharp feature in the ^{19}F NMR spectrum at −79 ppm, which corresponds to the ^{19}F NMR feature for free triflate (Appendix 4). This is consistent with outer sphere counterions for this complex. The crystal structure also shows an outer sphere triflate counterion and an average Co-N length of 2.00(1) Å consistent with a high spin Co^{2+} center.

The magnetic properties of **2-Co** were also investigated. By Evans' method, the complex was found to have a μ_{eff} of 2.94 μ_B in solution consistent with the expected overall spin of $S = 1$ for a high spin Co^{2+} metal center antiferromagnetically coupled to a single ligand-based radical. This assigned spin state is further supported by a χT of 1.55 cm^{3}K/mol in the solid state (Appendix 4). Additionally, **2-Co** exhibits an intense feature at 826 nm in its UV-vis spectrum consistent with the π-π* transition of an organic radical resulting from a ligand-based reduction (Appendix 4).[17]

Characterization of Electronic Structure

Additional experiments were conducted to rigorously assign ligand-based redox events. XAS was conducted on **1-Fe**, **3-Fe**, and $Fe(MeCN)_2(OTf)_2$ to investigate the oxidation state of Fe in these complexes where $Fe(MeCN)_2(OTf)_2$ acted as a control for Fe^{2+} (Figure 4 - 4). All three complexes show a pre-edge feature corresponding to the $1s \rightarrow 3d$ transition with the higher symmetry of **3-Fe** as compared to **1-Fe** resulting in a significantly more intense feature. The K-edge feature for **1-Fe**, **3-Fe**, and Fe(MeCN)$_2$(OTf)$_2$ corresponding to the $1s\rightarrow4p$ transition have points of inflection at 7118 eV, 7116 eV, and 7116 eV respectively as determined by the derivative plots of the K-edge energies (Appendix 4). Although these points of inflection are all close in value, even a change of a few eV can correspond to a change in metal oxidation state,[18] which could imply that **1-Fe** has an Fe center in a different oxidation state as compared to **3-Fe** and Fe(MeCN)$_2$(OTf)$_2$. However, given that coordination number also influences the energy at which the inflection point of the K-edge is observed, the difference in energy may be due to the fact that **1-Fe** is five-coordinate while both **3-Fe** and Fe(MeCN)$_2$(OTf)$_2$ are four-coordinate. Furthermore, the same coordination number and energy for the point of inflection between **3-Fe** and Fe(MeCN)$_2$(OTf)$_2$ supports that **3-Fe** has an Fe^{2+} center. Thus, we assign the reductions of **1-Fe** to **3-Fe** as ligand-based.

Figure 4 - 4. X-ray absorption spectra of **1-M**, **2-Co**, and **3-M**. The spectra of the Fe complexes are compared to the spectrum of Fe(MeCN)$_2$OTf$_2$ as an Fe^{2+} reference. The K-edges have points of inflection at 7116 eV, 7118 eV, and 7116 eV for Fe(MeCN)$_2$OTf$_2$, **1-Fe**, and **3-Fe** respectively. For Co, the K-edges have points of inflection at 7717 eV, 7717 eV, and 7716 eV for complexes **1-Co**, **2-Co**, and **3-Co** respectively.

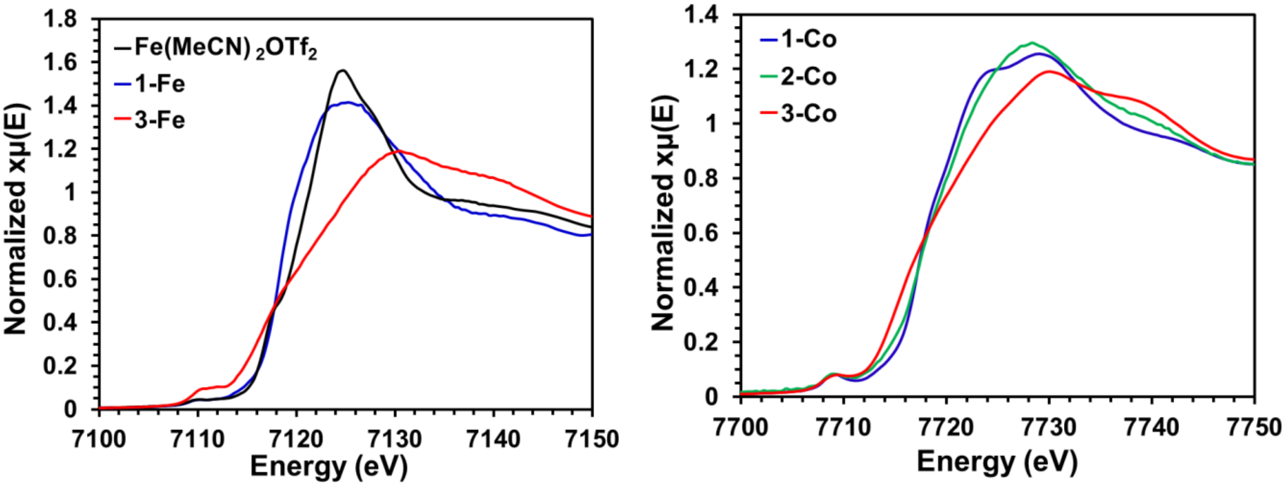

The electronic structure of the Fe complexes was further investigated using Mössbauer spectroscopy (Figure 4 - 5).[19] The data was fit for either the presence of a single species or two species. Good fits were only found when fitting to a single species for both **1-Fe** and **3-Fe**, although **3-Fe** was fit with a Voigt line shape. The isomer shifts were found to be 1.186(2) mm/s and 0.787(1) mm/s for **1-Fe** and **3-Fe** respectively. The most likely change in metal oxidation state from **1-Fe** to **3-Fe** is from Fe^{2+} to Fe^{+1} or Fe^{0}. If such a reduction on the metal had occurred, the isomer shift for **3-Fe** would be expected to increase to a more positive value from the 1.186(2) mm/s isomer shift of **1-Fe**. The decrease in the value of the isomer shift of **3-Fe** suggests that such a metal-based reduction has not occurred. Rather, the decrease in isomer shift is likely due to both a decrease in coordination number as well as an increase in covalency between the metal center and the ligand as the neocuproine changes from neutral to anionic. Furthermore, the isomer shifts of **1-Fe** and **3-Fe** both fall within the usual range for Fe^{2+} complexes. The quadrupole splittings of 3.404(3) and 1.427(3) for **1-Fe** and **3-Fe** respectively also fall within the normal range for high spin Fe^{2+} species and are also consistent with the higher symmetry of **3-Fe**.[78]

Figure 4 - 5. 80 K Mössbauer spectra of **1-Fe** and **3-Fe**. (complex: δ, ΔE_Q). **1-Fe**: 1.186(2) mm/s, 3.404(3) mm/s. **3-Fe:** 0.787(1) mm/s, 1.427(3) mm/s.

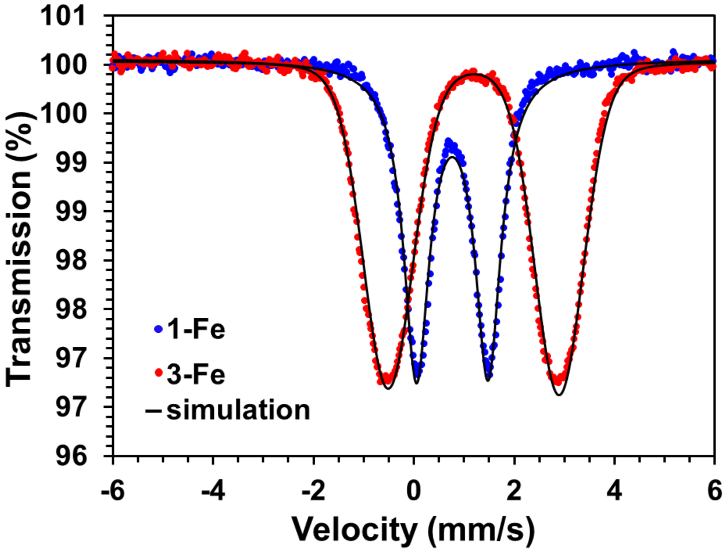

Similarly, XAS was conducted on the series of Co complexes (Figure 4 - 4). As with the Fe complexes, **1-Co**, **2-Co**, and **3-Co** all exhibit a K-edge feature corresponding to the 1*s*→3*d* transition. The K-edge features corresponding to the 1*s*→4*p* transition for **1-Co**, **2-Co**, and **3-Co** have points of inflection at 7717 eV, 7716 eV, and 7716 eV respectively as determined by the derivative plots of the K-edge energies (Appendix 4). Given that the inflection points are within 1 eV of each other, and that a change in coordination number occurs upon reduction, these data suggest that no change in the oxidation state of Co occurs upon reduction of the complexes. Furthermore, the isolation and characterization of these species in three oxidation states provides evidence towards ligand-based reduction. Looking specifically at the Co-N bond lengths between **1-Co** and **2-Co** we observe a decrease in bond length of 0.104 Å, 0.059 Å, 0.109 Å, and 0.089 Å for Co1-N1 through Co1-N4 respectively. This shortening of metal-ligand distances suggests that upon reduction, neocuproine has become a stronger donor to the Co metal center which would be expected for an anionic radical neocuproine. Furthermore, if reduction had occurred on the Co metal center rather than the ligand, one would anticipate an increase in Co-N bond lengths from **1-Co** to **2-Co** since the Co metal center should increase in size from the addition of an electron while the donor strength of neocuproine would remain unchanged. Therefore, the decrease in Co-N distance aligns best with a ligand-based reduction. A slight decrease in the C6-C7 and C20-C21 bond lengths from **1-Co** to **2-Co** is also observed. While the change in bond length is outside of error, it is qualitatively small. This is reasonable given that each **2-Co** complex should crystallize with a random alignment of the reduced neocuproine ligand relative to the unreduced neocuproine ligand. Thus, the crystal structure represents an average of the reduced and unreduced bond lengths and this shortening of the C6-C7 and C20-C21 bonds supports ligand-based reduction.

Three scenarios for the electronic structure of **3-Co** were considered: Co^{2+} where both neocuproines feature ligand radicals, Co^{1+} with one neutral neocuproine ligand and one neocuproine radical ligand, as well as Co^{0} with two neutral neocuproine ligands. The Co-N bond lengths obtained from the SXRD data show a general decrease in bond length from **1-Co** and **2-Co** to **3-Co**. As with the reduction from **1-Co** to **2-Co**, this trend is consistent with ligand-based reduction and is inconsistent with reduction to Co^{1+} or Co^{0}. Furthermore, the presence of hyperfine coupling to the neocuproine nitrogen atoms in **3-Co** in the EPR spectrum suggests that unpaired spin on the complex is coupled to the four N atoms. Other N-containing aromatic ligand-based radicals complexed to Cu or Al respectively show similar magnitudes in their N hyperfine coupling parameters, although the obtained hyperfine coupling constants in the current system must be interpreted cautiously due to broadening and convolution.[20] Thus the presence and magnitude of the observed N hyperfine coupling in **3-Co** supports our assignment of **3-Co** is as a Co^{2+} center with two reduced neocuproine ligands.

DFT analyses were also performed to better understand the localization of electron density in the Co complexes upon reduction (Figure 4 - 6). When summed separately, the spin density for both **2-Co** and **3-Co** was shown to be of opposite sign on the ligand as compared to the Co center in alignment with an antiferromagnetically coupled system between the Co center and the neocuproine ligands (Appendix 4). A significant increase in spin density on the ligand is seen upon reduction from **2-Co** to **3-Co**, supporting that this reduction is predominantly ligand-centered rather than metal centered (Figure 4 - 6, Appendix 4). Furthermore, the spin density on the Co center increases in **3-Co** relative to **2-Co**. A reduction at Co should result in a decrease in magnitude of the spin density due to electron pairing. Therefore, the increase in spin density at Co is not consistent with a metal-based reduction upon the addition of an electron to the complex.

Given these trends, the computational analysis aligns with the experimental data to suggest ligand-based reductions on neocuproine.

Figure 4 - 6. Spin density plots of **2-Co** and **3-Co** at an iso value of 0.003. Mulliken spin density (Co, ligands): **2-Co**: 2.25, -0.25, **3-Co**: 2.41, -1.54.

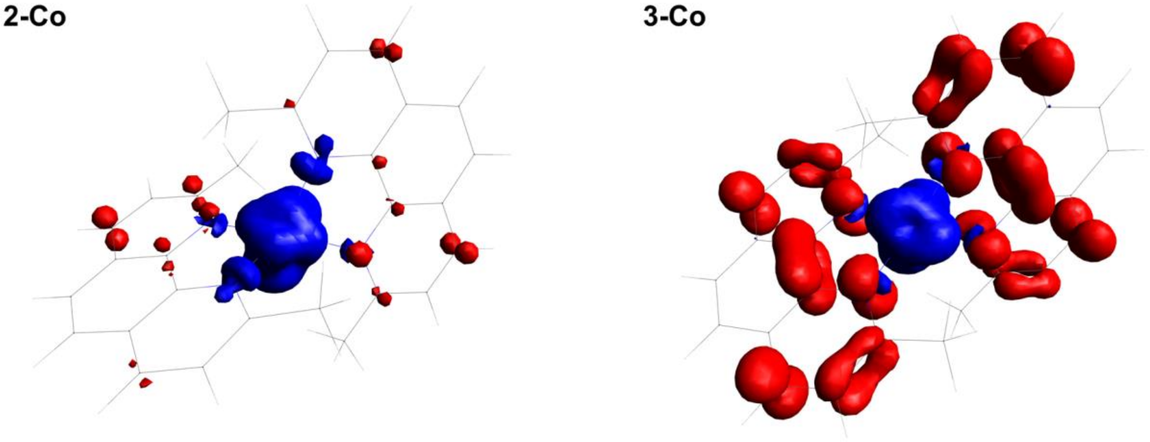

2-Co

3-Co

The sum of experimental and theoretical data point toward the redox noninnocence of neocuproine in these series, but the question of why a singly reduced complex is chemically accessible with Co^{2+} but not with Fe^{2+} must be addressed. From our characterization of **1-Co** and **1-Fe**, the triflate anions are rapidly exchanging in solution. This was further verified by taking ^{19}F NMR spectra in the presence of 1,2-difluorobenzene as an internal standard. When three equivalents of 1,2-difluorobenzene were added to one equivalent of **1-Fe** or **1-Co**, the peak integrated in a roughly 1:0.9 ratio (Appendix 4). This suggests that the single peak in the ^{19}F NMR spectra accounts for all triflate in solution. We have been unable to resolve this feature further with low-temperature NMR measurements (Appendix 4). This fluxionality suggests that the difference in stability of the **2-M** congeners is likely to be unrelated to the binding of triflate.

Regardless of whether acetonitrile displaces triflate or not, it is likely that **1-Co** has the form (neocuproine)$_2$CoOTf$^+$ or (neocuproine)$_2$CoNCMe^{2+} which both have 17 valence electrons. Binding of an additional triflate or solvent molecule would result in a 19 valence electron complex which would likely be susceptible to ligand dissociation. Reduction of this 5-coordinate complex should form a relatively stable 18 electron complex that can be chemically isolated. While the solid-state structure of **2-Co** is 4-coordinate, a 5-coordinate acetonitrile adduct is reasonable in solution. By similar arguments, it is reasonable that **1-Fe** should be 6-coordinate with 18 valence electrons with either two triflate or acetonitriles bound. Reduction of this 18 valence electron complex would generate a 19 electron complex which should again be susceptible to ligand dissociation to now generate a 5-coordinate 17 valence electron intermediate. As outlined for Co, the reduction of this putative 17 valence electron Fe intermediate should be facile to generate a filled shell 18 valence electron complex **3-Fe**. While simplistic and speculative, this valence electron argument provides a feasible explanation for the differential redox stability of these Fe and Co complexes.

Conclusion

Here we show a series of Fe^{2+} and Co^{2+} complexes with noninnocent neocuproine ligands upon reduction. Each neocuproine can act as a sink for a single electron, allowing for diradical complexes to form. In the case of the Fe complexes, two distinct electronic states have been thoroughly characterized, while in the case of the Co complexes, three distinct electronic states can be isolated. Both Fe and Co feature a third, more negative reversible couple in their CV assigned to metal centered reduction. This study demonstrates that neocuproine can act as an electron reservoir and adds to a growing family of redox-active, chelating, heterocyclic ligands.

Experimental

General Methods. All chemicals were purchased from commercial suppliers and used without further purification. All manipulations were carried out under an atmosphere of N_2 using standard Schlenk and glovebox techniques. Glassware was dried at 180 °C for a minimum of two hours and cooled under vacuum prior to use. Solvents were dried on a solvent purification system from Pure Process Technologies and stored over 4 Å molecular sieves under N_2. Tetrahydrofuran (THF) was stirred over NaK alloy and run through an additional alumina column prior to use to ensure dryness. Solvents were tested for H_2O and O_2 using a standard solution of sodium-benzophenone ketyl radical anion. C_6D_6, $CDCl_3$, and CD_2Cl_2 were dried over 4 Å molecular sieves under N_2. ^1H and $^{13}C\{^1H\}$ NMR spectra were recorded on Bruker DRX 400 or 500 spectrometers. Chemical shifts are reported in ppm units referenced to residual solvent resonances for ^1H and $^{13}C\{^1H\}$ spectra. UV-Vis Spectra were recorded on a Bruker Evolution 300 spectrometer and analyzed using VisionPro software. Experiments requiring a dip probe utilized Hellma Analytics Excalibur Standard Tauchsonde Granzquarz-Tauchsonde (serial no. 13594). IR spectra were obtained on a Bruker Tensor II spectrometer with the OPUS software suite. All IR samples were prepared as KBr pellets in a homemade press. EPR spectra were recorded on an Elexsys E500 Spectrometer with an Oxford ESR 900 X-band cryostat and a Bruker Cold-Edge Stinger. EPR data was fit using a least-squares fit in SpinCount. Electrochemical measurements were performed using a BAS Epsilon potentiostat and analyzed using BAS Epsilon software version 1.40.67NT. Cyclic voltammetry measurements were made using a glassy carbon working electrode, platinum wire counter electrode, and silver wire pseudo-reference electrode, and referenced to internal Fc/Fc^+. Magnetic measurements were performed on either a Quantum Design MPMS 3 equipped with a superconducting quantum interference device (SQUID) or using a Quantum Design MPMS-XL SQUID magnetometer. Corrections were made for the diamagnetic contributions from the polycarbonate capsules and eicosane used to secure the sample by measuring field vs. moment in duplicate for each to determine a moment per gram correction. The χ values reported are the molar magnetic susceptibilities. Magnetic data (χT vs. T) plots and reported values have been normalized to one formula unit. Zero-field ^{57}Fe Mössbauer spectra were obtained at 80 K using a ^{57}Co/rhodium source. Samples were prepared in an MBraun nitrogen glove box. A typical sample contained approximately 60 mg of compounds suspended in a plastic cap. Another cap with a slightly smaller diameter was squeezed into the previous sample cap to completely encapsulate the solid sample mixture. All spectra were analyzed using the WMOSS Mössbauer Spectral Analysis Software. Complex **1-Fe** was fit with a Voigt line shape. Note that the accuracy of the fit parameters may be overestimated as the error in the Fe foil calibration is 0.01 mm/s. Single crystal X-ray diffraction data were collected in-house using Bruker D8 Venture diffractometer equipped with Mo microfocus X-ray tube (λ = 0.71073 Å) or at the Advanced Photon Source of Argonne National Laboratory (beamline 15-ID-B,C,D) using X-ray radiation with a wavelength of λ = 0.41328 Å. X-ray near-edge absorption spectra (XANES) and X-ray absorption fine structure (XAFS) spectra were employed to probe the local environment around Fe. Data were acquired at the Advanced Photon Source at Argonne National Labs with a bending magnet source with ring energy at 7.00 GeV. Fe K-edge data were acquired at the MRCAT 10- BM beam line. EXAFS data were collected in the fluorescence mode using fluorescence ion chamber in Stern-Heald geometry. Absorption was calibrated and concurrently referenced during measurement to a Fe foil. Data collected was processed using the Demeter software suite[21] by extracting the EXAFS oscillations χ(k) as a function of photoelectron wavenumber k. The theoretical paths were generated using FEFF6 and the models were done in the conventional way using the fitting program Artemis. The initial model was taken from an X-ray crystal structure of the Fe-compound. EXAFS data were modelled in R-space with k-weights of 1, 2 and 3 until a satisfactory fit describing the system was obtained.

X-ray diffraction. Suitable crystals reported in this manuscript were mounted on a cryo-loop and transferred into the cold nitrogen stream of a Bruker D8 Venture diffractometer. Crystal structure of complex **1-Fe** (CCDC 189232) and **3-Co** (CCDC 1898231) were collected at The Advanced Photon Source at Argonne National Laboratory (beamline 15-ID-B,C,D). The diffraction data were measured at 100 K using synchrotron X-ray radiation with a wavelength of λ = 0.41328 Å. Data were collected using ϕ scans. Data reduction and integration were performed with the Bruker APEX3[22] software package. Data were scaled and corrected for absorption effects using the multi-scan procedure as implemented in SADABS.[23] The structure was solved by SHELXT[24] and refined by a full-matrix least-squares procedure using OLEX2[25] (XL refinement program[26]). The crystallographic data of **1-Co (**CCDC 1898228), **1-Co** and [Co(neocuproine)(OTf)$_2$MeCN] (CCDC 1898233), **2-Co (**CCDC 1898229) and **3-Fe** (CCDC 1898230) were collected by using Mo K$_\alpha$ radiation (0.71073 Å). The final unit cell was obtained from the xyz centroids of 19263 (**1-Co**), 16878 (**1-Co** and [Co(neocuproine)(OTf)$_2$MeCN]), 8164 (**2-Co**), 7799 (**3-Co**), 15933 (**1-Fe**), and 8042 (**3-Fe**) reflections after integration. Intensity data were corrected for Lorentz and polarization effects, scale variation for decay and absorption: a multiscan absorption correction was applied, based on the intensities of symmetry-related reflections measured at different angular setting (*SADABS*).[27] The structures were solved by direct methods using the program *SHELXS*[28] integrated in Olex 2.[29] Most of the hydrogen atoms were generated by geometrical considerations and constrained to idealized geometries and allowed to ride on their carrier atoms with an isotropic displacement parameter related to the equivalent displacement parameter of their carrier atoms. Structure refinement was performed with the program package *SHELXL*[27] integrated in Olex 2.[30] Crystallographic data are presented in the table below. B-level alerts are present for 8042 (**3-Fe**) and 7799 (**3-Co**). This is a direct reflection of the low quality of data that could be obtained for these single crystals despite multiple collection attempts in house and at Argonne National Lab using synchrotron radiation. The limitations of the collected data should be considered in any analyses of the aforementioned crystal structures.

Density Functional Theory. Geometry optimization calculations were performed with ORCA[31] software suite using density functional theory (DFT). Geometries were fully optimized starting from coordinates generated from a molecular model built in Avogadro. The B3P functional was used with a basis set of def2-SVP on H, def2-TZVPP on Co and N, and def2-TZVP on C atoms. The resulting structures were confirmed to be minima on the potential energy surface by frequency calculations using ORCA[10]. Frequency calculations were also conducted using the B3P functional and previously listed basis sets for each atom type. Single point broken symmetry calculations using flipspin were then run to obtain the final spin density plots and Mulliken spin densities.

[Fe(neocuproine)$_2$(OTf)][OTf] (1-Fe). Fe(MeCN)$_2$(OTf)$_2$ (1.60 g, 3.67 mmol) and neocuproine (1.54 g, 7.37 mmol) were dissolved separately in acetonitrile (7 mL each). The solutions were combined with stirring for 30 minutes to form a deep yellow solution. The reaction mixture was concentrated under vacuum to a saturated solution in acetonitrile (4 mL) and crystallized via two layer crystallization with Et$_2$O (13 mL) overnight. Yield: 1.541 g (2.00 mmol, 83.3%). Single crystals of **1-Fe** suitable for X-ray diffraction were obtained by vapor diffusion of Et$_2$O into a concentrated solution of **1-Fe** in acetonitrile. ^{1}H NMR (400 MHz, CD$_3$CN, RT): δ = 55.5 (s, 4H), 32.6 (s, 4H), 1.1 (s, 4H), −34.3 (bs, 12H). ^{19}F{^{1}H} NMR (500 MHz, CD$_3$CN, RT): δ −64 (bs). Magnetic Susceptibility: Evans' Method (CD$_3$CN, RT, μ_B): μ_{eff} = 5.06; SQUID: χT = 3.65 cm^{3}K/mol. IR (KBr pellet, cm^{-1}): 3066 (C–H, w), 1594 (m), 1500 (m). Mössbauer (80 K, mm/s)

δ = 1.186(2); ΔE_Q = 3.404(3). UV-vis, nm in acetonitrile, (ε, $M^{-1}cm^{-1}$): 450 (140). Anal. Calc. C, 46.76; H, 3.14; N, 7.26; Found: C, 46.58; H, 3.30; N, 7.08.

[Co(neocuproine)$_2$(OTf)][OTf] (1-Co). [Co(MeCN)]$_6$[(OTf)$_2$] (1.70 g, 2.18 mmol) and neocuproine (2.70 g, 12.96 mmol) were dissolved separately in acetonitrile (7 mL each). The solutions were combined with stirring overnight to form a deep purple solution. The reaction mixture was concentrated under vacuum to a saturated solution in acetonitrile (4 mL) and washed with benzene (10 mL x 5) to remove excess neocuproine. This was then crystallized via two layer crystallization using a concentrated solution of **1-Co** in acetonitrile (4 mL) with Et_2O (13 mL) overnight. Yield: 1.10 g (1.42 mmol, 50.5%). Single crystals of **1-Co** suitable for X-ray diffraction were obtained by vapor diffusion of Et_2O into a concentrated solution of **1-Co** in acetonitrile. ^{1}H NMR (400 MHz, CD_3CN, RT): δ = 58.5 (s, 4H), 44.9 (s, 4H), 13.2 (s, 4H), −65.6 (bs, 12H). ^{19}F{^{1}H} NMR (500 MHz, CD_3CN, RT): δ = −75 (bs). Note: when excess neocuproine is present in solution, a single, very broad peak at δ = 12 ppm can be seen in the ^{1}H NMR spectrum. Magnetic Susceptibility: Evans' Method (CD_3CN, RT, μ_B): μ_{eff} = 4.30; SQUID: χT = 2.78 cm^3K/mol. EPR (g_z, g_x, g_y): 2.35, 2.08, 1.87. IR (KBr pellet, cm^{-1}): 3076 (C–H, w), 1598 (m), 1503 (m). UV-vis, nm in acetonitrile, (ε, $M^{-1}cm^{-1}$): 427 (620), 521 (210), 541 (210), 577 (250). Anal. Calc. C, 46.57; H, 3.13; N, 7.24; Found: C, 46.38; H, 3.29; N, 7.21.

[Fe(neocuproine-radical)$_2$] (3-Fe). 1-Fe (210 mg, 0.27 mmol) and KC_8 (70 mg, 0.52 mmol) were stirred in Et_2O (15 mL) to form a suspension, which turned deep red-black over 30 minutes. The reaction was allowed to stir overnight, then condensed to a solid under vacuum. This was taken up in benzene (200 mL) and filtered through dry Celite to remove graphite and salt byproducts. This was condensed under vacuum to produce a pure, dark maroon powder. Yield: 45 mg (0.095 mmol, 34.9%). Crystals used to confirm connectivity by SXRD were obtained by vapor diffusion of petroleum ether into a concentrated solution of **3-Fe** in THF. ^{1}H NMR (400 MHz, C_6D_6, RT): δ = 119.9 (s, 4H), 25.5 (s, 4H), −78.6 (bs, 12H). Magnetic Susceptibility: Evans' Method (C_6D_6, RT, μ_B): μ_{eff} = 2.90; SQUID: χT = 1.05 cm^{3}K/mol. IR (KBr pellet, cm^{-1}): 2919 (C–H, w), 1615 (m), 1590 (m), 1503 (s). Mössbauer (80 K): δ = 0.787(1); ΔE_Q = 1.427(3). UV-vis, nm in benzene, (ε, M^{-1}cm^{-1}): 365 (4700), 397 (3400), 487 (4100), 523 (3200), 782 (1400). Anal. Calc. C, 71.20; H, 5.12; N, 11.86; Found: C, 71.19; H, 5.18; N, 11.88.

[Co(neocuproine-radical)$_2$] (3-Co). 1-Co (1.00 g, 1.29 mmol) and KC_8 (350 mg, 2.59 mmol) were stirred in a mixture of Et_2O:THF (3:1, 15 mL) to form a suspension that began to turn deep red-black immediately. The reaction was allowed to stir 1 hour, filtered through dry Celite to remove graphite, then condensed to a solid under vacuum. This was taken up in benzene (700 mL) and filtered to remove salt byproducts. This was condensed under vacuum to produce a dark maroon powder. Yield: 169 mg (0.35 mmol, 27.5%). Crystals used to confirm connectivity by SXRD were obtained by vapor diffusion of petroleum ether into a concentrated solution of **3-Co** in THF. ^{1}H NMR (400 MHz, C_6D_6, RT): δ = 59.4 (s, 4H), 20.1 (s, 8H), −54.3 (bs, 12 H). Magnetic Susceptibility: Evans' Method (C_6D_6, RT, μ_B): μ_{eff} = 2.08; SQUID: χT = 0.56 cm^{3}K/mol. EPR (g_z, g_x, g_y): 2.70, 2.36, 2.063. IR (KBr pellet, cm^{-1}): 3036 (C–H, w); 2916 (C–H, w), 1617 and 1590 (s), 1494 (s). UV-vis, nm in benzene, (ε, M^{-1}cm^{-1}): 358 (2500), 400 (1600), 500 (3600), 634 (1200), 884 (1500 M^{-1}cm^{-1}). Anal. Calc. C, 55.77; H, 3.87; N, 8.97; Found: C, 55.04; H, 4.17; N, 8.24. Note that the combustion analysis for this compound is slightly off of the predicted value. We anticipate that this is due to the sensitivity of this reduced complex.

[Co(neocuproine-radical)(neocuproine)][OTf] (2-Co). 3-Co (20 mg, 0.04 mmol) was dissolved in THF (10 mL) and a solution of AgOTf (11 mg, 0.04 mmol) in THF (5 mL) was added slowly with stirring. This was allowed to stir for an hour, filtered to remove Ag^0, then concentrated under vacuum to a black powder. Yield: 18 mg (0.03 mmol, 66.7%). Single crystals suitable for X-ray diffraction could be obtained via vapor diffusion of petroleum ether into a concentrated solution of **2-Co** in THF or via vapor diffusion of Et_2O into a concentrated solution of **2-Co** in acetonitrile. SXRD data reported was obtained from the latter conditions of Et_2O and acetonitrile. ^{1}H NMR (400 MHz, CD_3CN, RT): $\delta = 48.4, 47.4$ (two s, 8H), 23.0 (s, 4H), −29.8 (bs, 12H). ^{19}F{^{1}H} NMR (500 MHz, CD_3CN, RT): $\delta = -79$. Magnetic Susceptibility: Evans' Method (CD_3CN, RT, μ_B): $\mu_{eff} = 2.94$; SQUID: $\chi T = 1.54$ cm^{3}K/mol. IR (KBr pellet, cm^{-1}): 3065 (C–H, w), 1593 (m), 1498 (m). UV-vis, nm in acetonitrile, (ε, M^{-1}cm^{-1}): 508 (2000), 826 (2000). Anal. Calc. C, 70.73; H, 5.09; N, 11.78; Found: C, 70.18; H, 5.19; N, 11.09. Note that the combustion analysis for this compound is slightly off of the predicted value. We anticipate that this is due to the sensitivity of this reduced complex.

References

---

[1] (a) Joannou, M. V; Darmon, J. M.; Bezdek, M. J.; Chirik, P. J.; *Polyhedron* **2019**, *159*, 308–317.; (b) Vasilopoulos, A.; Zultanski, S. L.; Stahl, S. S.; *J. Am. Chem. Soc.* **2017**, *139*, 7705–7708.; (c) Connick, W. B.; Bilio, A. J. Di; Hill, M. G.; Winner, J. R.; Gray, H. B.; *Inorganica Chim. Acta* **1995**, *240*, 169–173.; (d) Rizvi, M. A. *Russ. J. Gen. Chem.* **2015**, *85*, 959–973.; (e) Wang, M.; Weyhermüller, T.; Wieghardt, K.; *Eur. J. Inorg. Chem.* **2015**, 3246–3254.; (f) Wang, M.; England, J.; Weyhermüller, T.; Wieghardt, K.; *Eur. J. Inorg. Chem.* **2015**, 1511–1523.; (g) England, J.; Bill, E.; Weyhermu, T.; Neese, F.; Atanasov, M.; Wieghardt, K.; *Inorg. Chem.* **2015**, *54*, 12002–12018.

[2] (a)Burks, D. B.; Vasiliu, M.; Dixon, D. A.; Papish, E. T.; *J. Phys. Chem. A* **2018**, *122*, 2221–2231.; (b) Siek, S.; Burks, D. B.; Gerlach, D. L.; Liang, G.; Tesh, J. M.; Thompson, C. R.; Qu, F.; Shankwitz, J. E.; Vasquez, R. M.; Chambers, N.; Szulczewski, G. J.; Grotjahn, D. B.; Webster, C. E.; Papish, E. T.; *Organometallics* **2017**, *36*, 1091–1106.; (c) Bowman, A. C.; England, J.; Sproules, S.; Weyhermu, T.; Wieghardt, K.; *Inorg. Chem.* **2013**, *52*, 2242–2256.; (d) Lancaster, K. M.; Gerken, J. B.; Durrell, A. C.; Palmer, J. H.; Gray, H. B.; *Coord. Chem. Rev.* **2010**, *254*, 1803–1811.

[3] (a) Ansari, M. A.; Beyer, K.; Schwederski, B.; Kaim, W.; Lahiri, G. K.; *Chem. Asian J.* **2018**, *13*, 2947–2955.; (b) Horak, K. T.; Agapie, T.; *J. Am. Chem. Soc.* **2016**, *138*, 3443–3452.; (c) Henthorn, J. T.; Agapie, T.; *Inorg. Chem.* **2016**, *55*, 5337–5342.; (d) Buss, J. A.; Agapie, T.; *J. Am. Chem. Soc.* **2016**, *138*, 16466–16477.

[4] (a) Broere, D. L. J.; Mercado, B. Q.; Lukens, J. T.; Vilbert, A. C.; Banerjee, G.; Lant, H. M. C.; Lee, H.; Bill, E.; Sproules, S.; Lancaster, K. M.; Holland, P. L.; *Eur. J. Chem.* **2018**, *24*, 9417–9425.; (b) Lewis, R. A.; Macleod, K. C.; Mercado, B. Q.; Holland, P. L.; *Chem. Commun.* **2014**, *50*, 11114–11117.; (c) Goswami, S.; Sengupta, D.; Paul, N. D.; Mondal, T. K.; Goswami, S.; *Chem. Eur. J.* **2014**, *20*, 6103–6111.; (d) Ghosh, P.; Samanta, S.; Roy, S. K.; Joy, S.; Krämer, T.; McGrady, J. E.; Goswami, S.; *Inorg. Chem.* **2013**, *52*, 14040–14049.; (e) Budzelaar, P. H. M.; *Eur. J. Inorg. Chem.* **2012**, No. 3, 530–534.; (f) Hübner, R.; Weber, S.; Strobel, S.; Sarkar, B.; Záliš, S.; Kaim, W.; *Organometallics* **2011**, *30*, 1414–1418.

[5] (a) Reşat, A.; Kubilay, G.; Birsen, D.; Mustafa, O.; Saliha, E. C.; Burcu, B.; Berker, K. I.; Dilek, O.; *Molecules* **2007**, *12*, 1496–1547.; (b)Apak, R.; Gluclu, K.; Ozyurek, M.; Karademir, S. E.; *J. Agric. Food Chem.* **2004**, 7970–7981.

[6] Bhat, P. A.; Chat, A.; Dar, A. A.; *New J. Chem* **2018**, *42*, 6695–6706.

[7] Langer, R.; Fuchs, I.; Vogt, M.; Balaraman, E.; Milstein, D.; *Chem. Eur. J.* **2013**, *19*, 3407–3414.

[8] Schaefer, B. A.; Margulieux, G. W.; Small, B. L.; Chirik, P. J.; *Organometallics* **2015**, *34*, 1307–1320.

[9] (a) Wang, D.; Weinstein, A. B.; White, P. B.; Stahl, S. S.; *Chem. Rev.* **2018**, *118*, 2636–2679.; (b) Zheng, C.; Stahl, S.; *Chem. Commun.* **2015**, *15*, 12771–12774.

---

[10] Ferretti, F.; Rimoldi, M.; Ragaini, F.; Macchi, P.; *Inorganica Chim. Acta* **2018**, *470*, 284–289.

[11] (a) Moragas, T.; Gaydou, M.; Martin, R.; *Angew. Chem. Int. Ed.* **2016**, *55*, 5053–5057.; (b) Moragas, T.; Cornella, J.; Martin, R.; *J. Am. Chem. Soc.* **2014**, *136*, 17702–17705.; (c) Lennartson, A.; *J. Coord. Chem.* **2010**, *63*, 4177–4187.; (d) Fischer, R.; Langer, J.; Malassa, A.; Walther, D.; Görls, H.; Vaughan, G.; *Chem. Commun.* **2006**, No. 23, 2510–2512.; (e) Uddin, M.; Lalia-Kantouria, M.; Hadjikostas, C. C.; Voutsas, G.; *Z. Anorg. Allg. Chem.* **1998**, *624*, 1699–1705.; (f) Figg, D. C.; Berber, R. H.; Potenza, J. A.; *Inorg. Chem.* **1992**, *31*, 2111–2117.; (g) Konig, E.; Ritter, G.; Madeja, K.; **1981**, *43*, 2273–2280.

[12] (a)Vallejo, J.; Castro, I.; Ruiz-García, R.; Cano, J.; Julve, M.; Lloret, F.; De Munno, G.; Wernsdorfer, W.; Pardo, E.; *J. Am. Chem. Soc.* **2012**, *134*, 15704–15707.; (b) Goldsmith, C. R.; Jiang, W.; *Inorganica Chim. Acta* **2012**, *384*, 340–344.; (c) Youinou, M. T.; Ziessel, R.; Lehn, J. M.; *Inorg. Chem.* **1991**, *30*, 2144–2148.; (d) Dietrich-Buchecker, C.; Sauvage, J. P.; Kern, J. M.; *J. Am. Chem. Soc.* **1989**, *111*, 7791–7800.; (e) Dietrich-Buchecker, C. O.; Kern, J. M.; Sauvage, J. P.; *J. Chem. Soc. Chem. Commun.* **1985**, No. 12, 760–762.

[13] Powers, D. C.; Anderson, B. L.; Nocera, D. G.; *J. Am. Chem. Soc.* **2013**, *135*, 18876–18883.

[14] (a) Chang, M.-C.; Jesse, K. A.; Filatov, A. S.; Anderson, J. S. Reversible Homolytic Ativation of Water via Metal–Ligand Cooperativity in a T-Shaped Ni(II) Complex. *Chem. Sci.* **2019**.; (b) Chang, M.-C.; McNeece, A. J.; Hill, E. A.; Filatov, A. S.; Anderson, J. S.; *Chem. Eur. J.* **2018**, *24*, 8001–8008.; (c) McNeece, A. J.; Chang, M.-C.; Filatov, A. S.; Anderson, J. S.; *Inorg. Chem.* **2018**, *57*, 7044–7050.

[15] Shirasawa, N.; Nguyet, T. T.; Hikichi, S.; Moro-oka, Y.; *Organometallics* **2001**, *20*, 3582–3598.

[16] (a) R.; Cotton, F. A.; Dunbar, K. R.; Lu, T.; Murillo, C. A.; Wang, X.; *Inorg. Chem.* **2000**, *39*, 3065–3070.; (b) Suescun, L.; Mariezcurrena, R. A.; Mombru, A. W.; *Acta Cryst.* **1999**, *C55*, 2065–2068.

[17] Takaichi, J.; Morimoto, Y.; Ohkubo, K.; Shimokawa, C.; Hojo, T.; Mori, S.; Asahara, H.; Sugimoto, H.; Fujieda, N.; Nishiwaki, N.; Fukuzumi, S.; Itoh, S.; *Inorg. Chem.* **2014**, *53*, 6159–6169.

[18] (a)Tomson, N. C.; Williams, K. D.; Dai, X.; Sproules, S.; DeBeer, S.; Warren, T. H.; Wieghardt, K.; *Chem. Sci.* **2015**, *6*, 2474–2487.; (b) Chandrasekaran, P.; Chiang, K. P.; Nordlund, D.; Bergmann, E.; Holland, P. L.; DeBeer, S.; Debeer, S.; *Inorg. Chem.* **2013**, *52*, 6286–6298.

[19] Edwards, P. R.; Johnson, C. E.; Williams, R. J. P.; *J. Chem. Phys.* **1967**, *47*, 2074–2082.

[20] (a) Gamba, I.; Mutikainen, I.; Bouwman, E.; Reedijk, J.; Bonnet, S.; *Eur. J. Inorg. Chem.* **2013**, No. 1, 115–123.; (b) Li, J.; Zhang, K.; Huang, H.; Yu, A.; Hu, H.; Cui, H.; Cui, C.; *Organometallics* **2013**, *32*, 1630–1635.

---

[21] (a) Ravel, B., Newville, M., ATHENA, ARTEMIS, HEPHAESTUS: data analysis for X-ray absorption spectroscopy using IFEFFIT. *J. Synchr. Radn.*, **2005**, *12*, 537-541; (b) Newville, M., IFEFFIT: interactive EXAFS analysis and FEFF fitting. *J. Synchr. Radn.* **2001**, *8*, 322-324; (c) Rehr, J. J.; Albers, R. C. *Rev. Mod. Phys.* **2000**, *72*, 621-654.

[22] Bruker AXS, version 2015.5-2, **2015**.

[23] Bruker AXS, version 2014/5, Krause, Herbst-Irmer, Sheldrick & Stalke, *J. Appl. Cryst.* **2015**, *48*, 3-10.

[24] Version 2018/2: Sheldrick, G. M. *Acta Crystallogr*. **2015**, *A**71***, 3-8.

[25] Version 1.2.10; O. V. Dolomanov, L. J. Bourhis, R. J. Gildea, J. A. K. Howard and H. Puschmann. *J. Appl. Crystallogr.* **2009**, *42*, 339-34.

[26] Version 2018/3, *Sheldrick, G. M. Acta Crystallogr.* **2015**, *C71*, 3-8.

[27] Bruker. APEX3 (Version 2015.9-0), SAINT (Version 8.37A) and SADABS (Version 2016/2). Bruker AXS Inc., Madison, Wisconsin, USA, **2015**.

[28] G. Sheldrick, *Acta Cryst. A* **2008**, 64, 112-122.

[29] O. V. Dolomanov, L. J. Bourhis, R. J. Gildea, J. A. K. Howard, H. Puschmann, *J. Appl. Cryst.* **2009**, 42, 339-341.

[30] Fenn, T. D., Schnieders, M. J. & Brunger, A. T. *Acta Crystallogr.* **2010**, D66, 1024-1031.

[31] Neese, F. "The Orca Program System" *Wiley Interdisciplinary Reviews: Computational Molecular Science* **2012**, *2*, 73-78.; H - Kr: A. Schaefer, H. Horn and R. Ahlrichs, *J. Chem. Phys.* **1992**, *97*, 2571; Rb - Xe: A. Schaefer, C. Huber and R. Ahlrichs, *J. Chem. Phys.* **1994** *100*, 5829; F. Weigend, R. Ahlrichs, *Phys. Chem. Chem. Phys.* **2005**, 7, 3297.

Appendix 1: Supporting Data for Chapter 1

NMR Spectra

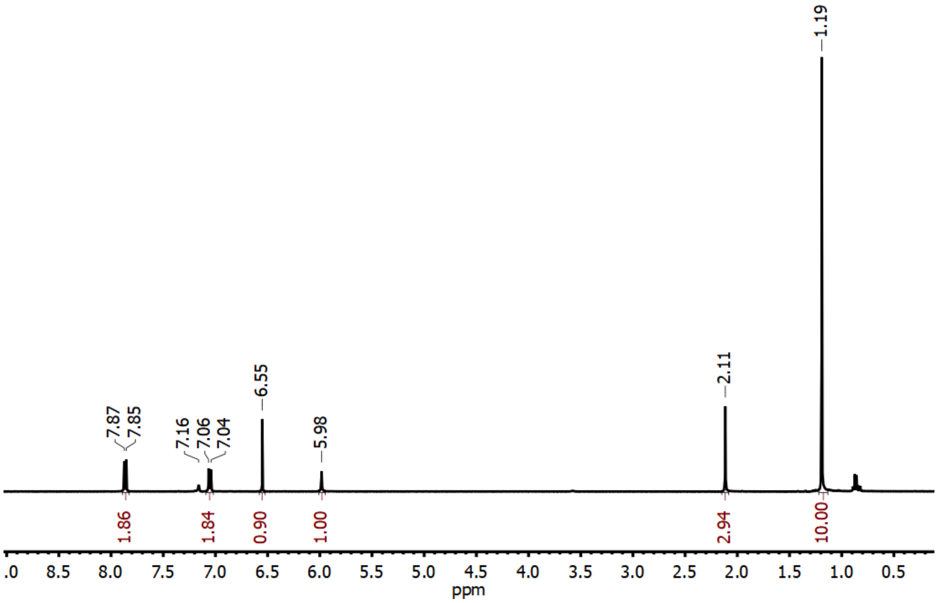

Figure 1A - 1. ^{1}H NMR of **1** in C_6D_6.

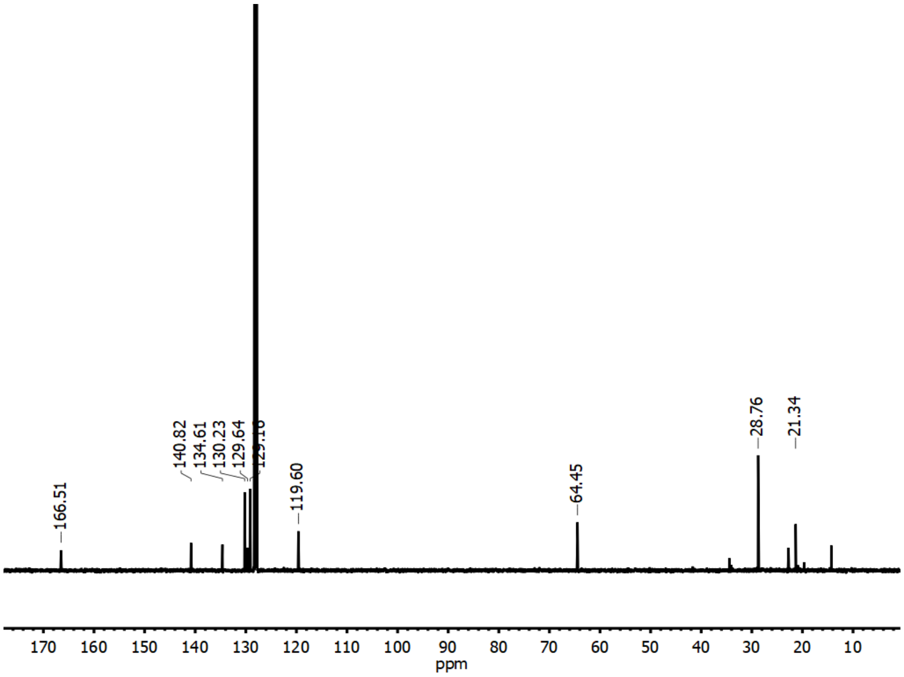

Figure 1A - 2. $^{13}C\{^1H\}$ NMR of **1** in C_6D_6.

Figure 1A - 3. ^{1}H NMR of **2** in C_6D_6.

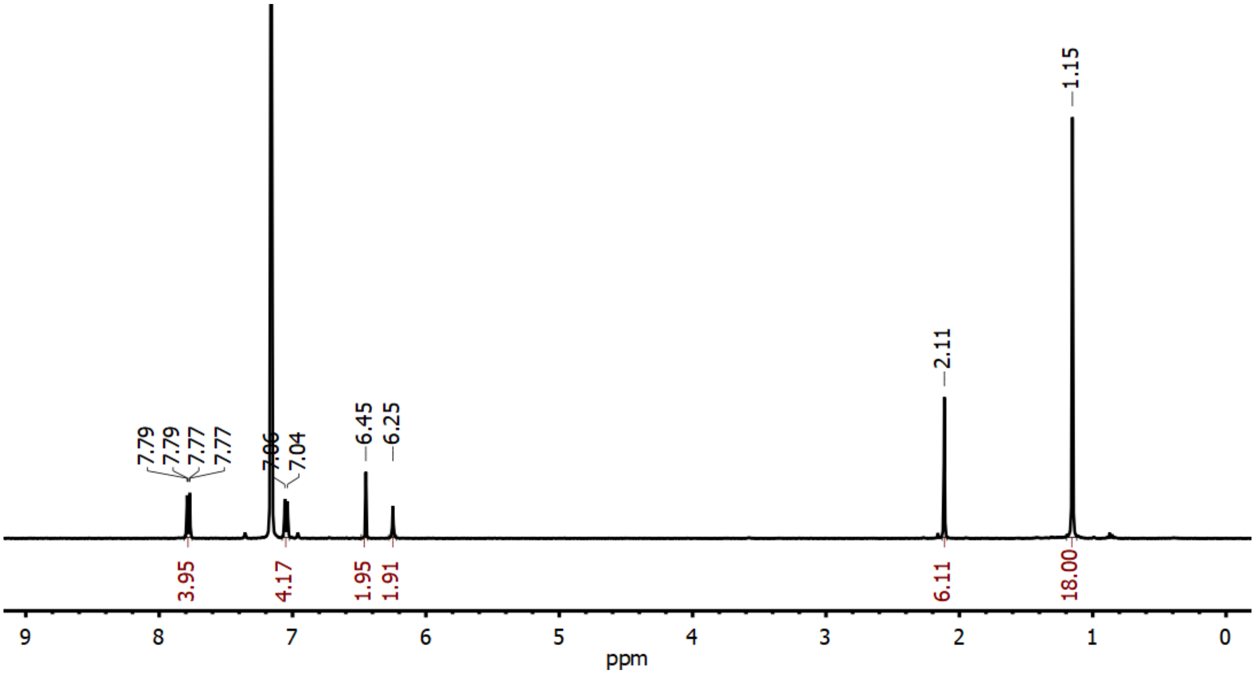

Figure 1A - 4. $^{19}F\{^{1}H\}$ NMR of **2** in C_6D_6.

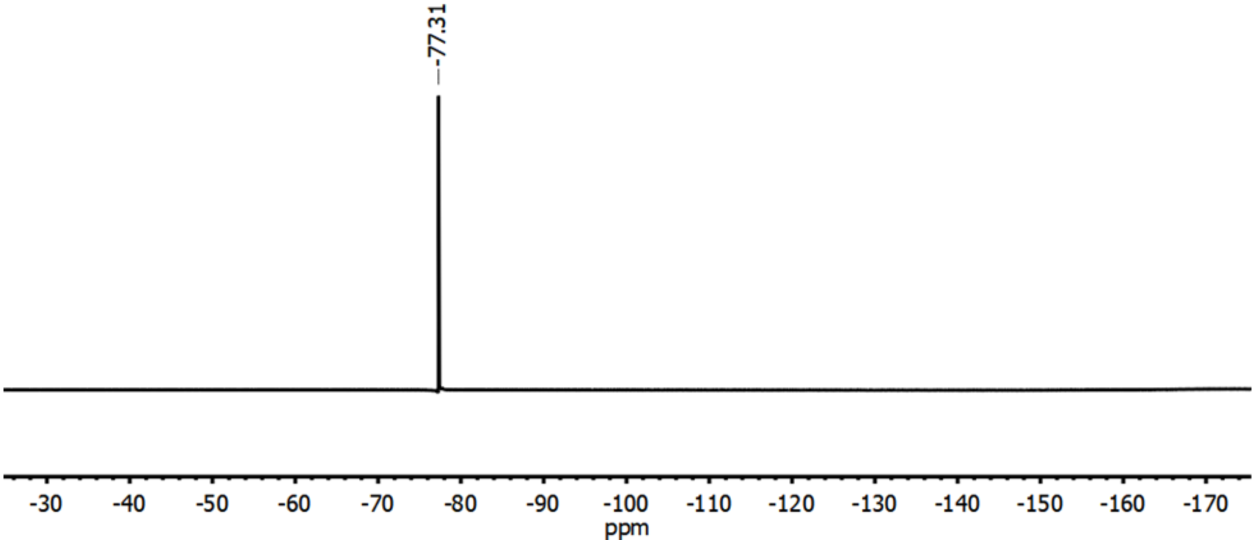

Figure 1A - 5. $^{13}C\{^1H\}$ NMR of **2** in C_6D_6.

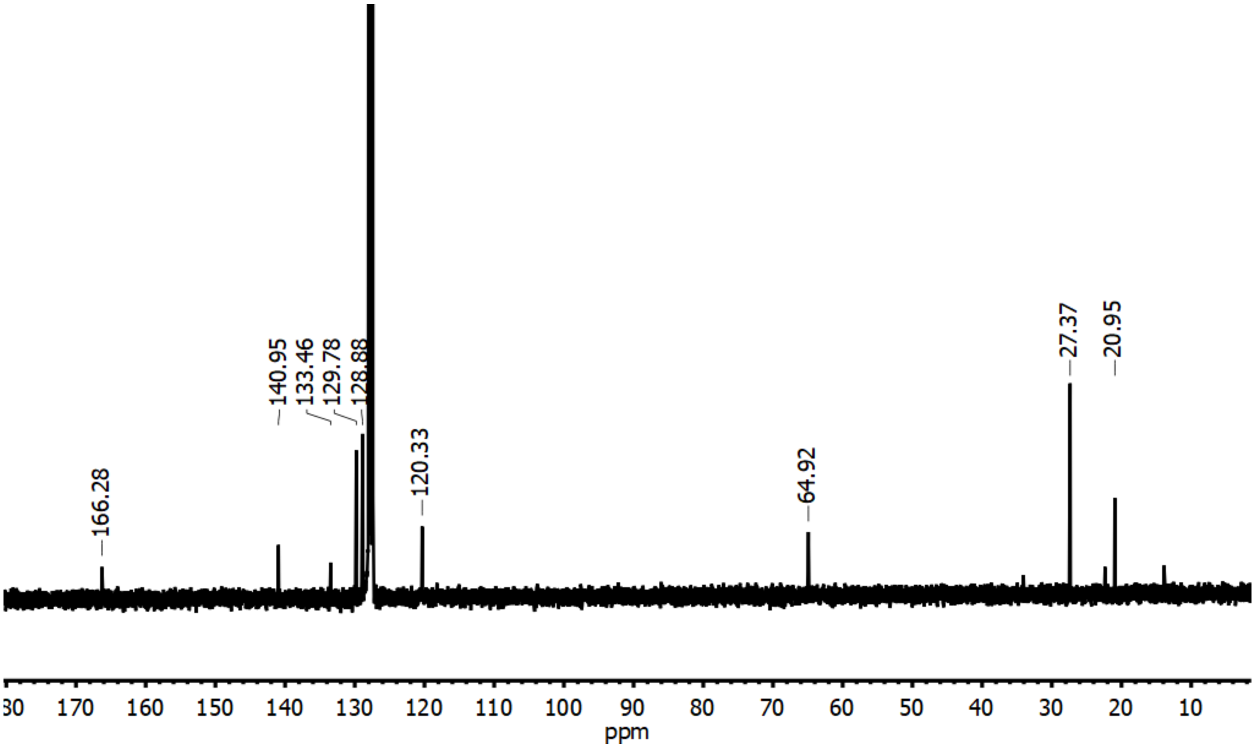

Figure 1A - 6. ^1H NMR in C_6D_6 of H_2 splitting by **3** to form **2**.

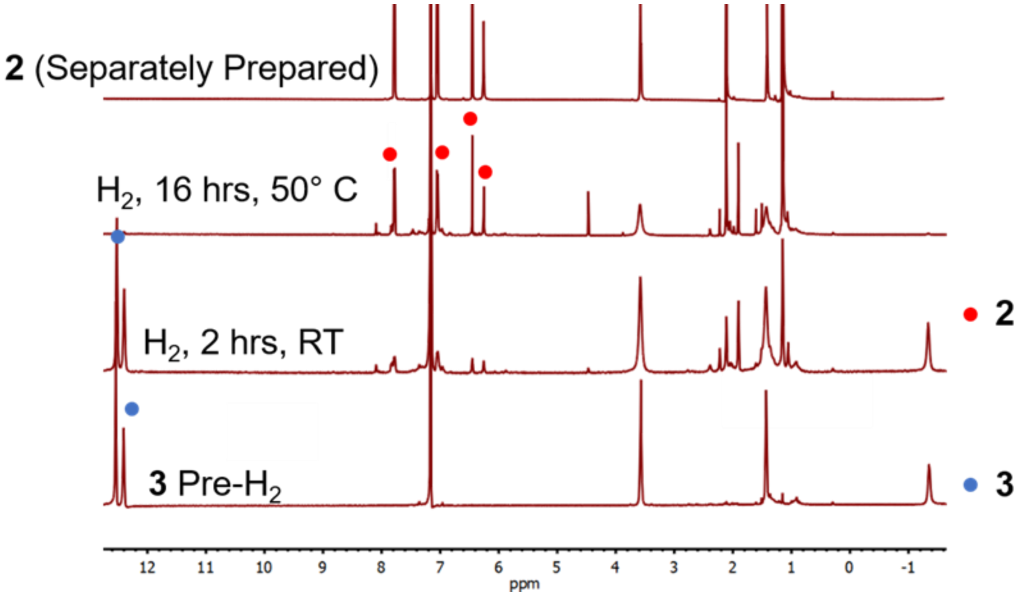

Figure 1A - 7. ^{1}H NMR in d_8-toluene of the transformation of **2** to form **3** in the presence of 13 eq benzoquinone (BQ).

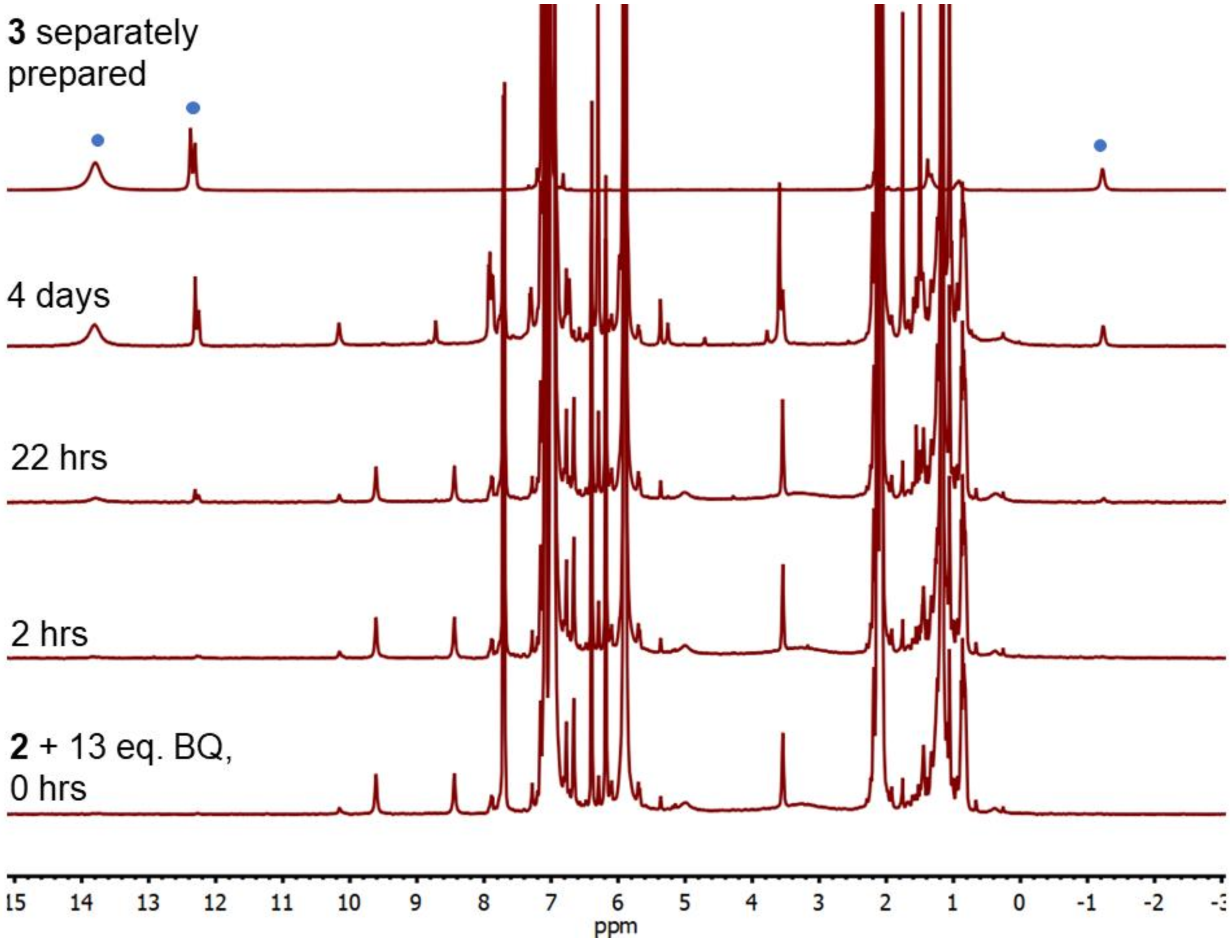

Figure 1A - 8. ^{9}F{^{1}H} NMR of **2** in THF (bottom) and in the presence of 10 eq LiOTf (top).

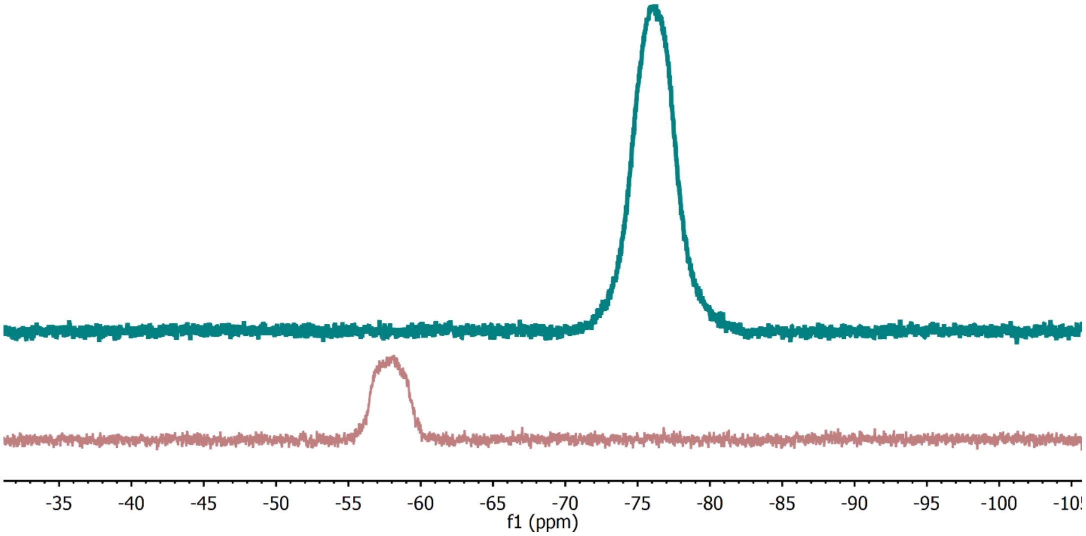

Figure 1A - 9**.** ^{1}H NMR of the reaction of **2** with H_2 and benzoquinone showing appearance of **2** and 2 equivalents of hydroquinone.

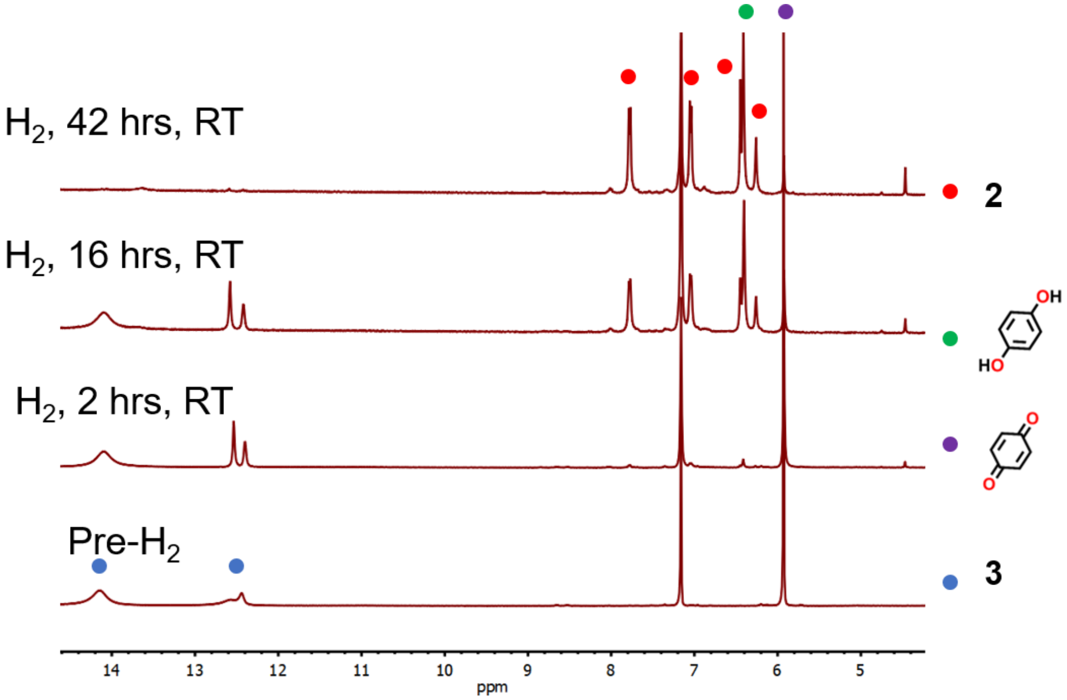

UV-vis Spectra

Figure 1A - 10. UV-vis of a 0.31 mM solution of **1** in THF

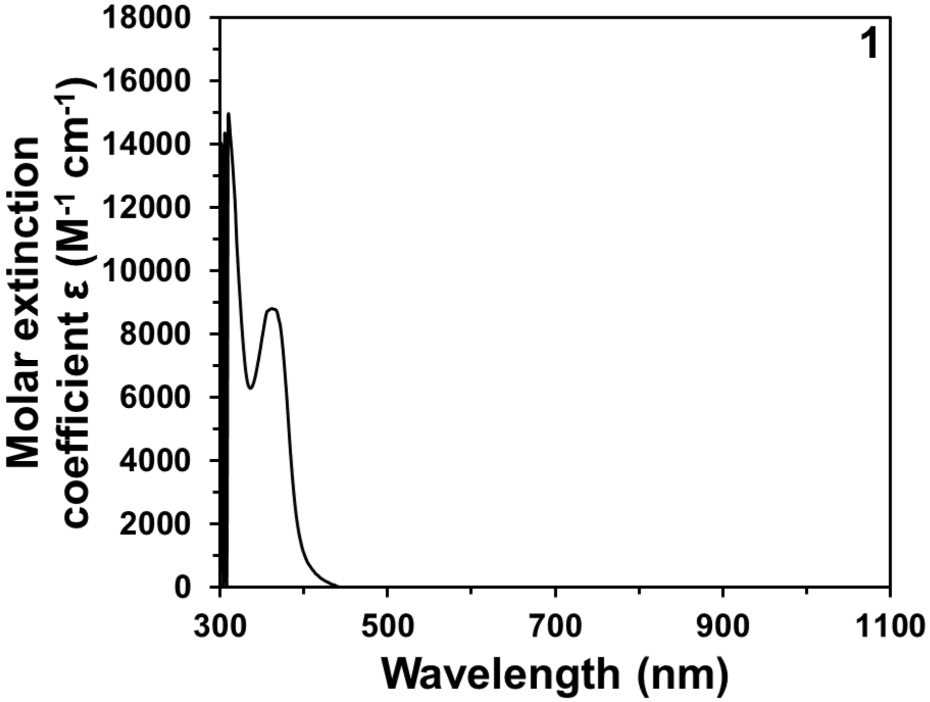

Figure 1A - 11. UV-vis of a 0.25 mM solution of **2** in THF.

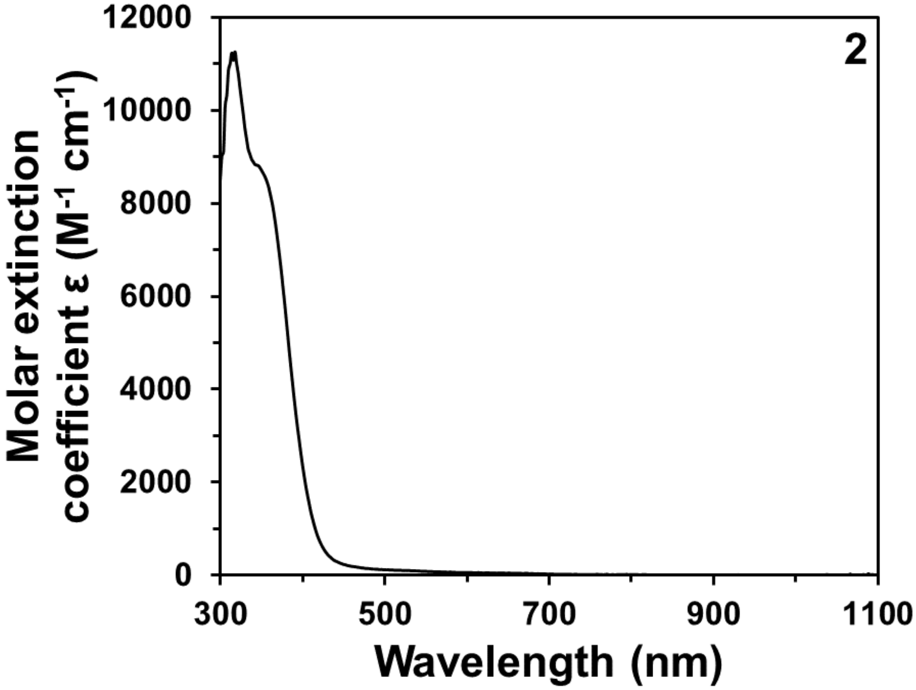

IR Spectra

Figure 1A - 12. IR (THF solution, CaF_2 windows) of **1**. The large features at ~3000 and 1100 cm^{-1} are from an imperfect solvent subtraction.

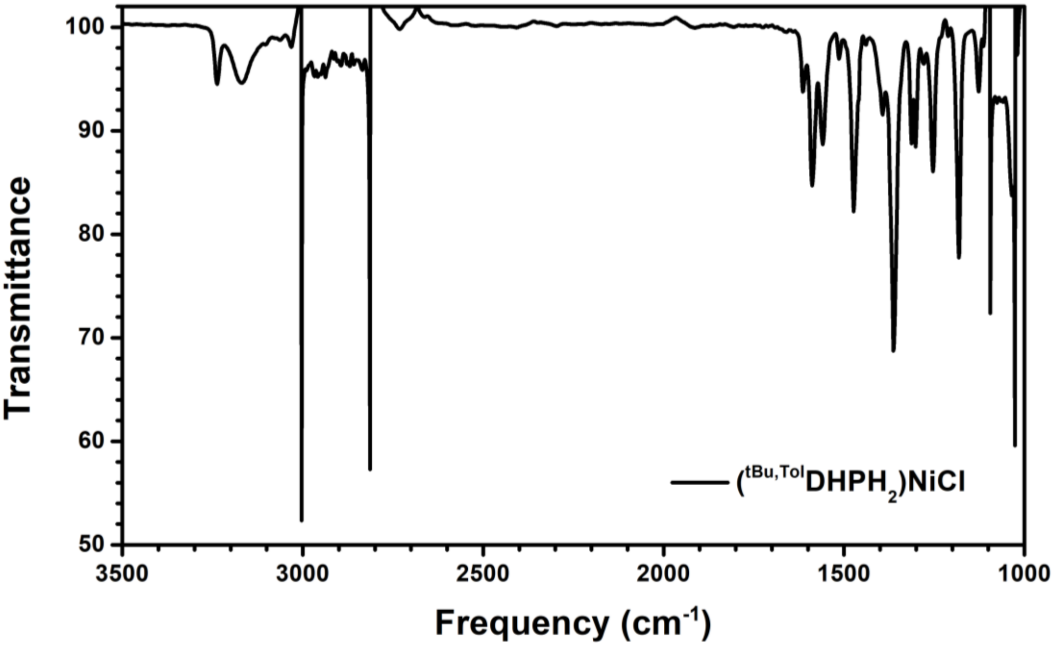

Figure 1A - 13. IR (THF solution, CaF_2 windows) of **2**.

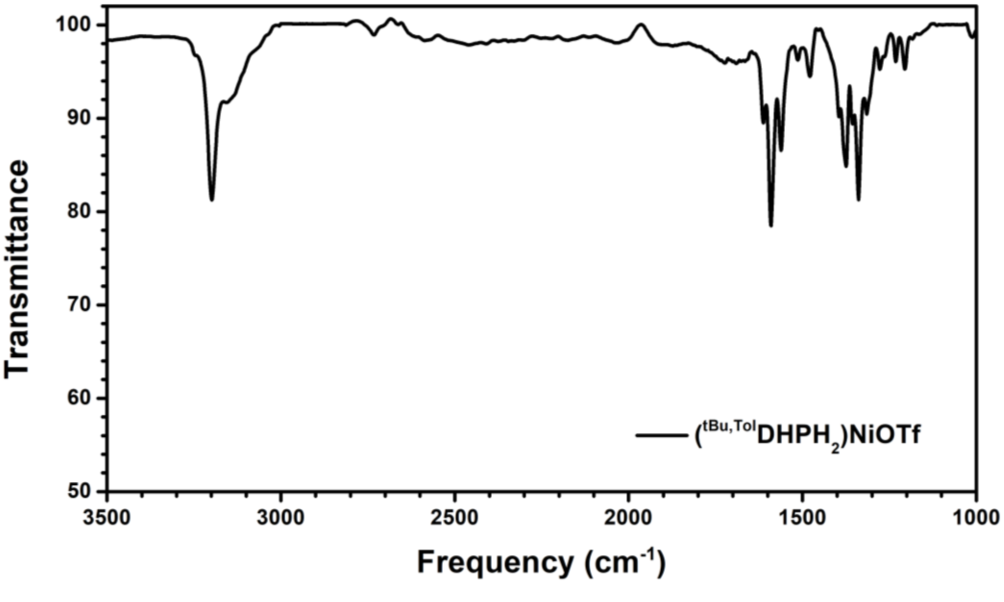

Kinetics Studies

Figure 1A - 14. (A) Determination of the mole fraction of H_2 at variable pressure at a given temperature. (B) Determination of the mole fraction per MPa and temperature.

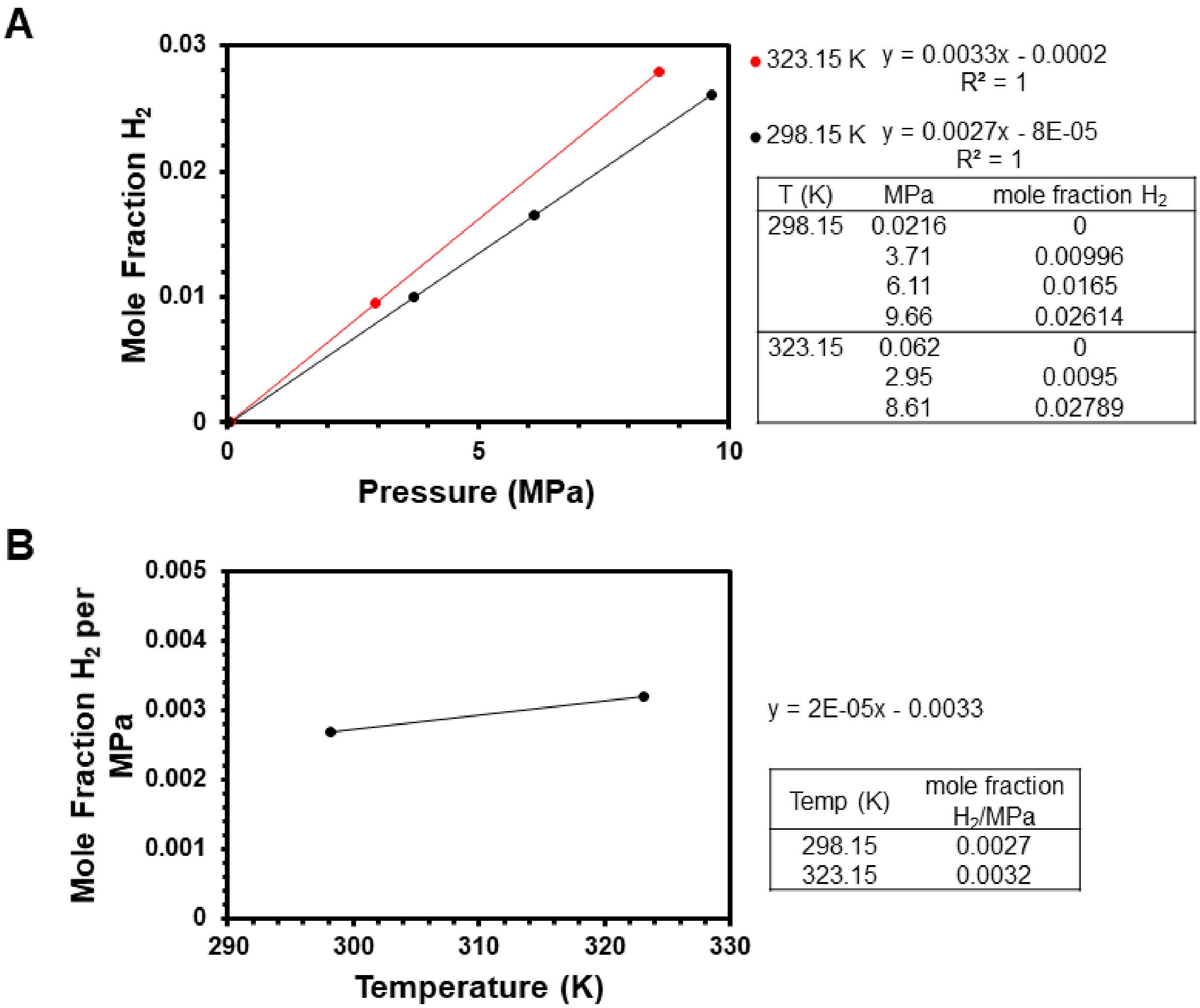

Table 1A - 1. Calculation of $[H_2]$ in UV-vis samples.

T (K)	mole fraction H_2/MPa	mole fraction H_2/atm	mole fraction H_2 (0.2 partial pressure)	moles THF (in 2 mL)	moles H_2	$[H_2]$ (M)
303	0.00276	0.000279657	5.59E-05	0.0246568	1.38E-06	0.00069
313	0.00296	0.000299922	6.00E-05		1.48E-06	0.00074
323	0.00316	0.000320187	6.40E-05		1.58E-06	0.00079
333	0.00336	0.000340452	6.81E-05		1.68E-06	0.00084

Table 1A - 2. Rates of reaction of **3** with H_2 at 650 nm.

Sample	[Ni] (mM)	Temp (K)	k_{obs} (s^{-1})	[H2] at 0.2 atm partial pressure	k ($M^{-1}s^{-1}$)	average k ($M^{-1}s^{-1}$)
60-1	0.4	333	0.0004793	0.000839502	0.570885934	0.628939385
60-2	0.2		0.000562		0.669449106	
60-3	0.2		0.0005427		0.646483115	
50-1	0.4	323	0.0002788	0.000789529	0.353152486	0.340871741
50-2	0.4		0.0002885		0.365364836	
50-3	0.4		0.0002401		0.3040979	
40-1	0.4	313	0.0001277	0.000739555	0.172691576	0.167812069
40-2	0.4		0.0001176		0.159042837	
40-3	0.4		0.000127		0.171701793	
30-1	0.2	303	4.57E-05	0.000689583	0.066205981	0.074499149
30-2	0.4		6.33E-05		0.091715757	
30-3	0.4		4.96E-05		0.071893044	
30-4	0.4		4.70E-05		0.068181814	

Table 1A - 3. Calculated data for the Eyring Analysis at 650 nm.

1/T (K^{-1})	average ln(k/T)	Standard Deviation
0.003003	−6.274167219	0.083714763
0.003096	−6.887515759	0.097647693
0.003195	−7.593751103	0.045965973
0.0033	−8.413692173	0.148299394

Table 1A - 4. Rates of **3** to **2** under pseudo first-order conditions at 50 °C.

Conditions	k_{obs} (s^{-1})
Benzene	0.00035061
THF, 50 eq LiOTf	0.000290449

Table 1A - 4 shows that no significant change in rate occurs in non-coordinating solvent or in the presence of excess triflate. Thus, triflate dissociation does not play a significant role in the H_2 association and splitting reaction observed.

Table 1A - 5. Raw data for kinetic studies at 650 nm at 60 °C.

60-1, 0.2 mM		60-2, 0.4 mM		60-3, 0.2 mM	
time (s)	absorbance	time (s)	absorbance	time (s)	Absorbance
0	1.890283195	0	3.570384856	0	1.832635219
1800	0.854176401	300	3.136487697	300	1.620444971
3600	0.35957588	600	2.759195736	600	1.399083991
5400	0.165227704	900	2.352544066	900	1.171749601
7200	0.093990015	1200	2.002209621	1200	0.970275385
9000	0.063683872	1500	1.688591921	1500	0.799313844
10800	0.053140115	1800	1.416001979	1800	0.651953986
12600	0.049813534	2100	1.186452367	2100	0.528372595
14400	0.049195837	2400	0.991261272	2400	0.424442436
16200	0.047926218	2700	0.829063138	2700	0.338263428
18000	0.047479822	3000	0.692275977	3000	0.268178025
19800	0.048096229	3300	0.577724536	3300	0.20931287
21600	0.047971323	3600	0.48255444	3600	0.16208952
23400	0.047984793	3900	0.404004137	3900	0.121984548
25200	0.047938539	4200	0.333918358	4200	0.092899858
27000	0.048805522	4500	0.279035844	4500	0.063892178
28800	0.048686157	4800	0.231211151	4800	0.041540117
30600	0.046955981	5100	0.192333457	5100	0.029283975
32400	0.046029091	5400	0.159673438	5400	0.006733981
34200	0.046629939	5700	0.132064186	5700	-0.005051218
36000	0.047033108	6000	0.113600984	6000	-0.015234615
37800	0.04603749	6300	0.089617688	6300	-0.023890332
39600	0.046488859	6600	0.073063581	6600	-0.030545321
		6900	0.062025061	6900	-0.036479596
		7200	0.049606076	7200	-0.039705178

Table 1A - 6. Raw data for kinetic studies at 650 nm at 50 °C.

50-1, 0.4 mM		50-2, 0.4 mM		50-3, 0.4 mM	
time (s)	absorbance	time (s)	absorbance	time (s)	Absorbance
0	4.008520458	0	3.977733347	0	XXX.XXX
600	3.385814201	600	3.522644038	600	3.821428501
1200	2.990883534	1200	2.96763303	1200	3.260752605
1800	2.566842292	1800	2.54012253	1800	2.844134553
2400	2.206073521	2400	2.150226372	2400	2.497876592
3000	1.878159566	3000	1.819146901	3000	2.181618155
3600	1.596820922	3600	1.533352766	3600	1.89146839
4200	1.35760805	4200	1.285371519	4200	1.633021059
4800	1.16778466	4800	1.07884437	4800	1.399530712
5400	1.012741187	5400	0.903982607	5400	1.193846489
6000	0.885591141	6000	0.757269686	6000	1.017217501
6600	0.763098019	6600	0.63464645	6600	0.862676371
7200	0.658425248	7200	0.532661024	7200	0.732801049
7800	0.5857333	7800	0.447448177	7800	0.623136744
8400	0.509079025	8400	0.37874074	8400	0.530511221
9000	0.453117413	9000	0.320568194	9000	0.453227332
9600	0.408541065	9600	0.272603577	9600	0.390945466
10200	0.360368057	10200	0.2345189	10200	0.337873759
10800	0.322829661	10800	0.202502109	10800	0.292830801
11400	0.293687	11400	0.176945582	11400	0.257984091
12000	0.26568	12000	0.156766195	12000	0.228254934
12600	0.242049354	12600	0.141815644	12600	0.203863654
13200	0.223385211	13200	0.126016532	13200	0.185494188
13800	0.209577671	13800	0.11643304	13800	0.169578277
14400	0.195279779	14400	0.108135145	14400	0.15719953

Table 1A - 7. Raw data for kinetic studies at 650 nm at 40 °C.

40-1, 0.4 mM		40-2, 0.4 mM		40-3, 0.4 mM	
time (s)	absorbance	time (s)	absorbance	time (s)	Absorbance
0	4.392795508	0	3.933200333	0	3.481915845
600	3.65695004	900	4.163802073	900	2.969607959
1200	3.346371695	1800	3.425020986	1800	2.689605514
1800	3.112726848	2700	3.145668641	2700	2.46146734
2400	2.927998613	3600	2.848209411	3600	2.252023224
3000	2.715295711	4500	2.541259214	4500	2.077044406
3600	2.513855645	5400	2.26882784	5400	1.922379095
4200	2.345193263	6300	2.026873084	6300	1.788993321
4800	2.166494931	7200	1.803169996	7200	1.67167419
5400	2.002556683	8100	1.602821126	8100	1.561031519
6000	1.846734789	9000	1.420456288	9000	1.472844616
6600	1.703140495	9900	1.256309392	9900	1.395500597
7200	1.566636842	10800	1.108332755	10800	1.322488141
7800	1.441505477	11700	0.97759465	11700	1.255843888
8400	1.322050597	12600	0.860115085	12600	1.198266029
9000	1.213868125	13500	0.757161938	13500	1.144215202
9600	1.113677274	14400	0.66688717	14400	1.094239457
10200	1.025673636	15300	0.587287521	15300	1.050259082
10800	0.942061645	16200	0.518159929	16200	1.009190912
11400	0.866776546	17100	0.45734472	17100	0.969797284
12000	0.796556375	18000	0.404665635	18000	0.936218128
12600	0.735007097	18900	0.357890801	18900	0.90395764
13200	0.67488927	19800	0.318243351	19800	0.872167771
13800	0.622193688	20700	0.28415098	20700	0.841748009
14400	0.572568278	21600	0.25340203	21600	0.815197211
15000	0.528170468				
15600	0.487197658				
16200	0.449958078				
16800	0.414333458				
17400	0.384476375				
18000	0.355717056				
18600	0.330194749				
19200	0.306347093				
19800	0.284503808				
20400	0.265042285				
21000	0.245580391				
21600	0.231392008				
22200	0.215755274				

Table 1A - 8. Raw data for kinetic studies at 650 nm at 30 °C.

30-1, 0.2 mM		30-2, 0.4 mM		30-3, 0.4 mM		30-4, 0.4 mM	
time (s)	absorbance	time (s)	absorbance	time (s)	Absorbance	time (s)	absorbance
0	2.194978723	0	5.732766758	0	5.210163346	0	XXX.XXX
1800	2.035520154	1800	4.190530172	1800	4.112193101	3600	XXX.XXX
3600	1.878928855	3600	4.559967371	3600	3.84332777	7200	3.657142625
5400	1.722835163	5400	3.885274666	5400	3.357662994	10800	2.999521464
7200	1.583581452	7200	3.341032134	7200	3.112714935	14400	2.550484801
9000	1.455933701	9000	2.986444374	9000	2.873172733	18000	2.185895985
10800	1.339635038	10800	2.73211702	10800	2.628095644	21600	1.872093196
12600	1.235433361	12600	2.518407118	12600	2.389502075	25200	1.601460762
14400	1.138126435	14400	2.294030042	14400	2.186333871	28800	1.339885623
16200	1.029800232	16200	2.087604205	16200	1.98953023	32400	1.1059832
18000	0.955531271	18000	1.895394113	18000	1.814140409	36000	0.902342431
19800	0.881349719	19800	1.72596645	19800	1.651720997	39600	0.735387251
21600	0.808513967	21600	1.570130941	21600	1.504924262	43200	0.569649785
23400	0.745006601	23400	1.412090808	23400	1.369276824	46800	0.455533063
25200	0.685163718	25200	1.273856065	25200	1.245337841	50400	0.363926982
27000	0.633188444	27000	1.148043778	27000	1.132833842	54000	0.284568404
28800	0.585816374	28800	1.041253072	28800	1.030156849	57600	0.234786188
30600	0.539630049	30600	0.944358089	30600	0.935867496	61200	0.200872981
32400	0.496986538	32400	0.856449349	32400	0.851094029	64800	0.169077985
34200	0.456434748	34200	0.758919894	34200	0.771148491	68400	0.152240146
36000	0.420932602	36000	0.690711792	36000	0.699981978	72000	0.137240421
37800	0.380948623	37800	0.619243528	37800	0.632956063	75600	0.130512776
39600	0.345459885	39600	0.563841097	39600	0.573046668	79200	0.123308909
41400	0.312201655	41400	0.512972713	41400	0.516603241	82800	0.118942723
43200	0.28452183	43200	0.469458667	43200	0.465519207		

Table 1A - 9. Reaction rates used to calculate KIE at 650 nm.

Sample	Concentration (mM)	rate (s^{-1})	Average rate (s^{-1})	Standard Deviation
50-D2-1	0.4	−0.000320895	−0.000329324	1.06104E−05
50-D2-2	0.2	−0.000325839		
50-D2-3	0.2	−0.000341239		
50-1	0.4	−0.000278824	−0.000269128	2.56022E−05
50-2	0.4	−0.000288466		
50-3	0.4	−0.000240094		

Table 1A - 10. Raw data for kinetic studies with D_2 at 650 nm.

50-D2-1		50-D2-2		50-D2-3	
time (s)	abs	time (s)	abs	time (s)	abs
0	3.907567	0	2.289456	0	0.629055
3600	1.456463	1800	1.248725	1800	0.869496
7200	0.494954	3600	0.608157	3600	0.796192
10800	0.131833	5400	0.286295	5400	0.645058
14400	0.012704	7200	0.124566	7200	0.496543
18000	−0.015046	9000	0.040619	9000	0.375564
21600	−0.027081	10800	−0.013676	10800	0.294881
25200	−0.032393	12600	−0.050722	12600	0.22183
28800	−0.035543	14400	−0.074521	14400	0.175633
32400	−0.036263	16200	−0.089433	16200	0.14742
36000	−0.037009	18000	−0.098289	18000	0.128091
39600	−0.037608	19800	−0.103808	19800	0.111909
43200	−0.038501	21600	−0.107162	21600	0.102503
46800	−0.037347	23400	−0.109999	23400	0.09368
		25200	−0.11113	25200	0.088158
		27000	−0.111644	27000	0.089144
		28800	−0.113592	28800	0.088502
		30600	−0.112553	30600	0.085427
		32400	−0.113556	32400	0.083101
		34200	−0.113836	34200	0.083009
		36000	−0.113611	36000	0.084996
		37800	−0.114223	37800	0.086547
		39600	−0.113619	39600	0.085229
		41400	−0.114231		
		43200	−0.113527		

Density Functional Theory (DFT) Calculations

Figure 1A - 15. Calculated structure of **2**$^{+}$.

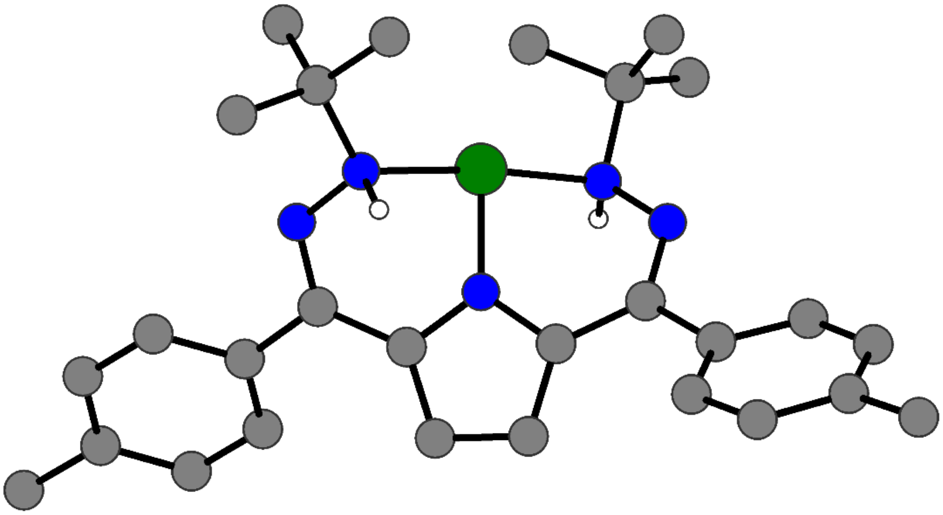

Table 1A - 11. Coordinates of calculated structure of **2**$^{+}$.

N	−1.4404	−0.1138	−0.4046
C	−2.5281	−0.934	−0.3909
C	−2.0656	−2.2576	−0.313
C	−0.6735	−2.2067	−0.2622
C	−0.3029	−0.8541	−0.3397
H	0.0072	−3.0439	−0.2149
H	−2.685	−3.1401	−0.2592
Ni	−1.5164	1.6797	−0.6611
C	1.0007	−0.2097	−0.3863
N	1.2137	0.956	−0.9239
N	0.1268	1.5484	−1.5974
C	0.3614	2.9926	−1.9612
C	1.1235	3.684	−0.8403
H	0.6501	3.5168	0.1318
H	1.1473	4.7592	−1.0321
H	2.1456	3.3147	−0.7759
C	−1.0723	3.5299	−2.0457
H	−1.6147	3.4667	−1.0577
H	−1.6661	3.0546	−2.8309
H	−1.0947	4.6094	−2.2176
C	1.0868	3.1104	−3.2907
H	2.0718	2.6435	−3.2281

Table 1A - 11. Coordinates of calculated structure of **2**$^+$ continued.

H	1.2264	4.1616	−3.554
H	0.5247	2.6332	−4.0997
N	−3.0996	1.6068	0.4762
N	−4.1372	0.861	−0.1285
C	−3.8657	−0.3649	−0.4603
C	−5.0164	−1.1358	−0.9623
C	2.1665	−0.7985	0.2927
C	−6.2958	−0.7993	−0.5129
C	−7.4135	−1.4266	−1.0288
C	−7.3014	−2.4134	−2.0082
C	−6.0211	−2.7579	−2.4464
C	−4.8938	−2.1354	−1.9322
H	−6.4038	−0.0335	0.2453
H	−8.3964	−1.1462	−0.6636
H	−5.9052	−3.5187	−3.2125
H	−3.9157	−2.4043	−2.3157
C	−8.5209	−3.0714	−2.5771
H	−9.4302	−2.7257	−2.0737
H	−8.4659	−4.1634	−2.4741
H	−8.6187	−2.8416	−3.6482
C	3.4576	−0.4334	−0.1013
C	4.556	−0.8064	0.6501
C	4.4092	−1.5479	1.824
C	3.1239	−1.9524	2.1861
C	2.0171	−1.5893	1.4367
H	3.5872	0.1689	−0.9923
H	5.5483	−0.5009	0.333
H	1.028	−1.8732	1.7773
H	2.9843	−2.5336	3.0922
C	−3.6618	2.8358	1.1623
C	−2.4878	3.547	1.826
H	−1.9708	2.8986	2.5411
H	−2.8522	4.4165	2.3758
H	−1.7572	3.9085	1.0953
C	−4.3524	3.7284	0.1451
H	−3.6509	4.1508	−0.5797
H	−4.8273	4.5647	0.6621
H	−5.1192	3.174	−0.3971
C	−4.6489	2.3649	2.2283
H	−4.1631	1.695	2.9467
H	−5.4901	1.8386	1.7763
H	−5.0347	3.2233	2.7824
C	5.5924	−1.8886	2.6763

Table 1A - 11. Coordinates of calculated structure of **2**$^{+}$ continued.

H	6.4541	−1.2562	2.4411
H	5.8959	−2.9336	2.5248
H	5.3556	−1.7629	3.7393
H	−2.696	1.0396	1.2313
H	−0.0708	1.0173	−2.4519

Figure 1A - 16. Calculated structure of **3**$^{+}$.

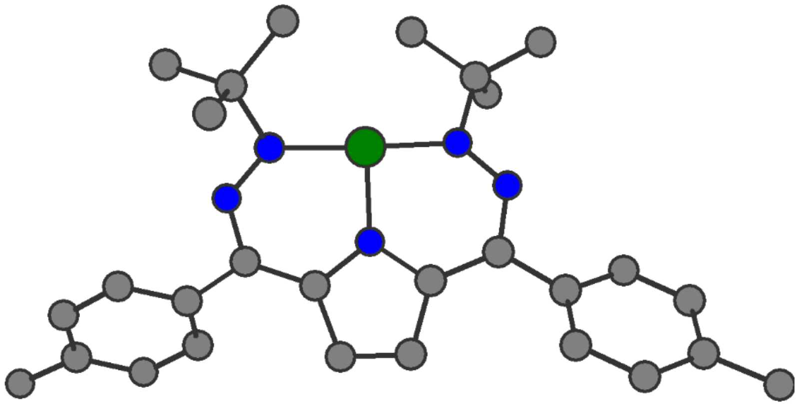

Table 1A - 12. Coordinates of calculated structure of **3**$^{+}$.

N	−1.80341	0.1806	−0.14201
C	−2.84915	−0.66817	−0.21687
C	−2.35948	−2.02091	−0.23045
C	−0.99881	−1.94566	−0.17401
C	−0.66037	−0.54644	−0.12135
Ni	−1.92218	2.08054	−0.06365
C	0.60256	0.08883	−0.12574
N	0.78205	1.36594	−0.55234
N	−0.10186	2.26254	−0.58412
C	0.35722	3.46843	−1.36182
C	1.61931	4.04055	−0.72062
H	1.45176	4.28974	0.33027
H	1.90598	4.95458	−1.24542
H	2.44558	3.33135	−0.78466
C	−0.77645	4.47968	−1.30951
H	−0.86138	4.93455	−0.31968
H	−1.73283	4.00727	−1.57259
H	−0.60977	5.28024	−2.03307
C	0.62714	3.02999	−2.80209

Table 1A -12. Coordinates of calculated structure of **3**$^+$ continued.

H	1.39716	2.25626	−2.83309
H	0.97621	3.88439	−3.38602
H	−0.27758	2.63532	−3.2734
N	−3.7423	1.99763	0.47226
N	−4.51598	1.01778	0.30776
C	−4.17907	−0.17505	−0.24177
C	−5.31433	−0.89136	−0.79348
C	1.85814	−0.57103	0.20156
C	−6.61917	−0.54204	−0.39934
C	−7.71779	−1.08682	−1.0282
C	−7.57404	−1.99695	−2.07853
C	−6.27676	−2.37442	−2.44781
C	−5.1683	−1.83752	−1.82388
H	−6.75113	0.16228	0.41131
H	−8.7128	−0.79637	−0.707
H	−6.13929	−3.07717	−3.26357
H	−4.17846	−2.09952	−2.18022
C	−8.76735	−2.53735	−2.79711
H	−9.68726	−2.05975	−2.45978
H	−8.86549	−3.61643	−2.63608
H	−8.67522	−2.37687	−3.87614
C	3.05438	−0.10676	−0.374
C	4.26875	−0.64721	−0.01197
C	4.35456	−1.65983	0.94507
C	3.1634	−2.13179	1.51364
C	1.93929	−1.60465	1.15077
H	3.00931	0.67372	−1.12123
H	5.17699	−0.2764	−0.4752
H	1.03983	−1.95251	1.64631
H	3.20487	−2.90931	2.27026
C	−4.3528	3.0611	1.34636
C	−3.3447	4.19643	1.43091
H	−2.37418	3.84181	1.79957
H	−3.69327	4.96107	2.12772
H	−3.20783	4.67349	0.45722
C	−5.65166	3.55042	0.70694
H	−5.47793	3.93222	−0.30256
H	−6.06785	4.36113	1.30869
H	−6.38622	2.74621	0.65356
C	−4.62332	2.45992	2.72665
H	−3.70548	2.07958	3.18336
H	−5.34089	1.6401	2.65763
H	−5.0409	3.22819	3.38095
C	5.68536	−2.20342	1.35574
H	6.4955	−1.7242	0.80618

Table 1A - 12. Coordinates of calculated structure of **3**$^+$ continued.

H	5.74399	−3.28225	1.17887
H	5.85789	−2.03841	2.42471
H	−2.96227	−2.91549	−0.26949
H	−0.30136	−2.76934	−0.17545

Figure 1A - 17. Calculated structure of an H_2 adduct of **3**$^+$.

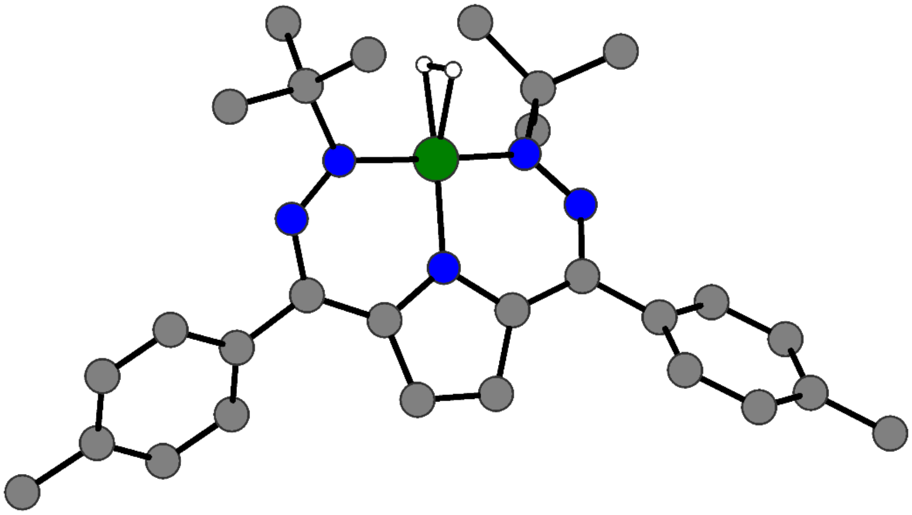

Table 1A - 13. Coordinates of structure of an H_2 adduct of **3**$^+$.

N	−1.8048	0.3158	−0.0838
C	−2.8639	−0.5113	−0.2966
C	−2.3862	−1.8695	−0.3389
C	−1.0431	−1.8281	−0.164
C	−0.6712	−0.4424	−0.0191
Ni	−1.8689	2.1248	0.1694
C	0.6085	0.1096	0.0222
N	0.8124	1.4004	−0.3053
N	−0.0704	2.2973	−0.3824
C	0.5273	3.5415	−1.0578
C	1.7615	3.9852	−0.2762
H	1.5017	4.2638	0.7491
H	2.1984	4.8614	−0.7605
H	2.5114	3.1955	−0.244
C	−0.4567	4.6987	−1.1462
H	−0.6429	5.1748	−0.1806
H	−1.4048	4.4108	−1.6124
H	−0.0159	5.4672	−1.7852
C	0.8985	3.1096	−2.4803
H	1.626	2.297	−2.4643
H	1.3386	3.9556	−3.0125

Table 1A - 13. Coordinates of structure of an H_2 adduct of $\mathbf{3}^+$ continued.

H	0.016	2.7749	−3.0329
N	−3.7251	2.0626	0.5161
N	−4.5146	1.1637	0.1174
C	−4.175	−0.0422	−0.3802
C	−5.2921	−0.8053	−0.9444
C	1.8347	−0.6633	0.2505
C	−6.605	−0.561	−0.5156
C	−7.673	−1.2143	−1.0975
C	−7.4854	−2.1429	−2.127
C	−6.1795	−2.3893	−2.5475
C	−5.1014	−1.7322	−1.975
H	−6.7772	0.1502	0.2827
H	−8.6778	−1.0021	−0.7446
H	−6.0055	−3.0903	−3.3574
H	−4.1078	−1.9061	−2.3733
C	−8.6507	−2.8285	−2.7713
H	−9.2981	−2.1053	−3.2778
H	−9.2654	−3.3459	−2.0289
H	−8.3248	−3.5609	−3.5112
C	3.0238	−0.2935	−0.3891
C	4.1949	−0.9912	−0.1661
C	4.2343	−2.0854	0.7002
C	3.0502	−2.4444	1.3484
C	1.8719	−1.7483	1.1342
H	3.0206	0.5475	−1.0712
H	5.1019	−0.6805	−0.6751
H	0.9834	−2.0261	1.6914
H	3.0557	−3.2732	2.0496
C	−4.4661	3.206	1.2127
C	−4.4338	4.4524	0.3251
H	−3.4355	4.8651	0.1621
H	−5.0227	5.2398	0.8021
H	−4.8806	4.2395	−0.6487
C	−5.9296	2.8309	1.4392
H	−6.4603	2.6807	0.5
H	−6.4073	3.6502	1.9806
H	−6.0266	1.9253	2.0409
C	−3.8187	3.444	2.5783
H	−2.8026	3.8433	2.5329
H	−3.798	2.5216	3.1627
H	−4.4148	4.1757	3.1278
C	5.5054	−2.8476	0.9183
H	6.3754	−2.2546	0.6304

Table 1A - 13. Coordinates of structure of an H_2 adduct of **3**$^+$ continued.

H	5.5163	−3.761	0.3149
H	5.6206	−3.1504	1.9617
H	−3.0087	−2.7418	−0.4621
H	−0.353	−2.6572	−0.1643
H	−1.9702	3.7144	0.2792
H	−1.7254	3.4777	0.9746

Figure 1A - 18. Calculated structure of transition state 1.

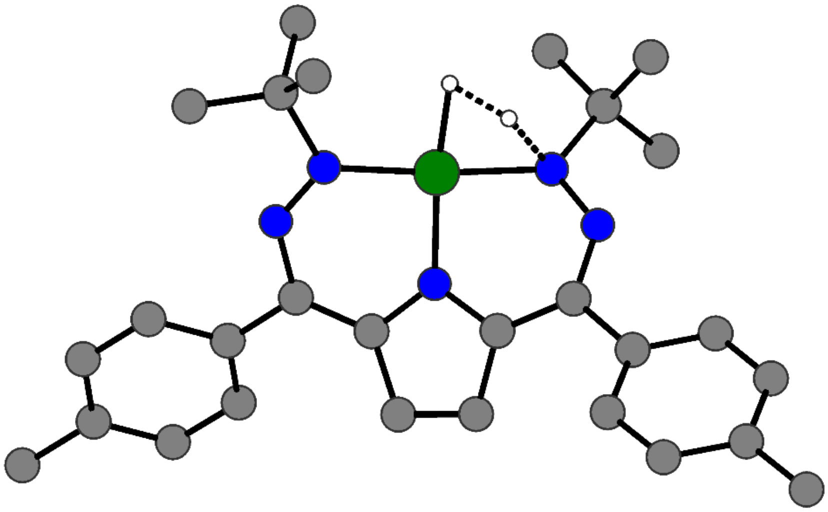

Table 1A - 14. Coordinates of calculated transition state 1.

N	−1.8051	0.3255	−0.2155
C	−2.9133	−0.4102	−0.3617
C	−2.5516	−1.8077	−0.3125
C	−1.2012	−1.8663	−0.1687
C	−0.7265	−0.5047	−0.113
Ni	−1.8071	2.1638	−0.0887
C	0.561	0.0165	−0.0952
N	0.8309	1.3172	−0.4568
N	0	2.2471	−0.5698
C	0.6231	3.5206	−1.1194
C	0.5779	4.5787	−0.0169
H	−0.4407	4.8081	0.298
H	1.03	5.4988	−0.3933
H	1.1469	4.2535	0.8573
C	−0.1939	3.9378	−2.341
H	−1.2343	4.1569	−2.0951

Table 1A - 14. Coordinates of calculated transition state 1 continued.

H	−0.1681	3.163	−3.1114
H	0.245	4.845	−2.7622
C	2.0717	3.2952	−1.5352
H	2.7042	3.027	−0.6885
H	2.447	4.2274	−1.9628
H	2.1601	2.5168	−2.2959
N	−3.6294	2.2193	0.4839
N	−4.52	1.3618	−0.0036
C	−4.2209	0.1726	−0.4763
C	−5.3474	−0.5906	−1.0434
C	1.7656	−0.7561	0.1749
C	−6.6606	−0.3239	−0.6367
C	−7.7262	−0.9859	−1.2139
C	−7.5328	−1.9395	−2.2203
C	−6.2263	−2.1989	−2.6253
C	−5.1496	−1.5373	−2.051
H	−6.8359	0.4153	0.1354
H	−8.7335	−0.7607	−0.8768
H	−6.0472	−2.9199	−3.4163
H	−4.1511	−1.7351	−2.4262
C	−8.6946	−2.6437	−2.852
H	−9.3479	−1.9346	−3.3703
H	−9.3044	−3.1534	−2.1002
H	−8.3638	−3.3868	−3.5791
C	2.9848	−0.3784	−0.4107
C	4.1369	−1.0978	−0.1691
C	4.1328	−2.2162	0.6677
C	2.9223	−2.5783	1.27
C	1.7616	−1.8672	1.0339
H	3.0124	0.4785	−1.0705
H	5.064	−0.7869	−0.6397
H	0.854	−2.1433	1.5586
H	2.8987	−3.4221	1.9524
C	−4.2897	3.192	1.4605
C	−5.2445	4.1026	0.6953
H	−4.7048	4.7263	−0.0258
H	−5.7576	4.7724	1.3901
H	−5.993	3.5161	0.16
C	−5.042	2.3636	2.4975
H	−5.8217	1.7589	2.0358
H	−5.512	3.0431	3.2129
H	−4.3626	1.7058	3.0466
C	−3.2161	4.0039	2.17
H	−2.7212	4.7222	1.5141

Table 1A - 14. Coordinates of calculated transition state 1 continued.

H	−2.4619	3.3565	2.6253
H	−3.697	4.5757	2.9671
C	5.3835	−2.9999	0.9095
H	6.269	−2.4364	0.6114
H	5.3712	−3.9285	0.3292
H	5.4851	−3.2817	1.9604
H	−3.2425	−2.6338	−0.3782
H	−0.5872	−2.7525	−0.1376
H	−3.06	3.1153	−0.2687
H	−2.0446	3.659	−0.2176

Figure 1A - 19. Calculated structure of a Ni-hydride intermediate.

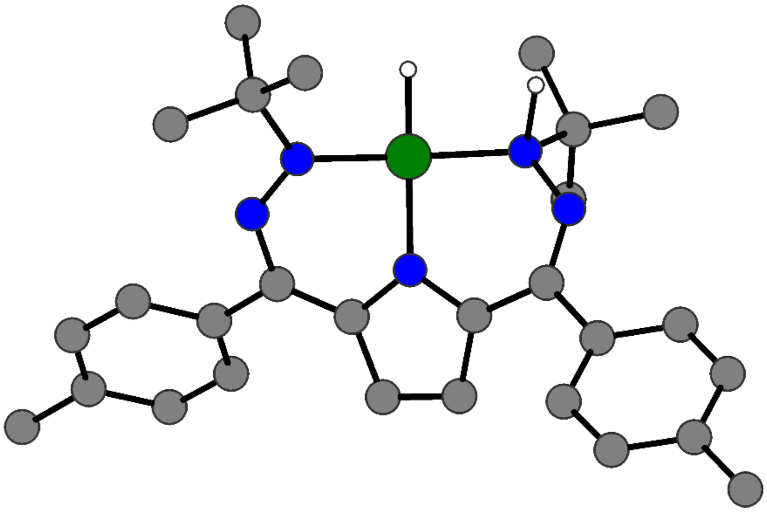

Table 1A - 15. Coordinates of a calculated Ni-hydride intermediate.

N	−1.8922	0.5242	−0.3582
C	−3.0242	−0.1569	−0.3457
C	−2.7644	−1.5481	−0.0935
C	−1.4143	−1.6732	0.0509
C	−0.8623	−0.356	−0.1054
Ni	−1.7267	2.393	−0.1541
C	0.4457	0.1011	−0.0962
N	0.7687	1.3082	−0.6941
N	0.0169	2.2922	−0.7847
C	0.6074	3.4072	−1.6224
C	1.0863	4.483	−0.6461
H	0.2635	4.8697	−0.0443

Table 1A - 15. Coordinates of a calculated Ni-hydride intermediate continued.

H	1.5163	5.3052	−1.2227
H	1.8599	4.0886	0.0176
C	−0.5021	3.9377	−2.5252
H	−1.3394	4.3249	−1.9415
H	−0.8679	3.1636	−3.2049
H	−0.1018	4.7567	−3.127
C	1.7812	2.9082	−2.4532
H	2.6275	2.6206	−1.829
H	2.1063	3.7202	−3.1063
H	1.5025	2.0586	−3.0809
N	−3.614	2.5748	0.2836
N	−4.5742	1.7434	−0.3756
C	−4.3068	0.5082	−0.61
C	−5.3842	−0.28	−1.2418
C	1.6102	−0.6369	0.3497
C	−6.7243	0.0107	−0.9674
C	−7.7375	−0.6754	−1.6082
C	−7.4546	−1.6633	−2.5582
C	−6.118	−1.9444	−2.8321
C	−5.0943	−1.2708	−2.1824
H	−6.9597	0.7847	−0.247
H	−8.7702	−0.4381	−1.3717
H	−5.8734	−2.6974	−3.5741
H	−4.0652	−1.4983	−2.442
C	−8.5559	−2.3932	−3.2635
H	−9.2004	−1.6974	−3.8095
H	−9.192	−2.9303	−2.5531
H	−8.1606	−3.1178	−3.9772
C	2.8687	−0.3504	−0.2101
C	3.9943	−1.0324	0.1993
C	3.9242	−2.0246	1.1807
C	2.6748	−2.2934	1.7551
C	1.5393	−1.619	1.3537
H	2.9407	0.3938	−0.9916
H	4.9511	−0.7984	−0.2558
H	0.5979	−1.8166	1.8526
H	2.601	−3.0358	2.5435
C	−4.0465	2.8312	1.7395
C	−5.5249	3.2241	1.7627
H	−5.7218	4.0657	1.0947
H	−5.7957	3.5334	2.7746
H	−6.1744	2.4002	1.4693
C	−3.8081	1.5665	2.544
H	−4.3984	0.7279	2.1681

Table 1A - 15. Coordinates of a calculated Ni-hydride intermediate continued.

H	−4.1143	1.7402	3.5788
H	−2.7523	1.2832	2.545
C	−3.2181	3.9894	2.2806
H	−3.3214	4.8806	1.6569
H	−2.1588	3.7402	2.3505
H	−3.5836	4.2408	3.2797
C	5.1445	−2.7868	1.5857
H	6.0544	−2.2253	1.3673
H	5.2004	−3.7297	1.0309
H	5.1317	−3.0403	2.648
H	−3.5073	−2.3304	−0.0487
H	−0.8564	−2.583	0.2083
H	−3.8913	3.754	−0.2869
H	−1.572	3.81	0.1607

Figure 1A - 20. Calculated structure of transition state 2.

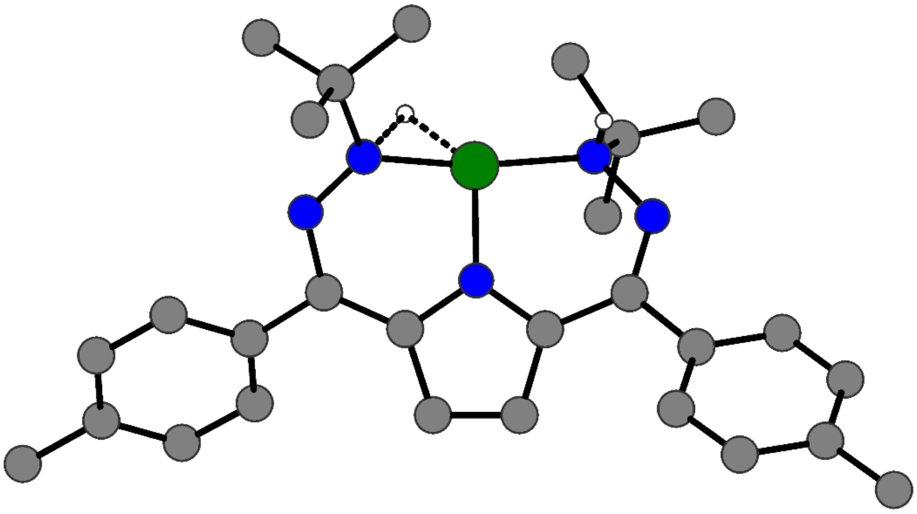

Table 1A - 16. Coordinates of the calculated structure of transition state 2.

N	−1.8621	0.5013	−0.5155
C	−2.9832	−0.2099	−0.4703
C	−2.6566	−1.5748	−0.2197
C	−1.2909	−1.6453	−0.0905
C	−0.7888	−0.3193	−0.2298
Ni	−1.7429	2.3026	−0.298

Table 1A - 16. Coordinates of the calculated structure of transition state 2 continued.

C	0.5157	0.192	−0.0948
N	0.8723	1.4373	−0.4989
N	0.0037	2.3528	−0.7106
C	0.5084	3.4881	−1.5728
C	1.7082	4.1387	−0.8942
H	1.4386	4.5272	0.0918
H	2.0562	4.9752	−1.5038
H	2.5247	3.4261	−0.7792
C	−0.6356	4.4807	−1.729
H	−0.8885	4.9693	−0.783
H	−1.5296	4.0025	−2.1478
H	−0.3425	5.2625	−2.4319
C	0.8927	2.8946	−2.9289
H	1.6871	2.1553	−2.8199
H	1.2546	3.6942	−3.5783
H	0.0348	2.4186	−3.4115
N	−3.6209	2.5475	0.1952
N	−4.5785	1.6537	−0.4105
C	−4.2817	0.4275	−0.6893
C	−5.3698	−0.365	−1.2944
C	1.6463	−0.594	0.3961
C	−6.7058	−0.076	−0.9969
C	−7.7292	−0.754	−1.6294
C	−7.4617	−1.7348	−2.5915
C	−6.1298	−2.0203	−2.8822
C	−5.0954	−1.353	−2.2425
H	−6.9297	0.6924	−0.2666
H	−8.7587	−0.5159	−1.3773
H	−5.8971	−2.7704	−3.6308
H	−4.0712	−1.5796	−2.5151
C	−8.5748	−2.4503	−3.293
H	−9.2164	−1.7447	−3.8302
H	−9.2111	−2.9858	−2.5816
H	−8.1916	−3.1736	−4.0144
C	2.9367	−0.2887	−0.0599
C	4.0346	−0.9824	0.4064
C	3.9011	−1.9967	1.3557
C	2.6172	−2.2848	1.8291
C	1.5088	−1.6051	1.3594
H	3.064	0.4911	−0.7992
H	5.0201	−0.7339	0.0257
H	0.5358	−1.8219	1.7843
H	2.4884	−3.0475	2.5911
C	−4.0391	2.8489	1.6456
C	−5.5085	3.2668	1.6639

Table 1A - 16. Coordinates of the calculated structure of transition state 2 continued.

H	−5.6968	4.092	0.9651
H	−5.7708	3.6139	2.6655
H	−6.1706	2.4431	1.4002
C	−3.8131	1.6246	2.5171
H	−4.413	0.7785	2.1779
H	−4.1159	1.8529	3.5402
H	−2.7618	1.3275	2.5308
C	−3.1772	4.0171	2.1016
H	−3.3223	4.894	1.4605
H	−2.115	3.7596	2.1119
H	−3.4651	4.3055	3.1142
C	5.0945	−2.7422	1.8605
H	6.0103	−2.4058	1.3748
H	4.9882	−3.8167	1.6798
H	5.2121	−2.6028	2.9403
H	−3.3603	−2.3931	−0.1774
H	−0.7036	−2.5337	0.0795
H	−3.7466	3.1043	−0.1124
H	−0.6166	3.0647	0.496

Table 1A - 17. Free energies of calculated complexes and Mulliken Charges of H as H_2 is split.

	Free Energy		Mulliken Charge	
Complex*	Hartrees	kcal/mol	H68	H69
H_2	−1.18105314	−740.52031878	-	-
LNi + H_2	0	0	-	-
LNi(H_2)	0.01736033	10.9370079	0.01	0.08
TS1	0.04502982	28.3687866	0.10	−0.10
(LH)NiH	0.01280404	8.0665452	0.26	−0.06
TS2	0.04111216	25.9006608	0.25	0.02
(LH_2)Ni	−0.01029469	−6.4856547	0.25	0.26

*all complexes are cationic with the triflate removed for ease of calculation

Table 1A - 18. Calculated free energy differences between H_2 and D_2 isotopomers at 323 K.

Species	$\Delta H = H(H_2) – H(D_2)$	$T\Delta S = TS(H_2) – TS(D_2)$	$\Delta G = \Delta H – T\Delta S$
Free H_2	1.83 kcal/mol	−1.10 kcal/mol	2.93 kcal/mol
$LNiH_2$	2.90 kcal/mol	−0.57 kcal/mol	3.47 kcal/mol
TS1	2.48 kcal/mol	−0.33 kcal/mol	2.81 kcal/mol

Table 1A - 19. Calculated isotope effect (IE) at 323 K.

Starting Species	Final Species	$\Delta\Delta G = \Delta G(\text{Final}) - \Delta G(\text{Start})$	$IE = \exp(-\Delta\Delta G / RT)$
Free H_2	$LNiH_2$	+0.54 kcal/mol	0.4
Free H_2	TS1	−0.12 kcal/mol	1.2
$LNiH_2$	TS1	−0.66 kcal/mol	2.8
	Experimental	+0.3 kcal/mol	0.8

X–ray Crystallography

Table 1A - 20. Crystal structure and refinement data for **1** and **2**.

Identification code	**1**	**2**
Empirical formula	$C_{33}H_{48}ClN_5Ni$	$C_{29}H_{36}F_3N_5NiO_3S$
Formula weight	608.92	650.40
Temperature/K	100(2)	100(2)
Crystal system	triclinic	Monoclinic
Space group	P–1	$P2_1/c$
a/Å	10.3991(5)	9.57352(3)
b/Å	11.3467(5)	19.2736(6)
c/Å	15.9639(8)	16.4544(4)
α/°	90.377(2)	90
β/°	106.279(2)	94.3950(10)
γ/°	115.5700(10)	90
Volume/$Å^3$	1613.26(13)	3078.30(15)
Z	2	4
ρ_{calc}g/cm^3	1.254	1.403
μ/mm^{-1}	0.714	0.181
F(000)	652.0	1360.0
Crystal size/mm^3	0.59 × 0.47 × 0.34	0.2 × 0.1 × 0.1
Radiation	MoKα (λ = 0.71073)	synchrotron (λ = 0.41328)
2Θ range for data collection/°	4.498 to 52.874	1.896 to 34.38
Index ranges	$-13 \leq h \leq 13$, $-14 \leq k \leq 14$, $-19 \leq l \leq 19$	$-13 \leq h \leq 13$, $-27 \leq k \leq 27$, $-23 \leq l \leq 22$
Reflections collected	34504	119850
Independent reflections	6628 [R_{int} = 0.0325, R_{sigma} = 0.0278]	9365 [R_{int} = 0.0523, R_{sigma} = 0.0209]
Data/restraints/parameters	6628/0/371	9365/0/387
Goodness–of–fit on F^2	1.049	1.061
Final R indexes [I>=2σ (I)]	R_1 = 0.0445, wR_2 = 0.1135	R_1 = 0.0290, wR_2 = 0.0832
Final R indexes [all data]	R_1 = 0.0555, wR_2 = 0.1197	R_1 = 0.0322, wR_2 = 0.0852
Largest diff. peak/hole / e $Å^{-3}$	1.50/–0.72	0.46/–0.61

Gas Chromatography-Mass Spectrometry (GC-MS)

Figure 1A - 21. GC-MS of the catalytic hydrogenation of benzoquinone (20 eq) by **3** (1 eq.) in d_8-toluene under 1 atm H_2 at room temperature over 7 days. The relative integration of peaks corresponding to the protonated benzoquinone and hydroquionone are approximately 9:1, indicating a TON of ~2.

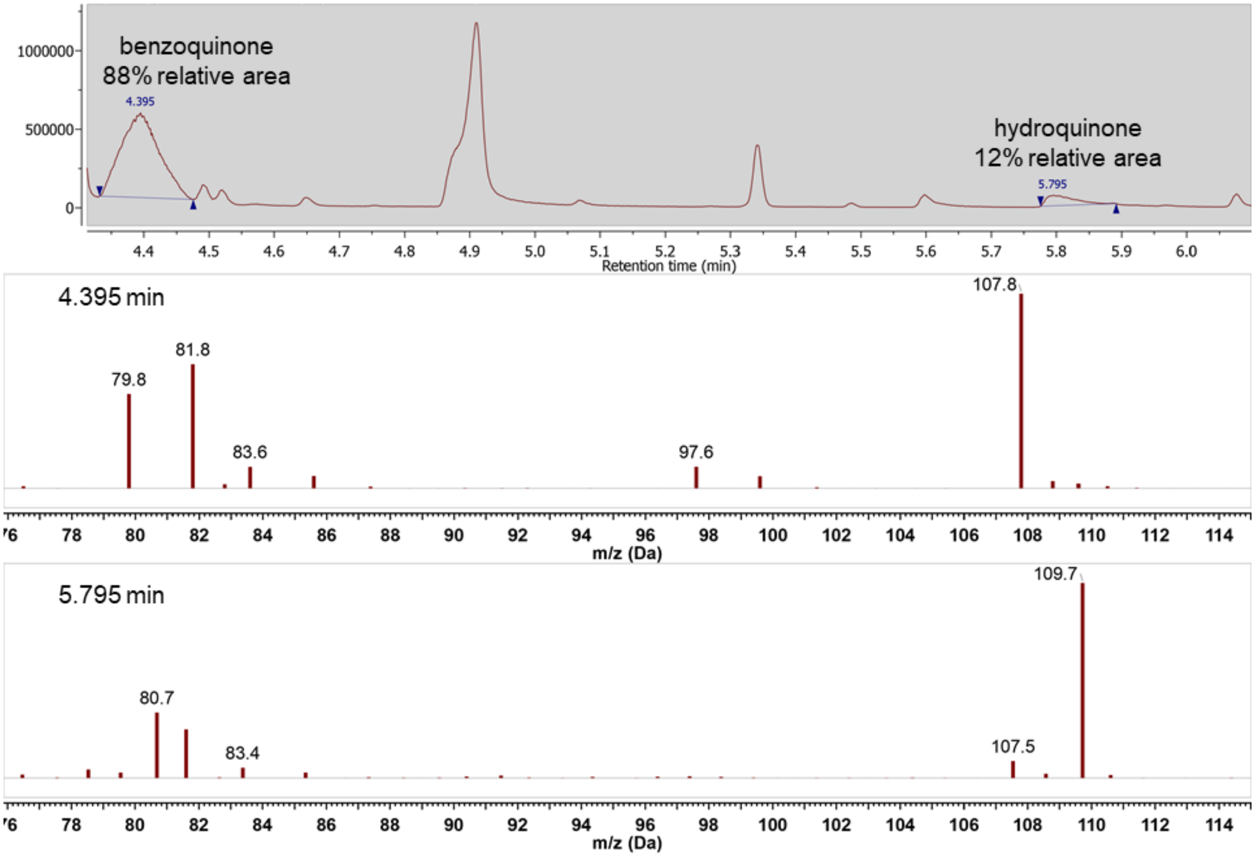

Appendix 2: Supporting Information for Chapter 2

NMR Spectroscopy

Figure 2A - 1. ^{1}H NMR of **1** in d_8-toluene.

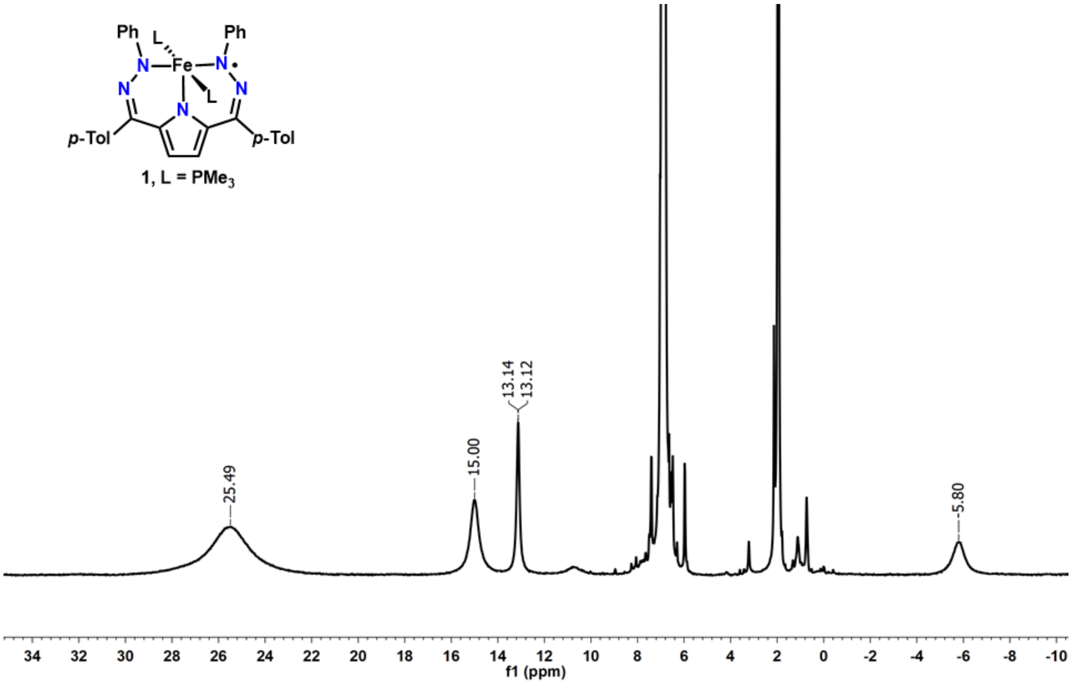

Figure 2A - 2. ^{1}H NMR of **2-MeCN** in CD_3CN.

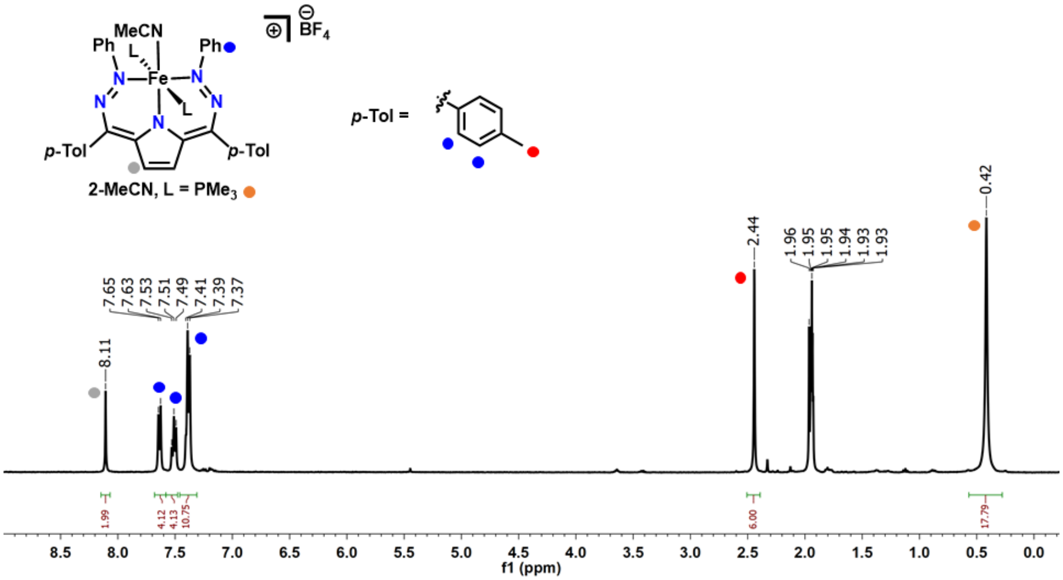

Figure 2A - 3. $^{13}C\{^{1}H\}$ NMR of **2-MeCN** in CD_3CN.

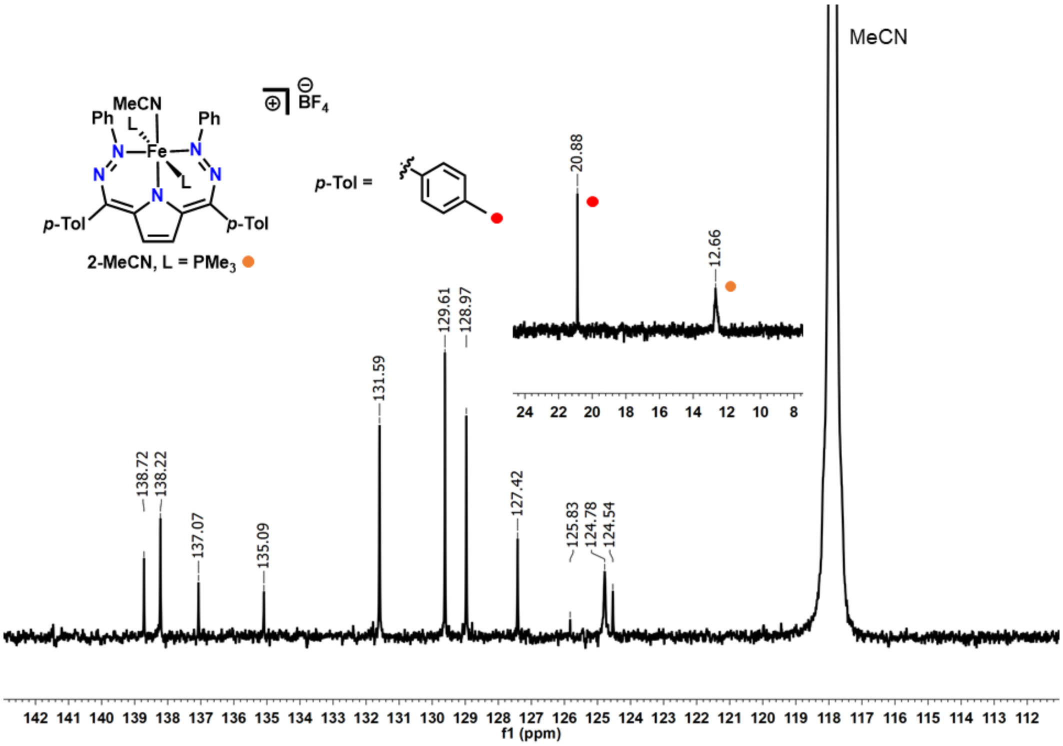

Figure 2A - 4. $^{31}P\{^{1}H\}$ NMR of **2-MeCN** in CD_3CN.

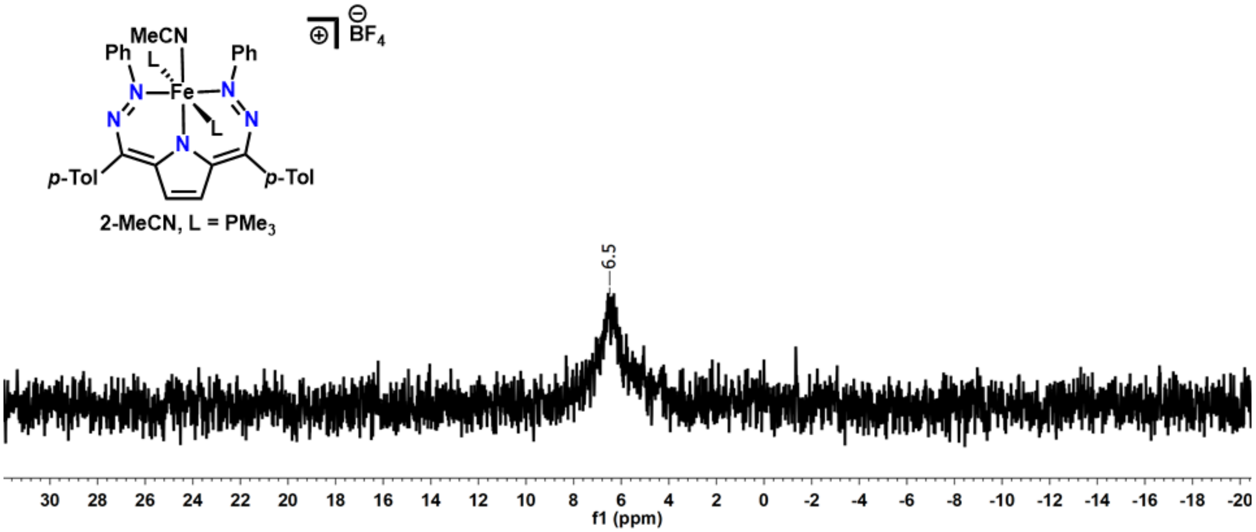

Figure 2A - 5. $^{19}F\{^1H\}$ NMR of **2-MeCN** in CD_3CN.

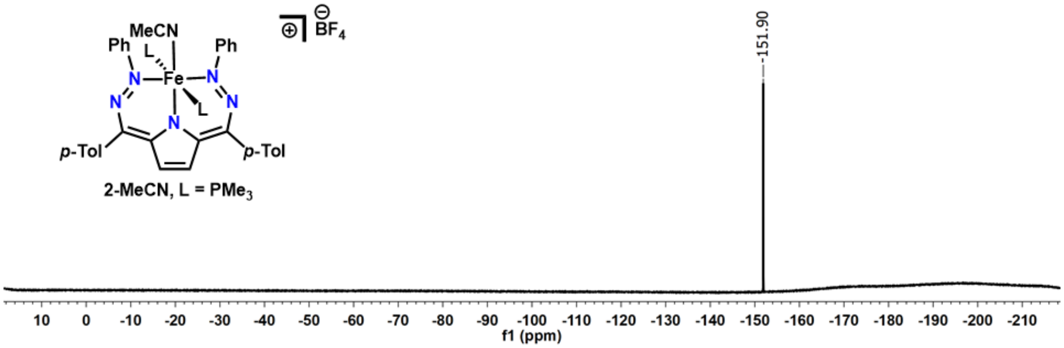

Figure 2A - 6. $^{11}B\{^1H\}$ NMR of **2-MeCN** in CD_3CN.

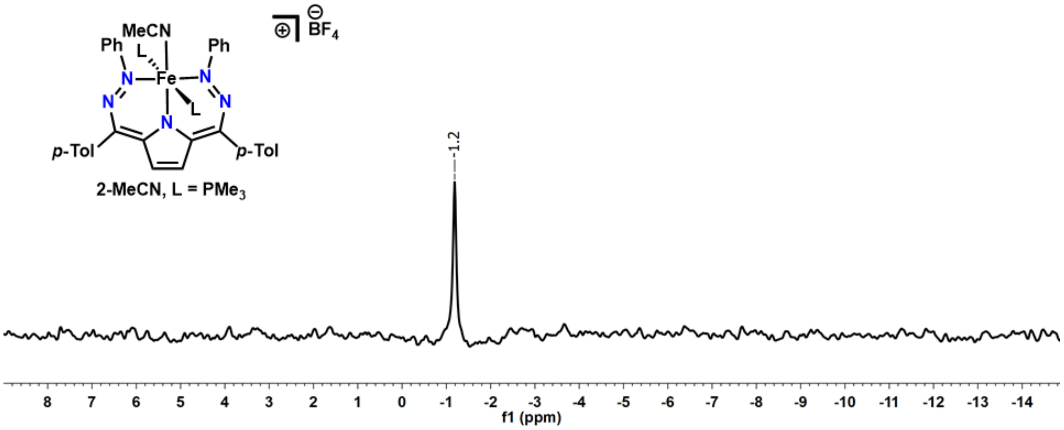

Figure 2A - 7. ^{1}H NMR of **2** in C_6D_6. (a) toluene; (b) THF; (c) diethylether; (d) petroleum ether; (e) silicon grease. Note: residual solvents visible in spectrum due to low solubility of **2** in benzene.

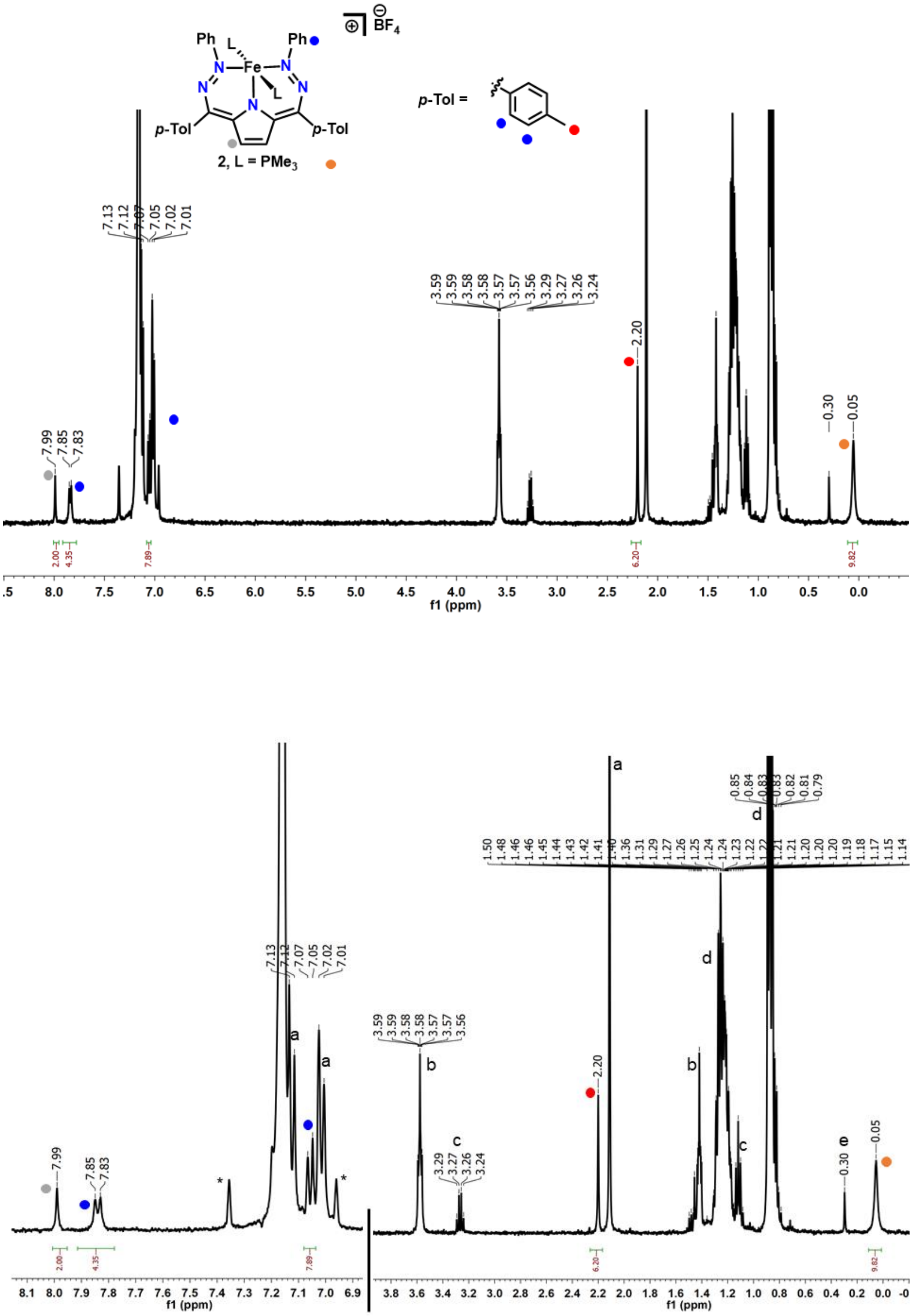

UV-vis Spectra

Figure 2A - 8. UV-vis spectrum of **1** in THF at RT (0.28 mM).

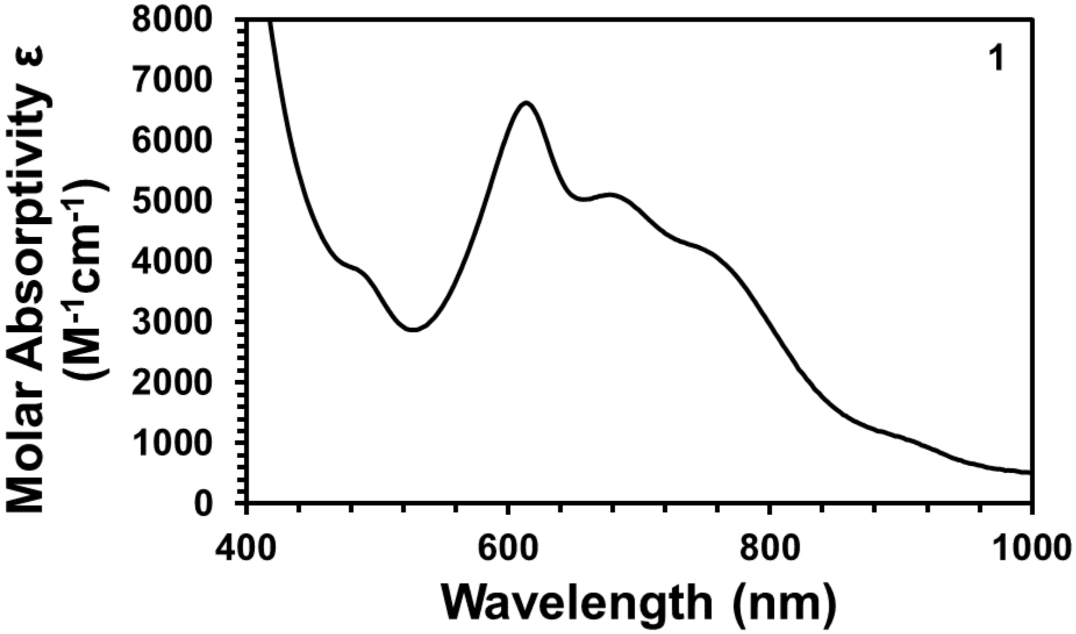

Figure 2A - 9. UV-vis spectrum of **2** in acetonitrile (blue, 0.46 mM) and benzene (red, 0.35 mM) at RT.

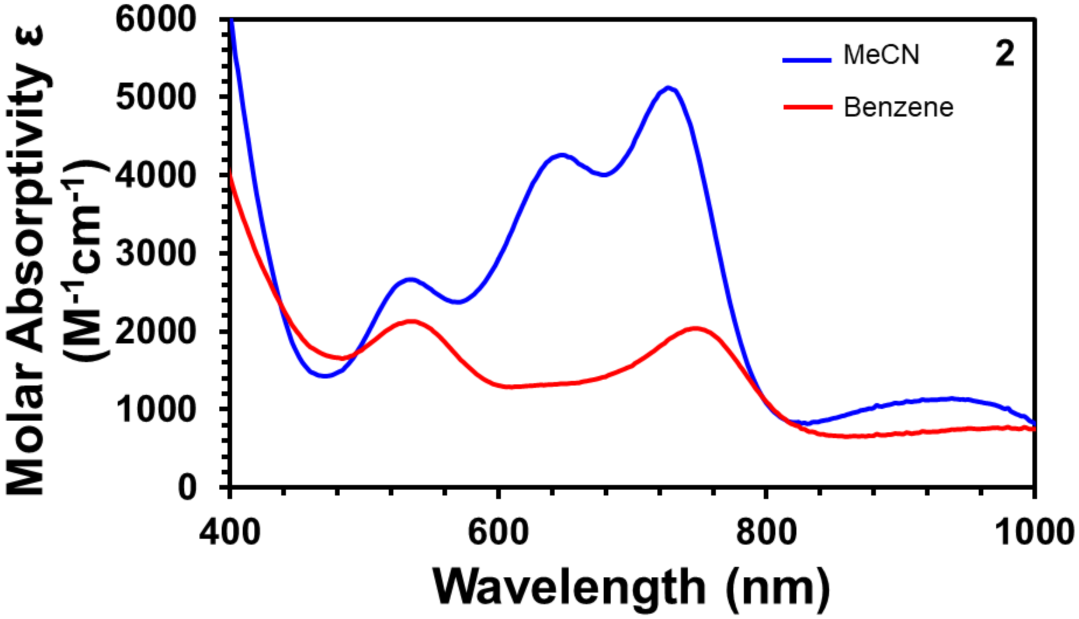

Figure 2A - 10. Variable temperature UV-vis spectra of **1**. This was done with a 0.47 mM solution in THF. Note: at this higher concentration, the absorbance at 768 nm is broadened such that the absorbance at 912 no longer appears as a distinct feature.

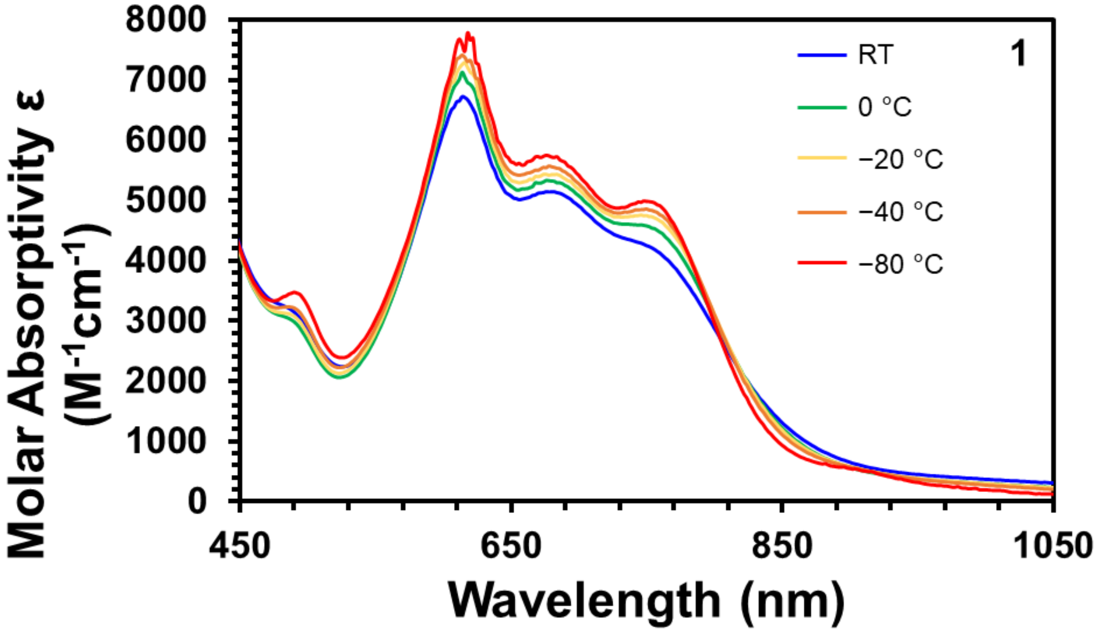

Figure 2A - 11. Complex **2** dissolved in various solvents.

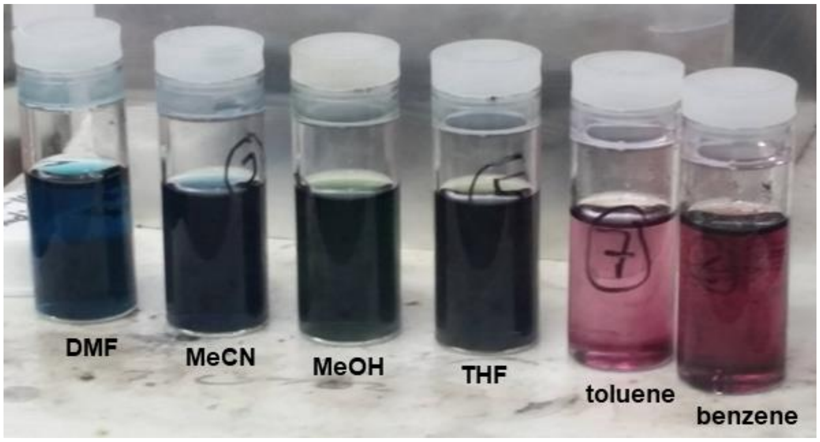

IR Spectra

Figure 2A - 12. IR (nujol) of **1**. Nujol peaks are labeled with (*).

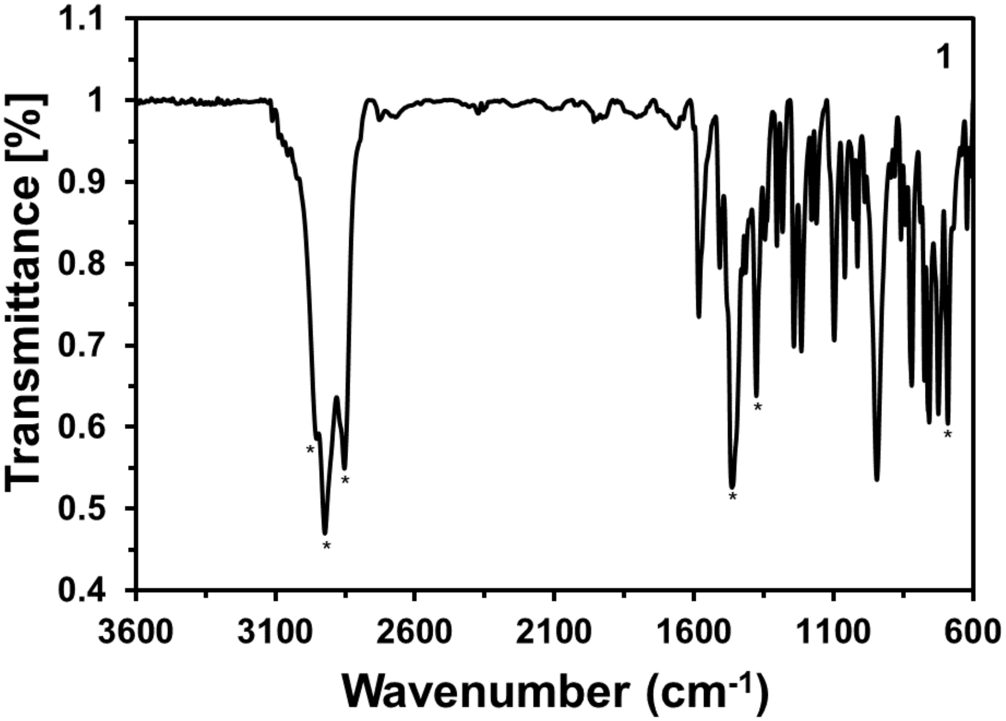

Figure 2A - 13. IR (nujol) of **2**. Nujol peaks are labeled with (*).

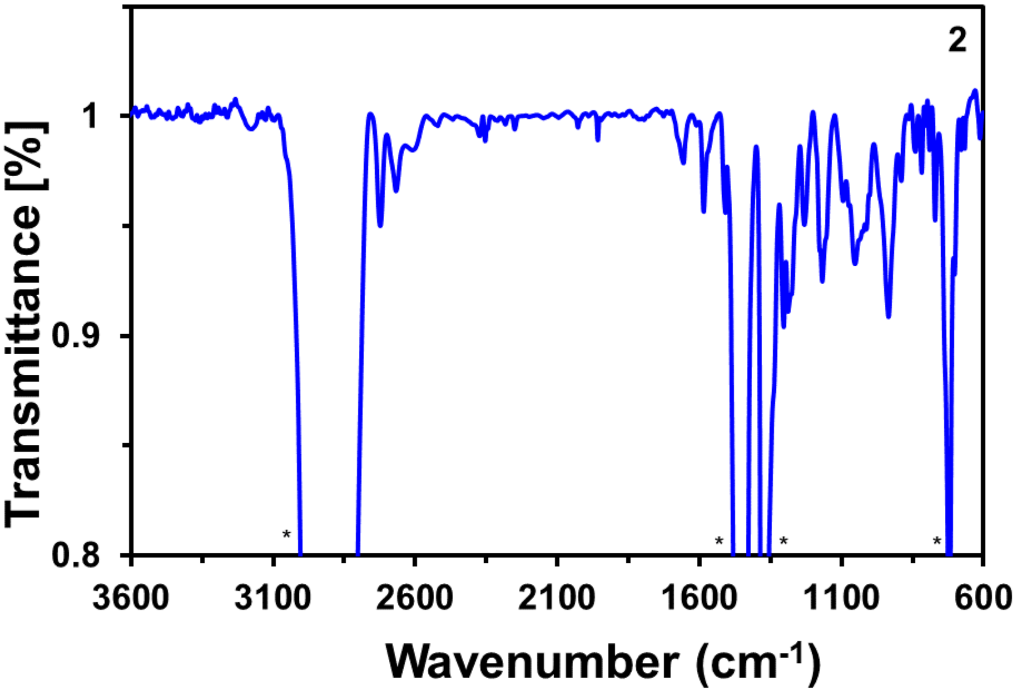

Figure 2A - 14. IR (nujol) of crude metalation to form **1** in the absence of TEMPO$^{\bullet}$. Nujol peaks are labeled with (*).

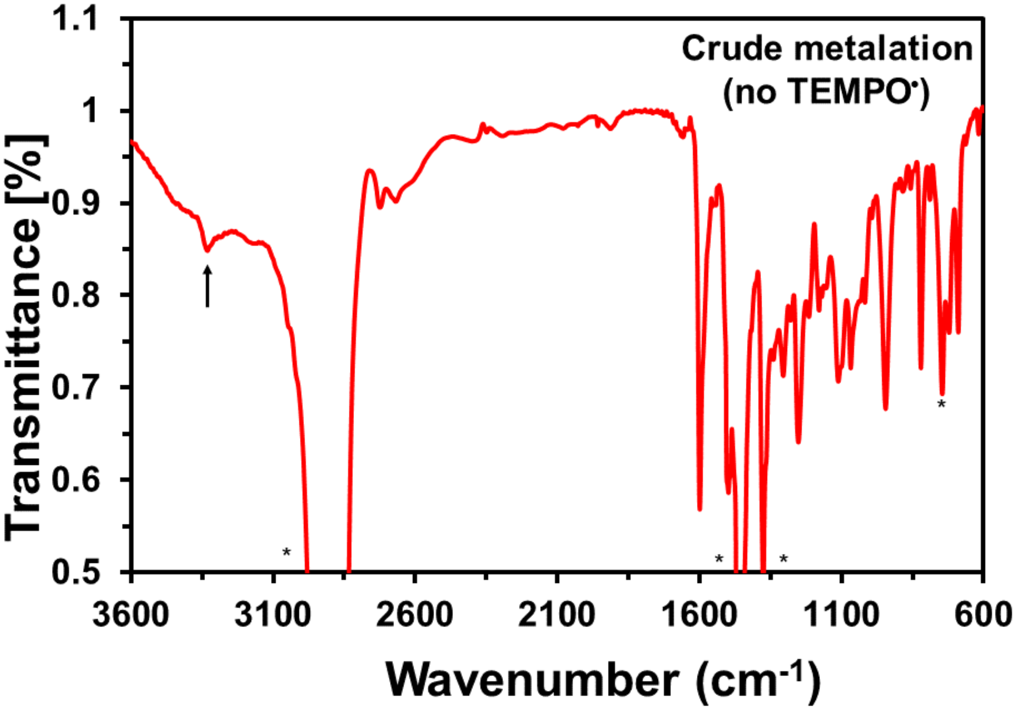

Cyclic Voltammetry (CV)

Figure 2A - 15. CV of 1.5 mM **1** in THF. Electrolyte: 0.5 M [Bu_4N][PF_6], Scan rate: 100 mV/s. Scanning oxidatively. The full scan is shown in black, the isolated L^{1-}/L^{2-} couple is shown in blue, and the isolated L^{2-}/L^{3-} couple is shown in red. Open circuit potential: −0.89 V.

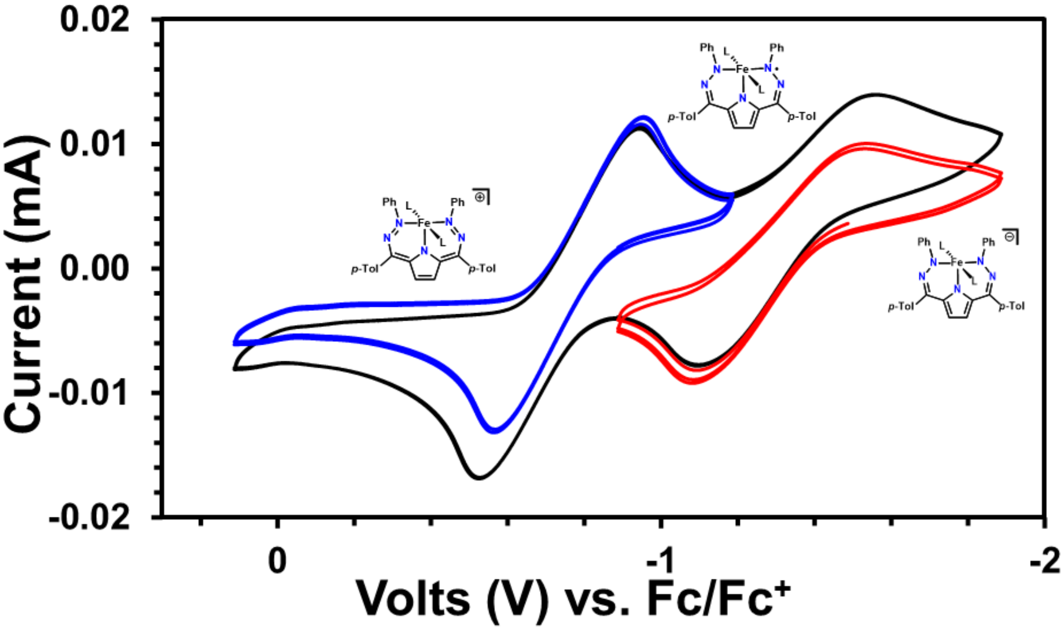

Electron Paramagnetic Resonance (EPR) Spectra

Figure 2A - 16. EPR spectrum of **1** in benzene, 15 K. MW power = 0.2 mW, MW frequency = 9.63 GHz. Simulated parameters: g_z = 2.17, g_x = 2.28, g_y = 1.98, D = 8.4, E/D = 0.24, sE/D = 0.021, Linewidth = 30.5. *The sharp features near 3300 gauss correspond to a small amount of an S = 1/2 impurity.

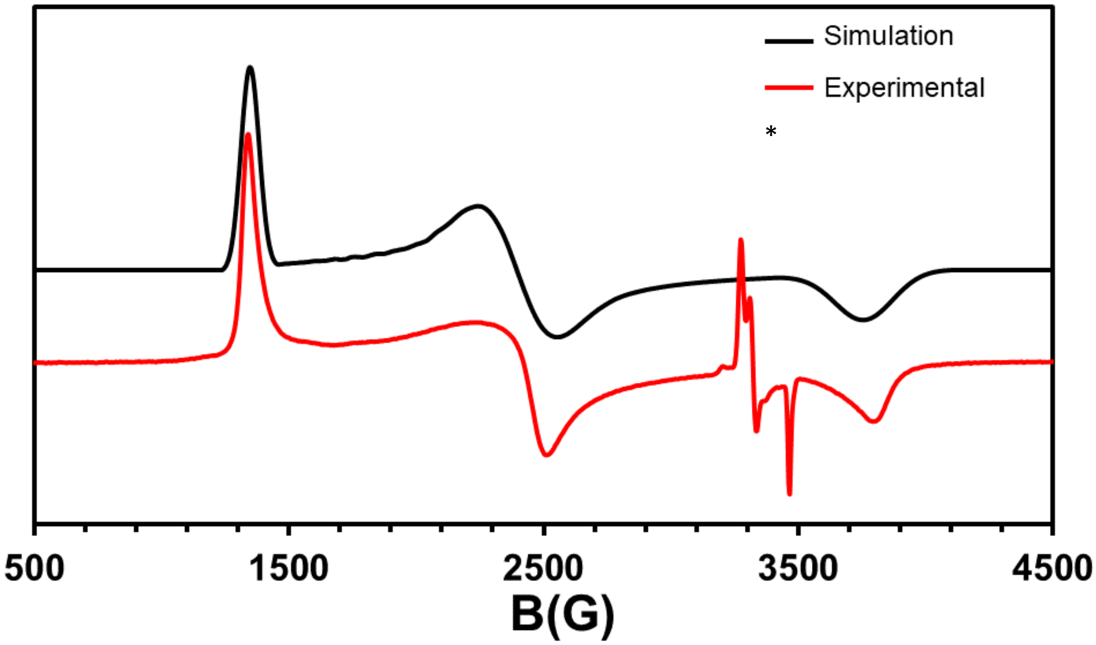

X-ray Crystallography

Table 2A - 1. Crystal structure and refinement for **1**, **2-MeCN** at RT and 100 K, and **2**.

Identification code	**1**	**2-MeCN, 100 K**	**2**	**2-MeCN, RT**
CCDC Deposition Number	20701164	2070163	2070165	2070162
Empirical formula	$C_{38}H_{44}FeN_5P_2$	$C_{40}H_{47}BF_4FeN_6P_2$	$C_{38}H_{44}BF_4FeN_5P_2$	$C_{40}H_{50}BF_4FeN_6P_2$
Formula weight	688.57	816.43	775.38	819.49
Temperature/K	100	100(2)	100(2)	298(2)
Crystal system	monoclinic	monoclinic	monoclinic	monoclinic
Space group	$P2_1/n$	C2/c	$P2_1/c$	C2/c
a/Å	12.1503(7)	12.8518(11)	16.2038(9)	13.0780(8)
b/Å	21.3895(11)	16.3260(11)	15.0217(9)	16.3442(9)
c/Å	13.3352(7)	19.7462(15)	17.0175(9)	19.9153(12)
α/°	90	90	90	90
β/°	96.952(2)	107.797(2)	106.981(2)	108.504(2)
γ/°	90	90	90	90
Volume/$Å^3$	3440.2(3)	3944.9(5)	3961.6(4)	4036.8(4)
Z	4	4	4	4
$\rho_{calc}g/cm^3$	1.329	1.375	1.3	1.3483
μ/mm^{-1}	0.567	0.128	0.513	0.508
F(000)	1452	1704	1616	1719
Crystal size/mm^3	0.545 × 0.503 × 0.282	0.1 × 0.1 × 0.05	0.3 × 0.2 × 0.1	0.322 × 0.255 × 0.192
Radiation	MoKα (λ = 0.71073)	synchrotron (λ = 0.41328)	MoKα (λ = 0.71073)	Mo Kα (λ = 0.71073)
2Θ range for data collection/°	4.284 to 56.762	2.418 to 29.944	4.084 to 54.256	4.32 to 55.26
Index ranges	$-16 \le h \le 16$, $-28 \le k \le 28$, $-17 \le l \le 17$	$-16 \le h \le 16$, $-20 \le k \le 20$, $-24 \le l \le 24$	$-20 \le h \le 19$, $-19 \le k \le 17$, $-21 \le l \le 20$	$-16 \le h \le 17$, $-21 \le k \le 21$, $-25 \le l \le 25$
Reflections collected	123204	49996	49463	55732
Independent reflections	8602 [R_{int} = 0.0508, R_{sigma} = 0.0201]	4006 [R_{int} = 0.0313, R_{sigma} = 0.0127]	8726 [R_{int} = 0.1203, R_{sigma} = 0.0874]	4682 [R_{int} = 0.0626, R_{sigma} = 0.0335]
Data/restraints/parameters	8602/0/454	4006/0/252	8726/0/468	4682/0/271
Goodness-of-fit on F^2	1.107	1.156	1.013	1.068
Final R indexes [I>=2σ (I)]	R_1 = 0.0489, wR_2 = 0.1314	R_1 = 0.0398, wR_2 = 0.1086	R_1 = 0.0516, wR_2 = 0.0940	R_1 = 0.0480, wR_2 = 0.1125
Final R indexes [all data]	R_1 = 0.0604, wR_2 = 0.1411	R_1 = 0.0402, wR_2 = 0.1090	R_1 = 0.1038, wR_2 = 0.1098	R_1 = 0.0787, wR_2 = 0.1286
Largest diff. peak/hole / e $Å^{-3}$	1.43/-0.62	0.44/-0.67	0.55/-0.46	0.49/-0.43

Table 2A - 2. Selected bond lengths of complex **1**, **2**, **2-MeCN** at RT, and **2-MeCN** at 100 K.

	1	**2 -MeCN 100 K**	**2-MeCN RT**	**2**
Fe-N1	1.930(2)	1.923(2)	1.920(2)	1.875(2)
Fe-N3	1.937(2)	1.916(2)	1.912(2)	1.861(2)
Fe-N5	1.916(2)	-	-	1.861(2)
Fe-P1	2.3980(6)	2.3343(5)	2.3398(6)	2.3657(9)
Fe-P2	2.4219(6)	-	-	2.3289(9)
N1-N2	1.351(2)	1.318(2)	1.310(2)	1.329(3)
N2-C8	1.306(3)	1.345(2)	1.340(3)	1.350(3)
C13-N4	1.316(3)	-	-	1.347(4)
N4-N5	1.356(3)	-	-	1.330(3)
C10-C11	1.393(3)	1.354(4)	1.339(5)	1.351(4)

X-ray Absorption Spectroscopy (XAS)

Figure 2A - 17. Fe K-edge X-ray absorption spectrum of **2-MeCN** as a matrix in polyethylene glycol and acetonitrile. The K-edge inflection point comes at 7120.3 eV. Inset: Derivative spectra of K-edge XAS.

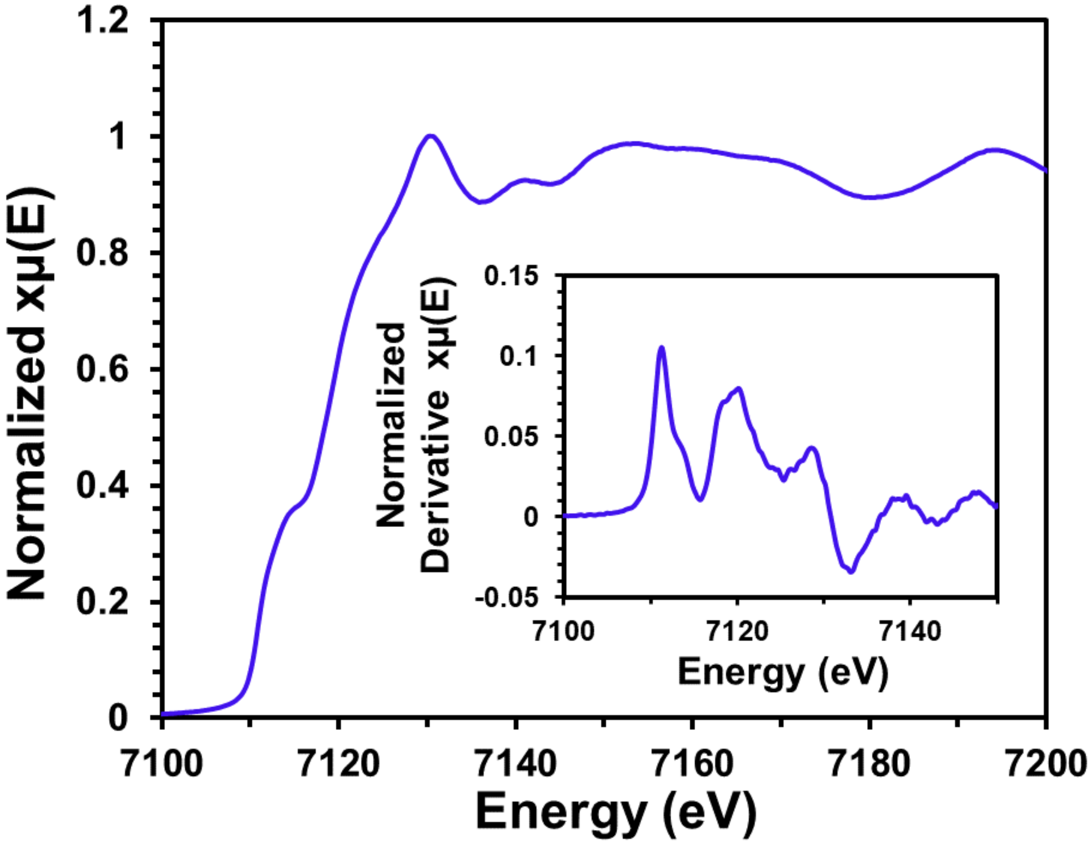

Density Functional Theory (DFT) Calculations

Table 2A - 3. Coordinates for the optimized structure of **1**.

Fe	5.676102	14.56413	2.687628
P	4.76113	16.15202	4.561143
P	6.910176	13.95397	0.409963
N	3.872706	14.79664	1.681626
N	5.050891	12.78964	3.353603
N	7.511393	14.23101	3.590342
H	7.252201	16.63314	2.555486
C	4.314862	17.89452	4.146666
C	3.146099	15.48714	5.13608
C	5.701065	16.34921	6.131117
C	8.456965	14.88923	0.052336
C	6.108784	13.87983	−1.2468
C	7.5334	12.23155	0.577895
N	2.777071	14.1061	1.882384
C	3.786379	15.67219	0.58869
C	3.799179	12.27879	3.187316
C	5.872594	11.7853	3.78336
N	7.975771	13.08392	4.041894
C	8.358323	15.31181	3.869362
C	8.071515	16.56197	3.281205
H	5.225674	18.46546	3.9054
H	3.795523	18.38951	4.985247
H	3.657527	17.90317	3.262518
H	2.450375	15.44793	4.283077
H	2.710461	16.10617	5.938283
H	3.282612	14.4582	5.503425
H	5.94763	15.3541	6.53319
H	5.124636	16.91342	6.883492
H	6.648353	16.87317	5.927401
H	9.038803	14.41468	−0.7557
H	6.786528	13.4379	−1.99735
H	5.195453	13.26868	−1.1826
H	8.133676	12.14832	1.495284
H	9.072611	14.94039	0.96475
H	8.203416	15.91918	−0.24661
H	5.812854	14.89025	−1.56788
H	6.680195	11.54189	0.672678
H	8.148581	11.93572	−0.28877
C	2.693693	13.0292	2.657137
C	2.882109	15.4812	−0.47683
C	4.679533	16.76021	0.520304

Table 2A - 3. Coordinates for the optimized structure of **1** continued.

C	3.819079	10.8782	3.502729
C	5.111756	10.56861	3.863162
C	7.262711	11.96491	4.092112
C	9.457715	15.23103	4.752128
C	8.815119	17.69669	3.60016
C	1.297333	12.58219	2.90577
H	2.197592	14.6317	−0.43134
C	2.891439	16.34039	−1.57305
C	4.684695	17.61595	−0.58107
H	5.351996	16.94124	1.365288
H	2.977878	10.19131	3.421249
H	5.500866	9.586479	4.12447
C	8.053058	10.76576	4.502
C	10.20218	16.36696	5.05637
H	9.690856	14.26173	5.19607
H	8.555905	18.65422	3.136458
C	9.882667	17.61158	4.499199
C	0.272499	12.90591	1.998152
C	0.925799	11.91539	4.088964
H	2.192287	16.16384	−2.39749
C	3.794481	17.40909	−1.63966
H	5.381034	18.46055	−0.6074
C	7.637034	9.895504	5.52367
C	9.255975	10.46564	3.843422
H	11.04308	16.28184	5.753066
H	10.46277	18.50087	4.762161
C	−1.05515	12.58401	2.263588
H	0.539169	13.43742	1.082377
H	1.687625	11.66942	4.833514
C	−0.405857	11.59452	4.34809
H	3.803926	18.07521	−2.5077
H	6.734948	10.13001	6.096049
C	8.359373	8.740961	5.824218
C	9.971337	9.306332	4.140352
H	9.624795	11.15214	3.075986
C	−1.427667	11.93169	3.448834
H	−1.825914	12.85584	1.534258
H	-0.660443	11.08441	5.283959
H	8.004249	8.077701	6.621425
C	9.524682	8.406355	5.118625
H	10.89207	9.088074	3.588484
C	−2.867967	11.6377	3.76849
C	10.23888	7.106427	5.373351

Table 2A -3. Coordinates for the optimized structure of **1** continued.

H	−3.00934	10.59064	4.087306
H	−3.522232	11.82446	2.902359
H	−3.228832	12.27325	4.59591
H	10.23675	6.8388	6.442668
H	11.28436	7.140159	5.027645
H	9.744794	6.278973	4.833778

Table 2A - 4. Coordinate for the optimized structure of **2**$^+$. MeCN ligand and the BF_4^- counterion was excluded for simplicity.

Fe	9.600459	4.463768	4.393341
P	9.382683	2.661273	5.89602
P	9.748703	6.26053	2.819354
N	11.1865	5.041219	5.233906
N	10.5849	3.352572	3.200891
N	8.517526	5.499937	5.573274
H	8.001514	3.563541	2.827047
C	7.88643	1.634429	5.716721
C	10.74882	1.463948	5.803685
C	9.33901	3.094297	7.664459
C	9.006118	7.83185	3.369375
C	8.974414	5.982829	1.184012
C	11.44411	6.750076	2.36734
C	11.25323	5.957429	6.233509
C	12.44913	4.779284	4.80308
N	11.86024	3.173932	3.067651
C	9.824878	2.506176	2.357725
N	8.856823	6.190837	6.61386
C	7.104966	5.352722	5.493052
C	8.45054	2.736007	2.279648
H	7.003071	2.240671	5.934714
H	7.920573	0.789755	6.411903
H	7.808374	1.25281	4.6964
H	10.77788	1.003981	4.813231
H	10.6252	0.678793	6.555742
H	11.69924	1.975803	5.973315
H	10.28534	3.550053	7.964678
H	9.173489	2.193321	8.262433
H	8.535328	3.804847	7.865801
H	7.934041	7.709803	3.543107
H	9.161327	8.615816	2.622471
H	9.468223	8.140107	4.310381
H	9.388524	5.082413	0.724311

Table 2A - 4. Coordinate for the optimized structure of $\mathbf{2}^{+}$. MeCN ligand and the BF_4^{-} counterion was excluded for simplicity continued.

H	9.160792	6.837988	0.527114
H	7.893653	5.849635	1.280064
H	11.99362	7.068244	3.256713
H	11.41654	7.578763	1.652772
H	11.97161	5.907882	1.914393
C	10.13223	6.402604	6.960373
C	12.6262	6.352785	6.4056
C	13.36217	5.630376	5.521229
C	12.75991	3.831021	3.807876
C	10.38008	1.446427	1.631578
C	6.311176	5.345871	6.646319
C	6.497163	5.18072	4.249085
C	7.638137	1.936396	1.490072
C	10.29353	7.089424	8.256288
H	12.97683	7.11027	7.090698
H	14.42447	5.695683	5.341321
C	14.16249	3.477317	3.503646
C	9.563399	0.650968	0.845077
H	11.44455	1.259904	1.699537
H	6.781805	5.499066	7.609506
C	4.944403	5.156622	6.546252
C	5.123538	4.996583	4.156112
H	7.090587	5.256516	3.344553
H	6.573901	2.140163	1.429673
C	8.194346	0.888997	0.767065
H	4.658407	4.884895	3.182117
C	9.415444	8.103038	8.650166
C	11.26801	6.672774	9.171971
C	15.11268	3.295607	4.513609
C	14.57087	3.279708	2.181839
H	10.00249	−0.169509	0.286458
H	4.339518	5.14542	7.447178
C	4.343284	4.978744	5.303332
H	7.56532	0.263378	0.142674
C	9.523212	8.686556	9.901865
H	8.644734	8.433393	7.961713
H	11.93565	5.856201	8.916265
C	11.3634	7.255021	10.42407
H	14.81697	3.376962	5.554445
C	16.42164	2.965505	4.208359
C	15.88333	2.950779	1.883249
H	13.84745	3.39466	1.381202
H	3.270269	4.83462	5.232444

Table 2A - 4. Coordinate for the optimized structure of **2**$^+$. MeCN ligand and the BF_4^- counterion was excluded for simplicity continued.

C	10.49314	8.273124	10.81715
H	8.835552	9.480893	10.17714
H	12.11876	6.898294	11.11931
H	17.13643	2.821876	5.014005
C	16.83887	2.797147	2.887936
H	16.17409	2.817847	0.844782
C	10.58626	8.877531	12.18617
C	18.26693	2.461859	2.579762
H	10.23274	8.169981	12.94479
H	9.976667	9.779554	12.26638
H	11.61892	9.133913	12.44024
H	18.39367	2.165958	1.536
H	18.62684	1.645874	3.21281
H	18.91758	3.323841	2.766254

Figure 2A - 18. Spin density plot of **1**.

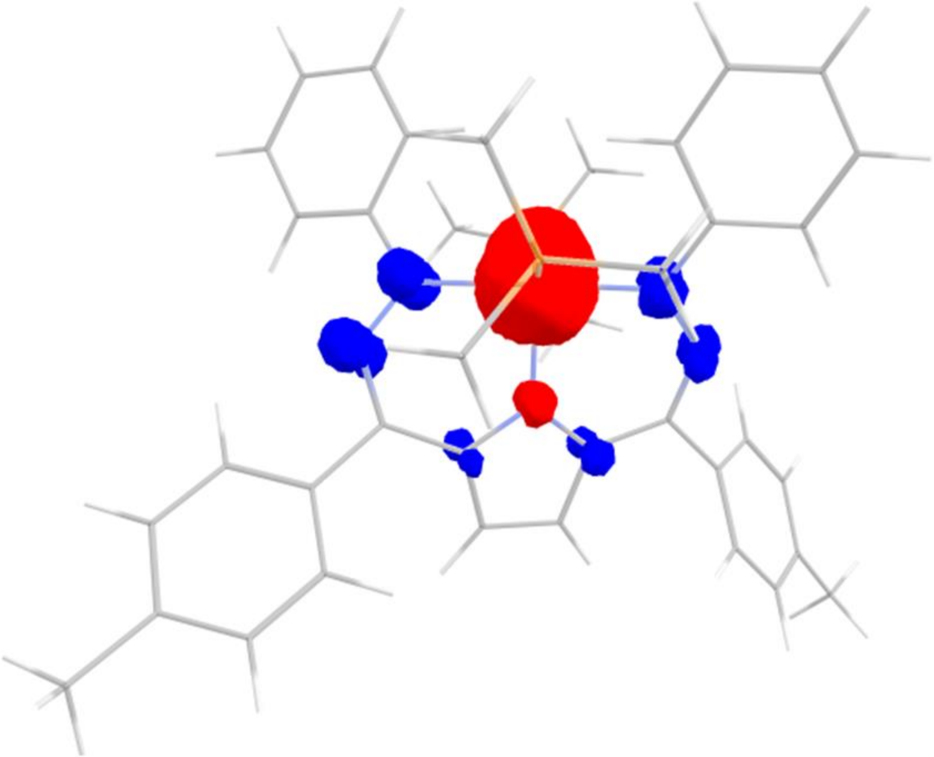

Table 2A - 5. Mulliken spin density on various atoms of **1**.

	spin density
Fe	3.724086
5 N’s	−0.456645
ligand	−0.724088

Appendix 3: Supporting Information for Chapter 3

NMR Spectra

Figure 3A - 1. ^{1}H NMR of **1** in C_6D_6.

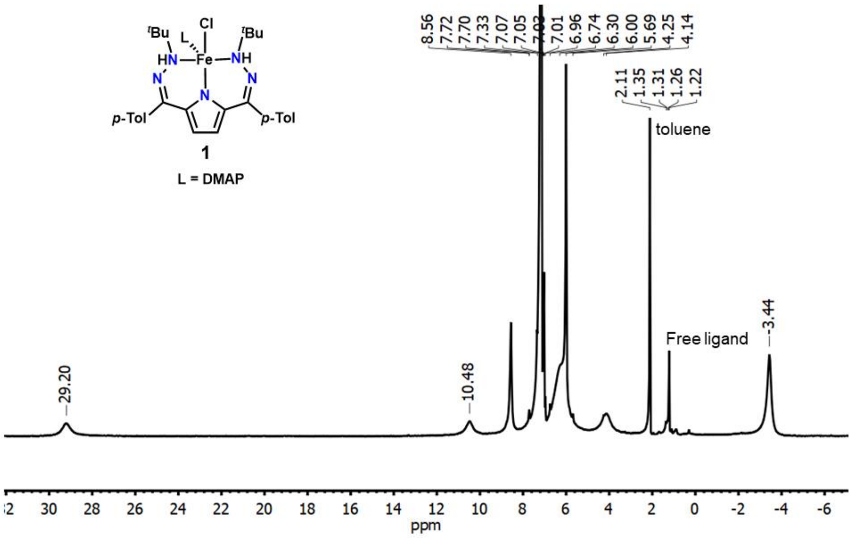

Figure 3A - 2. ^{1}H NMR of ^{tBu}DHP-$H_2 \cdot$ 2HCl (bottom) stacked with ^{tBu}DHP-$D_2 \cdot$ 2DCl (top, 93% enriched in deuterium) in C_6D_6.

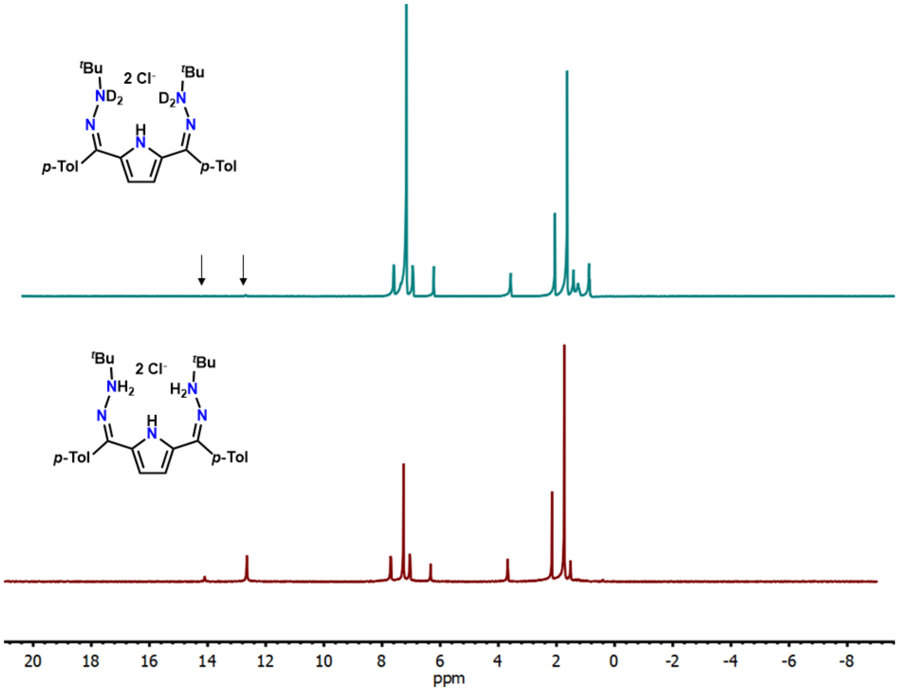

Figure 3A - 3. ^{1}H NMR of $^{tBu}DHP\text{-}D_2 \cdot 2DCl$ in C_6D_6. The compound is 94% enriched in deuterium based on integrations of the beta N peak relative to its theoretical integration of 4 in $^{tBu}DHP\text{-}H_2 \cdot 2HCl$.

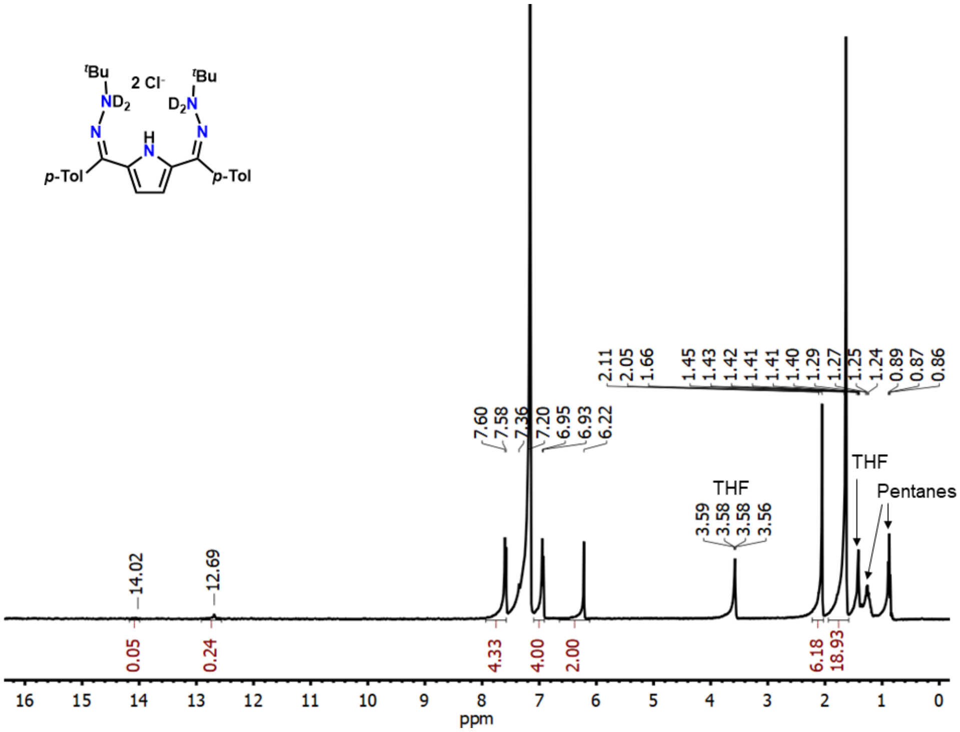

Figure 3A - 4. ^{2}H NMR spectra of D_2O in THF, THF, and the volatiles from the reaction of **1** with O_2 at room temperature after 5 minutes.

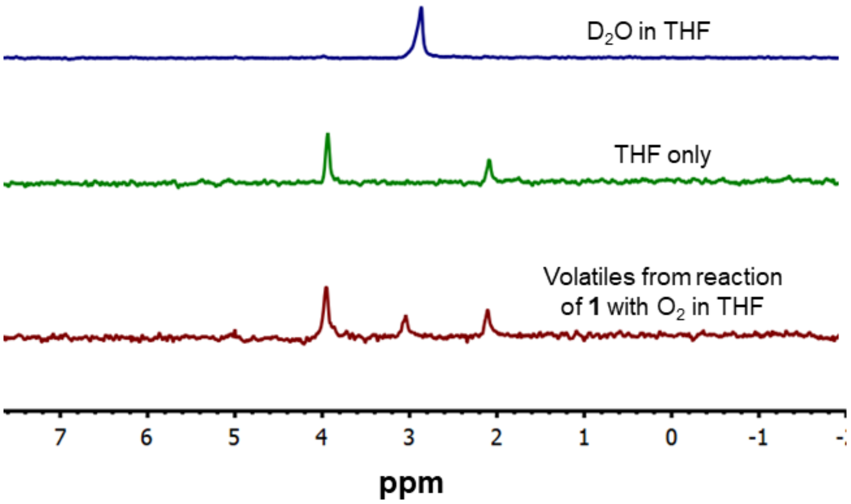

Figure 3A - 5. ^{31}P NMR of the reaction of **1** with 10 equivalents of PPh_3 at room temperature in toluene. Total integrated area is set to 10.

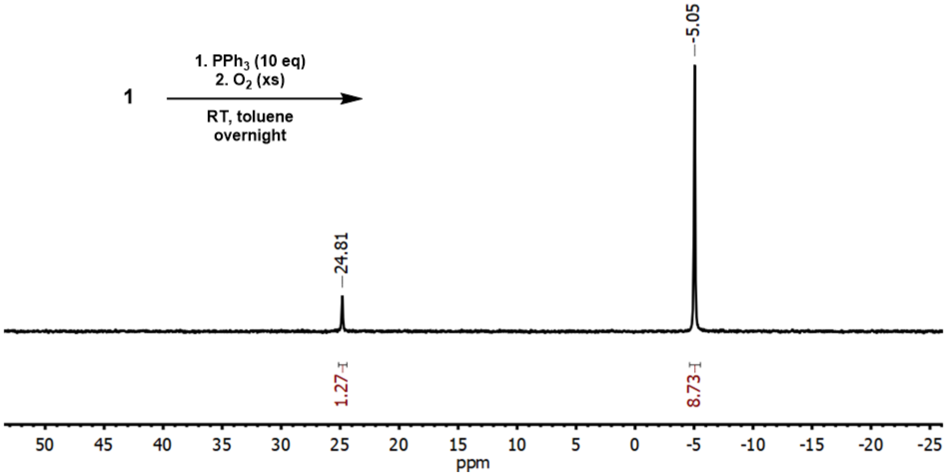

UV-vis spectroscopy

Figure 3A - 6. UV-vis of **1** as a 0.35 mM solution in toluene.

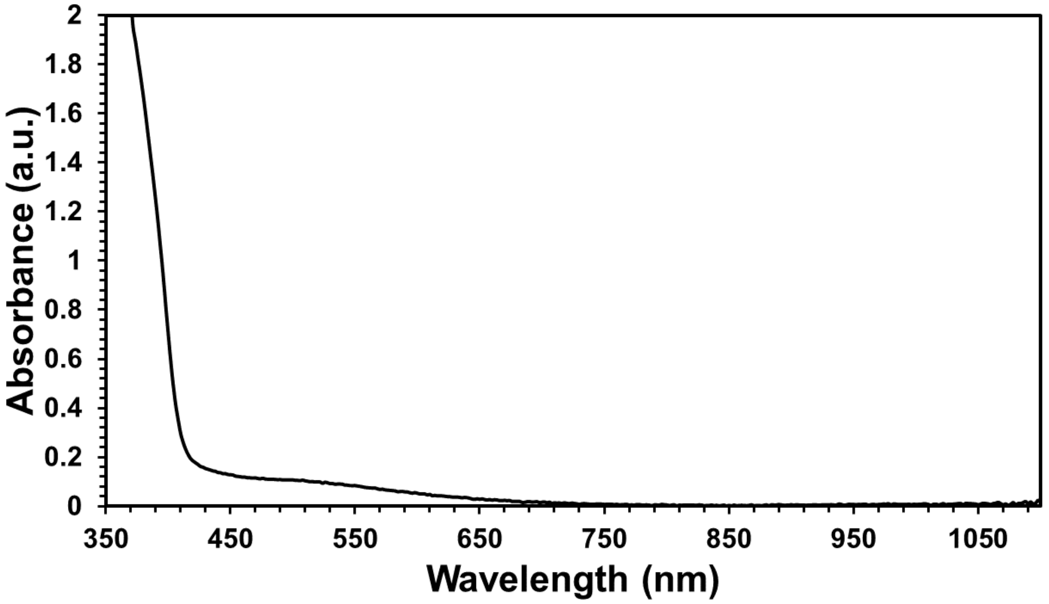

Figure 3A - 7. UV-vis of **4** to bleach at room temperature from a 0.35 mM solution of **1** in toluene.

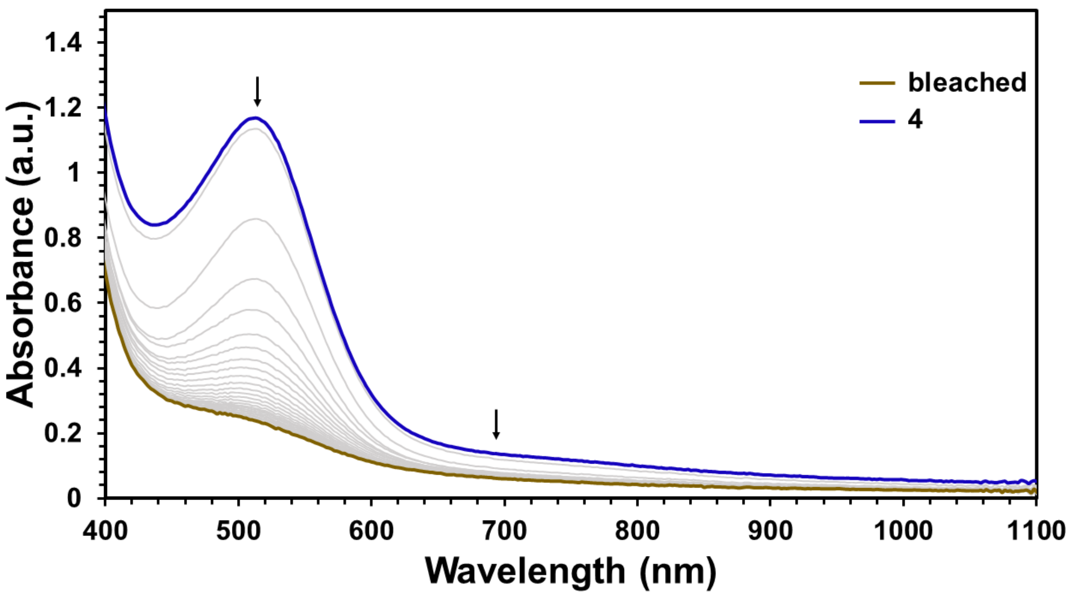

Figure 3A - 8. UV-vis of **3** from a 0.35 mM solution of **1** in toluene with PPh_3 (10 eq.) at −40 °C. Scans are shown every hour over 3 hours.

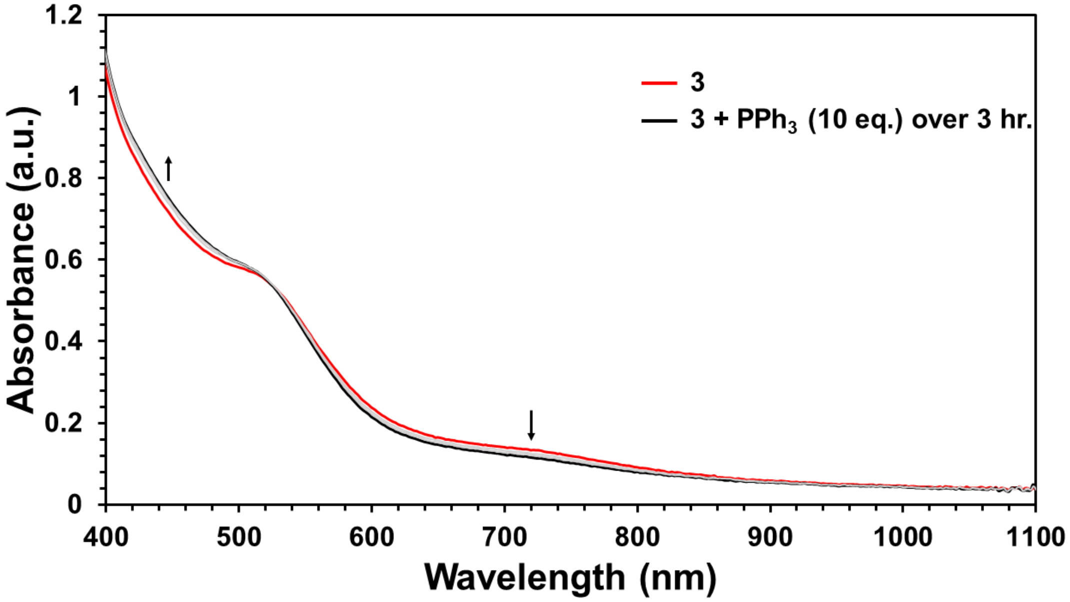

Figure 3A - 9. UV-vis of **3** from a 0.42 mM solution of **1** in toluene with diphenylhydrazine (20 eq.) at −40 °C. Scans are shown every 10 minutes over 4 hours.

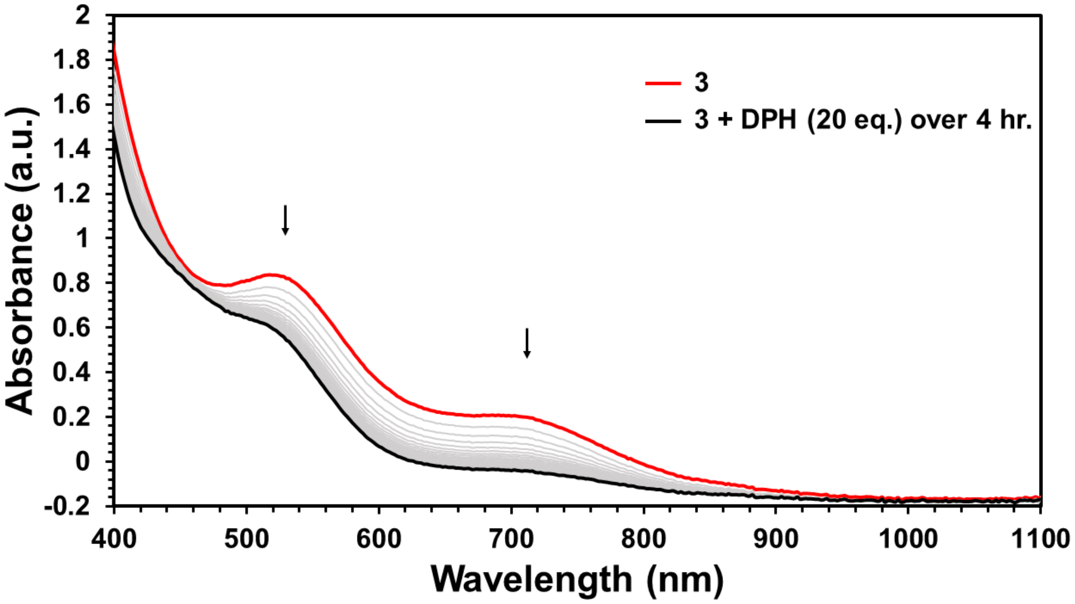

Figure 3A - 10. UV-vis of **3** from a 0.35 mM solution of **1** in toluene with DHA (10 eq.) in 27 µL of toluene at −40 °C. Gray traces move initially due to dilution, then are shown every 10 minutes for 30 minutes.

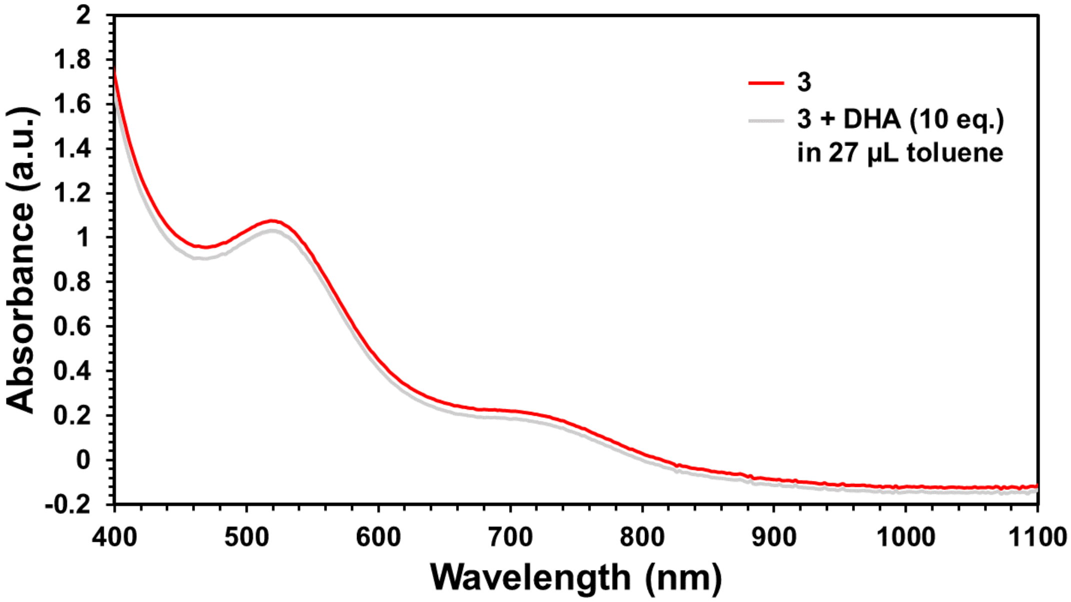

Figure 3A - 11. UV-vis of **3** from a 0.35 mM solution of **1** in toluene at−40 °C after generation with 0.5 or 1 equivalent of O_2 as compared to when excess O_2 is used.

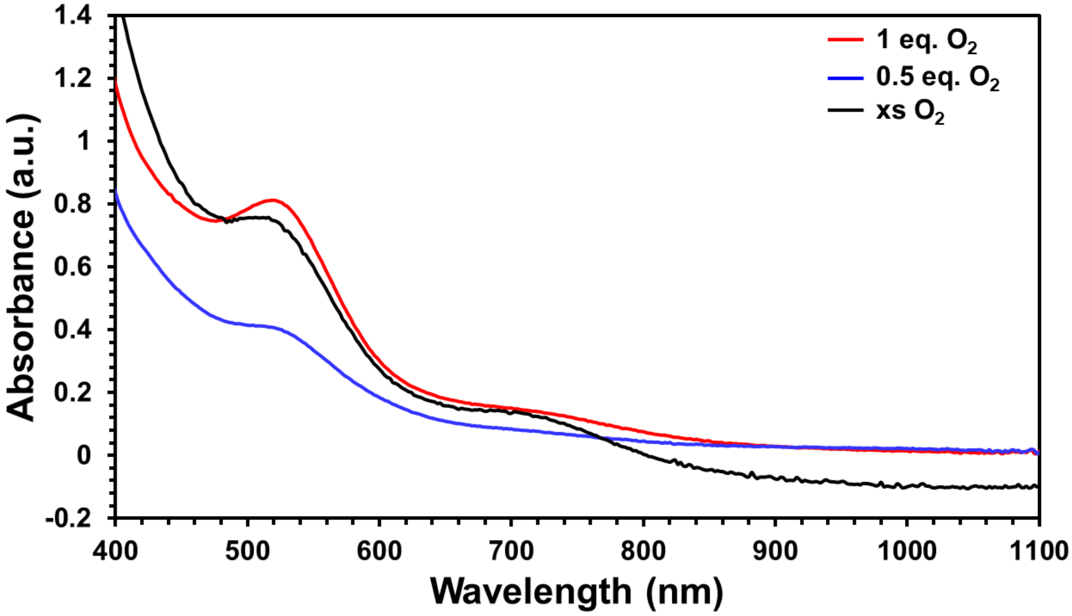

Figure 3A - 12. UV-vis of the reaction of 0.35 mM **1** in toluene with 2 equivalent of TEMPO$^{\bullet}$ after reacting overnight and **4**.

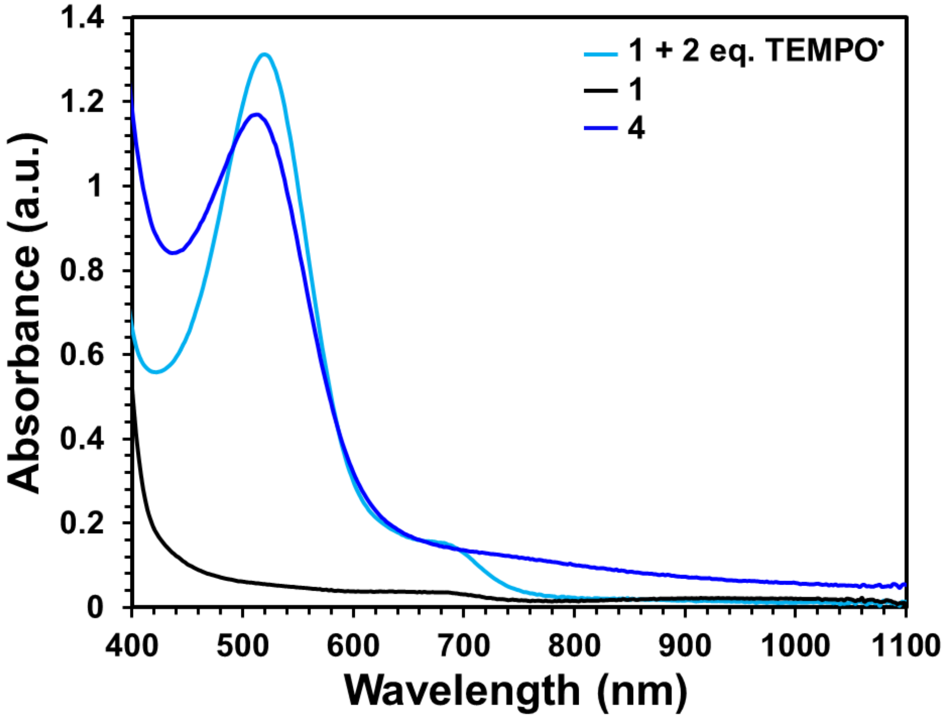

This shows that the second species which forms has features in the same locations as **4**, suggesting that they may be the same species. Eventually, bleaching was observed, which is again consistent with the second species being the same as **4**, which bleaches when allowed to sit at room temperature.

Figure 3A - 13. UV-vis of the reaction of 0.35 mM **1** in toluene with 1 equivalent of TEMPO$^{\bullet}$ with scans every 2 minutes stopping with the first species formed and **3**.

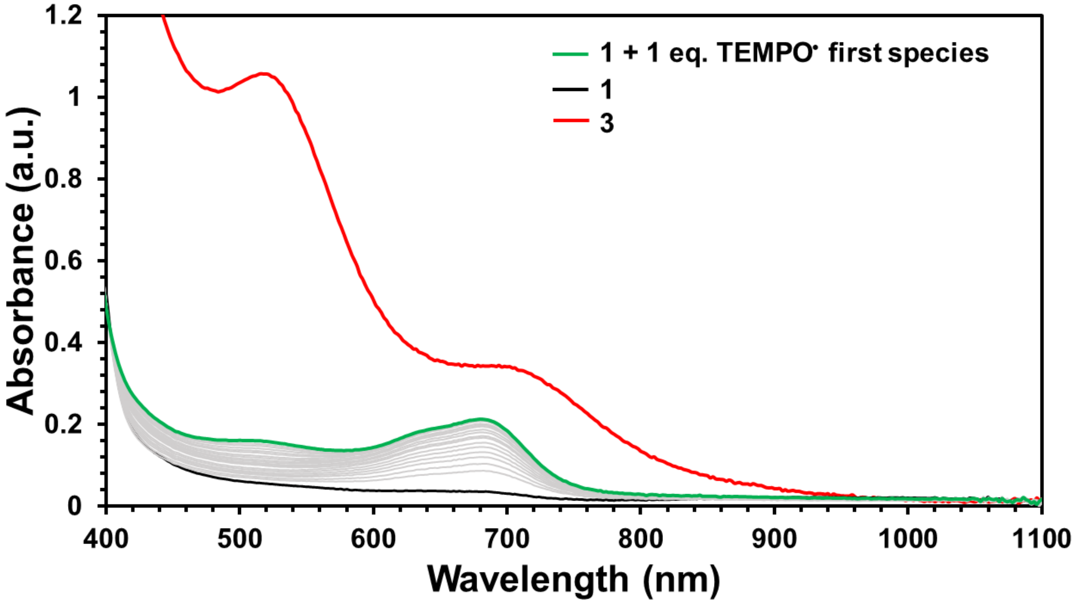

This shows that the first species which forms has features that do not align with **3**, suggesting that they are not the same species.

Figure 3A - 14. IR spectrum of **1** in nujol. Inset: N-H stretches.

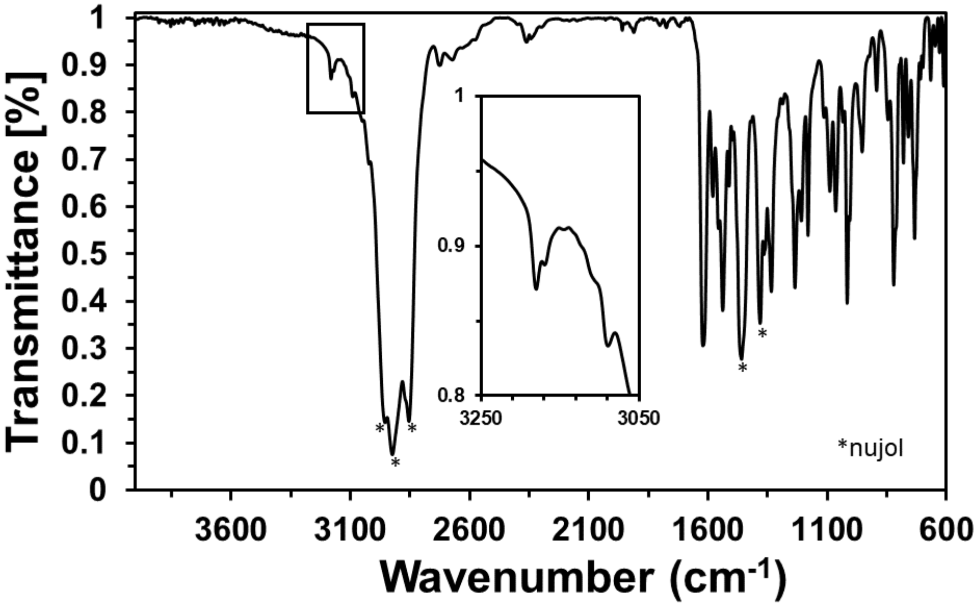

Figure 3A - 15. IR spectrum of **3** in a mixture of products as a thin film on KBr when formed using $^{16}O_2$ or $^{18}O_2$ at room temperature.

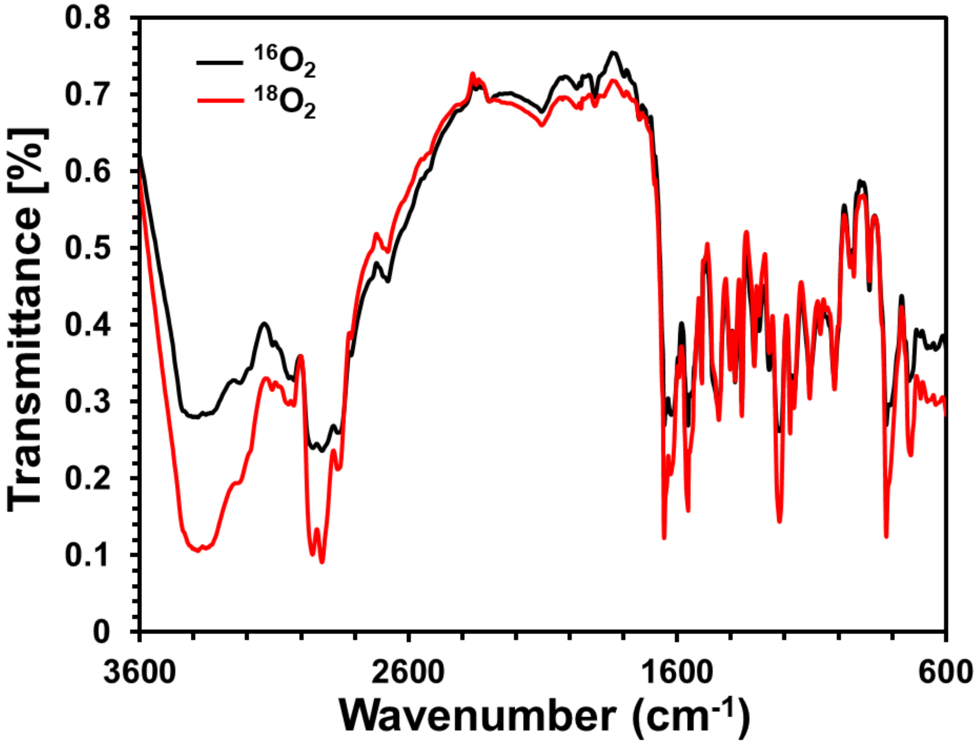

Figure 3A - 16. IR spectrum of **3** in a mixture of products in a concentrated solution of chlorobenzene when formed using $^{16}O_2$ or $^{18}O_2$ at room temperature to look for an O–O stretch. Inset: difference spectrum.

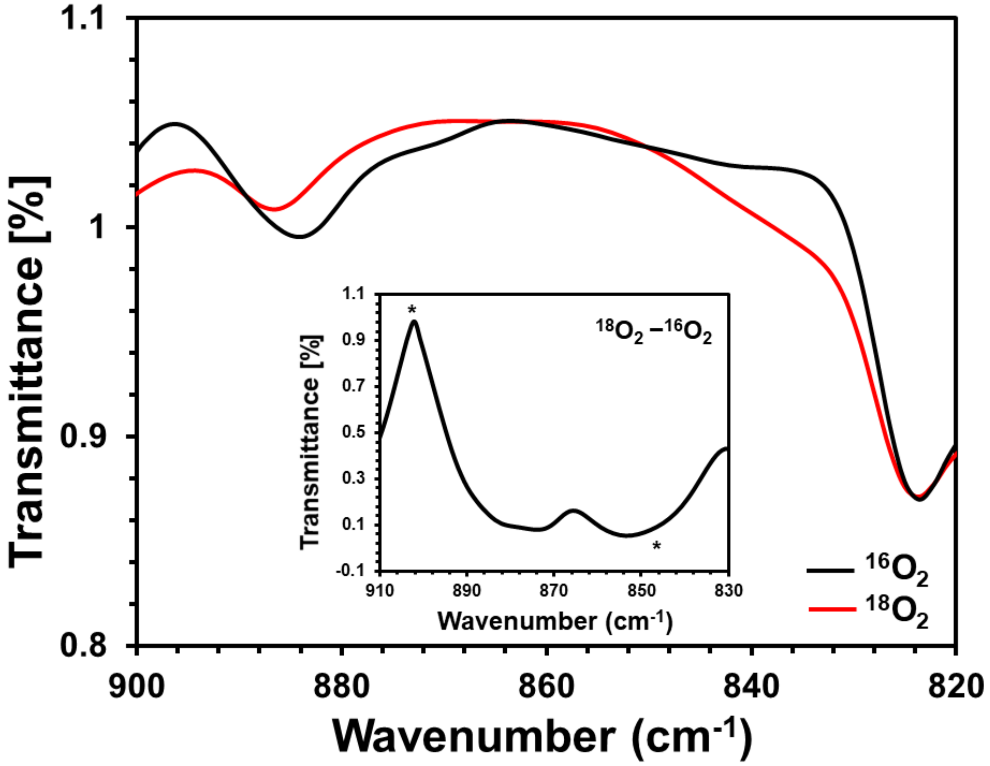

Figure 3A - 17. IR spectrum of **3** in a mixture of products in a concentrated solution of chlorobenzene when formed using $^{16}O_2$ or $^{18}O_2$ at room temperature.

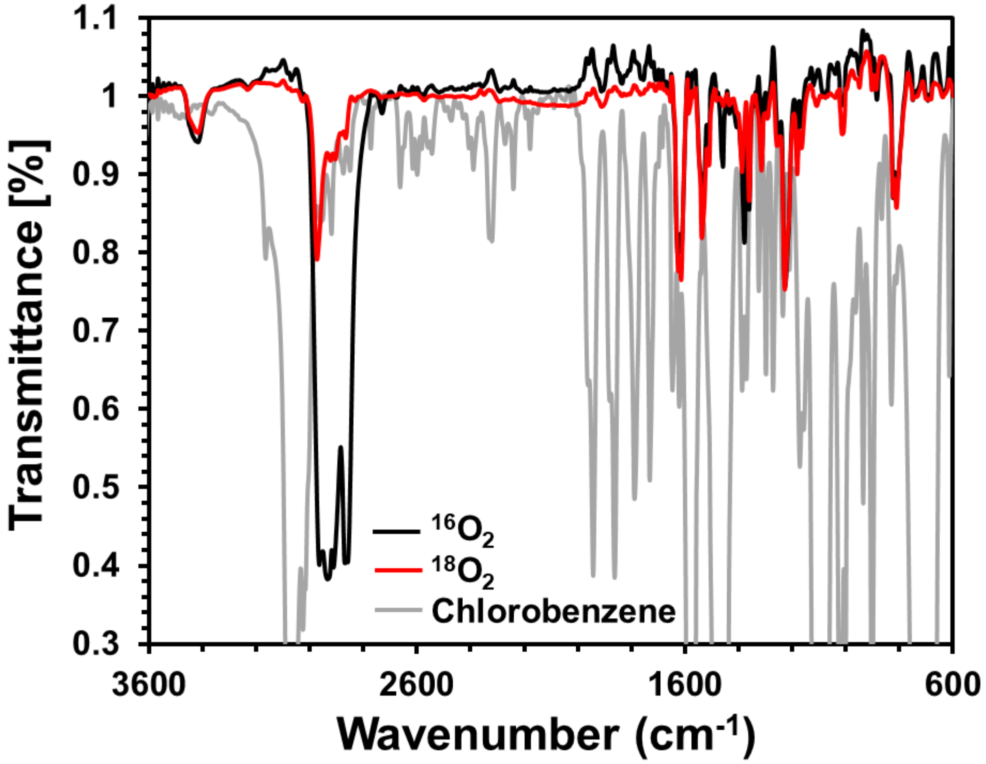

Figure 3A - 18. IR spectra of **3** as concentrated solution in chlorobenzene when proteo- and deuteron-**1** is reacted $^{16}O_2$. **1-H$_2$** and **1-D$_2$** are shown after the solvent subtraction. Chlorobenzene is shown as collected.

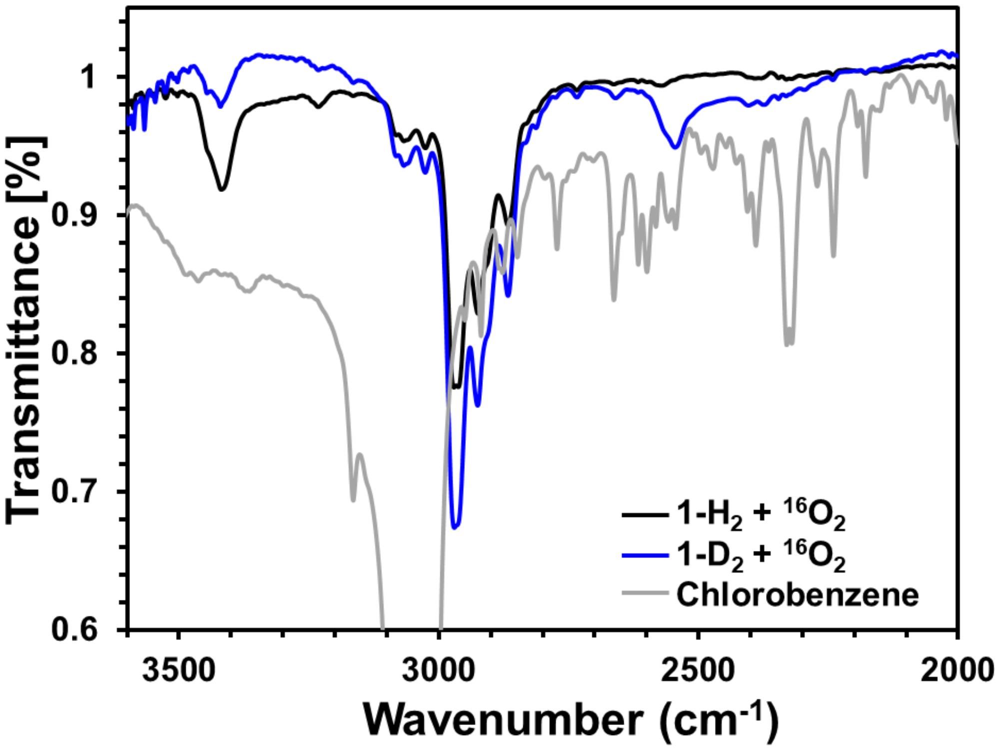

Electron Paramagnetic Resonance (EPR) Spectroscopy

Figure 3A - 19. EPR spectroscopy of a 15 mM solution of **1** in toluene at 15 K. Conditions: MW frequency, 9.392 GHz; MW power, 2.0 mW.

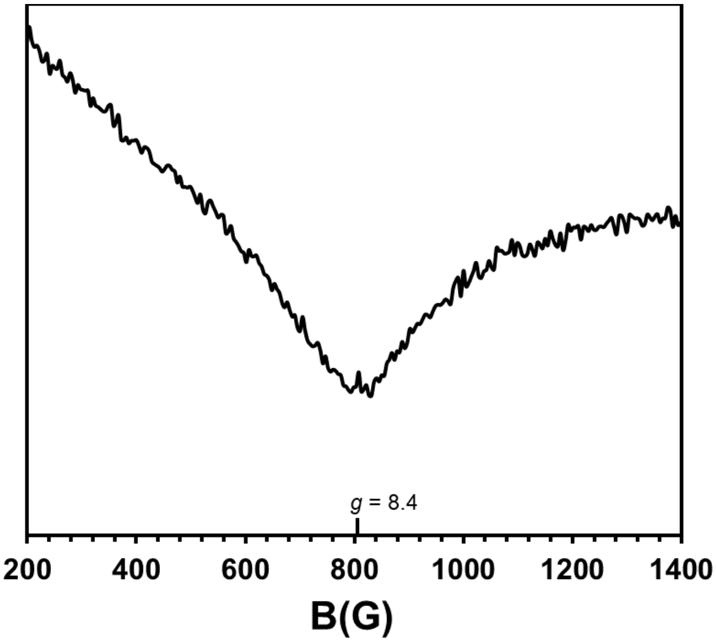

Figure 3A - 20. EPR spectroscopy of a 15 mM solution of **3** in toluene at 15 K. Conditions: MW frequency, 9.381 GHz; MW power, 2.0 mW.

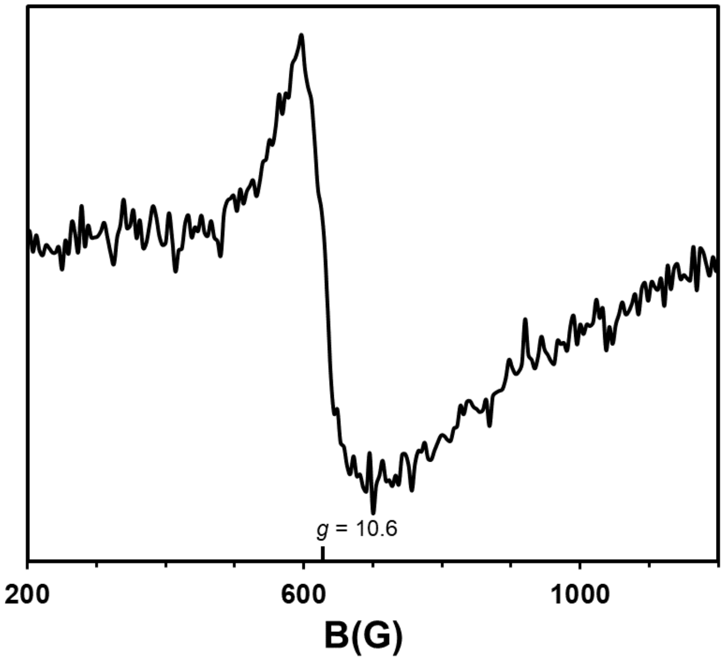

Mössbauer Spectroscopy

Figure 3A - 21. Mössbauer spectrum of **1** with fits. (A) Prepared as a powder. (B) Prepared as a frozen solution in toluene using ^{57}Fe enriched complex **1**. (Bottom, left) Isomer shift and quadrapole splitting parameters and (bottom, right) legend.

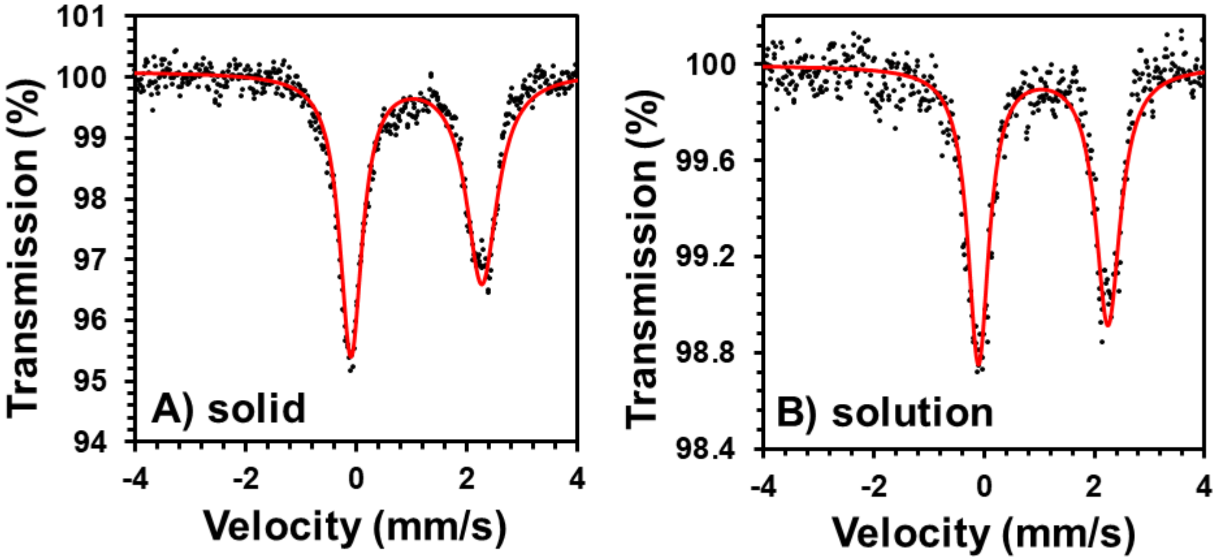

	δ (mm/s)	ΔE_Q (mm/s)
1 (solid)	1.09(0.006)	2.367(0.009)
1 (solution)	1.081(0.009)	2.347(0.016)

• **Raw data**
— **fit**

Figure 3A - 22. (Left) Mössbauer spectrum of **2** with fits. (Right) Parameters for all fits used in overall data fitting. Samples were prepared as a frozen solution in toluene using ^{57}Fe enriched complex **1** that were reacted with O_2 for 6 minutes at −60 °C.

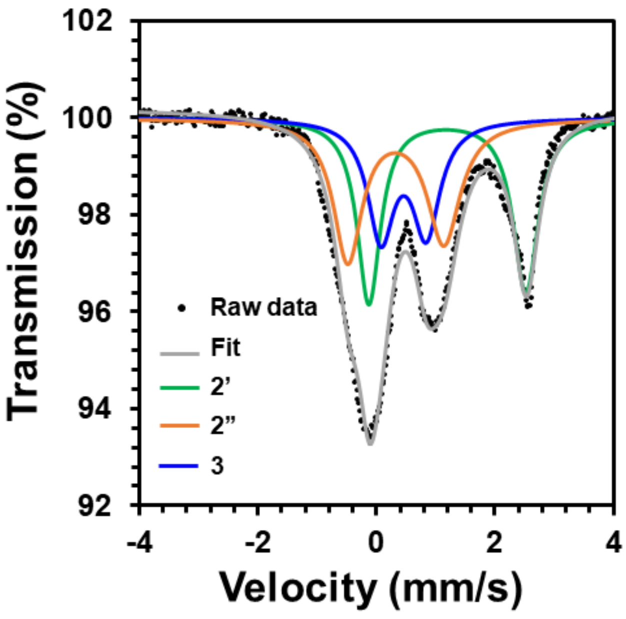

	δ (mm/s)	ΔE_Q (mm/s)	Rel. Area
2'	1.199(6)	2.650(8)	0.428(8)
2"	0.330(4)	1.622(17)	0.398(19)
3	0.460	0.765	0.303(12)

As suggested by other data, **2** is actually a mixture of products. By UV-vis, growth of **3** can be seen while **2** still has features. Therefore, when fitting these data, one Fe center was constrained to the parameters for **3** in all aspects except relative area. The rest was fit using one or two additional Fe species, and the best overall fit was found to require two Fe species in addition to **3**. It is unclear due to the convoluted nature of this reaction exactly what the assignments for **2'** and **2"** are, but from these data it seems that one is an Fe(III) complex and the other is an Fe(II) complex. It seems probable that **2"** may be an Fe(III)-superoxo, but this cannot be definitively assigned from the current data.

Figure 3A - 23. Mössbauer spectrum of **4** as a mixture with **3** with fits. Parameters for all fits used in overall data fitting. Samples were prepared as a frozen solution in toluene using ^{57}Fe enriched complex **1** and allowed to evolve from **3** via warming.

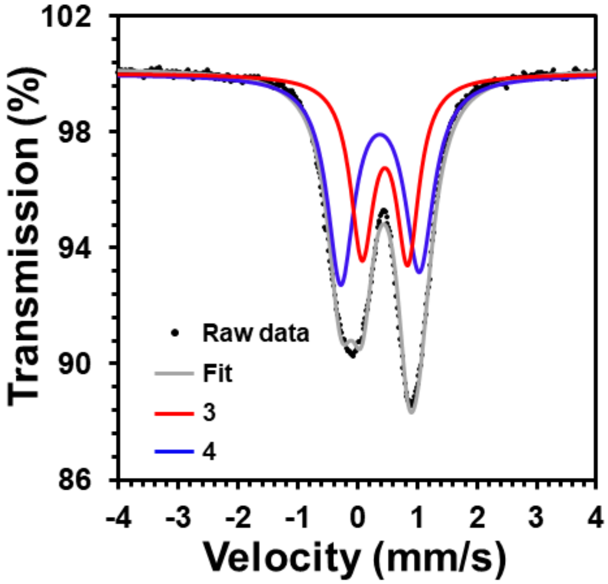

	δ (mm/s)	ΔE_Q (mm/s)	Rel. Area
3	0.460	0.765	0.472(11)
4	0.380(3)	1.315(17)	0.631(11)

X-ray Absorption Spectroscopy

Figure 3A - 24. X-ray absorption spectra of **1** and **3** with K-edge inflection points of 7120 and 7124 eV respectively and pre-edge features at 7112 and 7114 eV respectively. **1** was collected as a solid powder at room temperature and **3** was collected a frozen solution in THF. Inset: Pre-edge features.

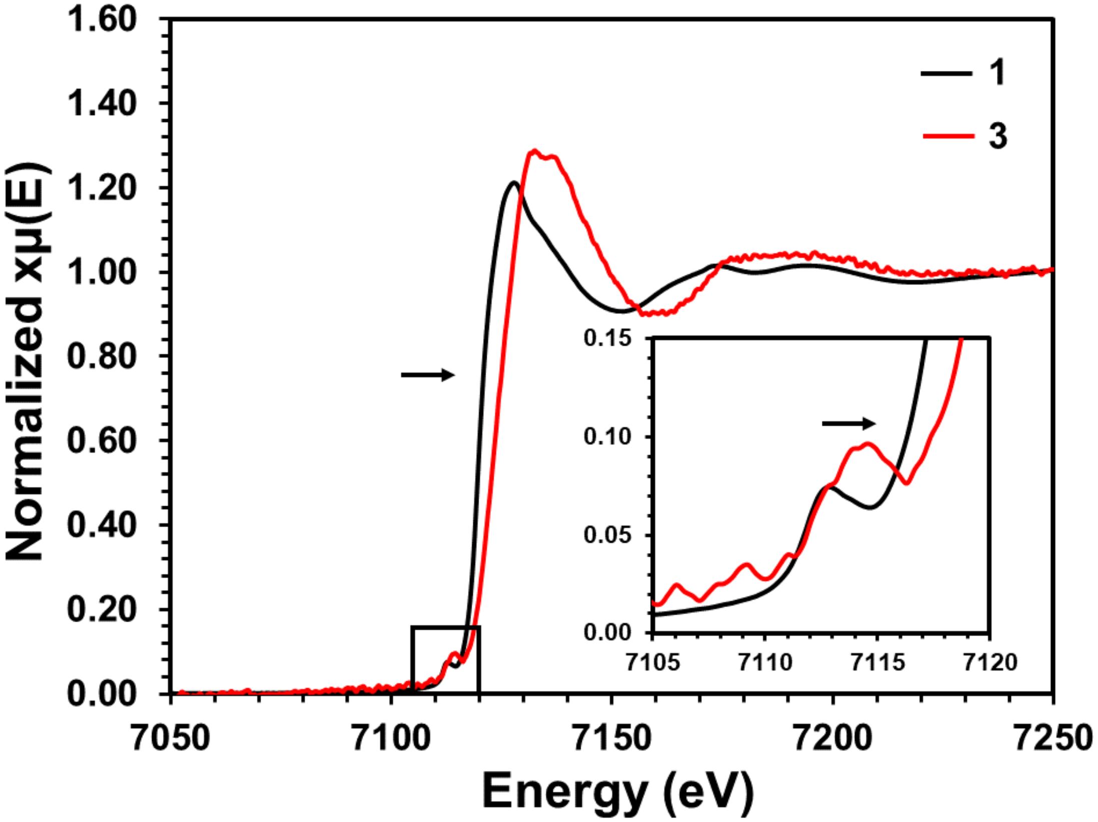

Single Crystal X-ray Diffraction

Table 3A - 1. SXRD of **1**.

Empirical formula	C39H50ClFeN6.5
Formula weight	701.15
Temperature/K	100(2)
Crystal system	triclinic
Space group	P-1
a/Å	14.4920(9)
b/Å	16.1734(10)
c/Å	18.9260(12)
α/°	107.242(2)
β/°	112.381(2)
γ/°	98.388(2)
Volume/Å3	3745.6(4)
Z	4
ρcalcg/cm3	1.243
μ/mm-1	0.510
F(000)	1490.0
Crystal size/mm3	0.1 × 0.1 × 0.02
Radiation	MoKα (λ = 0.71073)
2Θ range for data collection/°	4.082 to 56.844
Index ranges	-19 ≤ h ≤ 19, -21 ≤ k ≤ 21, -25 ≤ l ≤ 25
Reflections collected	127038
Independent reflections	18820 [Rint = 0.0664, Rsigma = 0.0569]
Data/restraints/parameters	18820/0/899
Goodness-of-fit on F2	1.020
Final R indexes [I>=2σ (I)]	R1 = 0.0579, wR2 = 0.1236
Final R indexes [all data]	R1 = 0.1001, wR2 = 0.1402
Largest diff. peak/hole / e Å-3	1.24/-0.73

Kinetic Measurements

Table 3A - 2. Calculated data for Eyring analysis of **2** to **3** at 996 nm.

1/T (1/K)	average ln(k/T)	standard deviation
0.004484305	−10.92381523	0.276300638
0.004587156	−11.04313989	0.239081968
0.004694836	−11.27880141	0.072683884
0.004807692	−11.82830624	0.07226749
0.004926108	−12.14165682	0.112592654

Table 3A - 3. Rates of the reaction of **2** to **3** at 996 nm.

Temperatur e (K)	rate	average rate (1/s)	1/T (1/K)	ln(k/T)	average ln(k/T)	standard deviation
223	0.00315	0.004135	0.004484	−11.1675	−10.9238152	0.27630063
	0.00519		0.004484	−10.6681		
	0.00318		0.004484	−11.1580		
	0.00502		0.004484	−10.7015		
218	0.00263	0.0035625	0.004587	−11.3252	−11.0431398	0.23908196
	0.00323		0.004587	−11.1197		
	0.00376		0.004587	−10.9678		
	0.00463		0.004587	−10.7596		
213	0.00266	0.0026966	0.004695	−11.2907	−11.2788014	0.07268388
	0.00291		0.004695	−11.2008		
	0.00252		0.004695	−11.3447		
208	0.00161	0.00152	0.004808	−11.7690	−11.8283062	0.07226749
	0.00155		0.004808	−11.8070		
	0.0014		0.004808	−11.9088		
203	0.00096	0.0010883	0.004926	−12.2617	−12.1416568	0.11259265
	0.0012		0.004878	−12.0386		
	0.001		0.004878	−12.2209		
	0.00127		0.004878	−11.9819		
	0.001		0.004878	−12.2209		
	0.0011		0.004878	−12.1256		

Table 3A - 4. Raw data for kinetic studies of **2** to **3** at −50 °C at 996 nm with a 0.7 mM solution in toluene.

50-1		50-2		50-3		50-4	
time (s)	intensity (a.u.)	time (s)	intensity (a.u.)	time (s)	intensity (a.u.)	time (s)	intensity (a.u.)
0	0.060367345	0	0.020802446	0	0.032047698	0	0.087381992
60	0.062211044	60	0.031027336	60	0.034477294	60	0.085973132
120	0.113161851	120	0.101999368	120	0.104371667	120	0.169699914
180	0.199385083	180	0.135781131	180	0.178863934	180	0.21977466
240	0.190726103	240	0.102634789	240	0.168836413	240	0.197595498
300	0.186178803	300	0.083724249	300	0.161091224	300	0.176583048
360	0.17455941	360	0.073013088	360	0.15334971	360	0.158349048
420	0.164192677	420	0.066659199	420	0.144541405	420	0.149174056
480	0.151188456	480	0.061674259	480	0.134548262	480	0.143297092
540	0.1379204	540	0.058417521	540	0.121438069	540	0.139520477
600	0.132764305	600	0.055152592	600	0.109927621	600	0.135400408
660	0.127506203	660	0.05351778	660	0.106053717	660	0.132970462
720	0.124907371	720	0.052205589	720	0.100733607	720	0.130464315
780	0.120676461	780	0.049477951	780	0.097191661	780	0.128917574
840	0.1188846	840	0.049794991	840	0.093564548	840	0.127232357
900	0.114258233	900	0.04762592	900	0.091678269	900	0.125760265
960	0.112768737	960	0.047421647	960	0.089230782	960	0.124608582
1020	0.109741714	1020	0.046109701	1020	0.085716787	1020	0.123576768
1080	0.108883698	1080	0.046301856	1080	0.084748855	1080	0.122435026
1140	0.10707703	1140	0.044758912	1140	0.083544204	1140	0.122276091
1200	0.106711538	1200	0.046551924	1200	0.079980764	1200	0.121261625
1260	0.105872208	1260	0.044855158	1260	0.079245849	1260	0.121857316
1320	0.104081662	1320	0.045775567	1320	0.077475427	1320	0.120396569
1380	0.102515702	1380	0.045847072	1380	0.076471059	1380	0.12093631
1440	0.10325185	1440	0.045609517	1440	0.076279856	1440	0.120314822

Table 3A - 5. Raw data for kinetic studies of **2** to **3** at −55 °C at 996 nm with a 0.7 mM solution in toluene.

55-1		55-2		55-3		55-4	
time (s)	intensity (a.u.)	time (s)	intensity (a.u.)	time (s)	intensity (a.u.)	time (s)	intensity (a.u.)
0	0.122669559	0	0.112180011	0	0.127406134	0	0.072407242
90	0.14435754	90	0.130778579	60	0.136138297	60	0.064009807
180	0.173077546	180	0.19059057	120	0.166797143	120	0.084685388
270	0.205497466	270	0.236579604	180	0.217680809	180	0.110170227
360	0.197338867	360	0.20609797	240	0.247902939	240	0.168534454
450	0.185537411	450	0.18769878	300	0.22528987	300	0.168637429
540	0.176982684	540	0.176902408	360	0.209027293	360	0.147780475
630	0.169602219	630	0.171150229	420	0.198413495	420	0.133048685
720	0.164921315	720	0.164745614	480	0.187713227	480	0.124566116
810	0.164476195	810	0.161871043	540	0.185163272	540	0.117082313
900	0.158206843	900	0.15875192	600	0.179594681	600	0.112228019
990	0.158121237	990	0.155154089	660	0.176002419	660	0.106899585
1080	0.153768033	1080	0.154890979	720	0.17369164	720	0.105371846
1170	0.153695476	1170	0.153696892	780	0.171026957	780	0.102241693
1260	0.153406123	1260	0.151096668	840	0.170433836	840	0.100205405
1350	0.150523995	1350	0.14973321	900	0.166018197	900	0.101120404
1440	0.150738243	1440	0.149520907	960	0.164814908	960	0.097214332
1530	0.148752478	1530	0.148332942	1020	0.163462749	1020	0.094760758
1620	0.149123888	1620	0.150092164	1080	0.162337816	1080	0.095142682
1710	0.148491818	1710	0.148394816	1140	0.162074698	1140	0.095799538
1800	0.147344385	1800	0.146959203	1200	0.161467575	1200	0.095221888
1890	0.147209969	1890	0.146785276	1260	0.159786348	1260	0.093901491
1980	0.146819099	1980	0.147852051	1320	0.158934911	1320	0.096048637
2070	0.147488335	2070	0.146538283	1380	0.15887744	1380	0.097279449
2160	0.148206703	2160	0.148408152	1440	0.159289601	1440	0.094076418

Table 3A - 6. Raw data for kinetic studies of **2** to **3** at −60 °C at 996 nm with a 0.7 mM solution in toluene.

60-1		60-2		60-3	
time (s)	intensity (a.u.)	time (s)	intensity (a.u.)	time (s)	intensity (a.u.)
0	0.038173918	0	0.031454992	0	0.055902154
90	0.046992605	90	0.035336517	90	0.067253089
180	0.070231125	180	0.067352131	180	0.082868718
270	0.102667692	270	0.106486734	270	0.113924596
360	0.142522428	360	0.139116698	360	0.155460343
450	0.126710999	450	0.117240443	450	0.154118526
540	0.111066177	540	0.098577616	540	0.138222161
630	0.098589549	630	0.089339646	630	0.12731475
720	0.090757405	720	0.078336858	720	0.117361032
810	0.08349553	810	0.07277705	810	0.111632827
900	0.077956815	900	0.067173524	900	0.105603637
990	0.074165846	990	0.063179638	990	0.097530933
1080	0.071851809	1080	0.05985622	1080	0.097088808
1170	0.06749191	1170	0.057483306	1170	0.092499769
1260	0.065421919	1260	0.055486793	1260	0.090881479
1350	0.063573005	1350	0.053968366	1350	0.088277244
1440	0.063388163	1440	0.052506304	1440	0.086896969
1530	0.060197258	1530	0.052325177	1530	0.086217788
1620	0.059666832	1620	0.050176005	1620	0.084564681
1710	0.060002091	1710	0.049525483	1710	0.084589641
1800	0.058807658				
1890	0.059104174				

Table 3A - 7. Raw data for kinetic studies of **2** to **3** at −65 °C at 996 nm with a 0.7 mM solution in toluene.

65-1		65-2		65-3	
time (s)	intensity (a.u.)	time (s)	intensity (a.u.)	time (s)	intensity (a.u.)
0	−0.008098454	0	−0.019902931	0	0.005023601
90	−0.015098372	90	−0.035465894	90	0.00214342
180	−0.010957906	180	−0.025711474	180	0.005707166
270	−0.003380267	270	−0.018687968	270	0.013750184
360	0.006992907	360	−0.004316518	360	0.025841984
450	0.023930803	450	0.012995775	450	0.041866409
540	0.052604096	540	0.040022507	540	0.072608848
630	0.115386475	630	0.09405642	630	0.114477221
720	0.162643302	720	0.142060011	720	0.134640819
810	0.153716057	810	0.140806006	810	0.138315322
900	0.139966979	900	0.137523927	900	0.13253262
990	0.123391266	990	0.129617235	990	0.120445362
1080	0.106579301	1080	0.12091972	1080	0.108559054
1170	0.092587229	1170	0.110100543	1170	0.099833806
1260	0.081080301	1260	0.093687865	1260	0.095569286
1350	0.070818262	1350	0.077647466	1350	0.086431166
1440	0.064181893	1440	0.069060898	1440	0.078830247
1530	0.055405251	1530	0.061644014	1530	0.074075219
1620	0.049619151	1620	0.052283168	1620	0.071682442
1710	0.045081861	1710	0.046700145	1710	0.066645755
1800	0.040373331	1800	0.04058199	1800	0.064743134
1890	0.03626537	1890	0.037992811	1890	0.059220324
1980	0.034681954	1980	0.034858346	1980	0.057504147
2070	0.0300981	2070	0.03178249	2070	0.05433391
2160	0.028723344	2160	0.026880324	2160	0.049219587

Table 3A - 8. Raw data for kinetic studies of **2** to **3** at −70 °C at 996 nm with a 0.7 mM solution in toluene.

70-1		70-2		70-3	
time (s)	intensity (a.u.)	time (s)	intensity (a.u.)	time (s)	intensity (a.u.)
0	−0.111086231	0	−0.047571219	0	−0.049016509
180	−0.113321874	180	−0.049448628	180	−0.045707223
360	−0.105994867	360	−0.0343815	360	−0.036968307
540	−0.101684529	540	−0.013193093	540	−0.022103876
720	−0.097664892	720	0.021146982	720	−0.003055319
900	−0.091458606	900	0.047809018	900	0.017737603
1080	−0.04406514	1080	0.029648363	1080	0.009835747
1260	−0.010567412	1260	0.017534631	1260	0.002669914
1440	0.026639319	1440	0.007276382	1440	−0.002435897
1620	0.011514591	1620	0.001952698	1620	−0.006123566
1800	−0.003168782	1800	−0.004119997	1800	−0.011442167
1980	−0.015450314	1980	−0.008556121	1980	−0.012940603
2160	−0.024974117	2160	−0.011210453	2160	−0.015530918
2340	−0.032652367	2340	−0.01567444	2340	−0.018462281
2520	−0.038747538	2520	−0.017610412	2520	−0.020184523
2700	−0.043972625	2700	−0.019530379	2700	−0.021930238
2880	−0.049626415	2880	−0.022292334	2880	−0.022829331
3060	−0.052732598	3060	−0.022157311	3060	−0.02359425
3240	−0.056571639	3240	−0.024912142	3240	−0.023952484
3420	−0.059044883	3420	−0.024370416	3420	−0.025226962
3600	−0.062663564	3600	−0.024298329	3600	−0.026712345
3780	−0.064041643	3780	−0.024988319	3780	−0.028086301
3960	−0.066978446	3960	−0.027191158	3960	−0.026466567
4140	−0.067155758	4140	−0.027855564	4140	−0.028905362
4320	−0.069596353	4320	−0.026368292	4320	−0.025987672

Table 3A - 8. Raw data for kinetic studies of **2** to **3** at −70 °C at 996 nm with a 0.7 mM solution in toluene. (continued)

70-4		70-5		70-6	
time (s)	intensity (a.u.)	time (s)	intensity (a.u.)	time (s)	intensity (a.u.)
0	0.00526947	0	0.074129176	0	0.096511924
180	0.003181292	180	0.075904449	180	0.097017546
360	0.007936812	360	0.084922389	360	0.109875984
540	0.01262428	540	0.095134391	540	0.124227115
720	0.022402183	720	0.108311649	720	0.138357787
900	0.034274308	900	0.130299284	900	0.166562038
1080	0.056161811	1080	0.163563658	1080	0.195176288
1260	0.097701934	1260	0.166300529	1260	0.183394631
1440	0.107968484	1440	0.150496021	1440	0.16980488
1620	0.084779464	1620	0.138973443	1620	0.160256923
1800	0.069873362	1800	0.131012377	1800	0.15227035
1980	0.060384784	1980	0.125029533	1980	0.147986292
2160	0.051190898	2160	0.118193783	2160	0.14327852
2340	0.043213012	2340	0.111983961	2340	0.139314339
2520	0.037983119	2520	0.108816732	2520	0.136449256
2700	0.034515965	2700	0.103255842	2700	0.134355937
2880	0.031846629	2880	0.101862274	2880	0.132033334
3060	0.027735758	3060	0.10075897	3060	0.130166687
3240	0.026353908	3240	0.098254518	3240	0.128078842
3420	0.023577265	3420	0.095069223	3420	0.126719427
3600	0.022623359			3600	0.124583773
3780	0.02173668			3780	0.123363445
3960	0.020826048			3960	0.124855821
4140	0.020161671			4140	0.122264148
4320	0.018557667			4320	0.121692849
				4500	0.122958441
				4680	0.121673643
				4860	0.121835691
				5040	0.122779357
				5220	0.119718142

Density Functional Theory (DFT) Calculations

Figure 3A - 25. Calculated structure of **1**. All C–H hydrogen atoms have been removed for clarity.

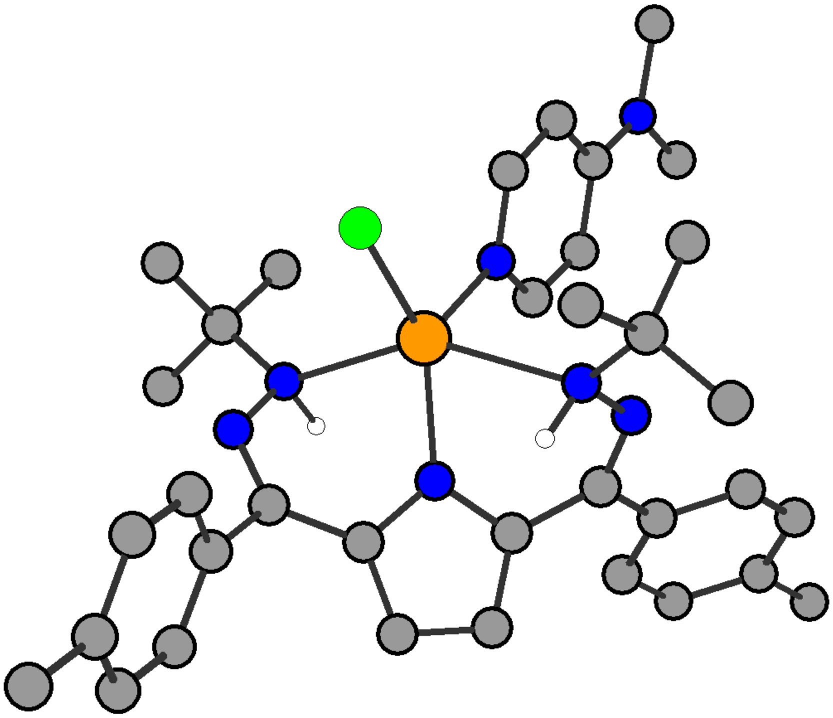

Table 3A - 9. Calculated coordinates of **1**.

N	−1.259456	−0.602763	−0.131906
C	−2.384772	−1.379178	−0.136305
C	−2.105695	−2.608823	−0.733955
C	−0.766892	−2.563555	−1.140810
C	−0.265614	−1.323849	−0.742116
H	−0.229242	−3.331987	−1.676225
H	−2.803262	−3.422062	−0.879058
Fe	−1.099062	1.398691	0.284837
C	1.041363	−0.705726	−0.970905
N	1.602045	0.159005	−0.204046
N	0.971178	0.527978	0.984936
C	1.956638	1.109920	1.946195
C	1.164563	1.663467	3.123025
H	0.504416	2.473153	2.803616
H	1.850978	2.055136	3.878795
H	0.553792	0.886296	3.597826
C	2.731828	2.228982	1.265187
H	2.049493	2.962341	0.829596

Table 3A - 9. Calculated coordinates of **1** continued.

H	3.361680	1.835809	0.466024
H	3.368643	2.727452	2.003434
C	2.911119	0.014560	2.419771
H	2.375079	−0.764207	2.975971
H	3.677549	0.433049	3.079664
H	3.408846	−0.448530	1.563441
N	−3.322643	1.096808	−0.855564
N	−4.069647	0.349399	0.036064
C	−3.654129	−0.830147	0.354670
C	−4.526378	−1.618394	1.254250
C	−1.737295	−0.928301	−2.269753
C	−5.850127	−1.227689	1.479804
C	−6.673559	−1.958156	2.317206
C	−6.221136	−3.114228	2.953443
C	−4.900348	−3.498400	2.736230
C	−4.064504	−2.763730	1.906865
H	−6.222672	−0.341643	0.978907
H	−7.699231	−1.633368	2.474782
H	−4.515127	−4.392255	3.220336
H	−3.038833	−3.084208	1.756825
C	−7.129976	−3.911496	3.838318
H	−8.169668	−3.595568	3.721039
H	−6.859715	−3.790174	4.894812
H	−7.071994	−4.980018	3.605891
C	1.911514	0.174177	−3.108542
C	2.520806	0.033864	−4.343504
C	2.986840	−1.204379	−4.783766
C	2.828941	−2.296071	−3.933693
C	2.210149	−2.165090	−2.695463
H	1.554344	1.144776	−2.778826
H	2.634976	0.906166	−4.982516
H	2.114573	−3.034241	−2.052018
H	3.197966	−3.270135	−4.243155
Cl	−0.241042	3.240868	−0.680213
C	−4.167806	2.045113	−1.632478
C	−4.750582	3.082377	−0.685628
H	−5.348478	2.600055	0.091288
H	−5.390869	3.774045	−1.242143
H	−3.954326	3.659529	−0.208759
C	−3.254550	2.701450	−2.657186
H	−2.452830	3.264663	−2.174738
H	−3.838154	3.379582	−3.287114
H	−2.796945	1.952096	−3.314366
C	−5.282710	1.284621	−2.349430
H	−5.929194	0.769929	−1.633525
H	−4.865452	0.535865	−3.032349
H	−5.894945	1.974101	−2.939678
N	−2.108422	2.096353	2.031403
C	−3.386329	1.752473	4.032304

Table 3A - 9. Calculated coordinates of **1** continued.

C	−3.581499	3.136244	4.211692
C	−2.990655	3.970128	3.241012
C	−2.288231	3.415306	2.196232
C	−2.660307	1.298027	2.954786
H	0.529637	−0.289158	1.420642
C	3.632246	−1.339583	−6.133435
H	2.933889	−1.059279	−6.929489
H	3.961957	−2.364614	−6.318693
H	4.503091	−0.682184	−6.224199
H	−2.516086	0.230259	2.818607
H	−3.800423	1.026367	4.718859
H	−2.823503	0.487387	−1.511443
H	−1.832917	4.048838	1.439966
H	−3.085145	5.047048	3.285529
N	−4.293237	3.634227	5.256511
C	−4.971568	2.733445	6.161525
C	−4.516484	5.058289	5.369239
H	−5.098580	5.453737	4.524901
H	−3.571090	5.608637	5.422380
H	−5.073188	5.260090	6.284061
H	−5.678112	2.080853	5.631080
H	−5.531294	3.320340	6.889372
H	−4.264167	2.099115	6.709754

Figure 3A - 26. Calculated structure of a high spin Fe(III)(^{tBu,Tol}DHP-H$_2$)(DMAP)(Cl)(OO$^{\bullet}$). All C–H hydrogen atoms have been removed for clarity.

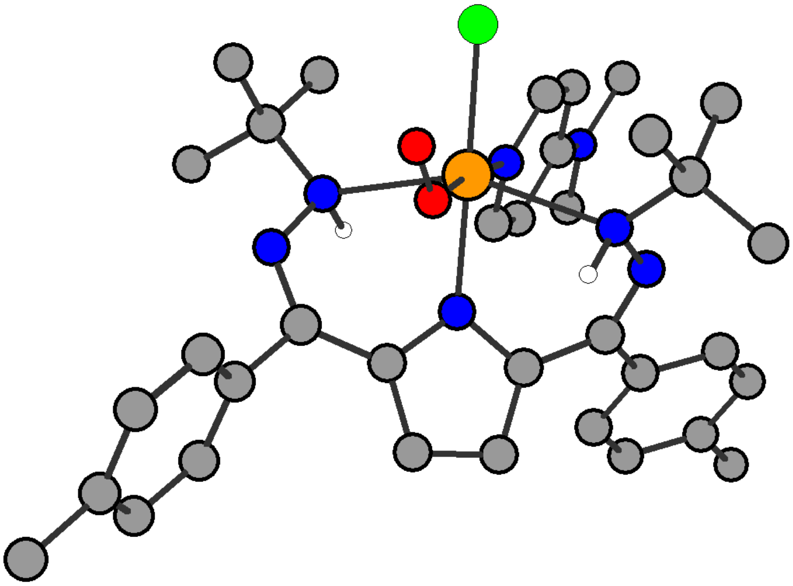

Table 3A - 10. Calculated coordinates of a high spin Fe(III)($^{t\text{Bu,Tol}}$DHP-H$_2$)(DMAP)(Cl)(OO$^{\bullet}$).

N	−1.506615	−0.064433	−0.423159
C	−2.622683	−0.849043	−0.513275
C	−2.280722	−2.117676	−0.984665
C	−0.904286	−2.103350	−1.206514
C	−0.445550	−0.836151	−0.825920
H	−0.305121	−2.908636	−1.602879
H	−2.963301	−2.937364	−1.160808
Fe	−1.476139	2.045426	−0.346653
C	0.913841	−0.326718	−0.886505
N	1.388341	0.722267	−0.312793
N	0.568132	1.460491	0.558340
C	1.440411	2.369466	1.381719
C	0.555233	3.085374	2.389109
H	−0.176119	3.723918	1.890518
H	1.181660	3.713052	3.030140
H	0.026349	2.374738	3.034969
C	2.116484	3.367814	0.455397
H	1.376792	3.968307	−0.080702
H	2.745673	2.848294	−0.270159
H	2.746203	4.040496	1.046475
C	2.476721	1.536307	2.131482
H	1.985976	0.822493	2.804399
H	3.108938	2.190354	2.740570
H	3.110766	0.979694	1.437774
N	−3.594987	1.564604	−1.379225
N	−4.377178	0.822568	−0.501435
C	−3.938422	−0.327560	−0.127054
C	−4.805673	−1.097992	0.795784
C	1.905369	−1.064509	−1.721382
C	−6.129948	−0.704208	1.021921
C	−6.922962	−1.369117	1.937576
C	−6.440095	−2.465477	2.658137
C	−5.127987	−2.863293	2.423814
C	−4.322008	−2.192213	1.513063
H	−6.519484	0.146247	0.474205
H	−7.943814	−1.032200	2.100981
H	−4.719240	−3.709791	2.969919
H	−3.296568	−2.514328	1.368173
C	−7.318677	−3.198788	3.627932
H	−7.930131	−2.508174	4.218142
H	−6.728530	−3.811176	4.315397
H	−8.007001	−3.868211	3.097515
C	2.500000	−0.447712	−2.818997
C	3.437820	−1.124799	−3.586275
C	3.819828	−2.428357	−3.278167

Table 3A - 10. Calculated coordinates of a high spin Fe(III)($^{t\mathrm{Bu,Tol}}$DHP-H$_2$)(DMAP)(Cl)(OO$^{\bullet}$) continued.

C	3.236371	−3.031738	−2.164369
C	2.293838	−2.363400	−1.398219
H	2.219064	0.569320	−3.072029
H	3.886133	−0.626340	−4.441854
H	1.869421	−2.849233	−0.525030
H	3.534397	−4.038145	−1.881717
O	−0.660087	1.911858	−2.212541
C	−4.439427	2.517090	−2.168043
C	−5.050415	3.537581	−1.221266
H	−5.658396	3.041696	−0.461275
H	−5.688199	4.223916	−1.787055
H	−4.266695	4.121388	−0.732019
C	−3.529907	3.197651	−3.178927
H	−2.766435	3.801482	−2.685401
H	−4.129467	3.852270	−3.818528
H	−3.035223	2.466235	−3.828094
C	−5.526916	1.739315	−2.905915
H	−6.177783	1.209889	−2.205414
H	−5.084455	1.003618	−3.587564
H	−6.138511	2.423814	−3.502166
N	−2.451510	2.014251	1.642802
C	−3.144952	0.824832	3.612662
C	−3.811978	1.952881	4.127118
C	−3.758920	3.111932	3.328297
C	−3.086270	3.091125	2.128288
N	−4.464361	1.924628	5.316266
H	−4.244033	4.030587	3.630033
C	−2.497061	0.911304	2.402574
H	0.107365	0.809141	1.204040
C	4.802858	−3.174301	−4.131206
H	5.421842	−2.491456	−4.719790
H	4.281519	−3.836201	−4.833592
H	5.463590	−3.799030	−3.521994
Cl	−1.396147	4.328231	−0.449509
H	−3.034714	3.983336	1.513516
H	−3.140998	−0.122793	4.134468
H	−3.117976	0.939644	−2.039647
C	−5.181530	3.093507	5.774994
C	−4.523687	0.698674	6.081596
H	−5.985605	3.377093	5.084140
H	−4.512414	3.953707	5.893808
H	−5.629728	2.876917	6.743943
H	−5.047751	−0.097230	5.536711
H	−5.061280	0.887250	7.010268

Table 3A - 10. Calculated coordinates of a high spin Fe(III)($^{t\mathrm{Bu,Tol}}$DHP-H$_2$)(DMAP)(Cl)(OO$^{\bullet}$) continued.

H	−3.521395	0.337412	6.338501
H	−1.997247	0.036508	1.999963
O	−0.217703	2.760876	−2.985738

Figure 3A - 27. Calculated structure of a high spin Fe(III)($^{t\mathrm{Bu,Tol}}$DHP-H$^{\bullet}$)(DMAP)(Cl)(OOH), **3**. All C–H hydrogen atoms have been removed for clarity.

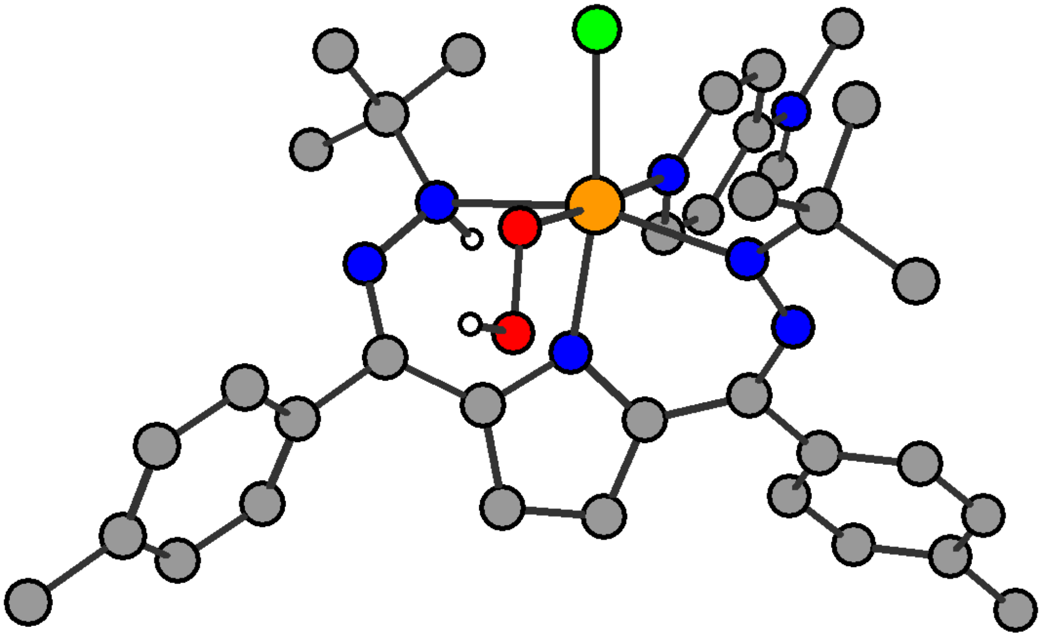

Table 3A - 11. Calculated coordinates of a high spin Fe(III)($^{t\mathrm{Bu,Tol}}$DHP-H$^{\bullet}$)(DMAP)(Cl)(OOH), **3**.

N	−1.506731	−0.144120	−0.273740
C	−2.585739	−0.979164	−0.205860
C	−2.169603	−2.312761	−0.447304
C	−0.816580	−2.263900	−0.702969
C	−0.422803	−0.913507	−0.566294
H	−0.182490	−3.090694	−0.980786
H	−2.814691	−3.177948	−0.494272
Fe	−1.659687	1.941493	−0.448400
C	0.897780	−0.335784	−0.776176
N	1.315025	0.783143	−0.301919
N	0.521166	1.507932	0.577135
C	1.385015	2.469534	1.341771

Table 3A - 11. Calculated coordinates of a high spin Fe(III)($^{t\mathrm{Bu,Tol}}$DHP-H$^{\bullet}$)(DMAP)(Cl)(OOH), **3** continued.

C	0.509810	3.179694	2.362167
H	−0.250487	3.789914	1.873172
H	1.137775	3.831662	2.976897
H	0.018606	2.464053	3.032388
C	1.994976	3.463681	0.365263
H	1.215249	4.006916	−0.173288
H	2.629430	2.945829	−0.356988
H	2.607982	4.183248	0.917365
C	2.477760	1.693126	2.074100
H	2.041891	0.980021	2.784481
H	3.110968	2.384445	2.639295
H	3.103544	1.140808	1.368816
N	−3.729213	1.582251	−1.022828
N	−4.418194	0.606842	−0.570568
C	−3.928466	−0.530826	−0.065230
C	−4.948139	−1.413013	0.519772
C	1.871351	−1.031637	−1.664251
C	−6.293953	−1.294648	0.152397
C	−7.261728	−2.103302	0.720668
C	−6.934664	−3.066097	1.675670
C	−5.595036	−3.179908	2.048957
C	−4.620351	−2.372960	1.488271
H	−6.564757	−0.563779	−0.599892
H	−8.295873	−1.994267	0.404471
H	−5.310524	−3.913282	2.799756
H	−3.590350	−2.473233	1.813412
C	−7.978234	−3.959225	2.274173
H	−8.974082	−3.712771	1.899607
H	−7.995190	−3.871266	3.366452
H	−7.777463	−5.009897	2.033115
C	2.416888	−0.354480	−2.754183
C	3.336715	−0.972954	−3.588100
C	3.750772	−2.284059	−3.361653
C	3.226244	−2.946578	−2.253148
C	2.301324	−2.335403	−1.419699
H	2.117559	0.671911	−2.935126
H	3.743243	−0.424766	−4.434300
H	1.937735	−2.869506	−0.547891
H	3.555762	−3.957783	−2.028406
O	−0.849292	1.968811	−2.153986
C	−4.570079	2.513902	−1.855938
C	−4.906562	3.748898	−1.017631
H	−5.449045	3.458377	−0.112584
H	−5.551588	4.411745	−1.603213

Table 3A - 11. Calculated coordinates of a high spin Fe(III)($^{t\mathrm{Bu,Tol}}$DHP-H$^{\bullet}$)(DMAP)(Cl)(OOH), **3** continued.

H	−4.006442	4.300407	−0.743291
C	−3.748039	2.899805	−3.082397
H	−2.799930	3.359853	−2.801209
H	−4.318017	3.613366	−3.684979
H	−3.535667	2.019521	−3.695900
C	−5.874536	1.857858	−2.301983
H	−6.551509	1.691471	−1.461759
H	−5.695633	0.901002	−2.799764
H	−6.369300	2.527008	−3.012365
N	−2.505517	1.945891	1.732558
C	−2.978389	0.923592	3.856991
C	−3.575099	2.099270	4.352725
C	−3.626900	3.183295	3.456109
C	−3.091885	3.058363	2.195785
C	−2.475830	0.904482	2.573821
H	0.066180	0.877673	1.245037
C	4.713794	−2.967436	−4.286438
H	5.291282	−2.245913	−4.871042
H	4.180284	−3.613772	−4.994305
H	5.414715	−3.599076	−3.731747
Cl	−1.474165	4.246297	−0.386704
H	−2.021502	−0.003713	2.189898
H	−3.102683	3.900870	1.512947
H	−4.074582	4.127910	3.734490
H	−2.907828	0.026555	4.458397
N	−4.068812	2.190521	5.613544
C	−4.688367	3.420106	6.056816
C	−3.952548	1.074628	6.524594
H	−5.516634	3.711012	5.400679
H	−3.970503	4.250332	6.091327
H	−5.090780	3.274386	7.058401
H	−2.904570	0.797937	6.695783
H	−4.483423	0.189864	6.152094
H	−4.388928	1.353363	7.483156
O	−0.935083	0.798721	−2.939653
H	−0.469141	1.084102	−3.741083

Figure 3A - 28. Spin density plot of **3** at an iso value of 0.003.

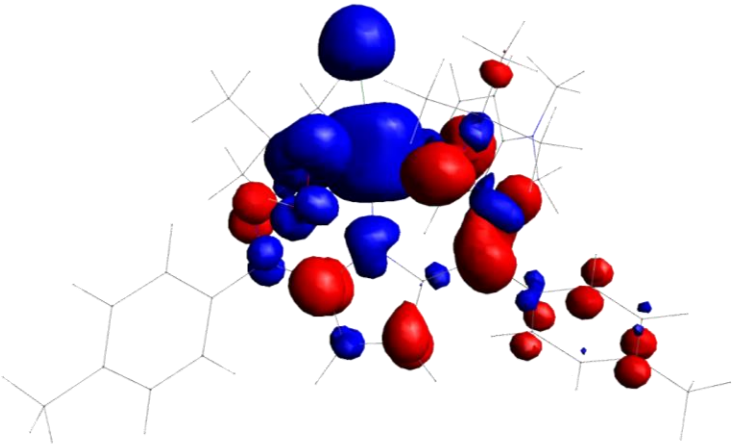

Figure 3A - 29. TDDFT of Fe(III)(^{tBu,Tol}DHP-H_2)(DMAP)(Cl)(OO$^\bullet$) (left) and Fe(III)(^{tBu,Tol}DHP-H$^\bullet$)(DMAP)(Cl)(OOH) (right), as compared to **3**.

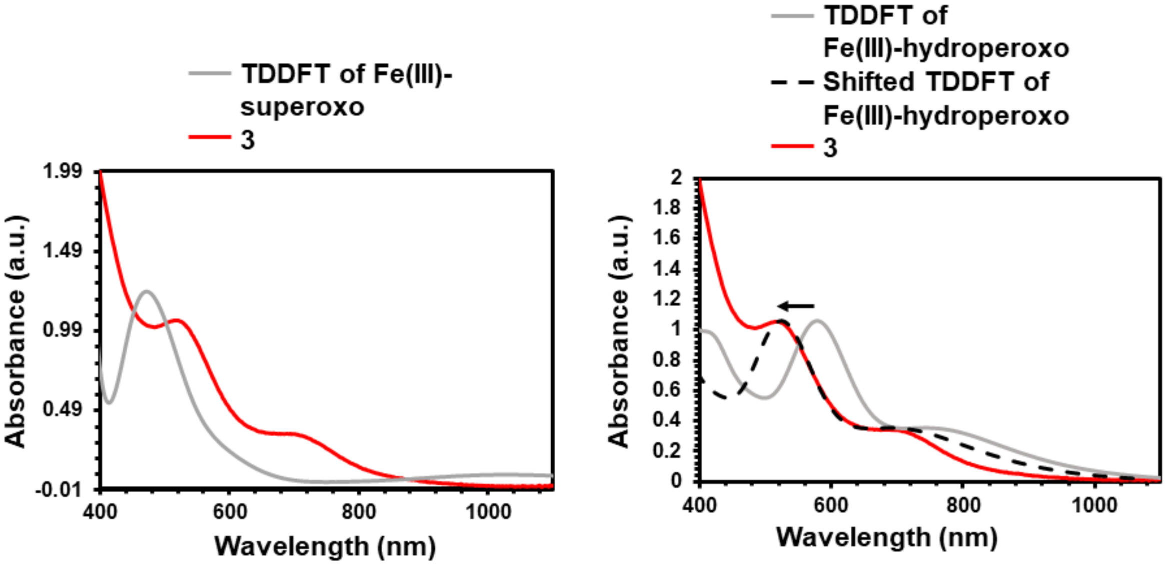

Figure 3A - 30. Molecular orbitals involved in transitions contributing to states involved in the major features by UV-vis spectroscopy in **3** as calculated by TDDFT. Percentages to the right of the transition show the contribution of that transition to each calculated state. Only contributions above 10% are listed.

State 4: 795 nm

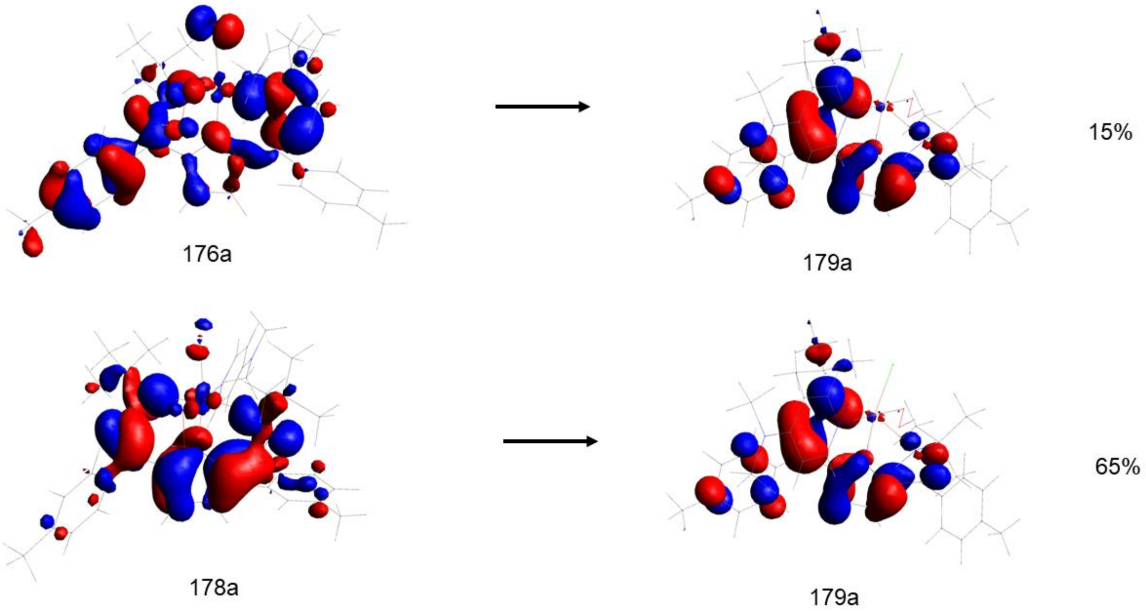

State 5: 714 nm

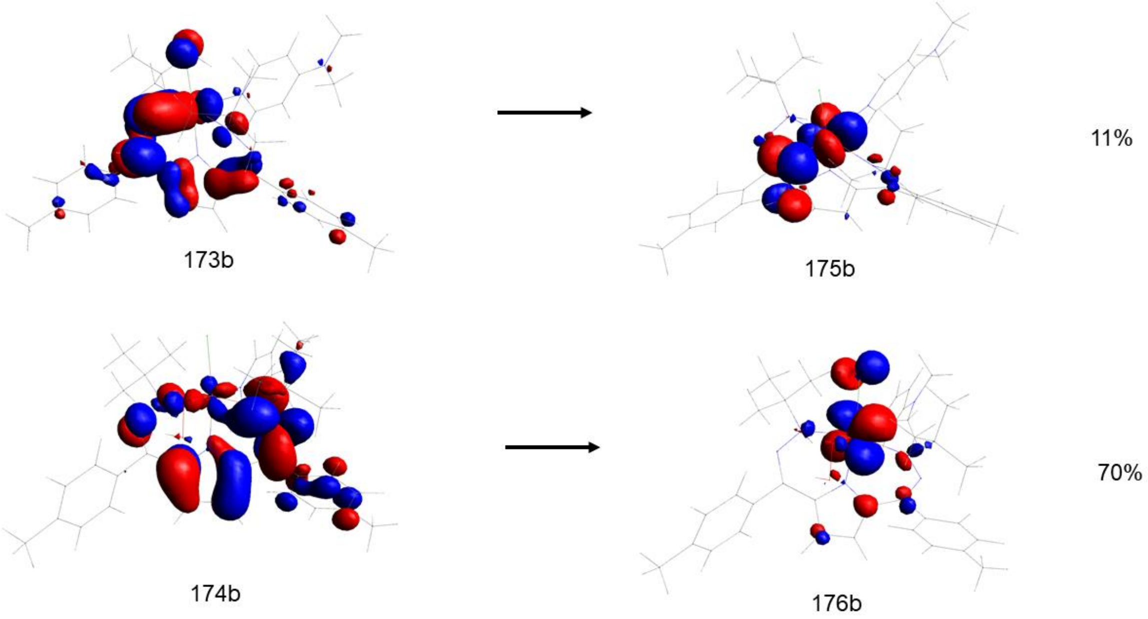

Figure 3A - 30. Molecular orbitals involved in transitions contributing to states involved in the major features by UV-vis spectroscopy in **3** as calculated by TDDFT. Percentages to the right of the transition show the contribution of that transition to each calculated state. Only contributions above 10% are listed continued.

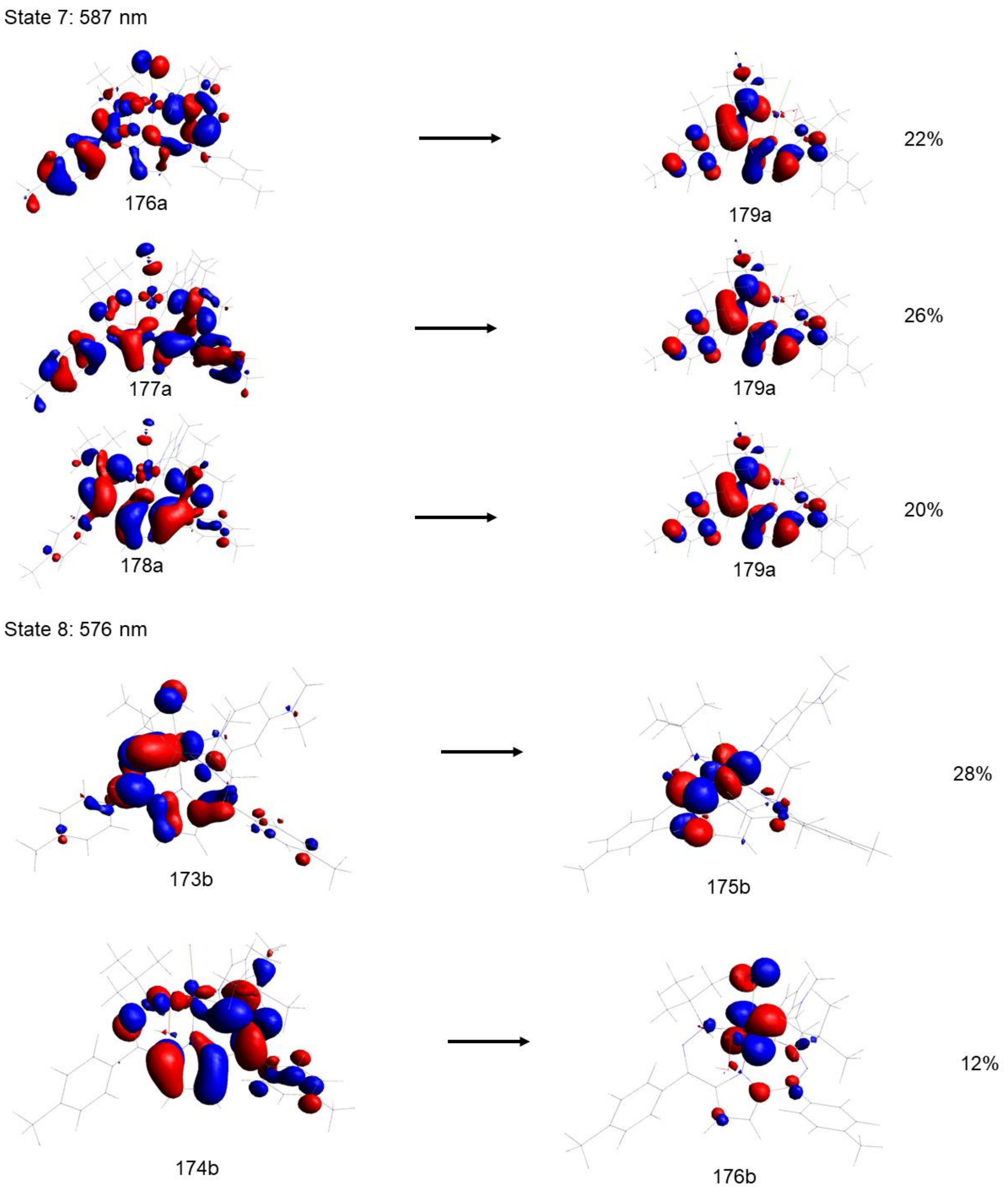

Gas Chromatography-Mass Spectrometry (GC-MS)

Figure 3A - 31. Mass spectrometry of the reaction of **1** with $^{16}O_2$ or $^{18}O_2$ and PPh_3 to form $OPPh_3$

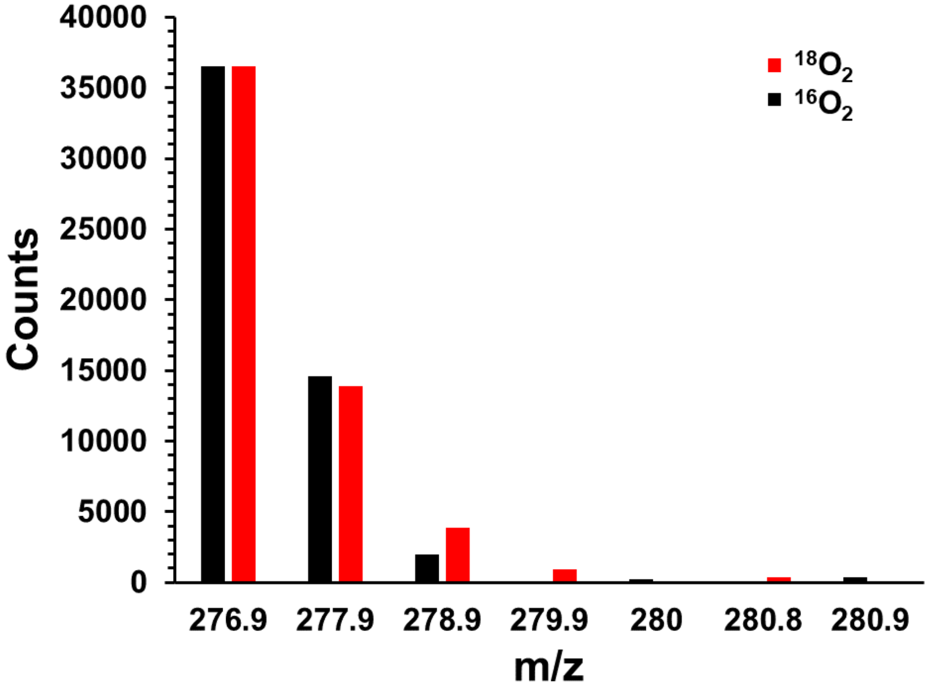

Scheme 3A - 1. Conditions and resulting products observed by GC-MS. Yields are relative to 1 equivalent of **1.**

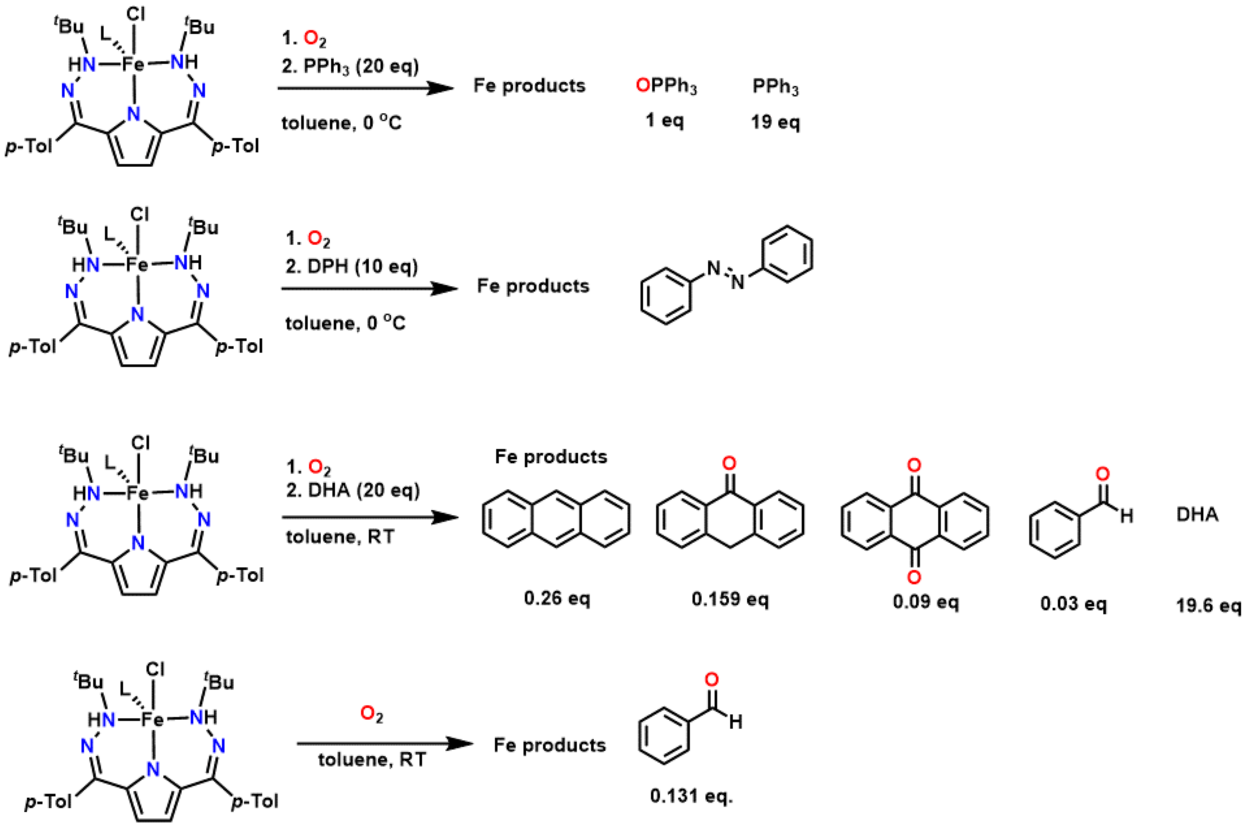

Appendix 4: Supporting Information for Chapter 4

NMR Spectra

Figure 4A - 1. ^{1}H NMR of **1-Fe** in CD_3CN.

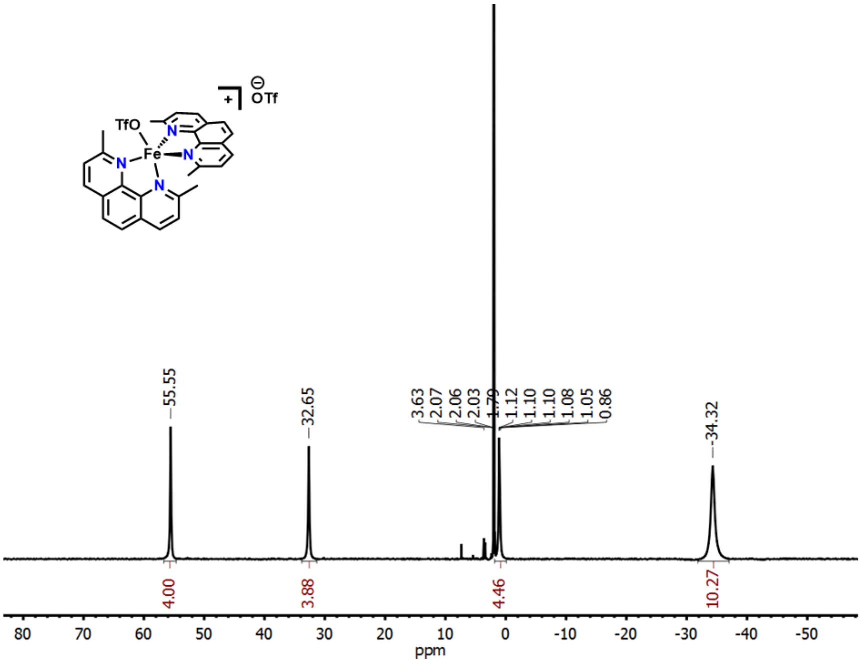

Figure 4A - 2. ^{19}F NMR of **1-Fe** in CD_3CN.

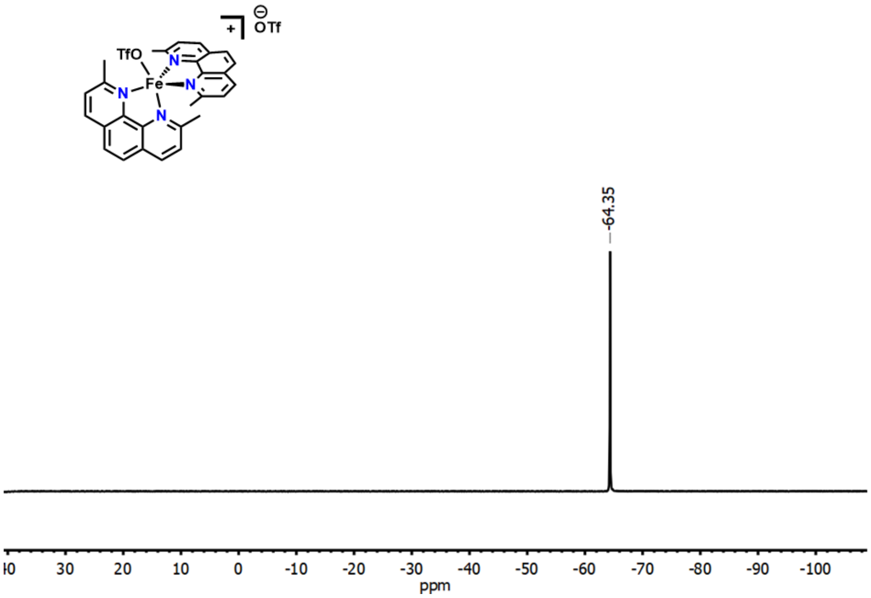

Figure 4A - 3. ^{1}H NMR of **3-Fe** in C_6D_6.

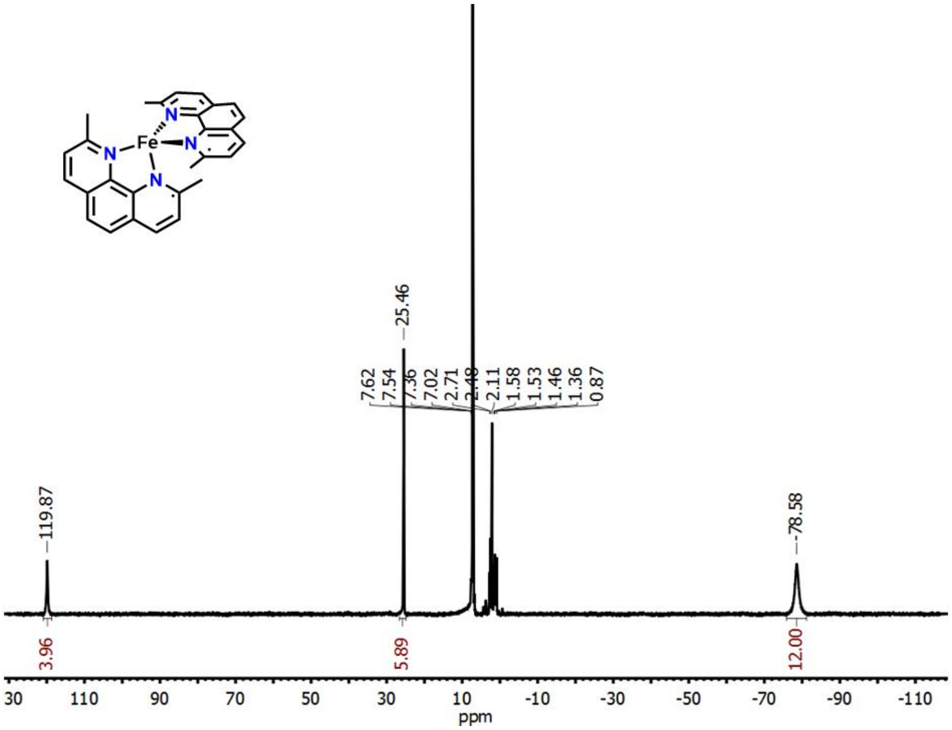

Figure 4A - 4. ^{1}H NMR of **3-Fe** with excess AgOTf in CD_3CN stacked with **1-Fe** and **3-Fe**.

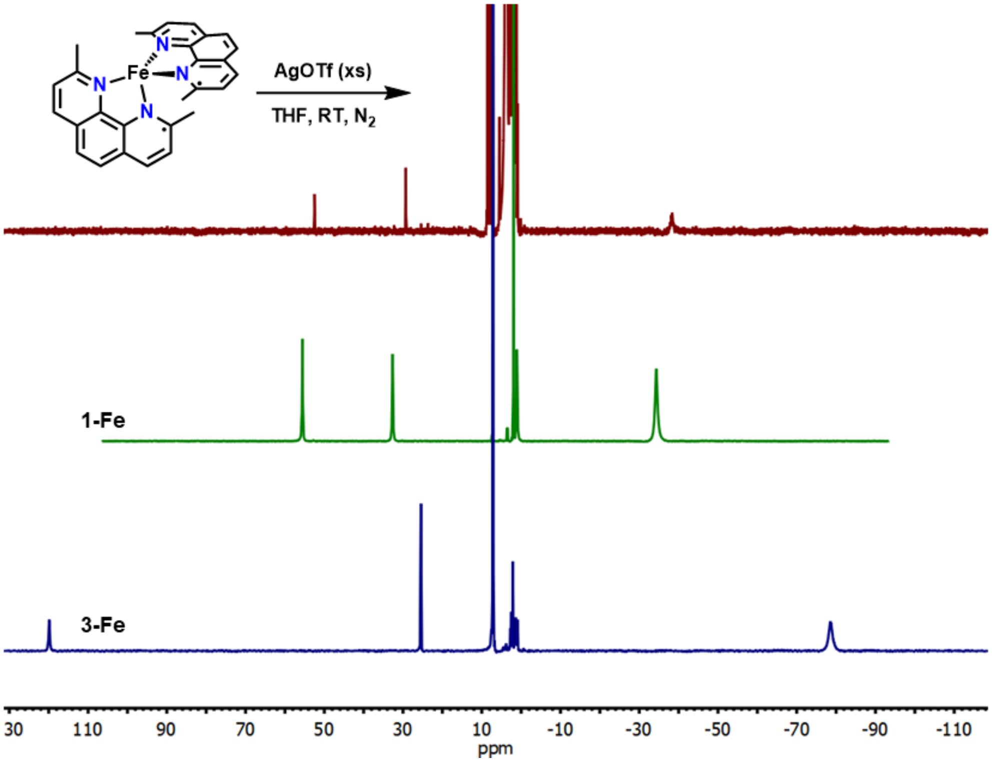

Figure 4A - 5. ^{1}H NMR of **1-Co** in CD_3CN.

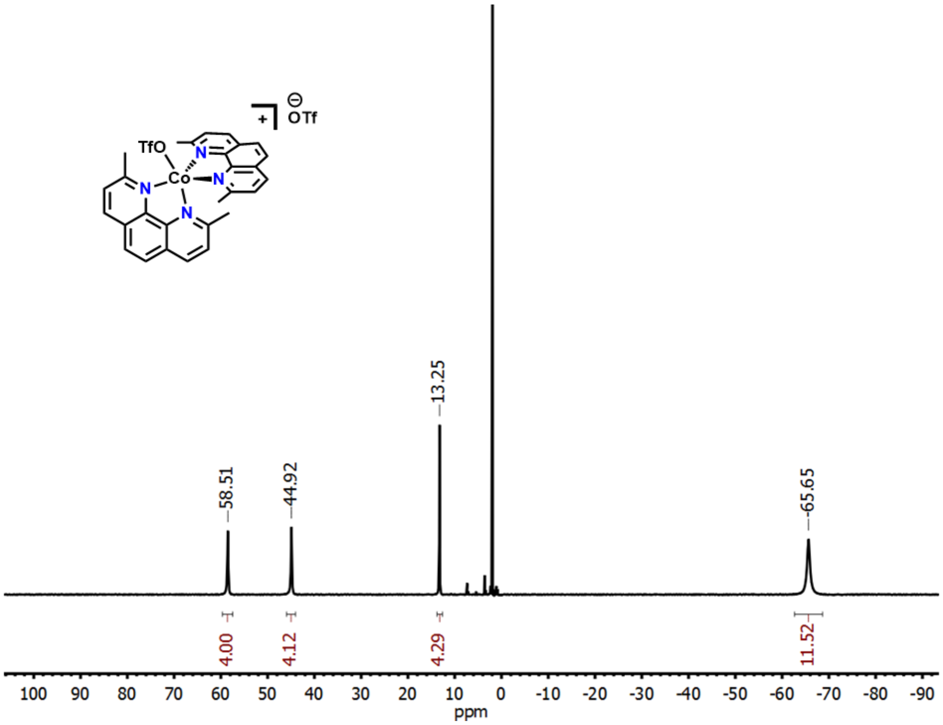

Figure 4A - 6. ^{1}H NMR of **1-Co** and [Co(neocuproine)$(OTf)_2$(MeCN)] in CD_3CN.

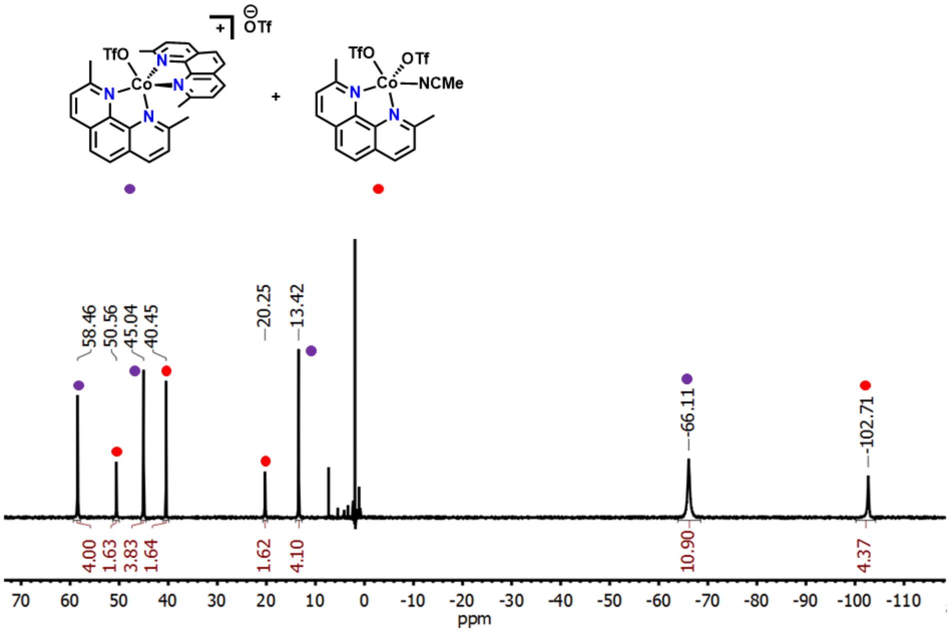

Figure 4A - 7. ^{19}F NMR of **1-Co** and [Co(neocuproine)(OTf)$_2$(MeCN)] in CD_3CN.

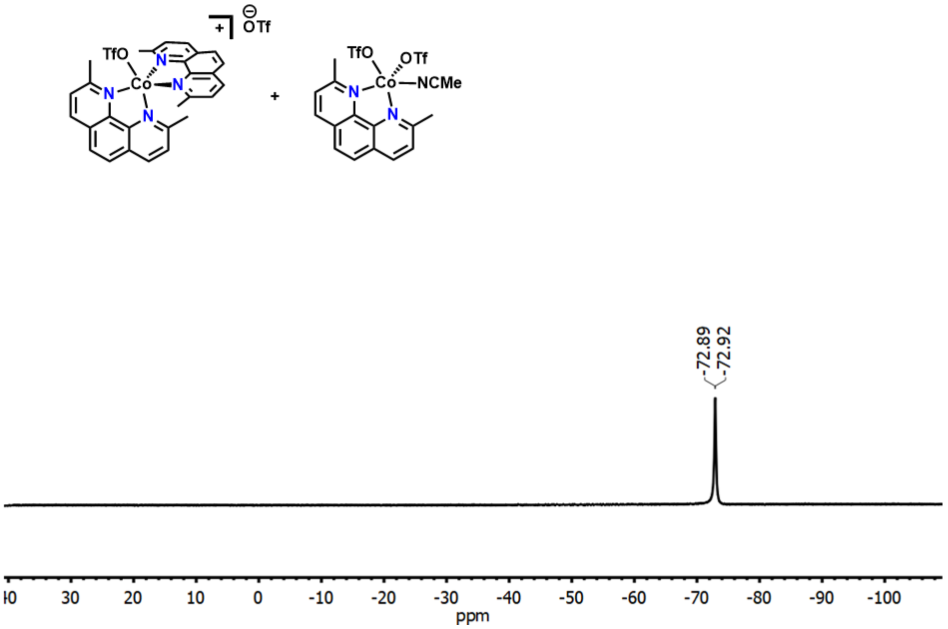

Figure 4A - 8. ^{19}F NMR of **1-Co** in CD_3CN.

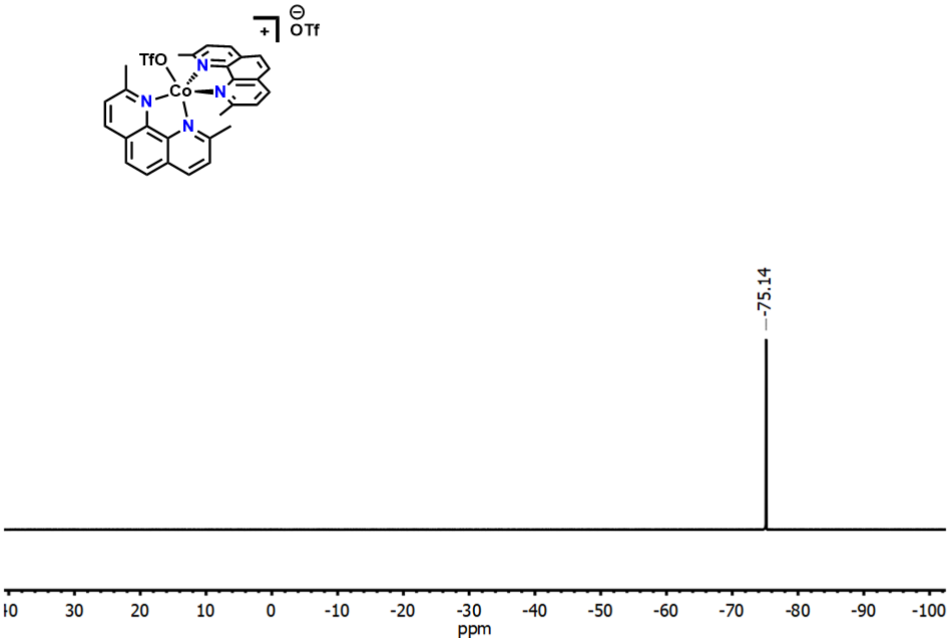

Figure 4A - 9. ^{1}H NMR of **2-Co** in CD_3CN.

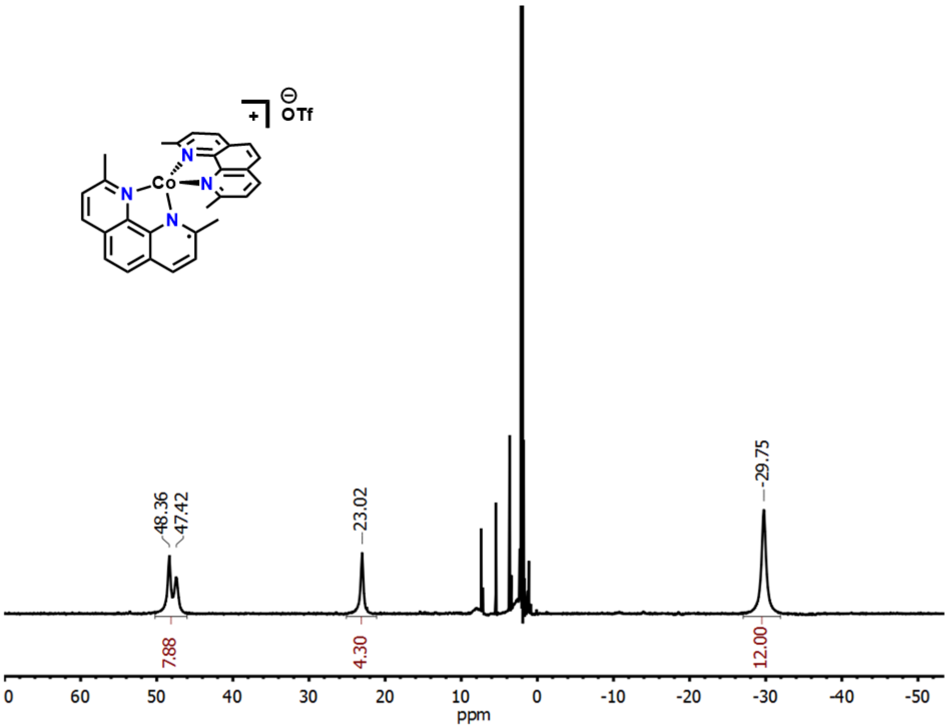

Figure 4A - 10. ^{19}F NMR of **2-Co** in CD_3CN.

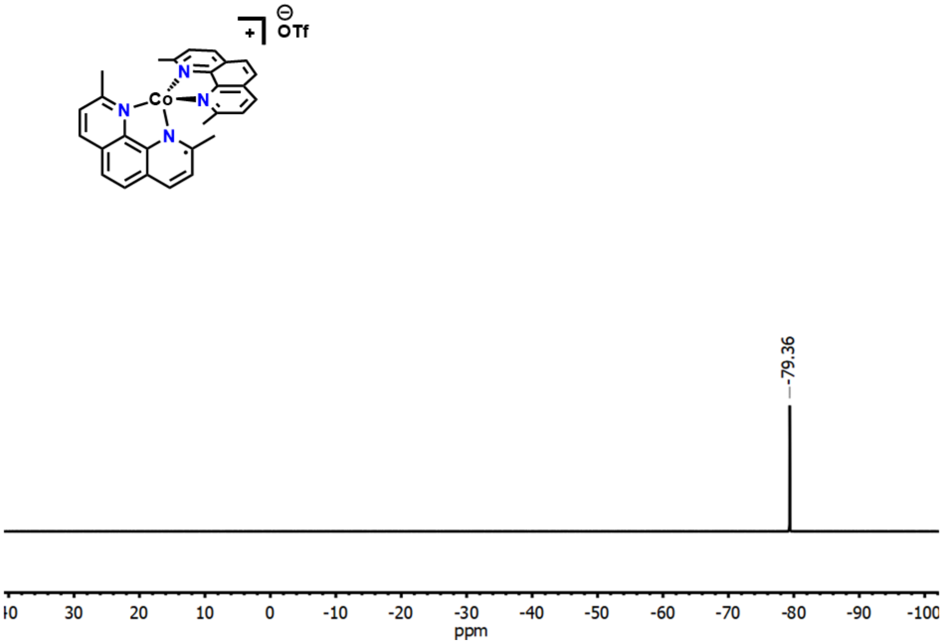

Figure 4A - 11. ^{1}H NMR of **3-Co** in C_6D_6.

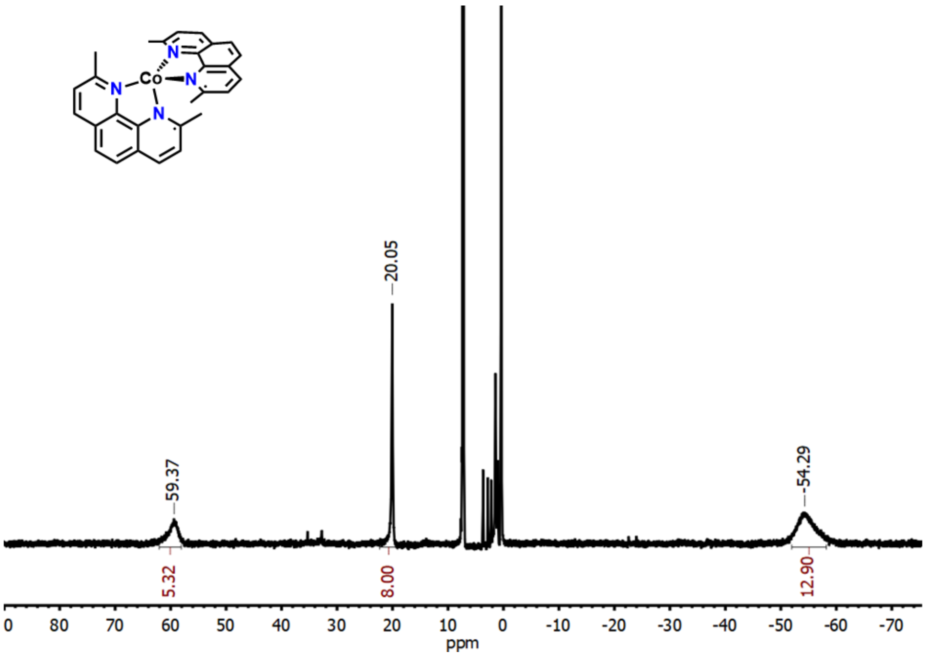

Figure 4A - 12. ^{1}H NMR of **3-Co** with excess AgOTf in CD_3CN stacked with **1-Co**, **2-Co**, and **3-Co** where **1-Co** and **2-Co** are in CD_3CN and **3-Co** is in C_6D_6.

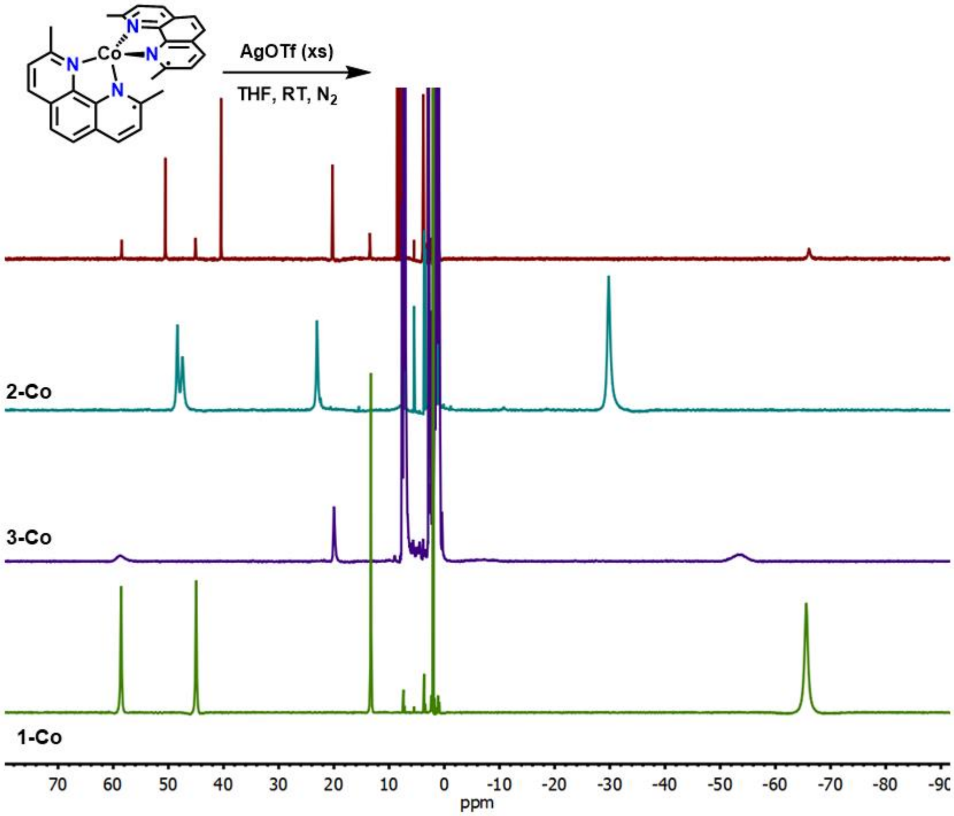

Figure 4A - 13. ^{9}F NMR of **1-Fe** with 3 equivalents of 1,2-difluorobenzene as an internal standard in acetonitrile.

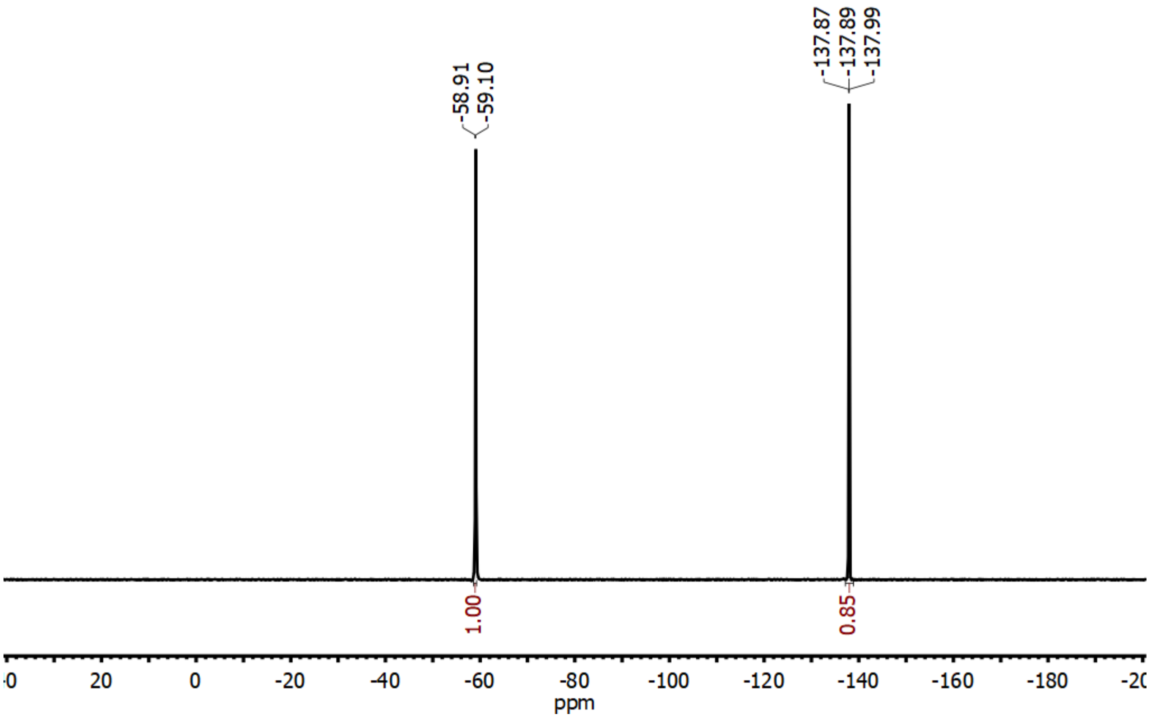

Figure 4A - 14**.** ^{19}F NMR of **1-Co** with 3 equivalents of 1,2-difluorobenzene as an internal standard in acetonitrile.

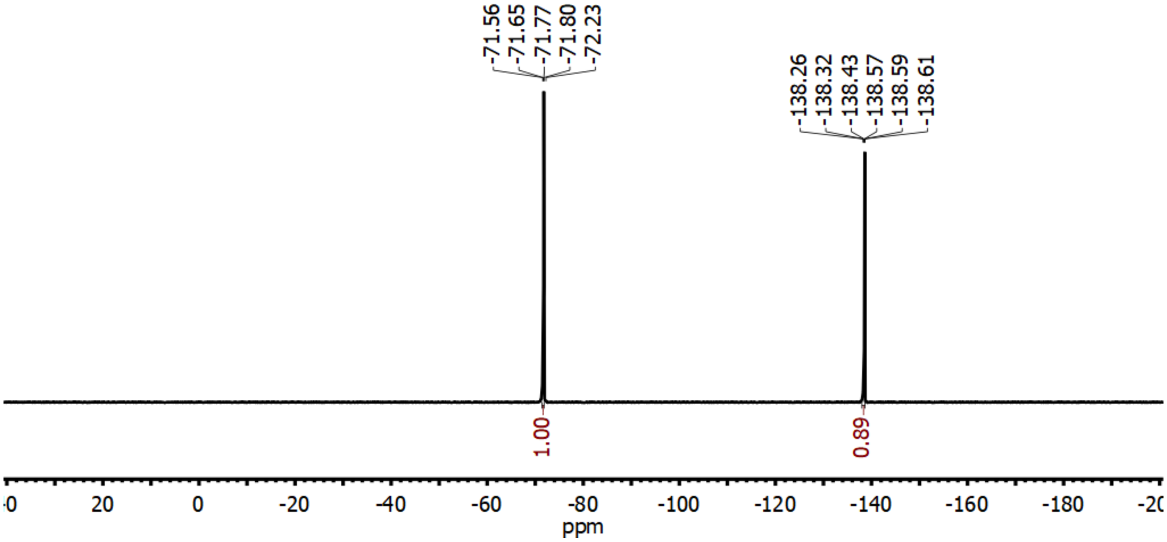

Figure 4A - 15. ^{19}F NMR of **1-Fe** at -30 °C and room temperature in CD_3CN.

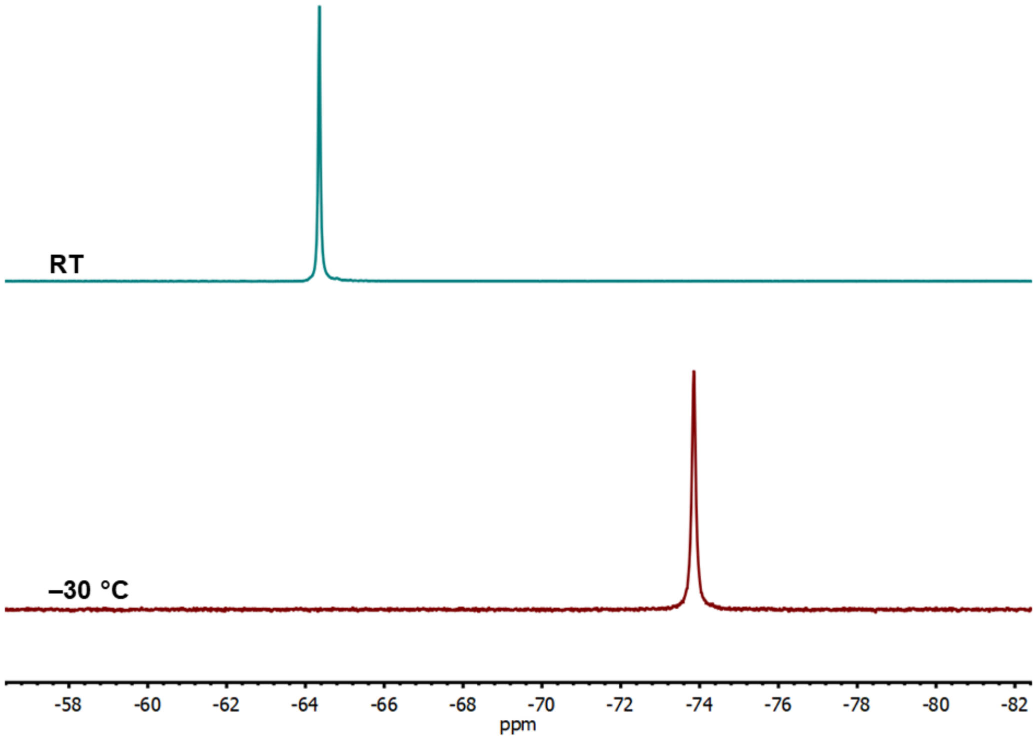

Figure 4A - 16. ^{19}F NMR of **1-Fe** at -30 °C and room temperature in CD_3CN.

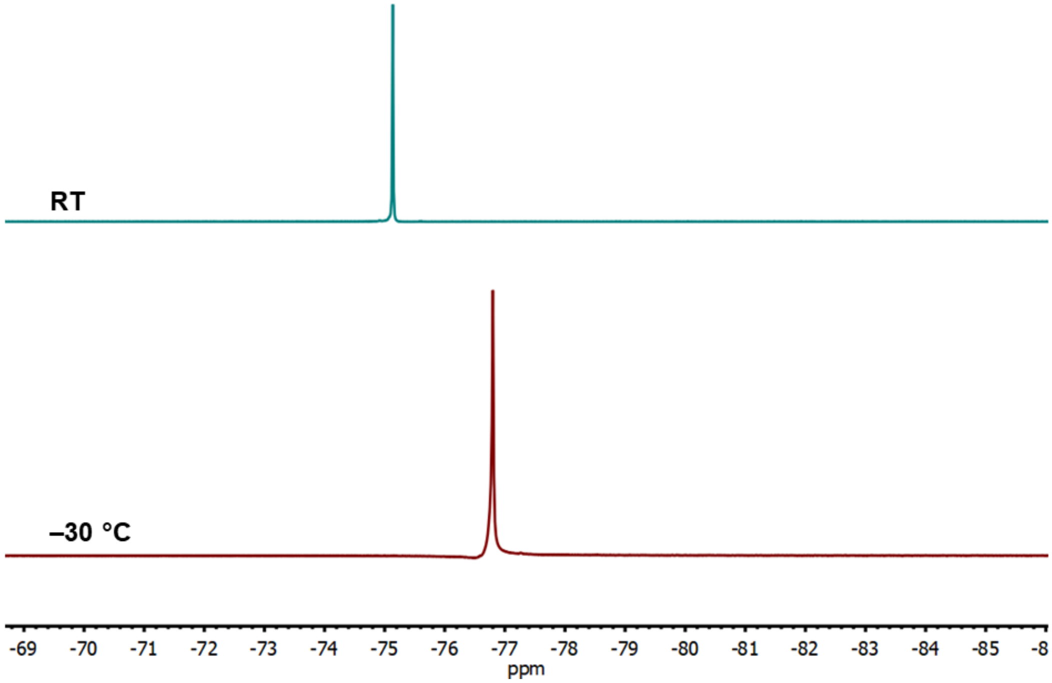

UV-vis Spectra

Figure 4A - 17. UV-vis spectrum of **1-Fe** in acetonitrile.

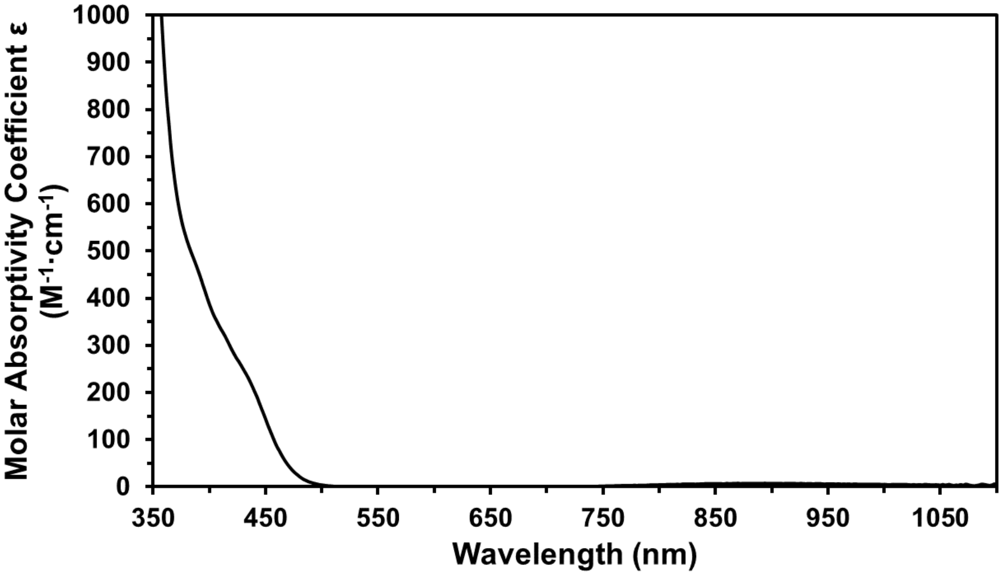

Figure 4A - 18. UV-vis spectrum of **3-Fe** in benzene.

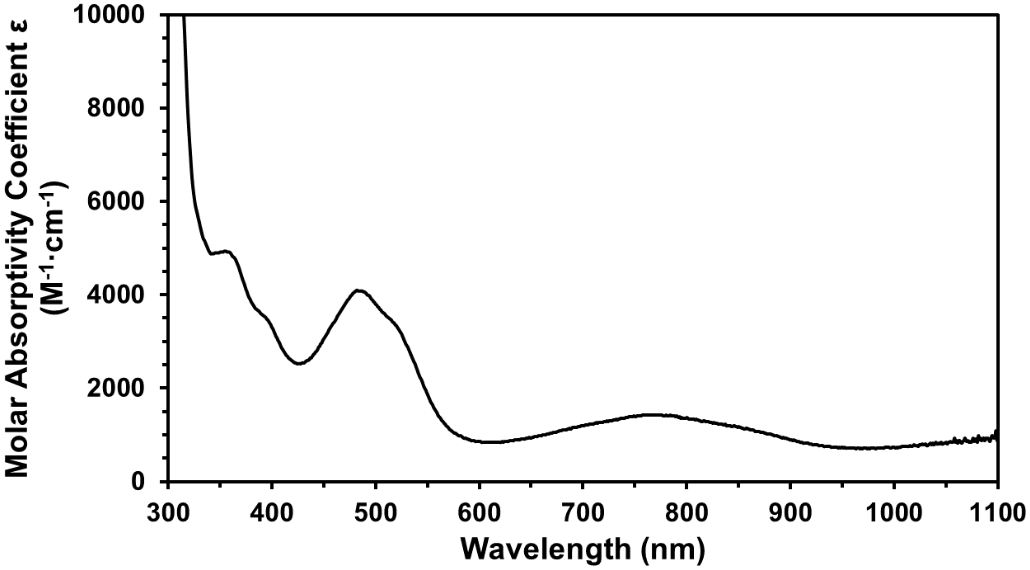

Figure 4A - 19. UV-vis spectrum of **1-Co** in acetonitrile.

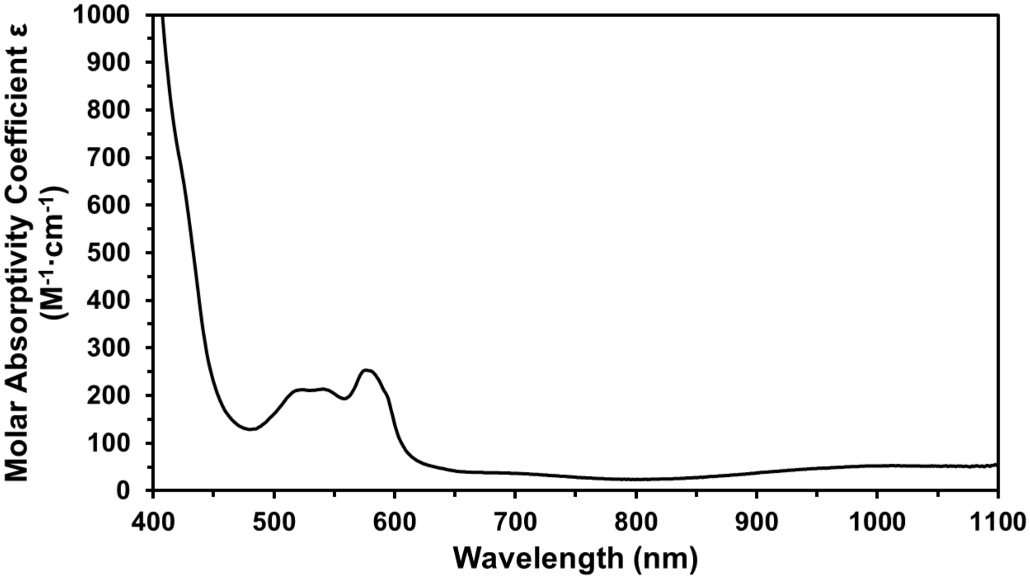

Figure 4A - 20. UV-vis spectrum of **2-Co** in acetonitrile.

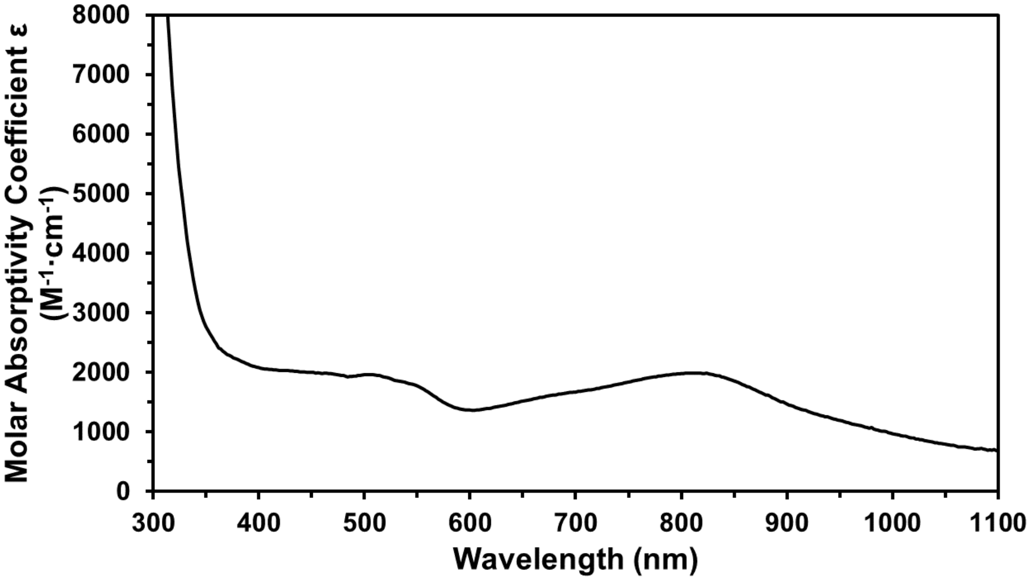

Figure 4A - 21. UV-vis spectrum of **3-Co** in benzene.

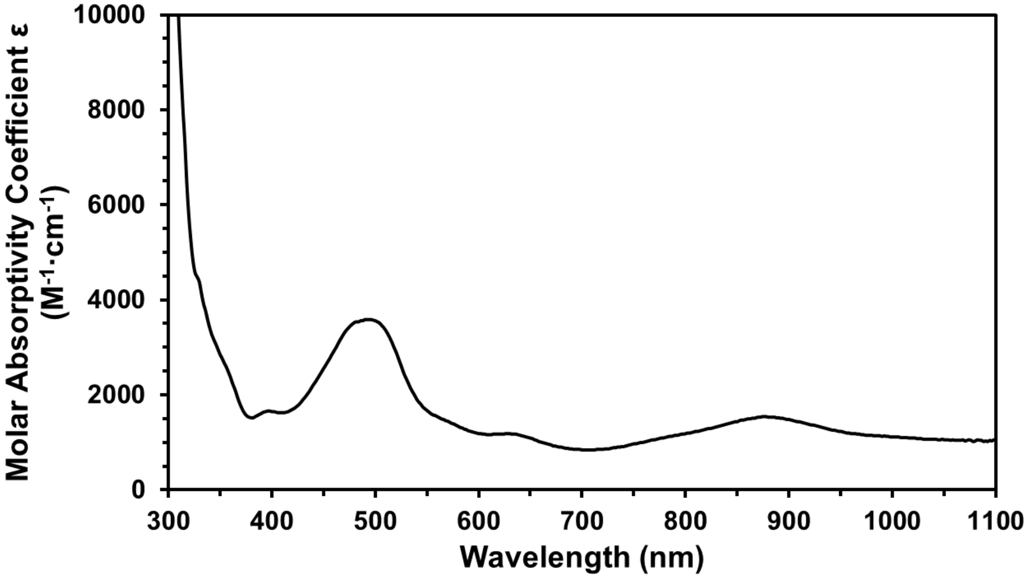

IR Spectra

Figure 4A - 22. IR (KBr pellet) of **1-Fe**.

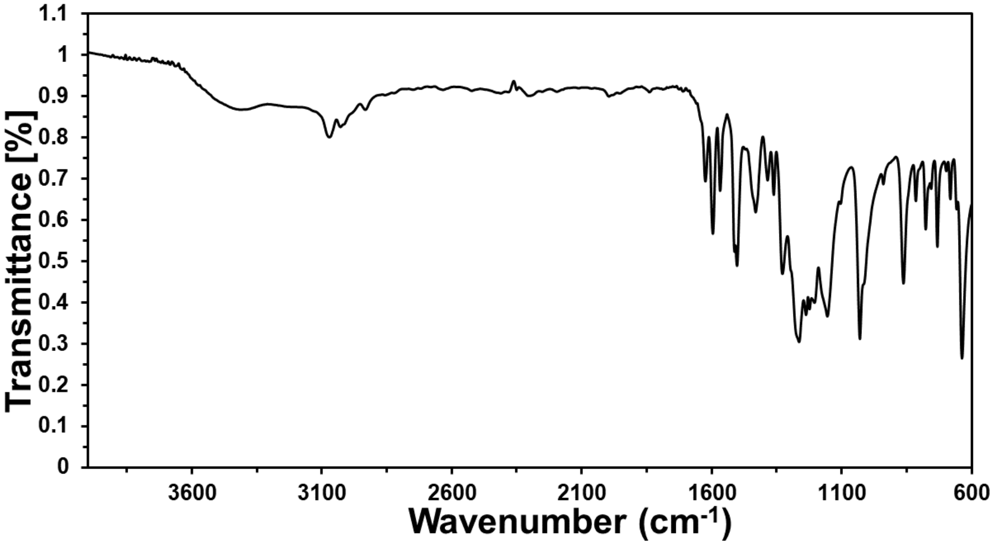

Figure 4A - 23. IR (KBr pellet) of **3-Fe**.

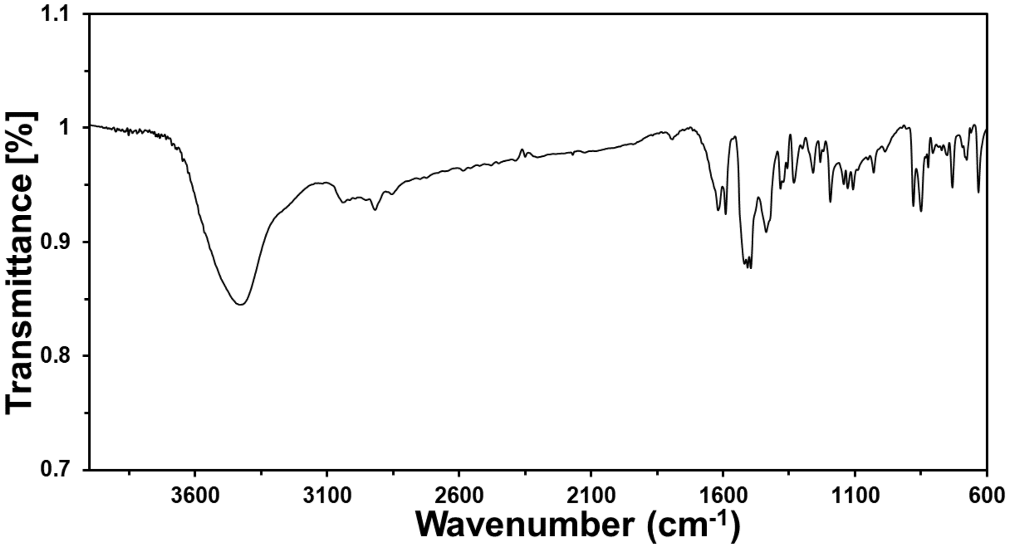

Figure 4A - 24. IR (KBr pellet) of **1-Co**.

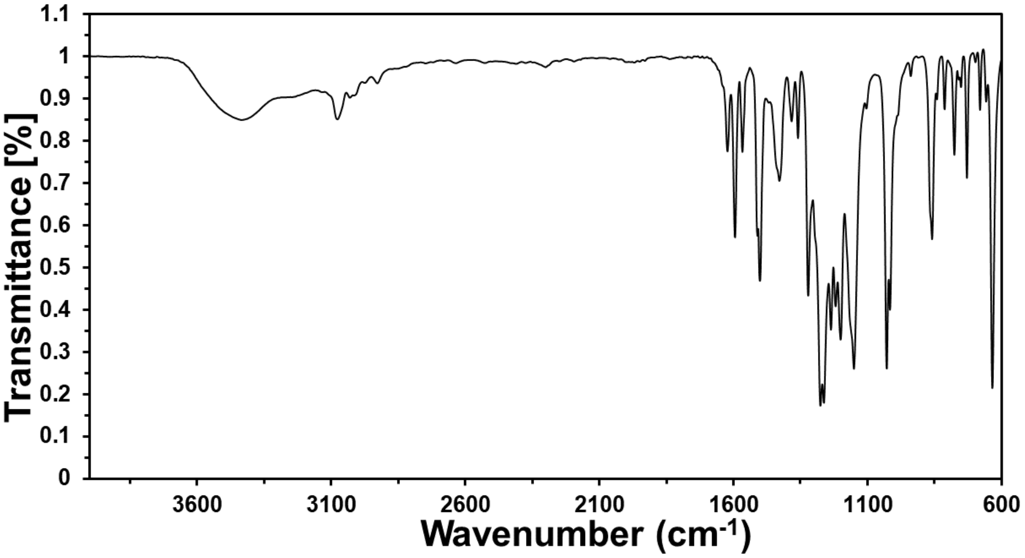

Figure 4A - 25. IR (KBr pellet) of **2-Co**.

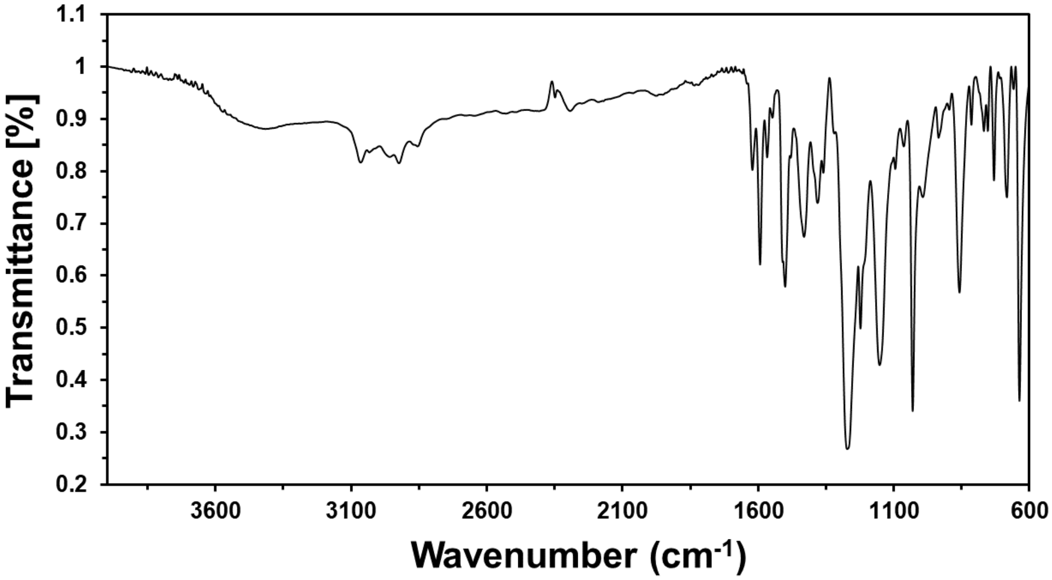

Figure 4A - 26. IR (KBr pellet) of **3-Co**.

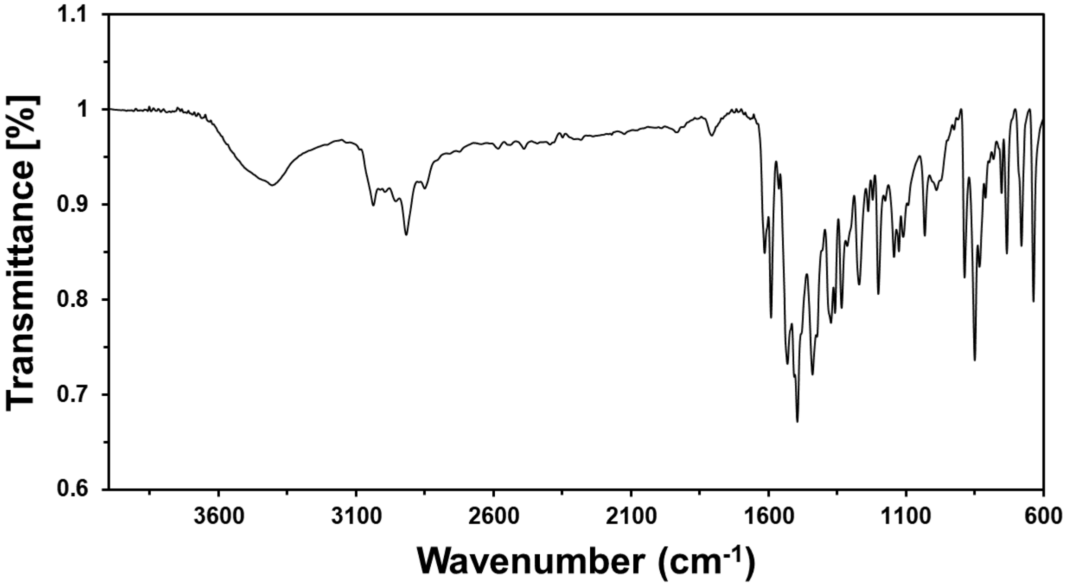

Electron Paramagnetic Resonance (EPR) Spectra

Figure 4A - 27. EPR spectrum of **1-Co** in acetonitrile, RT. MW power = 0.63 mW, MW frequency = 9.63 GHz. Simulated parameters: g_z = 2.35, g_y = 2.08, g_x = 1.87, A_z = 380, A_y = 30, A_x = 1, D = 3.2, E/D = 0.22, sD = 0.026, sE/D = 0.055, Linewidth =100. Co hyperfine splitting is in MHz. The nuclear spin of ^{59}Co is 7/2.

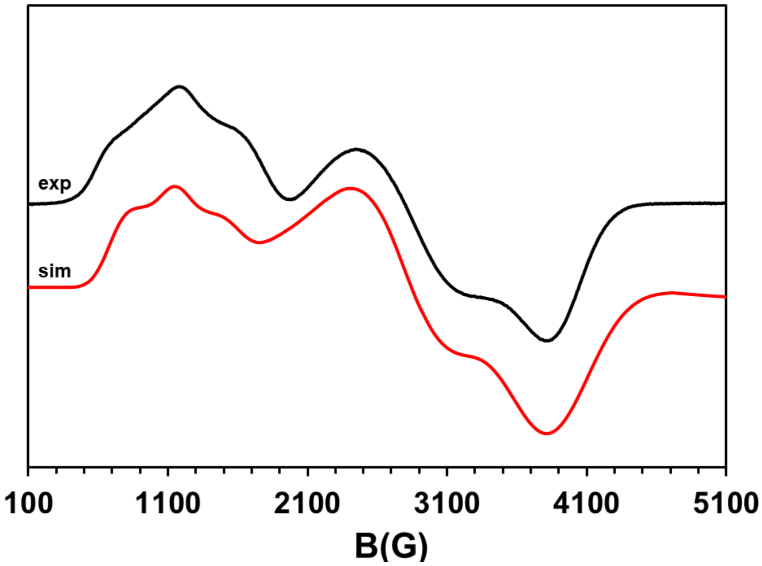

Cyclic Voltammetry (CV)

Figure 4A - 28. CV of 1.5 mM **1-Fe** in acetonitrile where L = neocuproine and L^{-1} = neocuproine radical ligand. Electrolyte: 5 mM $[Bu_4N][PF_6]$, Scan rate: 100 mV/s. Scanning oxidatively.

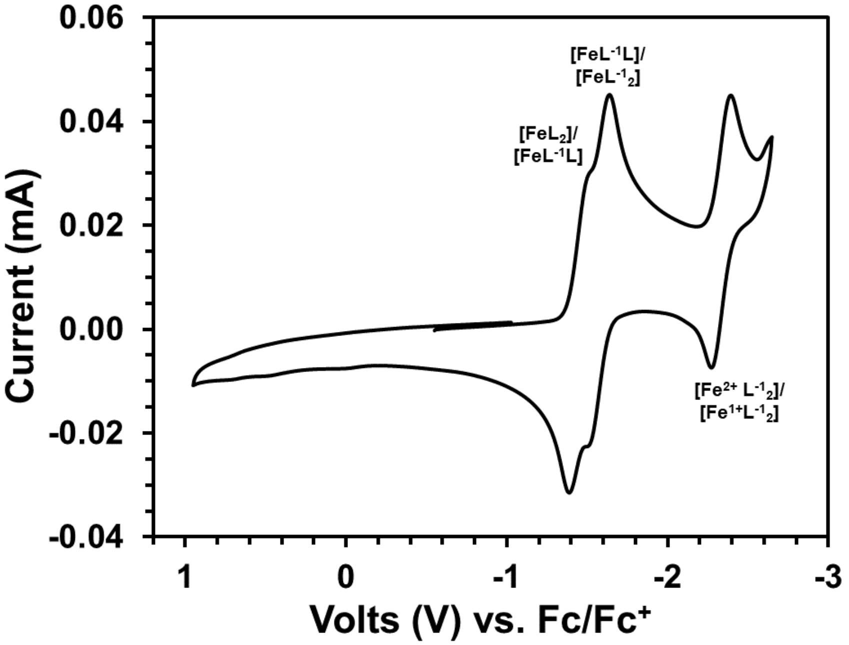

Figure 4A - 29. CV of 1.5 mM **1-Co** in acetonitrile where L = neocuproine and L^{-1} = neocuproine radical ligand. Electrolyte: 5 mM $[Bu_4N][PF_6]$, Scan rate: 100 mV/s. Scanning oxidatively.

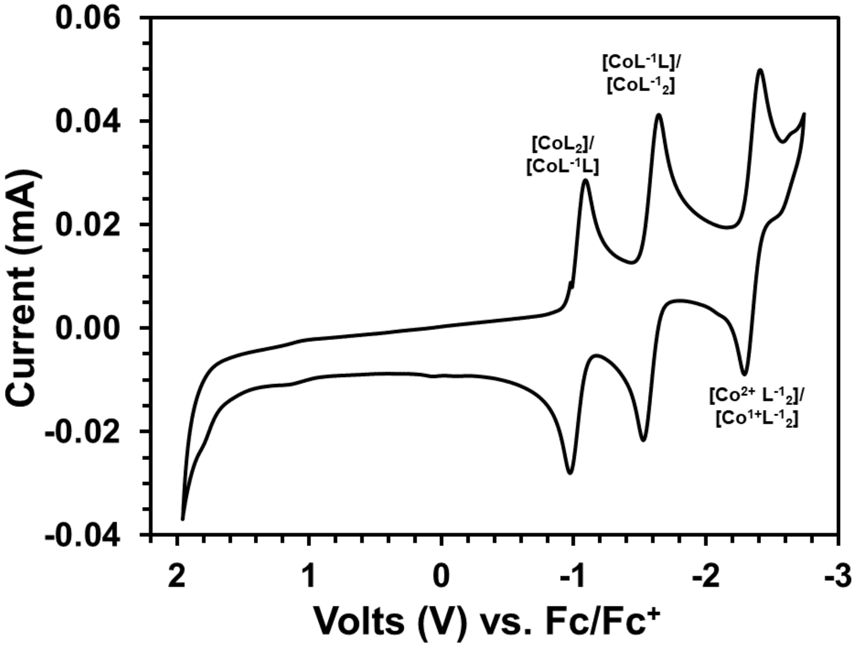

Solid State Magnetic Measurements (SQUID)

Figure 4A - 30. Variable temperature χT data of **1-Fe** at 1 Tesla.

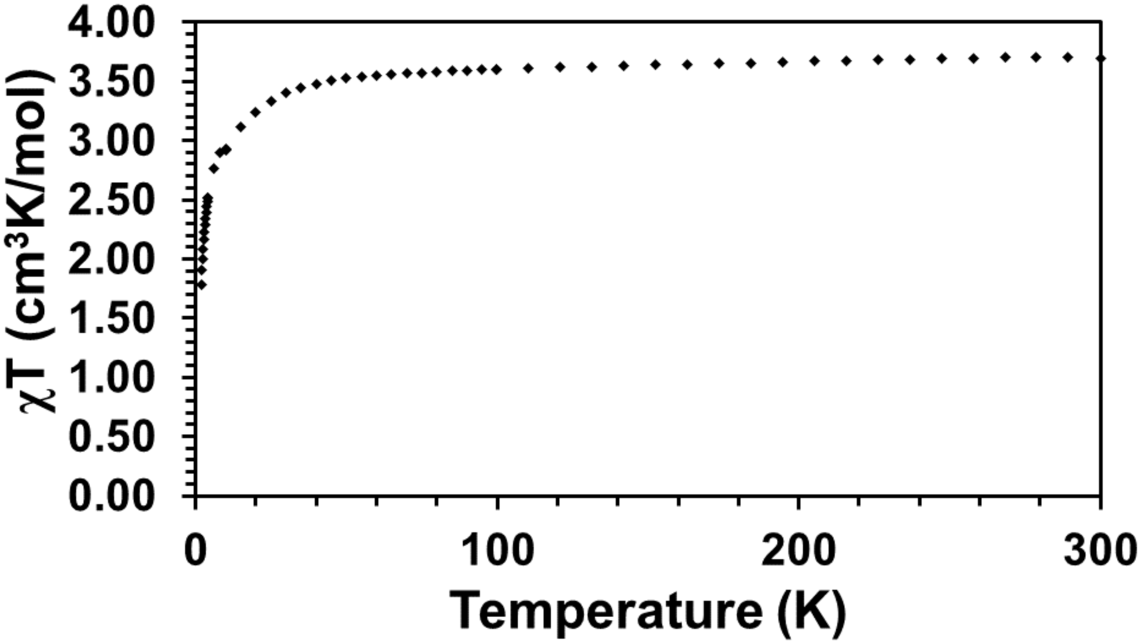

Figure 4A - 31. Variable temperature χT data of **3-Fe** at 1 Tesla.

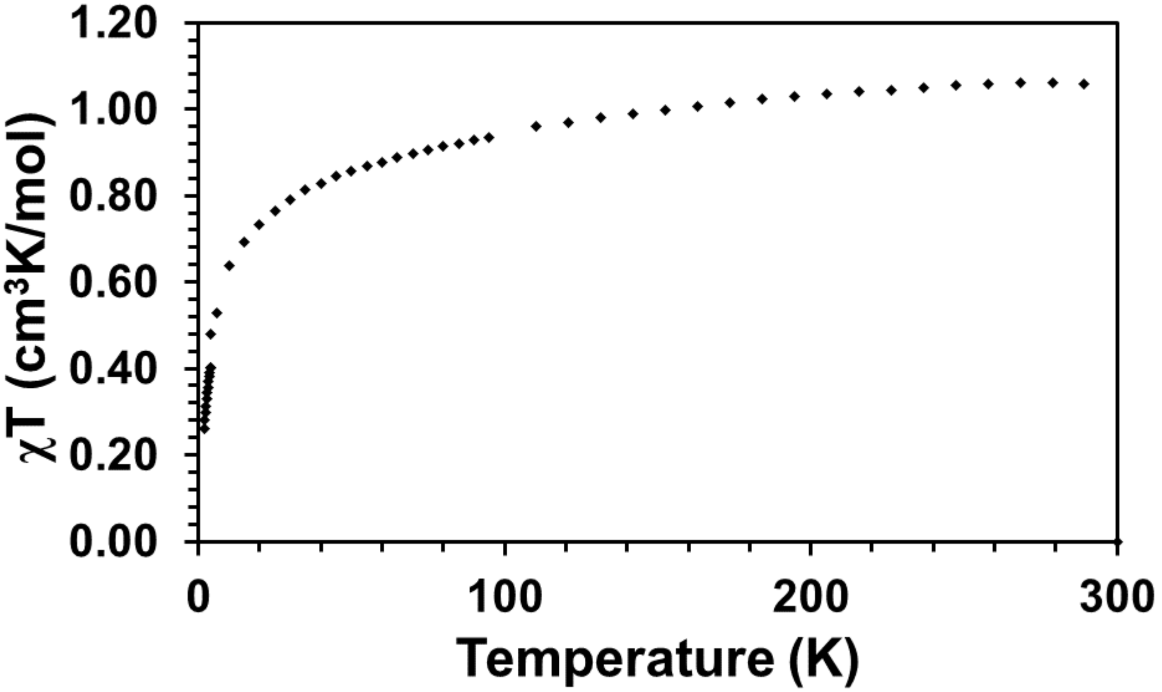

Figure 4A - 32. Variable temperature χT data of **1-Co** at 1 Tesla.

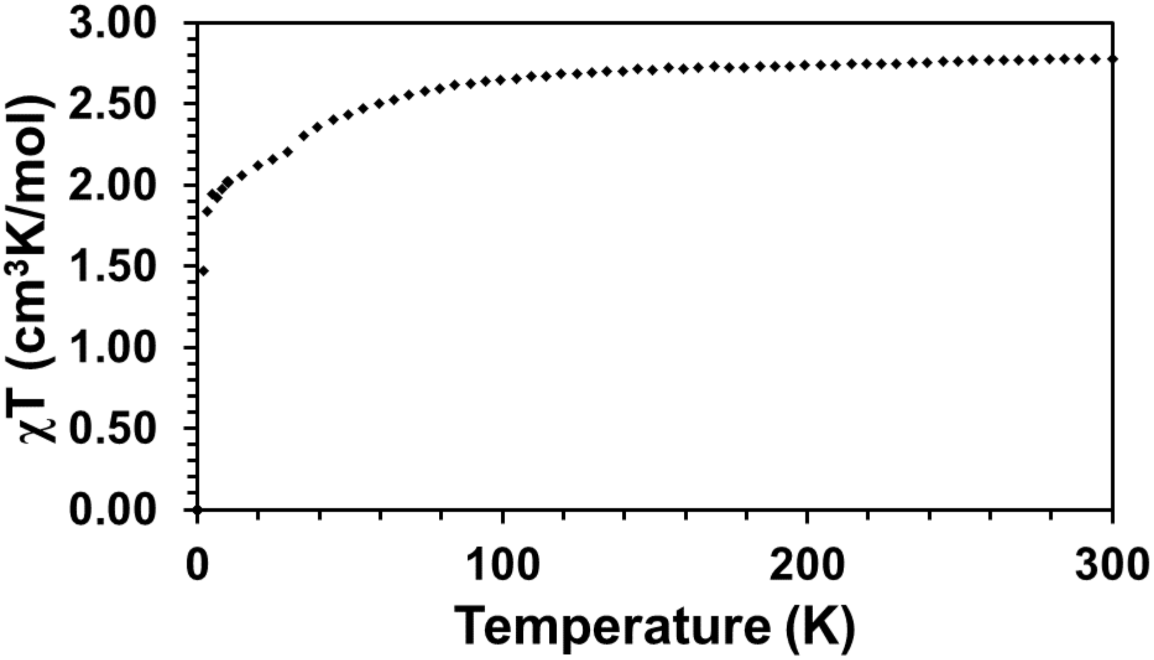

Figure 4A - 33. Variable temperature χT data of **2-Co** at 1 Tesla.

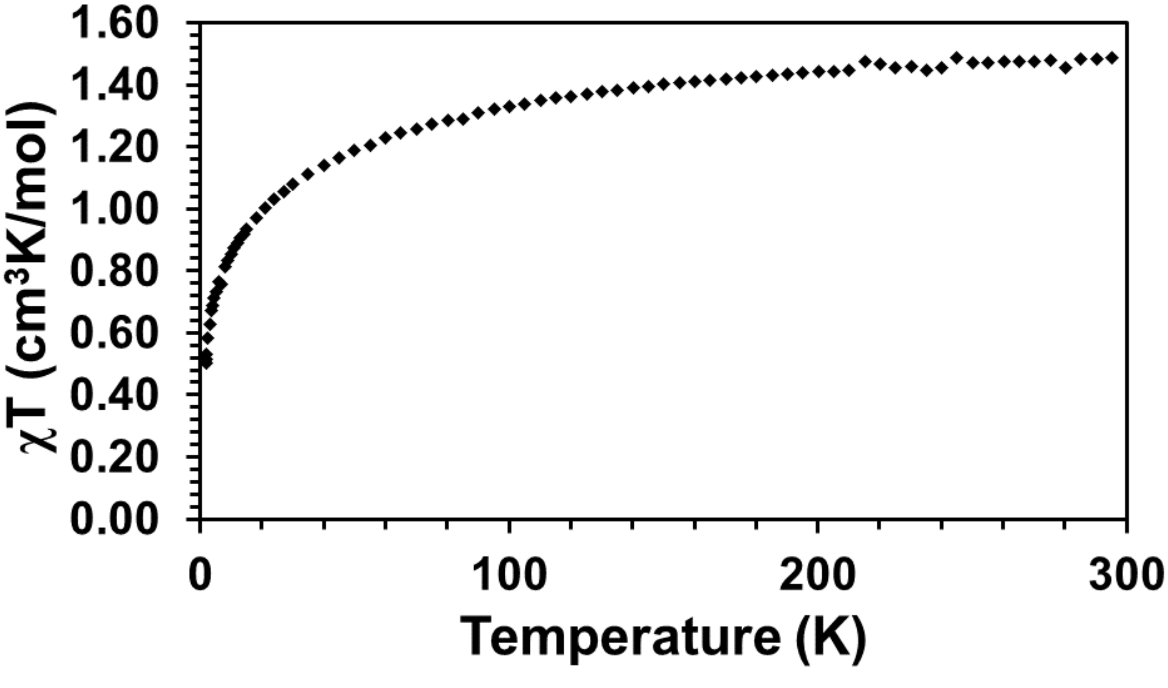

Figure 4A - 34. Variable temperature χT data of **3-Co** at 1 Tesla.

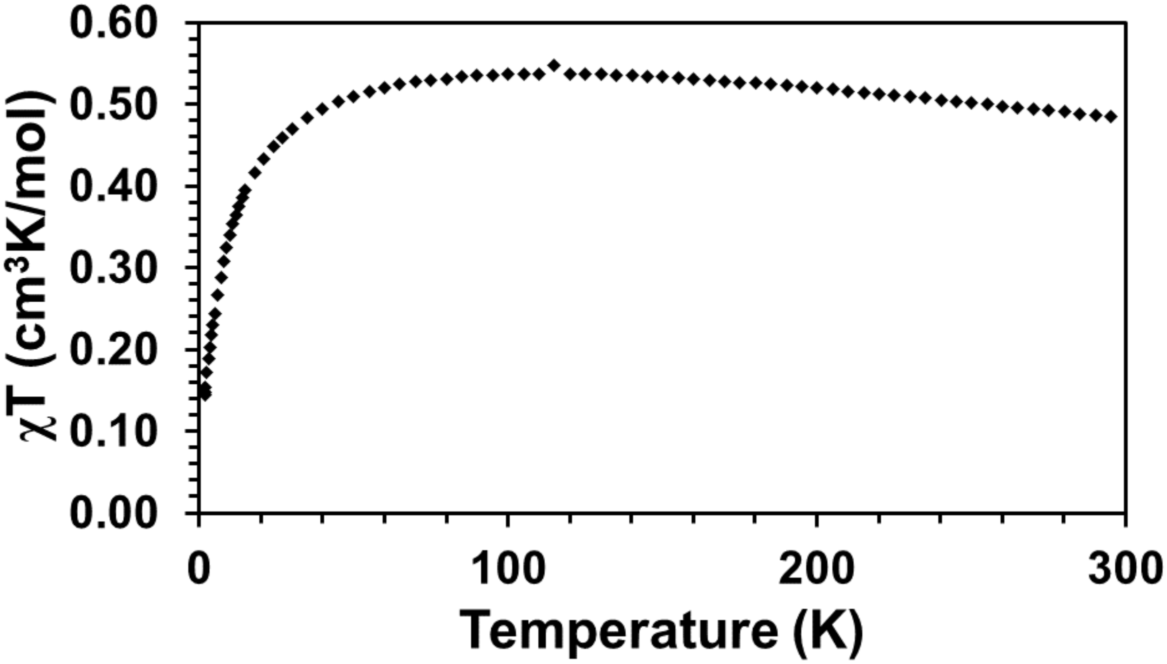

Figure 4A - 35. EXAFS spectrum in R-space at the Fe K-edge absorption of **3-Fe**. The experimental data (black), simulated fit (red), and window (dashed) are shown.

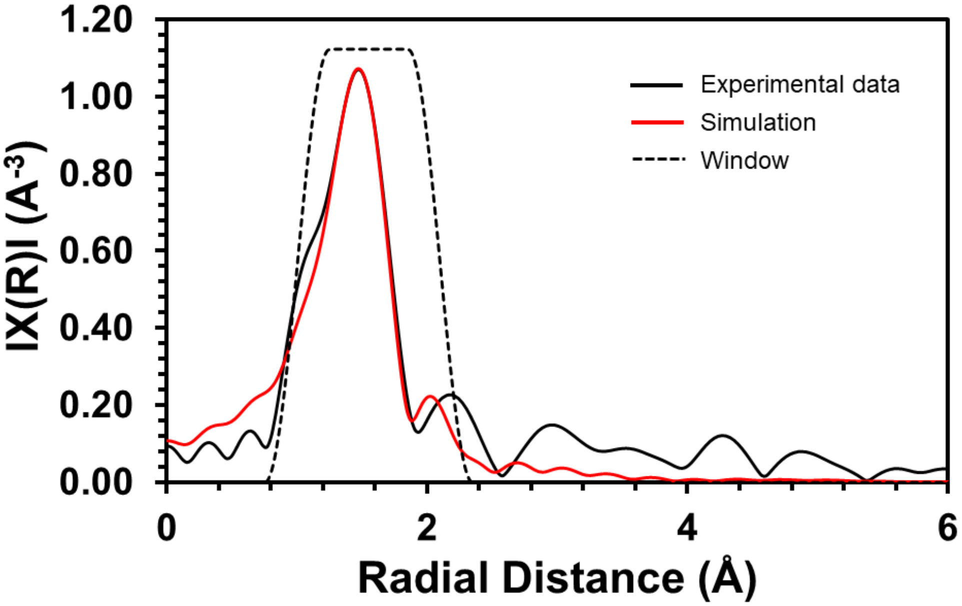

Figure 4A - 36. EXAFS spectrum in K-space at the Fe K-edge absorption of **3-Fe**. The experimental data (black), simulated data (red), and window (dashed) are shown.

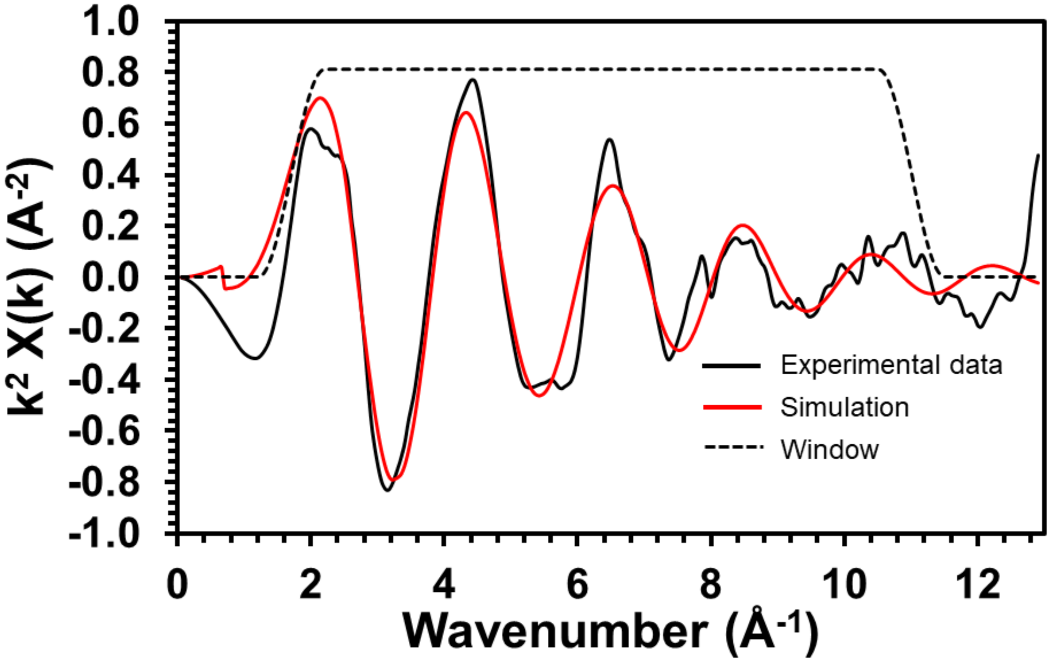

Table 4A - 1. EXAFS Fit Parameters for **3-Fe**.

*Complex 3-Fe	N	R (Å)	σ^2 (Å^2)	R-factor	Reduced chi-square
Fe-N1	2	1.95(1)	0.006(2)	0.014	5873
Fe-N2	2	2.02(1)			

ΔE_0 = 1.771 eV; S_0^2 = 0.882; Independent Points: 6; Fitting Range: k: 1.7-11 Å^{-1}; R: 1.0-2.1 Å

*N, Coordination numbers; R, interatomic distances; σ^2, Debye-Waller factors (the mean-square deviations in interatomic distance). The values in parentheses are the estimated standard deviations; ΔE_0, change in the photoelectron energy; S_0^2, amplitude reduction factor.

Figure 4A - 37. EXAFS spectrum in R-space at the Co K-edge absorption of **3-Co**. The experimental data (black), simulated fit (red), and window (dashed) are shown.

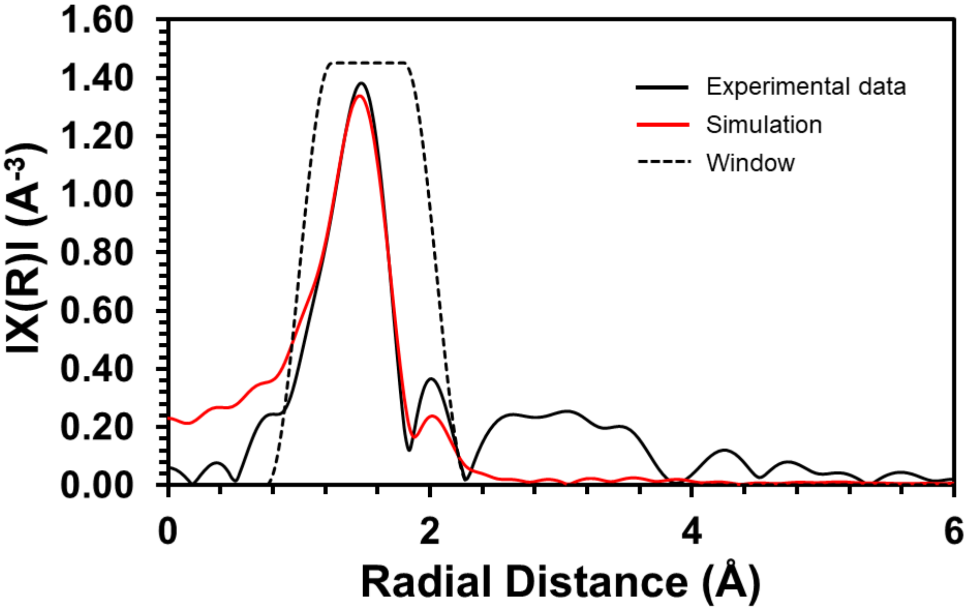

Figure 4A - 38. EXAFS spectrum in K-space at the Co K-edge absorption of **3-Co**. The experimental data (black), simulated data (red), and window (dashed) are shown.

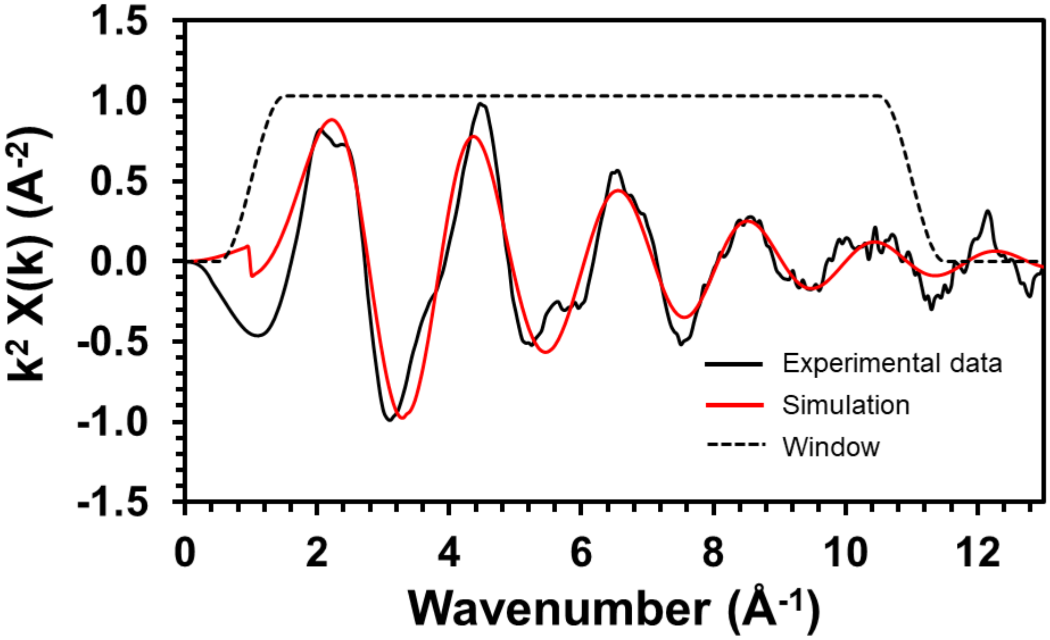

Table 4A - 2. EXAFS Fit Parameters for **3-Co**.

*Complex 3-Co	N	R (Å)	σ^2 (Å^2)	R-factor	Reduced chi-square
Co-N1	2	1.96(2)	0.006(3)	0.020	481
Co-N2	2	2.00(2)			

ΔE_0 =3.764 eV; S_0^2 = 0.995; Independent Points: 6; Fitting Range: k: 1.0-11 Å^{-1}; R: 1.0-2.05 Å

*N, Coordination numbers; R, interatomic distances; σ^2, Debye-Waller factors (the mean-square deviations in interatomic distance). The values in parentheses are the estimated standard deviations; ΔE_0, change in the photoelectron energy; S_0^2, amplitude reduction factor.

Figure 4A - 39. XAS of **1-Fe**, **3-Fe**, Fe(MeCN)$_2$(OTf)$_2$, and the Fe(0) foil. Inflection points (eV): **1-Fe** (7118), **3-Fe** (7116), Fe(MeCN)$_2$(OTf)$_2$ (7116), and Fe(0) foil (7112).

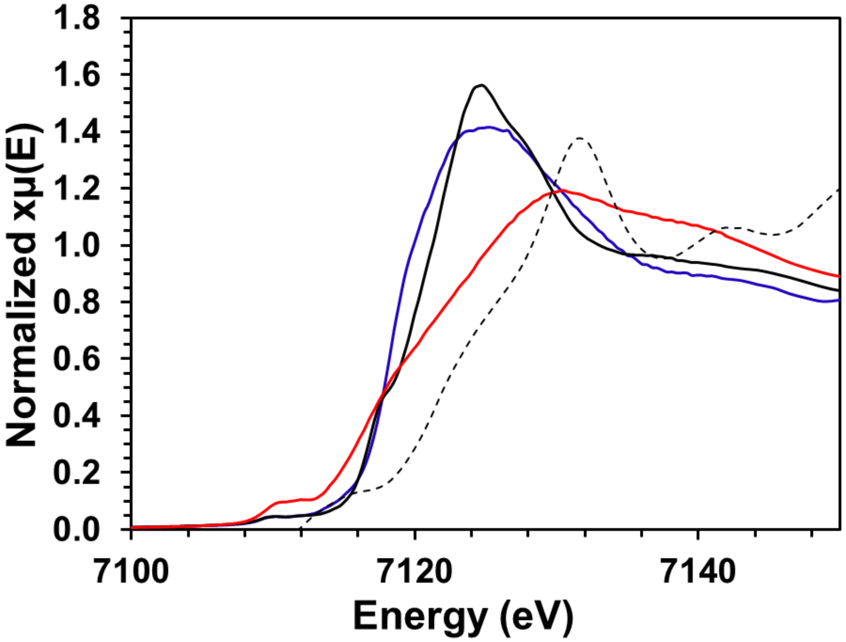

Figure 4A - 40. XAS K-edge derivative plot of **1-Fe**, **3-Fe**, Fe(MeCN)$_2$(OTf)$_2$, and the Fe(0) foil. Inflection points (eV): **1-Fe** (7118), **3-Fe** (7116), Fe(MeCN)$_2$(OTf)$_2$ (7116), and Fe(0) foil (7112).

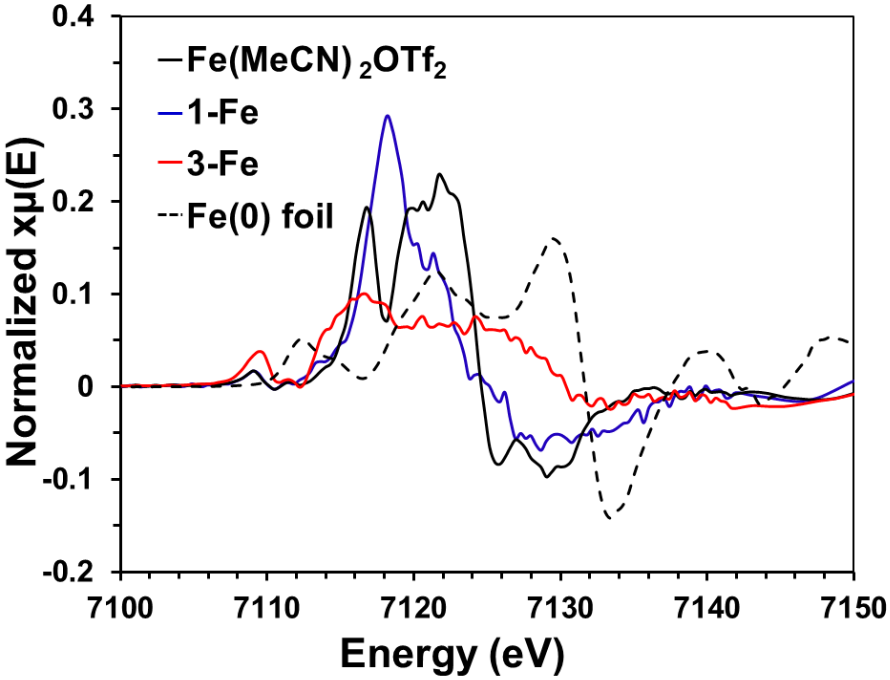

Figure 4A - 41. XAS of **1-Co**, **2-Co**, **3-Co** and the Co(0) foil. Inflection points (eV): **1-Co** (7717), **2-Co** (7717), **3-Co** (7716), and Co(0) foil (7709).

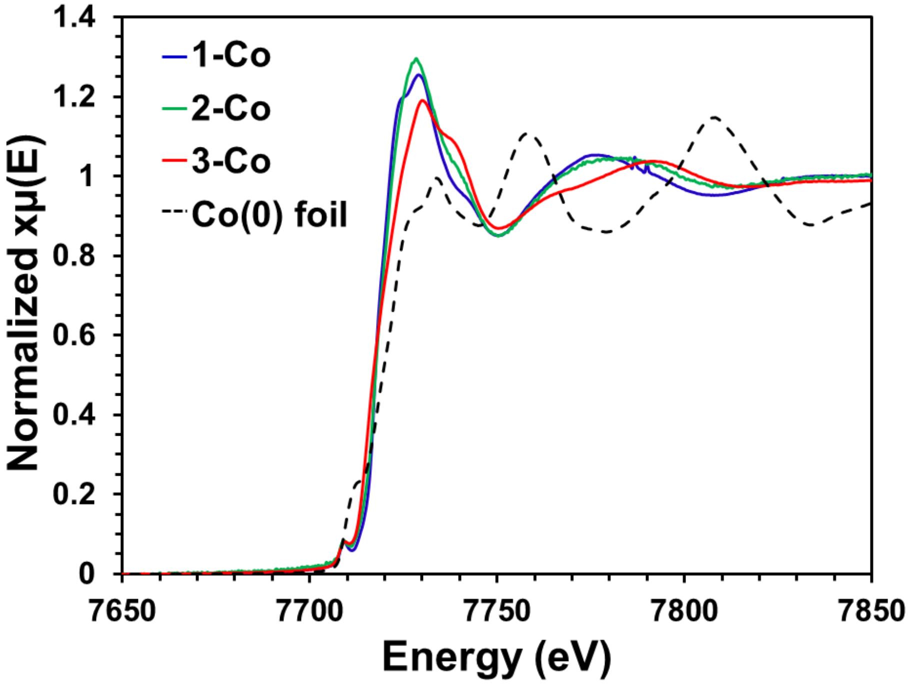

Figure 4A - 42. XAS K-edge derivative plot of **1-Co**, **2-Co**, **3-Co** and the Co(0) foil. Inflection points (eV): **1-Co** (7717), **2-Co** (7717), **3-Co** (7716), and Co(0) foil (7709).

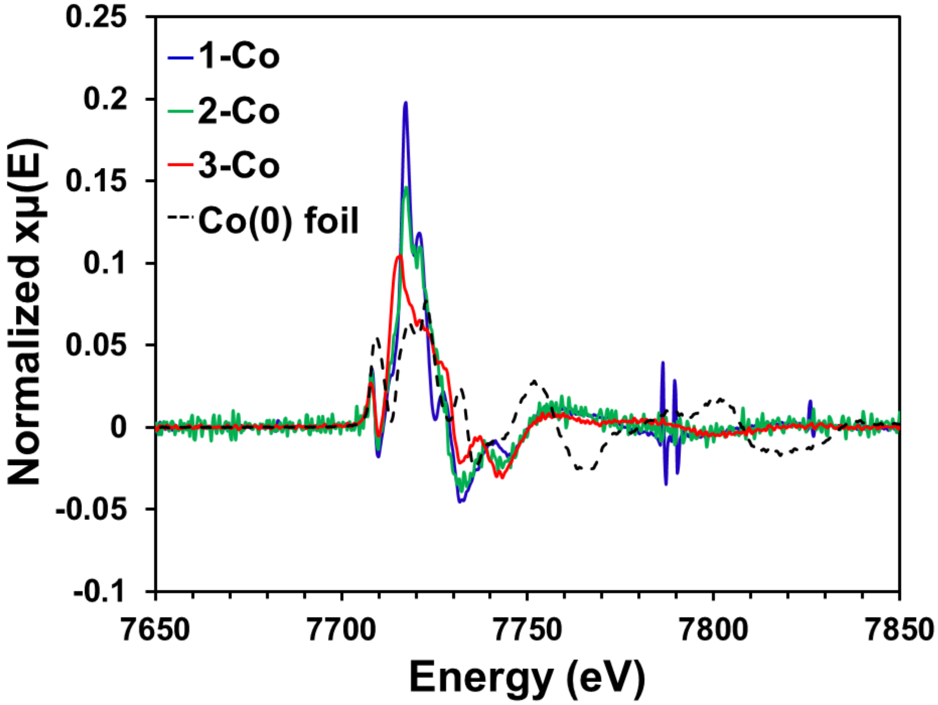

X-ray Crystallography

Table 4A - 3. Crystallographic Data.

	1-Fe	**1-Co**	**1-Co** and [Co(neocuproine)(OTf)$_2$MeCN]
Empirical formula	$C_{64}H_{58}F_{12}Fe_2N_8O_{13}S_4$	$C_{64}H_{57.66}Co_2F_{12}N_8O_{13}S_4$	$C_{48}H_{39}Co_2F_{12}N_7O_{12}S_4$
Formula weight	1615.12	1620.94	1379.96
Temperature/K	100(2)	100(2)	100(2)
Crystal system	monoclinic	monoclinic	monoclinic
Space group	$P2_1/c$	$P2_1/c$	$P2_1/c$
a/Å	15.5650(16)	15.5656(10)	17.7028(12)
b/Å	31.997(3)	31.720(2)	18.0869(13)
c/Å	14.5894(14)	14.5502(9)	17.8196(12)
α/°	90	90	90
β/°	108.194(2)	107.712(2)	106.615(2)
γ/°	90	90	90
Volume/Å^3	6902.8(12)	6843.4(8)	5467.4(7)
Z	4	4	4
ρ_{calc}g/cm^3	1.554	1.573	1.676
μ/mm^{-1}	0.155	0.708	0.868
F(000)	3304	3311	2792
Crystal size/mm^3	0.5 × 0.2 × 0.1	0.48 × 0.18 × 0.09	0.3 × 0.2 × 0.2
Radiation	synchrotron (λ = 0.41328)	MoKα (λ = 0.71073)	MoKα (λ = 0.71073)
2Θ range for data collection/°	1.48 to 31.418	4.226 to 59.56	4.45 to 63.892
Index ranges	$-20 \le h \le 20$, $-41 \le k \le 41$, $-18 \le l \le 18$	$-21 \le h \le 21$, $-44 \le k \le 42$, $-20 \le l \le 19$	$-26 \le h \le 26$, $-24 \le k \le 24$, $-26 \le l \le 24$
Reflections collected	175890	155696	98889
Independent reflections	15933 [R_{int} = 0.0763, R_{sigma} = 0.0280]	19263 [R_{int} = 0.0469, R_{sigma} = 0.0374]	16878 [R_{int} = 0.0440, R_{sigma} = 0.0371]
Data/restraints/parameters	15933/0/957	19263/0/957	16878/0/855

Table 4A - 3. Crystallographic Data continued.

Goodness-of-fit on F^2	1.029	1.065	1.03
Final R indexes [I>=2σ (I)]	R_1 = 0.0548, wR_2 = 0.1410	R_1 = 0.0580, wR_2 = 0.1278	R_1 = 0.0411, wR_2 = 0.0975
Final R indexes [all data]	R_1 = 0.0618, wR_2 = 0.1452	R_1 = 0.0888, wR_2 = 0.1414	R_1 = 0.0620, wR_2 = 0.1058
Largest diff. peak/hole / e $Å^{-3}$	1.34/-1.08	1.07/-0.99	1.08/-0.59

Table 4A - 3. Crystallographic Data continued.

	2-Co	**3-Fe**	**3-Co**
Empirical formula	C29H24CoF3N4O3S	C28H24FeN4	C28H24CoN4
Formula weight	624.51	472.36	475.44
Temperature/K	100(2)	100(2)	100(2)
Crystal system	monoclinic	tetragonal	monoclinic
Space group	P21/n	P41212	C2/c
a/Å	11.4765(5)	16.0367(17)	22.723(2)
b/Å	11.0667(5)	16.0367(17)	22.757(2)
c/Å	21.0321(10)	34.722(4)	18.3309(19)
α/°	90	90	90
β/°	98.187(2)	90	107.775(2)
γ/°	90	90	90
Volume/Å3	2644.0(2)	8930(2)	9026.3(16)
Z	4	16	16
ρcalcg/cm3	1.569	1.405	1.399
μ/mm-1	0.79	0.7	0.188
F(000)	1280	3936	3952
Crystal size/mm3	0.47 × 0.45 × 0.28	0.28 × 0.18 × 0.14	0.01 × 0.002 × 0.002
Radiation	MoKα (λ = 0.71073)	MoKα (λ = 0.71073)	synchrotron (λ = 0.41328)
2Θ range for data collection/°	4.322 to 63.868	4.29 to 50.402	1.51 to 28.34
Index ranges	-16 ≤ h ≤ 17, -16 ≤ k ≤ 15, -28 ≤ l ≤ 30	-19 ≤ h ≤ 19, -19 ≤ k ≤ 19, -41 ≤ l ≤ 41	-26 ≤ h ≤ 26, -26 ≤ k ≤ 26, -21 ≤ l ≤ 21
Reflections collected	46539	75194	91673

Table 4A - 3. Crystallographic Data continued.

Independent reflections	8164 [Rint = 0.0269, Rsigma = 0.0254]	8042 [Rint = 0.1829, Rsigma = 0.1167]	7799 [Rint = 0.1507, Rsigma = 0.0740]
Data/restraints/ parameters	8164/0/374	8042/1080/605	7799/1086/604
Goodness-of-fit on F2	1.039	1.084	1.166
Final R indexes [I>=2σ (I)]	R1 = 0.0375, wR2 = 0.0866	R1 = 0.1361, wR2 = 0.3045	R1 = 0.1616, wR2 = 0.3721
Final R indexes [all data]	R1 = 0.0513, wR2 = 0.0924	R1 = 0.2004, wR2 = 0.3403	R1 = 0.1666, wR2 = 0.3743
Largest diff. peak/hole / e Å-3	0.61/-0.43	2.21/-0.97	2.96/-1.44

Density Functional Theory (DFT) Calculations

Figure 4A - 43. Spin density plots of **2-Co** and **3-Co** at an iso value of 0.003. Mulliken spin density (Co, ligands): **2-Co**: 2.25, -0.25, **3-Co**: 2.41, -1.54. Plots were generated in ORCA using orca_plot as gaussian cube files with a grid density of 100 x 100 x 100 then modeled in Avogadro.

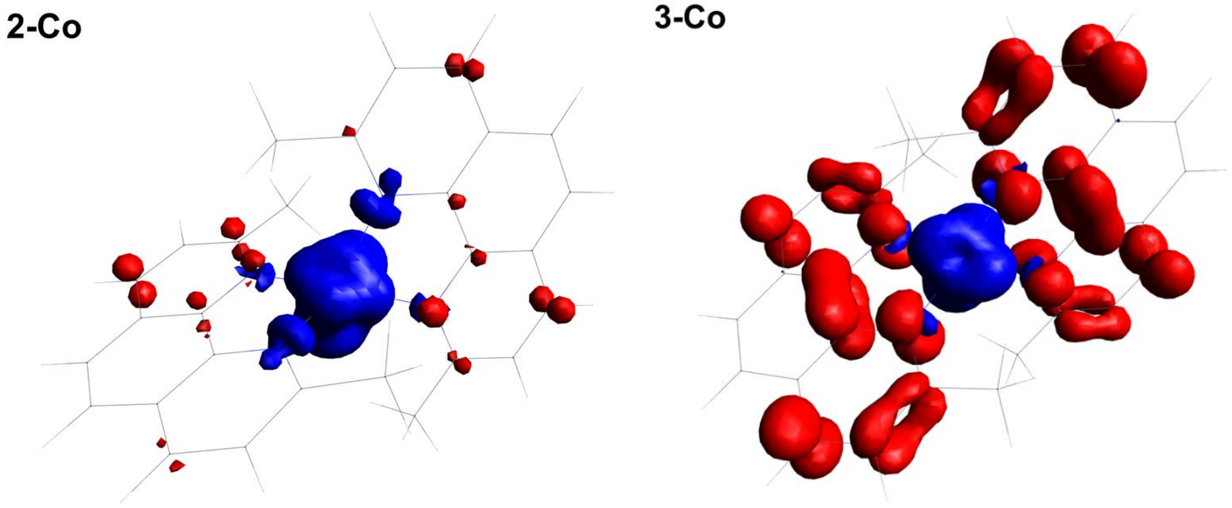

Table 4A - 4. Mulliken Spin Density on Ligand vs. Cobalt

	2-Co	**3-Co**
Spin density on Co	2.246546	2.411682
Spin density on ligands	−0.24655	−1.54113
Spin density on ligands − Spin density on N	−0.02311	−0.37009

Table 4A - 5. Corresponding Orbital Overlap from Broken Symmetry Calculations

	2-Co	**3-Co**
Orbital	overlap	overlap
0:00	1	1
1:00	1	1
2:00	1	1
3:00	1	1
4:00	1	1
5:00	1	1
6:00	1	1
7:00	1	1
8:00	1	1
9:00	1	1
10:00	1	1
11:00	1	1
12:00	1	1

Table 4A - 5. Corresponding Orbital Overlap from Broken Symmetry Calculations continued.

13:00	1	1
14:00	1	1
15:00	1	1
16:00	1	1
17:00	1	1
18:00	1	1
19:00	1	1
20:00	1	1
21:00	1	1
22:00	1	1
23:00	1	1
24:00:00	1	1
25:00:00	1	1
26:00:00	1	1
27:00:00	1	1
28:00:00	1	1
29:00:00	1	1
30:00:00	1	1
31:00:00	1	1
32:00:00	1	1
33:00:00	1	1
34:00:00	1	1
35:00:00	1	1
36:00:00	1	1
37:00:00	1	1
38:00:00	1	1
39:00:00	1	1
40:00:00	1	1
41:00:00	1	1
42:00:00	1	1
43:00:00	1	1
44:00:00	1	1
45:00:00	1	1
46:00:00	1	1
47:00:00	1	1
48:00:00	1	1
49:00:00	1	1
50:00:00	1	1
51:00:00	1	1
52:00:00	1	1
53:00:00	1	1

Table 4A - 5. Corresponding Orbital Overlap from Broken Symmetry Calculations continued.

54:00:00	1	1
55:00:00	1	1
56:00:00	1	1
57:00:00	1	1
58:00:00	1	1
59:00:00	1	1
60:00:00	1	1
61:00:00	1	1
62:00:00	1	1
63:00:00	1	1
64:00:00	1	1
65:00:00	1	1
66:00:00	1	1
67:00:00	1	1
68:00:00	1	1
69:00:00	1	1
70:00:00	1	1
71:00:00	1	1
72:00:00	1	1
73:00:00	1	1
74:00:00	1	1
75:00:00	1	1
76:00:00	1	1
77:00:00	1	1
78:00:00	1	1
79:00:00	1	1
80:00:00	1	1
81:00:00	1	1
82:00:00	1	1
83:00:00	1	1
84:00:00	1	1
85:00:00	1	1
86:00:00	1	1
87:00:00	1	1
88:00:00	1	1
89:00:00	1	1
90:00:00	1	1
91:00:00	1	0.99999
92:00:00	1	0.99999
93:00:00	1	0.99999
94:00:00	1	0.99999
95:00:00	1	0.99999
96:00:00	1	0.99999

Table 4A - 5. Corresponding Orbital Overlap from Broken Symmetry Calculations continued.

97:00:00	1	0.99999
98:00:00	1	0.99999
99:00:00	1	0.99999
100:00:00	1	0.99998
101:00:00	1	0.99998
102:00:00	1	0.99998
103:00:00	1	0.99998
104:00:00	1	0.99998
105:00:00	0.99999	0.99998
106:00:00	0.99999	0.99997
107:00:00	0.99999	0.99995
108:00:00	0.99999	0.99994
109:00:00	0.99998	0.99993
110:00:00	0.99998	0.99988
111:00:00	0.99997	0.99988
112:00:00	0.99997	0.99985
113:00:00	0.99997	0.99978
114:00:00	0.99996	0.99975
115:00:00	0.99994	0.99971
116:00:00	0.99992	0.99967
117:00:00	0.99982	0.99962
118:00:00	0.99892	0.99945
119:00:00	0.99764	0.99845
120:00:00	0.99344	0.99509
121:00:00	0.89337	0.60613
122:00:00	0	0.54091
123:00:00	0	0

Table 4A - 6. Optimized coordinates for **2-Co**.

C	5.920407	7.859000	4.281296
C	6.075995	6.456177	4.070344
C	5.098653	5.585557	4.425935
C	3.882298	6.049797	5.011957
C	3.689315	7.431072	5.202436
C	4.723189	8.349408	4.836342
H	7.000478	6.096116	3.629753
H	5.229257	4.518453	4.274210
C	1.592612	7.122920	6.153937
C	1.721161	5.733823	6.003519
C	2.849053	5.196166	5.431691
C	5.465888	10.544234	4.804538
C	6.690543	10.128511	4.253508

Table 4A - 6. Optimized coordinates for **2-Co** continued.

C	6.914598	8.803633	3.978322
C	0.363121	7.725634	6.750654
H	−0.231558	8.228963	5.979346
H	0.627001	8.477849	7.499883
H	−0.262537	6.965277	7.221761
C	5.232300	11.977917	5.145287
H	5.885234	12.634070	4.568219
H	5.440149	12.149821	6.207546
H	4.188671	12.251188	4.970884
N	4.495450	9.668916	5.063577
N	2.563122	7.952711	5.759809
H	7.451411	10.871688	4.042564
H	7.853641	8.477432	3.541889
H	0.914835	5.092082	6.341340
H	2.950849	4.122264	5.306869
Co	2.539470	9.964125	5.676234
N	1.511773	11.604903	5.087393
N	2.344394	10.852546	7.525611
C	1.439608	11.862781	7.461036
C	0.976902	12.248495	6.163176
C	0.965697	12.544459	8.598734
C	−0.015087	13.571369	8.449361
C	−0.469914	13.920717	7.221773
C	0.028206	13.281444	6.045716
C	2.866244	10.529520	8.708747
C	2.459845	11.180683	9.885340
C	1.505904	12.167447	9.838016
C	−0.364917	13.644618	4.749336
C	1.130574	11.976760	3.860659
C	0.189650	12.999882	3.670266
H	−0.091708	13.276722	2.660448
H	−1.093749	14.436628	4.607328
H	−0.384866	14.069751	9.339672
H	−1.211063	14.705848	7.109206
H	2.902016	10.881536	10.828928
H	1.170370	12.662435	10.744240
C	3.910874	9.465757	8.741925
H	3.631564	8.639799	8.083472
H	4.070643	9.091125	9.754014
H	4.861924	9.867673	8.374926
C	1.745643	11.273930	2.696672
H	2.833338	11.405280	2.703420
H	1.357075	11.659234	1.753707
H	1.539594	10.198833	2.740117

Table 4A - 7. Optimized coordinates for **3-Co.**

C	5.911765	7.877729	4.138619
C	5.985969	6.469294	3.894071
C	4.990439	5.634226	4.279567
C	3.815357	6.129541	4.929821
C	3.712114	7.524763	5.154597
C	4.757734	8.387725	4.784303
H	6.869626	6.078611	3.397077
H	5.067167	4.565805	4.096961
C	1.611656	7.285655	6.168536
C	1.673474	5.910850	5.998080
C	2.769414	5.321827	5.364633
C	5.602273	10.571795	4.742703
C	6.746083	10.129988	4.093638
C	6.908344	8.779836	3.781347
C	0.430728	7.938545	6.810756
H	−0.119252	8.544701	6.080723
H	0.747789	8.616793	7.609509
H	−0.250328	7.195061	7.230150
C	5.428484	12.005804	5.123197
H	6.236772	12.620078	4.722275
H	5.413421	12.114262	6.213533
H	4.473153	12.393219	4.752944
N	4.605433	9.726816	5.077608
N	2.606574	8.096832	5.748885
H	7.513822	10.850015	3.834143
H	7.803232	8.429422	3.276727
H	0.850494	5.300517	6.353799
H	2.811509	4.247532	5.212350
Co	2.791626	10.074740	5.851898
N	1.571343	11.497779	5.167042
N	2.402668	10.900933	7.628350
C	1.426288	11.864644	7.514212
C	0.995246	12.188881	6.216715
C	0.860095	12.506356	8.644587
C	−0.152446	13.494463	8.428290
C	−0.557857	13.817377	7.176666
C	0.003918	13.181171	6.023066
C	2.838910	10.567591	8.858487
C	2.318222	11.158987	10.000137
C	1.322244	12.132421	9.901554
C	−0.370648	13.482658	4.718333
C	1.185254	11.817280	3.910811
C	0.237346	12.798313	3.663887
H	−0.034867	13.020861	2.637904
H	−1.124613	14.239910	4.528291

Table 4A - 7. Optimized coordinates for **3-Co** continued.

H	−0.590332	13.981978	9.294273
H	−1.324745	14.571474	7.023159
H	2.699505	10.852938	10.967841
H	0.908525	12.598008	10.790828
C	3.910805	9.531237	8.923019
H	3.580473	8.607548	8.434538
H	4.189279	9.304083	9.953302
H	4.801523	9.875290	8.384869
C	1.825009	11.061220	2.794289
H	2.910908	11.210852	2.799286
H	1.434036	11.383547	1.827968
H	1.644180	9.985199	2.902736